A Novel Inverse Charge Constant On-Time Control for High Performance Voltage Regulators

Syed Bari

Dissertation submitted to the faculty of the
Virginia Polytechnic Institute and State University
in partial fulfillment of the requirements for the degree of

Doctor of Philosophy
in
Electrical Engineering

Qiang Li, Chair
Fred C. Lee
Rolando Burgos
Jaime De La Ree
Alfred L. Wicks

February 16th, 2018
Blacksburg, Virginia

Keywords: voltage regulators, constant on-time control, fast transient, charge control, multiphase, adaptive control, interleaving

A Novel Inverse Charge Constant On-time Control for High Performance Voltage Regulators

Syed Bari

ABSTRACT

One of the fundamental characteristics of the microprocessor application is its property of dynamic load change. Although idle most of the time, it wakes up in nanoseconds to support sudden workload demands, which are becoming increasingly severe in today's multi-core processors with large core count. From the standpoint of its voltage regulator (VR) design, it must have very good efficiency at light loads, while also supporting a very fast transient response. Thus, the variable-frequency constant on-time current-mode (COTCM) control scheme is widely used in the VRs, as it can automatically reduce its switching frequency during light-load conditions. But, from transient point of view, it has some limitations in response to heavy-load demands by microprocessors; this is resolved by adding different nonlinear controls in state-of-the-art control schemes. These nonlinear controls are difficult to optimize for the widely variable transient conditions in processors. Another major issue for this ripple-based COTCM control is that when the combined inductor-current ripple in multiphase operation becomes zero because of the ripple-cancellation effect, COTCM loses its controllability. Therefore, the goal of this research is to discover a new adaptive COT control scheme that is concurrently very efficient at light-load conditions and also provides a fast and optimized transient response without adding any nonlinear control; hence providing a complete solution for today's high-performance microprocessors.

Firstly, the overview of state-of-the-art COTCM control is discussed in detail, and its limitations are analyzed. Analysis shows that one issue plaguing the COTCM control is its slow transient

response in both single and multiphase operation. In this context, two methods have been proposed to improve the transient performance of conventional COTCM control in single and multiphase operations. These two methods can effectively reduce the output capacitor count in system, but the ripple-cancellation and phase overlapping issues in multiphase operation are yet to be improved. This provides motivation to search for a new COT control technique that can resolve all these problems together.

Therefore, a new concept of inverse charge constant on-time (IQCOT) control is proposed to replace the conventional ripple-based COTCM; the goals are to improve noise immunity at the ripple-cancellation point without adding any external ramp into the system, and to improve the load step-up transient performance in multiphase operation by achieving natural and linear pulse overlapping without adding any nonlinear control. Additionally, the transient performance of the proposed IQCOT has been further improved by naturally increasing or decreasing the T_{ON} time during the load step-up or step-down transient period without adding any nonlinear control. As this transient property is inherent in proposed IQCOT control, it is adaptive to the widely variable transient requirements of processors, and always produces an optimized transient response.

In order to design the proposed control with high bandwidth for supporting fast transient response, an accurate high-frequency small-signal model needs to be derived. Therefore, a high-frequency model for the proposed IQCOT control is derived using the describing function method. The model is also verified by simulation and hardware results in different operating conditions. From the derived model it is found that the quality factor (Q) of one double-pole set varies with changes in duty cycle. To overcome this challenge, an auto-tuning method for Q-value control is also proposed in this dissertation.

A Novel Inverse Charge Constant On-time Control for High Performance Voltage Regulators

Syed Bari

GENERAL AUDIENCE ABSTRACT

High performance microprocessors are the heart of all the fascinating computing devices in use today- ranging from the large servers in data centers to the small smartphones. To supply power to these high performance microprocessors, obviously high performance voltage regulators will be required and the expectations from these voltage regulators are increasing day by day with the complexities of the modern microprocessors. The main focus of this research work is to investigate the state-of-the-art control methodologies of today's voltage regulators, along with the study of their limitations for future challenging requirements, and therefore, propose some effective methodologies to overcome these limitations. In this regard, a novel control method, called 'Inverse Charge Constant On-Time (IQCOT)' control, has been proposed in this dissertation. The concept and the features of this new proposed control scheme, along with the comparison of its benefits with the conventional control methodologies, have been presented in detail in different chapters of this dissertation.

To My family

My Wife: Sajia Afrin

My Son: Ayaan Bari

My Father: Syed Golam Mustafa

My Mother: Selina Akhter

Acknowledgements

With immense appreciation in my heart, I would like to express my sincerest gratitude to my advisor, Dr. Qiang Li, for his continued support and encouragement, since I have been at Virginia Tech. Also, I want to thank him for his critical challenges and high expectations on me during every discussion, which drove me to use a fresh mind every time to pinpoint the problem, to self-exam my research work, and then seek for further improvement, instead of stopping by the satisfaction of the existing achievement. I have learned so much from his rich knowledge, logical thought and devoted attitude towards research, it will certainly influence my future career.

I would like to express my sincere gratitude to Dr. Fred C. Lee. His boundless energy, great vision, determination and persistency lead me to tackle all the challenges in my research work. It is his profound knowledge and rich experiences that helps me overcome the obstacles in the research path. It is his rigorous logic that prevents me from crashing into the dead end. It is him who shows me the strength and the right attitude to do research and pursue the beauty of power electronics. I believe everything I've learned from Dr. Lee will benefit my future career and life.

I am grateful to my committee members, Dr. Rolando Burgos, Dr. De La Ree, and Dr. Alfred Wicks, for their valuable comments and suggestions. They are always very helpful to inspire me to look at the issues from different angles, which helps me to see the bigger picture of my research.

I am also very grateful to Dr. Dushan Boroyevich, the CPES director, for all his supports from the beginning of my PhD life. I would like to give special thanks to all the wonderful CPES staffs who always come forward to help me out: Ms. Teresa Shaw, Ms. Teresa Rose, Ms. Marianne Hawthorne, Ms. Linda Long, Ms. Lauren Shutt, and Mr. David Gilham.

I want to acknowledge the valuable contributions of my teammates in Power Management Consortium (PMC) at Center for Power Electronics Systems (CPES). I'd like to thank all my current and ex-colleges: Dr. Pei-Hsin Liu, Dr. Yingyi Yan, Dr. Weiyi Feng, Dr. Daocheng Huang, Dr. Yipeng Su, Dr. Shuilin Tian, Dr. Xiucheng Huang, Dr. Weijing Du, Dr. Yan-Cun (Daniel) Li, Dr. Zhengyang Liu, Mr. Yuchen Yang, Mr. Chao Fei, Mr. Bin Li, Mr. Zhengrong Huang, Mr. Junjie Feng, Mr. Yi-Hsun (Eric) Hsieh, Mr. Mohamed Ahmed, Ms. Virginia Li, Mr. Yadong Lyu, Mr. Chen Li, Mr. Tao Liu, Mr. Zhongsheng Cao, Mr. Xuebing Chen, Mr. Shishuo Zhao, and Mr. Owen Jong. I find our culture with open-minded and diverse discussion is always mutually beneficial, and the wonderful tradition sparks many new concepts and influential research works.

I also appreciate all other colleagues and students outside PMC at CPES: Dr. Igor Cvetkovic, Dr. Marko Jaksic, Dr. Jun Wang, Dr. Hemant Bishnoi, Dr. Yang Jiao, Ms. Christina DiMarino, Mr. Qiong Wang, Ms. Bingyao Sun, Mr. Chi Li, Mr. Ming Lu, Ms. Yincan Mao, Mr. Ting Ge, Mr. Alex Chu, Mr. Joseph Kozak, Ms. Niloofar Rashidi, Mr. Alinaghi Marzoughi, Mr. Kumar Gandharva, Mr. Mudassar Khatib, Ms. Nidhi Haryani, and Ms. Grace Watt. It is a great fortune to have the opportunity to learn from each other in the past five years, and widen the knowledge of different areas in the vast power electronics field.

I want to thank Dr. Li Chen from Virginia Tech IP office for her support to submit two of my patent applications during my Ph.D. period. I want to express my heart felt gratitude to Dr. Dong Ha, for his extra-ordinary support during last five years. I also want to acknowledge the support from Dr. Brian Cheng (Texas Instruments), Dr. Hai Chen (Analog Devices), and Mr. Gregg Hughes (Analog Devices) during my internship period in Texas Instruments and Analog Derives.

I thank my parents, my parents in law, and my brother, who provide support and encourage throughout my further education. They are always there for me to charge my mental strength with endless love. Most importantly, I would like to thank my wife, Sajia Afrin, who supplies selfless support and understanding for all of my endeavors. Also, her thoughtful care for my son, Ayaan, allows me to pursue PhD study courageously with no worries.

\

This work was also supported by the members of Power Management Consortium at CPES (3M Company, Analog Devices, Chicony Power Technology Co., Ltd., CRRC Zhuzhou Institute Co., Ltd., Delta Electronics, Dialog Semiconductor, East China Research Institute of Microelectronics, Efficient Power Conversion, Eltek , Huawei Technologies Co., Ltd., Infineon, Intel, Inventronics, Lockheed Martin Corporation, Murata Manufacturing Co., Ltd., Navitas Semiconductor, NXP Semiconductors, ON Semiconductor, Panasonic Corporation, Silergy Corporation, Texas Instruments, Valeo, VERTIV).

The author would like to thank Mr. Shufan Chan from NXP Semiconductors, for his great support and suggestions. This work was conducted with the use of SIMPLIS software, donated in kind by Transim Technology of the CPES Industrial Consortium.

Table of Contents

List of Figures

List of Tables

Chapter 1. Introduction

This chapter presents the motivations, objectives and overview of this dissertation. First, the latest trend and the requirements of high-performance microprocessors are discussed. The challenges of the state-of-the-art voltage regulator (VR) control schemes are investigated to fulfill the power-delivery demand of these high-performance microprocessors. A review in this field is provided, followed by the dissertation outline and the scope of research.

1.1 Research Background

High-performance microprocessors are at the heart of every computing system in use today, from the tiny autonomous embedded control system to large scale powerful networked super computer, as presented in Figure.1.1. The rapid pace of advancement of microprocessor technology has shown no sign of diminishing and this pace is expected to continue in future. To understand the challenges of the VR design for these microprocessors, the latest trends in microprocessors and their applications must be discussed first.

Figure 1.1 Microprocessors - the heart of today's computing world.

1.1.1 Latest Trends in Microprocessors

The central processing units (CPUs) on a microprocessor are the basis of computation systems, such as laptops, desktops and servers. To achieve more powerful and effective computation and data processing, increasing numbers of transistors are integrated, and faster clocking is performed in today's microprocessors. The rapid growth in the use of transistors in microprocessors is reflected from the statistical data-where its growth increased from 2,300 to 1 billion transistors between 1974 and 2013 [A.1][A.2][A.3]. Also, based on the statistical data of clock frequency, the frequency has increased from 108 kHz to over 3 GHz operation [A.1][A.2][A.3]. The approximate power consumption (P_{CPU}) of a microprocessor is proportional to the clock frequency (f_{CLK}) and the square of the core voltage (V_{Core}) [A.4][A.5], which is:

$$P_{CPU} = C\ f_{CLK} V_{Core}^{\ 2}, \tag{1.1}$$

where C is the lumped parasitic capacitance of total logic gates. Based on (1.1), more transistors and higher levels of f_{CLK} significantly increase CPU power dissipation significantly, so the thermal issue will become a bottleneck for a high-performance CPU.

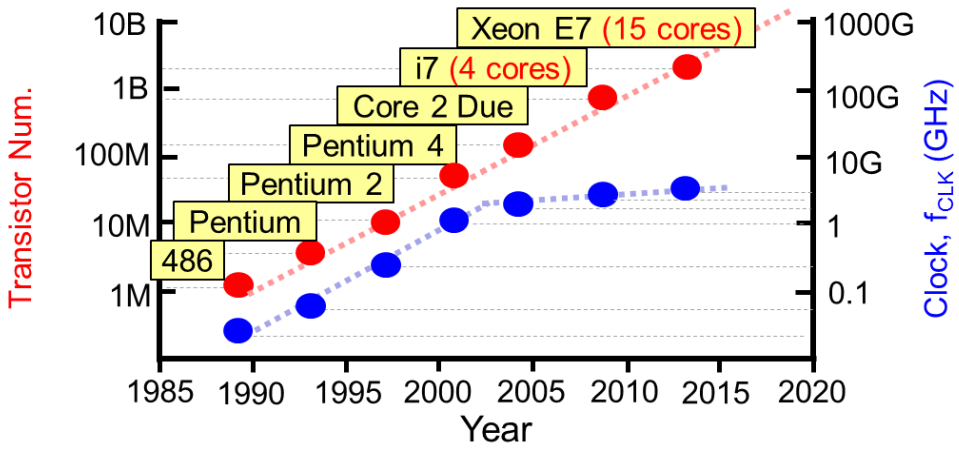

Figure 1.2 The trend in core counts on a microprocessor.

Since the multi-core technology has been introduced in 2005, the CPU performance can be boosted without increasing f_{CLK} higher than 5GHz, as shown Figure 1.2. This is because a multi-core CPU can perform multitasking by utilizing all cores at the same time to run different application software. In 2004, IBM introduced a 12-core POWER8 processor, while Intel announced a 15-core Xeon E7 processor in the same year. The core count keeps increasing every year due to the advancement of silicon technology [A.6][A.7][A.8]. According to the latest data up to August 2017, Intel Xeon Phi 7290F is operating with 72 cores in their processors targeted for mostly server application. Furthermore, clock frequency of each core can be adjusted based on its computational load demand, which helps to reduce the overall power dissipation, according to (1.1). Terminologically, thermal design power (TDP) is not the peak power of a CPU, but the maximum power which a CPU can draw for a thermally significant period while running software programs [A.5]. TDP is used to design the thermal operation point of the microprocessors. For example, Intel's Core 2 Duo E8300 with 2.83GHz clocking and 2 cores consumes 65W TDP, but the consumption of the latest Xeon E7 processor with 3.8GHz clocking and 15 cores only increases to 150W TDP. In order to further minimize TDP, each core has been powered by an individual voltage rail since 2013, such that V_{core} can also be adjusted dynamically according to its computation demand, as shown in Figure 1.3.

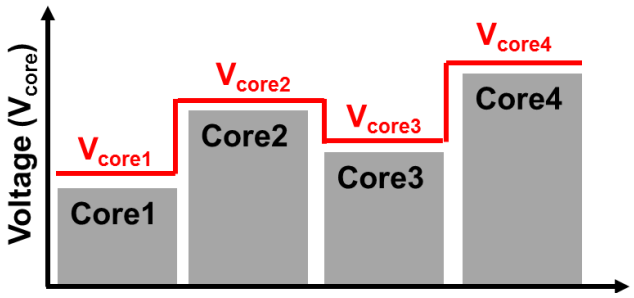

Figure 1.3 The multi-core operation in Haswell and Broadwell CPU.

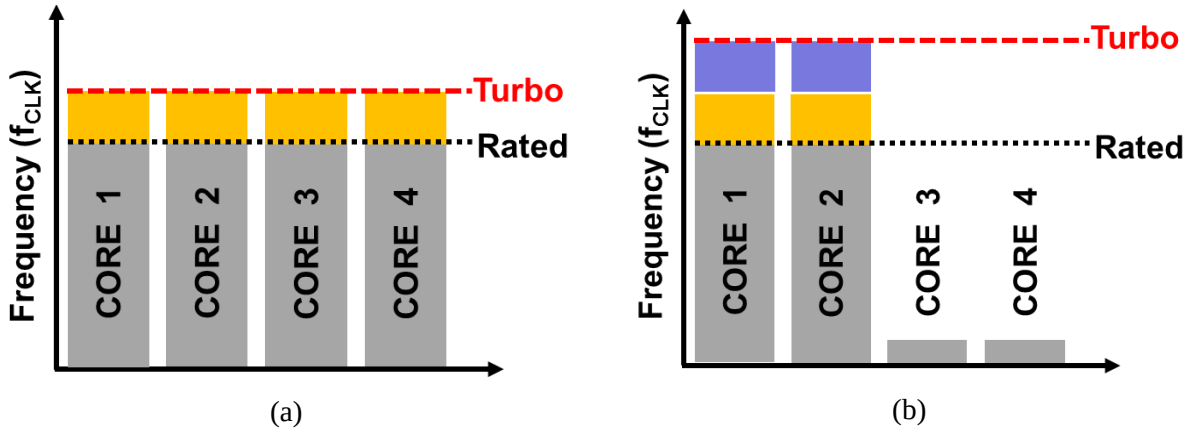

Figure 1.4 A quad-core CPU in turbo-boost operation with: (a) all cores, and (b) fewer cores [A.9]

As shown in Figure 1.4, turbo-boost mode forces many cores in a CPU activated with higher clock frequency (f_{CLK}) simultaneously for a short period of time, and the f_{CLK} can be even higher when smaller number of cores run in this mode [A.9]. The purpose is to enhance the core performance under a heavy workload, such as video gaming. However, the multi-core technology impose a new challenge to the external VR design, since a multi-core CPU can generate much higher transient current from its VR during turbo-boost mode [A.9][A.10][A.11], as shown in Figure 1.5.

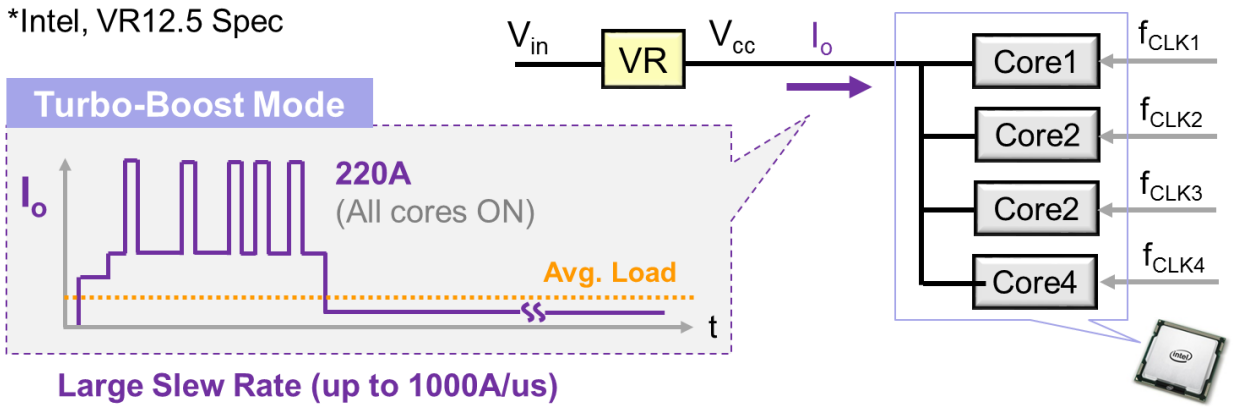

Figure 1.5 The instantaneous power demand in turbo-boost mode [A.10].

According to the instantaneous power demand example of Intel's latest CPU as Figure 1.5, the maximum power during turbo-boost mode can be at least two times higher than TDP [A.10]. For example, a Haswell CPU with TDP of 150W, the CPU takes only around 96A from its voltage regulator (VR) in TDP mode, but can sink around 200A in turbo-boost mode for a very short period of time [A.11]. Since activating turbo-boost mode can generate a large load current change with a high current slew rate (di/dt), a powerful multiphase VR with a very fast transient response is required to meet the load current demand.

1.1.2 Requirements for Microprocessor VRs

In general, multiphase buck converters are used as the VRs for microprocessors, as shown in Figure 1.6

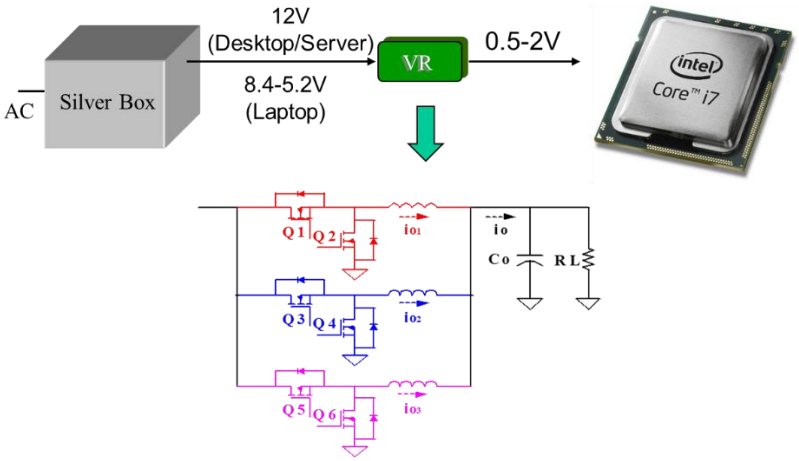

Figure 1.6 Multiphase buck converter as voltage regulator (VR) for microprocessor.

The high performance of today's microprocessors, mentioned in the previous section, has made their VR design very challenging. In this section, those challenges will be discussed briefly.

A. Large-Load Drive Capability with Fast Transient Response

A very obvious requirement for the VR is the incremental on-load demand as the number of transistors increases over time. While the number of cores is also increasing, the transitory spike load demand also must be addressed. Therefore, the VRs for these high-performance CPUs need to be ready to support very high load demands, which can be twice those of the TDP load. In turbo-boost mode the load requirement increases very quickly to a high value. This current increment can have a very high slew rate, of up to 1000 A/us for some applications.

To support this large microprocessor load current, multiphase operation is required in their VRs. Today's controllers most commonly support applications that need two to eight phases. As a general guideline, the maximum phase current should be kept between 30 to 40 A. Depending on budget, efficiency targets, and available cooling methods, the maximum phase current can be increased but it is highly recommended to do a thorough study of the ramifications before committing to the design. To support the large slew rate, all phases need to synchronize very quickly to increase load current at the fastest possible rate, otherwise a large undershoot at the output might be observed.

B. Higher Light-Load Efficiency

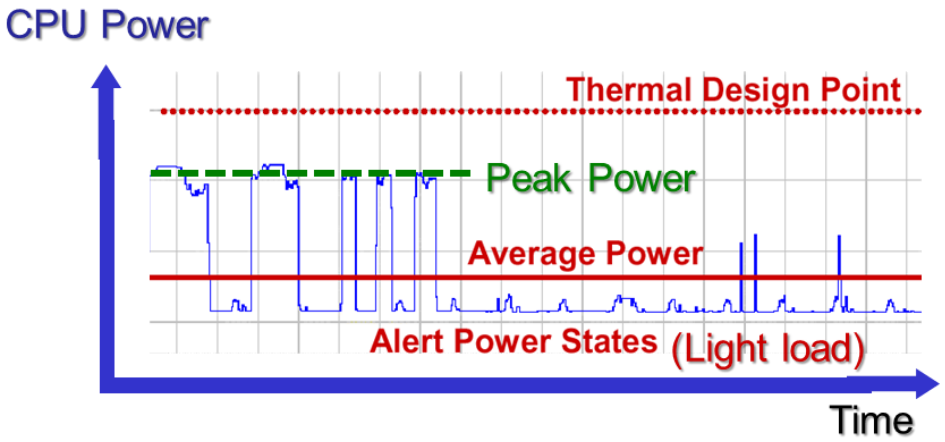

Figure 1.7 The instantaneous power demand in turbo-boost mode [A.10].

Figure. 1.7 shows that although there are some peak power spikes, the average power is very low for most of the CPU applications. Therefore, the VR must have very high light-load efficiency to achieve good overall system efficiency. This requirement is even more stringent for mobile devices in which battery life is very important.

C. Higher Power Density by High-Bandwidth Operation

The control-loop design of the VR needs to meet the load-line regulation with the well-known adaptive voltage position (AVP) control technique. In AVP control design, when the load current (I_o) increases gradually, the output voltage (V_o) needs to reduce gradually with a predetermined slope, defined as the load-line resistance (R_{LL}) [A.11][A.12]. Therefore, the steady state V_o can be defined as:

$$V_o = VID - I_o R_{LL}\,, \tag{1.2}$$

where, the VID (voltage identification) is the reference output voltage command sent from the CPU to the VR controller.

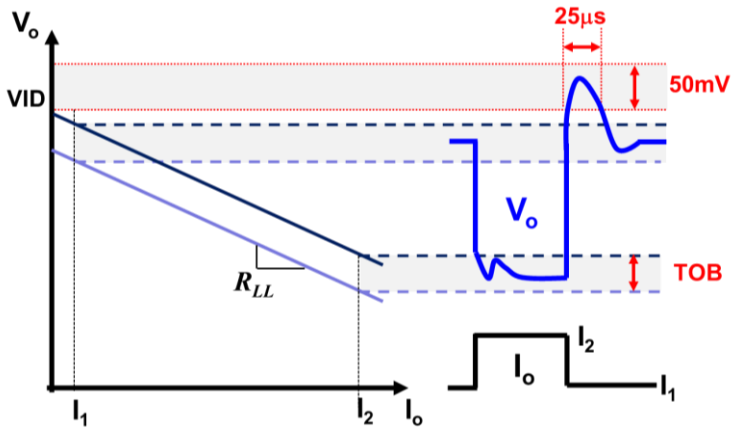

Figure 1.8 The relationship between the load-line specification and the permitted load transient [A.11][A.12].

Figure 1.8 shows the relationship between the load-line specification and the transient response waveform of V_o under the step-load change. For load step-up case, V_o should step down and settle within the tolerance band (TOB) around +/-20 mV. The voltage undershoot cannot be less than the lower boundary, because a larger undershoot may cause system lock-up or data corruption. For load step-down case, V_o should step up and settle within the TOB under a permitted transient overshoot window, whose voltage cannot exceed the overshoot relief (VID+50mV) and the duration of which is within 25uS. A larger overshoot can cause a higher processor operating temperature, which may result in damage or a reduced processor life [A.11][A.12].

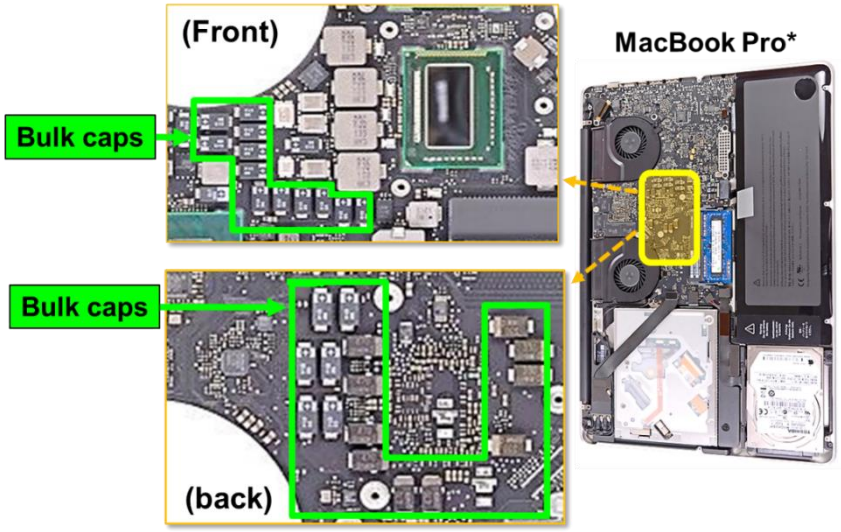

Figure 1.9 Motherboard of a laptop computer with an Intel i7 microprocessor.

To minimize the transient spike, there are different kinds of output capacitors along the power-delivery path in voltage regulators (VR). Figure 1.9 shows an example of today's motherboards, using Intel's quad-core i7 microprocessor for an Apple's laptop computer [A.13][A.14] It is found that the VR relies on many bulky output capacitors on the motherboards to meet the stringent AVP requirement by CPU, since the AVP response of the control loop is not fast enough; i.e., the control-

loop bandwidth (BW) is relatively low. These bulky capacitors not only occupy valuable motherboard space, but also increase the component cost. Since the trend of today's electronic devices suggests they will continue to become lighter and thinner in the future, the space for the CPU VR will be further limited. Therefore, the implementation of high-BW design is very critical to remove these bulky capacitors to improve the power density in today's motherboards.

To meet the stringent AVP requirement without any bulky capacitors, the BW target is identified and two design guidelines have been addressed to meet the AVP requirement: the first is maintaining a sufficient phase margin at the control BW to prevent the peaking of closed-loop output impedance (Z_{oc}) from being higher than R_{LL}, and the second is to choose the output capacitors properly to avoid Z_{oc} peaking at the frequency range higher than the control BW design point [A.11][A.12][A.15][A.16].

D. Higher Duty-Cycle Requirements

Originally, the power delivery of CPU VRs directly steps down high input voltage (V_{in}) into low output voltage (V_o), so that the duty cycle is very small during normal operation. For server and desktop VRs, the 12V input from the AC/DC converter can range from 10.8-12.5 V, so the duty cycle can vary from 0.04 to 0.15, considering the possible V_o scaling from 0.5-2 V, as shown in Figure 1.10. [A.11][A.12][A.17]. However, the duty-cycle range becomes even smaller for conventional laptop VRs, because of a higher V_{in} of 19 V from the adaptor. Under such a small duty-cycle operation, it is very difficult to achieve good efficiency for switching frequencies higher than 300 kHz.

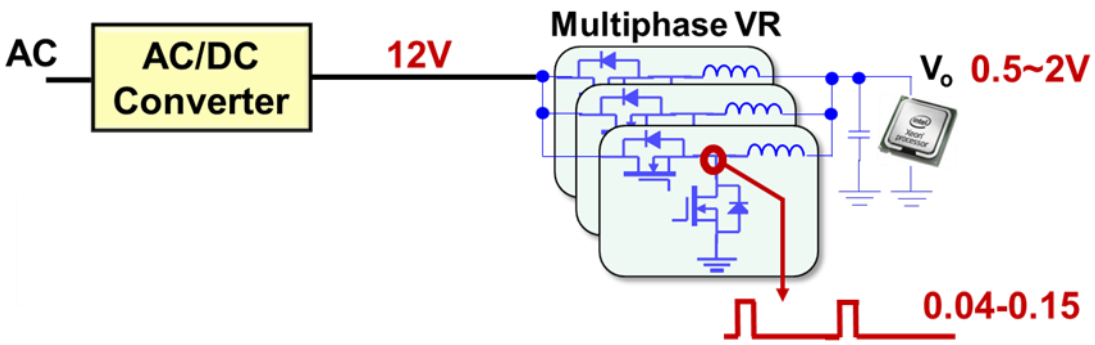

Figure 1.10 Power-delivery structure for server and desktop applications.

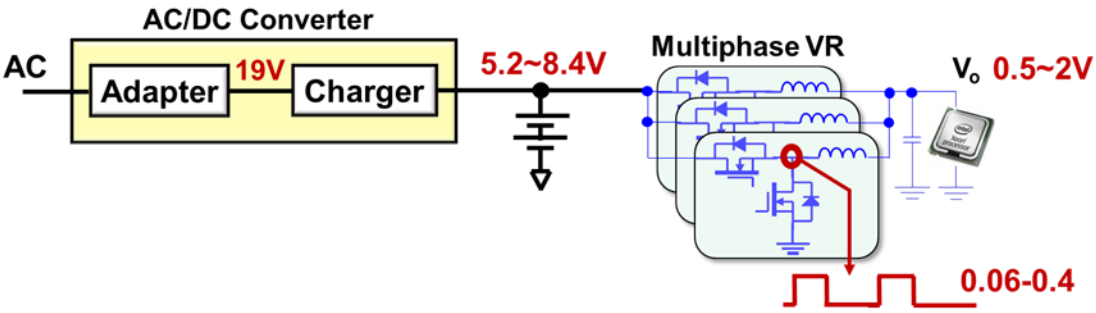

Figure 1.11 Power-delivery structure for mobile battery-powered electronic applications.

A two-stage power-delivery architecture has been introduced to boost the efficiency for higher switching frequency operation [A.18][A.19][A.20][A.21]. Recently, a similar concept has been applied into the latest laptop by utilizing the battery charger as the first-stage VR to step down 19V to a lower voltage, such that the operating duty-cycle range for the second-stage VR becomes higher. The V_{in} range of the second-stage VR is between 5.2-8.4 V, because two serially connected battery cells are placed at the battery charger output [A.22][A.23][A.24][A.25], as shown in Figure 1.11. The duty cycle can vary from 0.06 to 0.4, based on the possible V_o scaling from 0.5-2 V, as presented in Figure 1.11.

Therefore, from control standpoint, it is necessary that the control-loop design of the VR considers a wide duty cycle variation for different levels of V_{IN} and V_O operating conditions of the latest power-delivery structure; especially in multiphase operation with high phase count.

1.2 State-of-the-Art Control Schemes to Meet Latest VR Requirements

In this section, the performances of the existing control schemes are evaluated according to different requirements by the VRs of high-performance microprocessors. Then, their advantages and design challenges are discussed.

1.2.1 Overview of Constant-Frequency and Variable-Frequency Control

A. Constant-Frequency Peak-Current-Mode Control

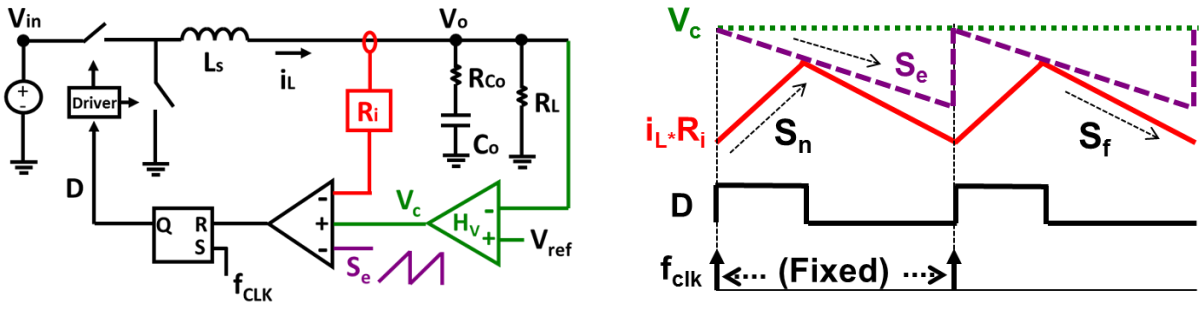

(a) (b)

Figure 1.12 Implementation of constant-frequency peak-current-mode control: (a) block diagram, and (b) operation principle.

Figure 1.12 shows the block diagram and operation principle of constant-frequency peak-current-mode (PCM) control [A.26][A.27][A.28]. The operation principle is that a fixed-frequency reference clock (f_{CLK}) initiates the turn-on instance, and then the inductor-current sense voltage

($i_L \cdot R_i$) is compared with the voltage difference between the compensator voltage (V_c) and an external ramp (S_e) to determine the turn-off instance. There are some benefits for this clocked operation in fixed-frequency PCM control. One benefit is that the efficiency and output filter can be optimized for a fixed f_{sw}. The second benefit is that it is easy to achieve interleaving in multiphase operation by phase shifting the f_{CLK} of each phase [A.29]. But it suffers from switching action delay in its transient response, which significantly hampers its ability to be applied in VR controllers where fast transient response is one of the primary requirements.

B. Variable-Frequency Constant On-Time Control

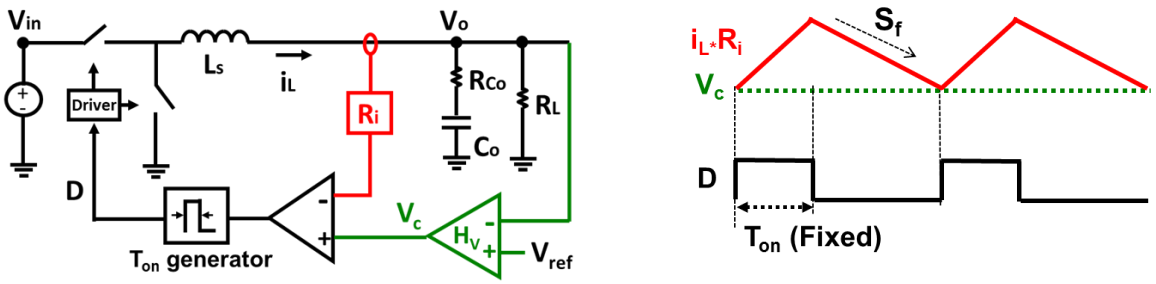

(a) (b)

Figure 1.13 Implementation of constant on-time current-mode control: (a) block diagram, and (b) operation principle.

Figure 1.13 shows the block diagram of current-mode control with constant on-time (COT) modulation [A.30][A.31][A.32]. The operation principle is that the compensator output V_c is compared with the inductor-current sense voltage to determine the turn-on instance, and then the fixed on-time pulse is generated by comparing a fixed threshold voltage (V_{TH}) with a fixed ramp in the on-time generator (S_r). The benefits of this variable frequency constant on-time over the fixed frequency peak current mode control are – it has smaller delay in transient which helps to

produce faster transient response; it also has higher efficiency in the light-load operation, which is very important factor for mobile applications; it also has the higher bandwidth design capability for better small signal property. All these benefits of variable frequency constant on-time control are discussed in the following sections.

C. Smaller Switching Delay for Constant On-Time Control

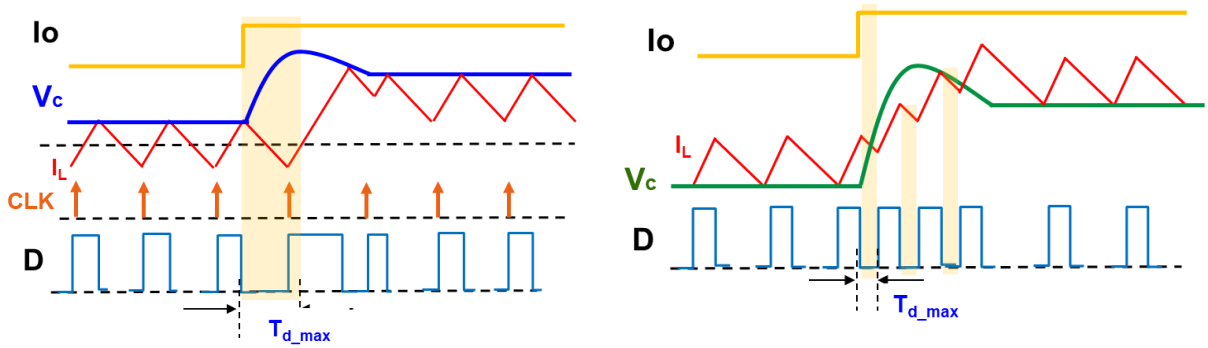

(a) (b)

Figure 1.14 Switching action delay at load step-up transient: (a) fixed-frequency PCM control, and (b) variable-frequency COTCM control.

One of the major disadvantages of fixed frequency PCM control is its slower transient response due to larger switching delay [A.33]. In Figure 1.14 the switching delay in current-mode control and COTCM control is compared. Figure 1.14 (a) shows clearly that after the load step-up transient occurs, the inductor-current increment has to wait for the next T_{ON} time for the next clock signal to trigger. The worst case is when the load transient happens right at the turn-off edge of the top switch. The maximum delay can be easily derived from the waveforms shown in Figure 1.14 (a), as follows:

$$\text{Max. Switching Delay, } T_{d\_max} = T_s\left(1 - D + \frac{D}{2}\right), \tag{1.3}$$

where, D is the steady-state duty cycle, and Ts is the switching period. From (1.3), the smaller steady-state duty cycle corresponds to larger switching-action delays. For VRMs with the same output voltages, in the worst case, the higher input voltages result in longer switching-action delays.

On the contrary, in COT control, this switching delay is much smaller, as shown in Figure 1.14 (b). This is because when the step-up transient occurs and V_C becomes high, the next on-time pulse does not need to wait for the clock signal. Therefore, in the worst case,

$$\text{Max. Switching Delay, } T_{d\_max} = T_{off_{min}}, \tag{1.4}$$

where, T_{off_min} is the minimum off-time in COTCM control, which is conventionally much smaller than the switching period. This aspect is particularly important for load transients with high slew rates, in which the first delay after the load transient is actually crucial. Therefore, for the heavy-load transients for VR applications, variable-frequency COTCM control performs better than fixed-frequency PCM control.

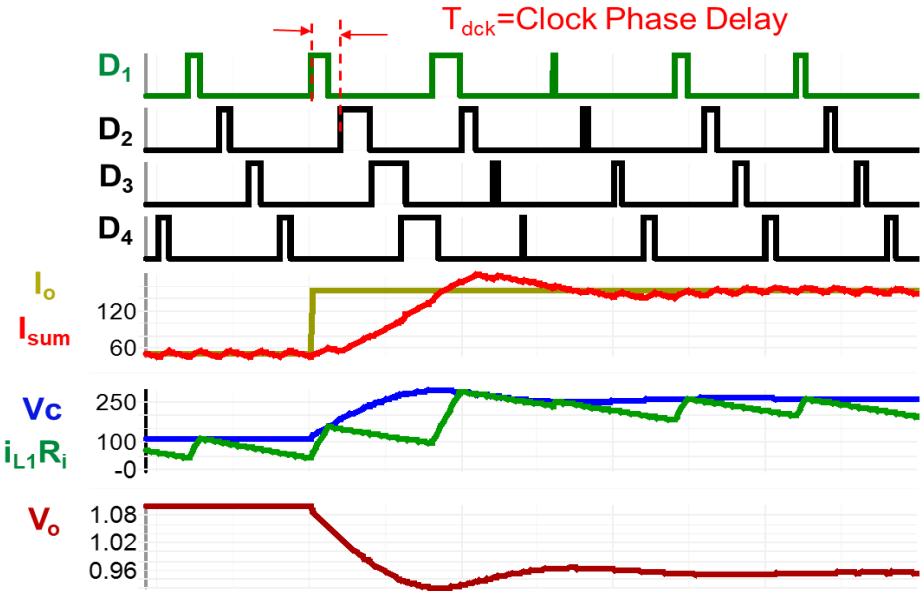

Figure 1.15 Switching action delay of fixed-frequency PCM control at load step-up in multiphase.

The load step-up transient in multiphase operation for fixed-frequency PCM control is presented in Figure 1.15, which shows that after a heavy load step-up with high slew rate, when the total inductor current (I_{sum}) must increase very quickly, the clock delay between phases (T_{dck}) is limiting the I_{sum} increment, which creates undershoot at the output. Obviously, this delay T_{dck} will be larger with lower operation frequencies and with smaller numbers of phases.

D. Higher Light-Load Efficiency for Variable-Frequency COTCM Control

Another advantage of COT control is that it is easier to improve light-load efficiency than when using constant-frequency control. Since COT control is a valley-current mode control, f_{sw} drops naturally with decreases in load without additional effort, when the inductor current falls into discontinuous-conduction mode (DCM) [A.30][A.32]. As for constant-frequency control, an additional COT loop or a pulse-skipping loop is needed to improve light-load efficiency [A.27]. The DCM mode in COT control in light-load operation is shown in Figure 1.16.

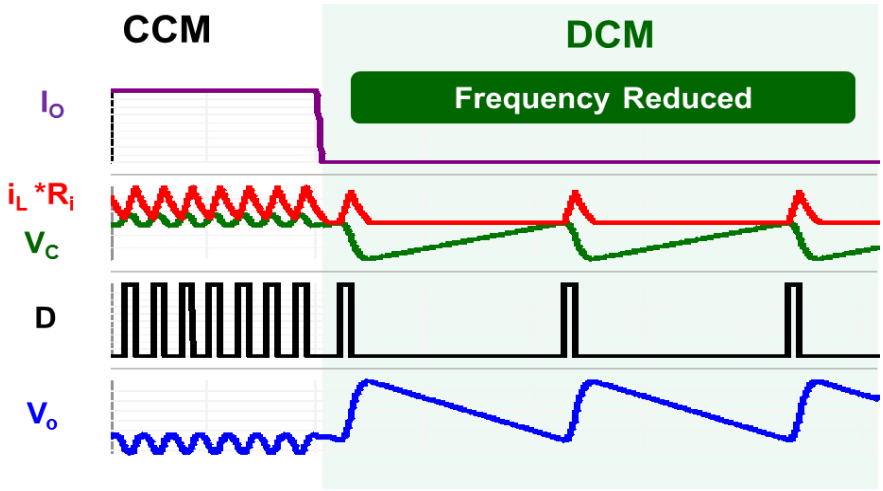

Figure 1.16 Light-load operation in DCM mode in COT control.

Since T_{ON} is fixed in COT control in Figure 1.16, Vo increases at light-load operation, as there is a very small sinking current from the output capacitor. Then Vo (also Vc) takes a long time to come back to its regulation point. As a result, the next pulse occurs after a long time. Obviously, the lighter the load, the lower the switching frequency in COT control. Conceptually, in multiphase operation, efficiency increases with reduction of phases as shown in Figure 1.17. When it moves to single phase, efficiency can further be reduced by going to DCM mode in COT control.

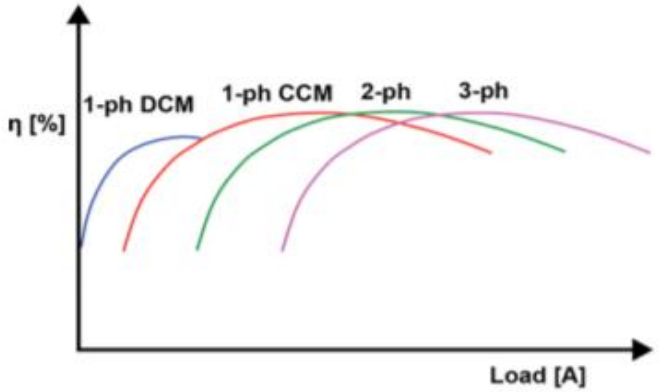

Figure 1.17 Efficiency vs phase number.

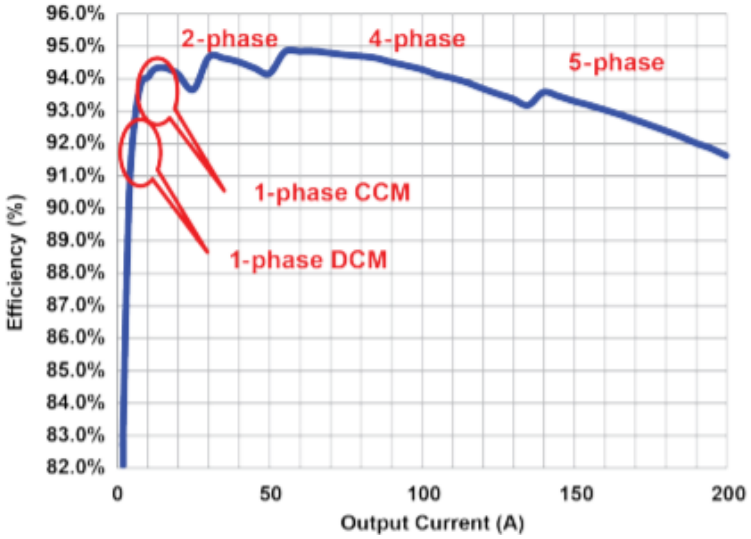

Figure 1.18 TPS53661 5-phase efficiency curve.

Figure 1.18 depicts an efficiency curve of a five-phase design using the TPS53661 controller and CSD95372B power stage [A.34]. The design called for V_{IN} = 12 V, V_{OUT} = 1.8 V, and used a switching frequency of 600-kHz and 150-nH inductors. An efficiency > 90% is maintained from 5A to 200A, a feat which for all intents and purposes is impossible to do with only a single-phase buck.

E. Higher Bandwidth Design for COTCM Control

In current-mode control, since the the inner current loop directly feeds back through inductor current, all high-frequency components are coupled to the modulator. When V_c generates a small-signal perturbation at frequency f_m to the modulator, the perturbed i_L contains many frequency components, including the fundamental component at f_m, the switching frequency component (f_{sw}), its harmonic (nf_{sw}), and the sideband components ($f_{sw}\pm f_p$, $nf_{sw}\pm f_p$), as shown in Figure 1.19.

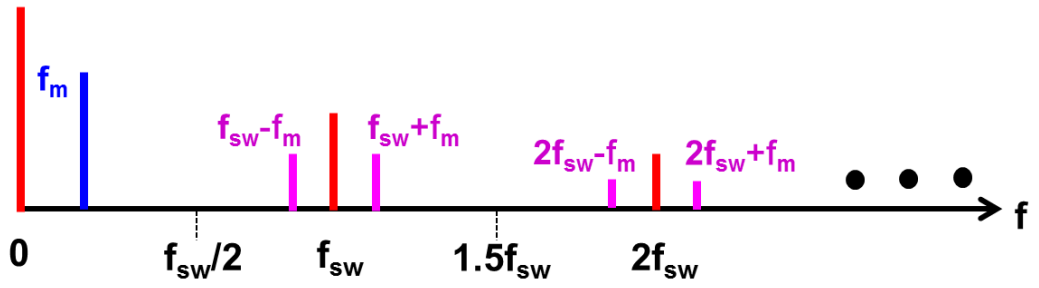

(a)

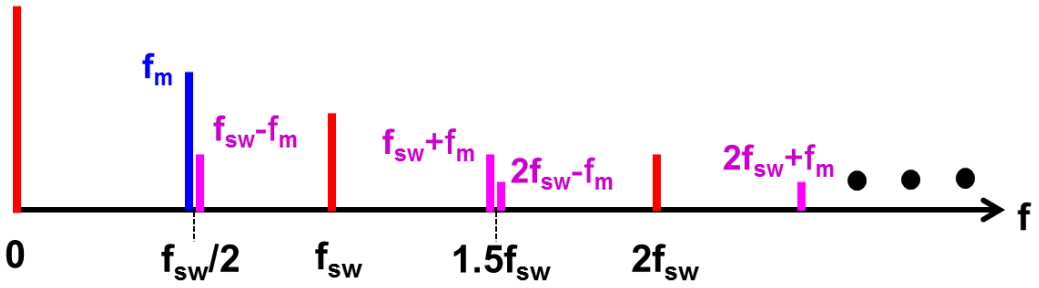

(b)

Figure 1.19 Spectrum of perturbed i_L in constant-frequency control: (a) $f_m << f_{sw}/2$, and (b) $f_m \approx f_{sw}/2$.

From Figure 1.19, it is found that when f_m moves toward $f_{sw}/2$, the primary sideband component (f_{sw}-f_p) also moves toward $f_{sw}/2$. When $f_m=f_{sw}/2$, the combination of two components causes an amplification effect of f_m at $f_{sw}/2$, so a double pole at $f_{sw}/2$ is observed in the transfer function of the open-loop gain with a closed-current loop (T_2) [A.35][A.36][A.37]. Furthermore, it is found that the duty-cycle change affects this double-pole damping, as shown in Figure 1.20. When D is close to 50%, the double pole becomes under-damped, and it is possible to cause a second crossover without a sufficient phase margin for the T_2 loop gain. In the case of a small D, the double pole can be over-damped, which lowers the phase margin. Therefore, the double pole at $f_{sw}/2$ and phase margin variation with duty cycle becomes a bottleneck for any high-BW design of constant-frequency control.

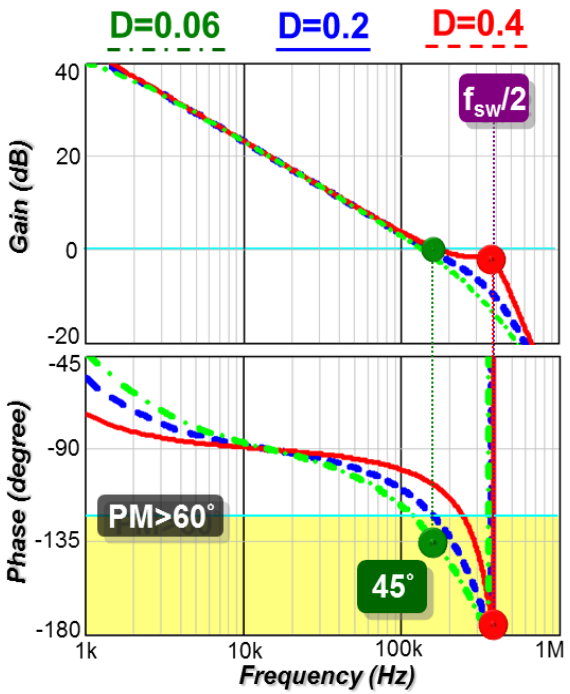

Figure 1.20 Q-value variation with duty cycle in T_2 of PCM control.

The high-bandwidth performance of constant-frequency PCM control is analyzed with a unified three-terminal switch model for current-mode control in [A.26][A.36][A.37]. The simplified T_2 loop gain is expressed as

$$T_2(s) \approx \frac{1}{R_i C_o s} \frac{1}{1+\frac{s}{\omega_2 Q}+\frac{s^2}{\omega_2^2}}, \text{ and} \tag{1.5}$$

$$Q = \frac{1}{\pi\left(\frac{s_n+s_e}{s_n+s_f}-0.5\right)} \tag{1.6}$$

where S_n and S_f are the rising and falling slopes, respectively, of inductor current. For a buck converter, $S_n=(V_{in}-V_o)R_i/L$ and $S_f=V_oR_i/L$. R_i is the current-sensing gain, L is the converter inductance, and C_o is the output capacitance. The model shows that the current feedback introduces a double pole at $f_{sw}/2$. When duty cycle (D) is higher than 50% and the external ramp compensation (S_e) is zero, its Q in (1.6) is negative, so the system becomes unstable. Therefore, the design of S_e is a critical parameter for stabilizing the system.

In case of constant on-time current mode (COTCM) control, based on the unified three-terminal switch model in [A.35][A.36][A.37], the current loop also contributes a double pole on the T_2 loop gain, but it is far away from $f_{sw}/2$ and the Q is always constant.

The model of simplified T_2 loop gain for COT control is

$$T_2(s) \approx \frac{1}{R_i C_o s} \frac{1}{1+\frac{s}{\omega_1 Q_1}+\frac{s^2}{\omega_1^2}}, \tag{1.7}$$

where $Q_1=2/\pi$, $\omega_1=\pi/T_{ON}$, and T_{ON} is the fixed on-time [A.26][A.36][A.37]. The COTCM control T_2 loop gain is shown in Figure 1.21, which indicates that the double pole caused by the direct inductor current feedback loop is located higher than $f_{sw}/2$ and the Q is always constant. With a small duty cycle ($D\approx0.1$), the double pole moves to $5\cdot f_{sw}$ and can be negligible, so the equivalent circuit model behaves like an ideal voltage-controlled current source. The ideal plant characteristic enables COTCM to design a high-BW control loop in wide D range, as shown in Figure 1.21. Since Q is constant, COTCM does not require any external ramp compensation.

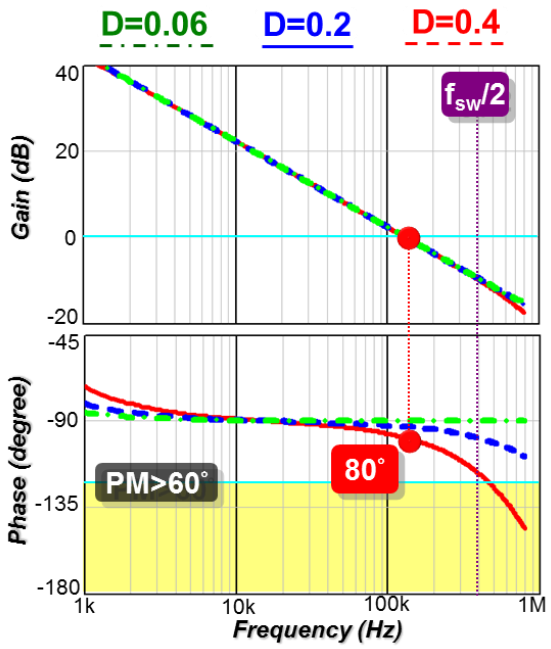

Figure 1.21 Effect of the side-band component on T_2 of COT control in high-BW design.

Analyzing the VR controllers used in the power-management IC industry reveals that many VR controller companies prefer COTCM for their VR controller for its various advantages.

1.2.2 Limitations of Constant On-Time Control for VR Applications

Although widely used in the industry, the COTCM control has some limitations in single and multiphase operations. These limitations are discussed in the following section.

A. Load Transient Response Limitations

Constant on-time (COT) control still has some limitations in load step-up and load step-down transient responses. When a fast and large load step-up is applied, as shown in Figure 1.22, inductor current cannot immediately increase. Therefore, the duty cycle becomes saturated and energy is supplied from the output capacitor, which creates an undershoot at the output. It is clearly seen that the longer the inductor current I_L takes to catch the stepped-up load, the larger the resulting undershoot will be. When the duty cycle is saturated (box area in Figure 1.22), Vc is higher than V_{iL} and T_{ON} cannot begin with the intersection of Vc and V_{iL} no longer behaving like they are in steady-state operation. Instead, a new T_{ON} is generated after the minimum off-time (T_{OFF_MIN}), which is required to charge the bootstrap capacitor of the high-side gate driver and which is fixed by the system power stage and load. Figure 1.22 shows that the inductor-current increment is limited by the length of T_{ON} and T_{OFF_MIN}. If T_{ON} is small and T_{OFF_MIN} is large, a large undershoot can occur at the output.

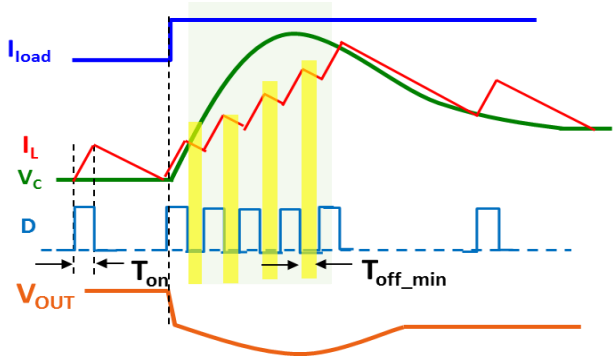

Figure 1.22 Transient-response issue at load step-up.

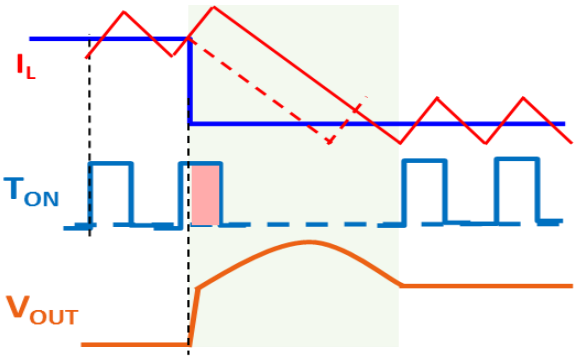

Figure 1.23 Transient-response issue at load step-down.

On the other hand, in the load step-down case, for a given power stage, the overshoot can be very large if load release occurs at the beginning of the T_{ON}, as shown in Figure. 1.24. In this figure, a load step-down occurs at the beginning of the second pulse, and the inductor current is expected to start decreasing right at that point. But because of the fixed T_{ON} time, I_L keeps increasing until T_{ON} expires; this extra inductor energy will be dumped in the output capacitor, and hence will create an overshoot at the output. It is easily understood that the value of the overshoot will be higher for a larger T_{ON}, provided that load step-down happens at the beginning of the T_{ON}.

B. Ripple-Cancellation Issue for Multiphase Operation

In COT control, for multiphase operation interleaving, the pulse-distribution method [A.38][A.39] is very popular because of its design simplicity. Figure. 1.25 shows a pulse-distribution structure for two-phase operation, in which the basic control method is as follows: When the summation of phase-inductor currents (i_{Sum}) is equal to the compensator output Vc, a T_{ON} pulse is initiated, and is called D_{Sum}, and then the phase-manager block distributes this D_{Sum} in phases. Although this structure is widely used for its many advantages, it suffers from slower transient response because of its aforementioned interleaving method.

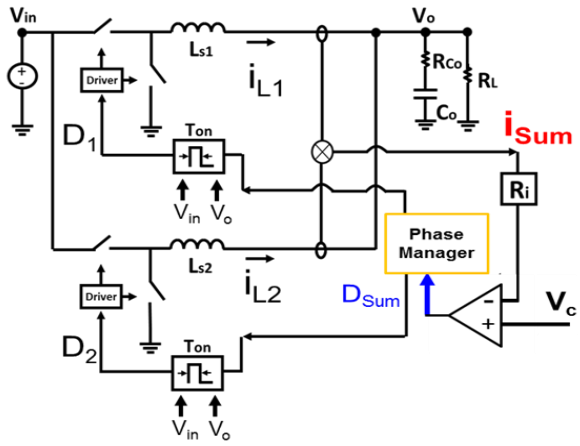

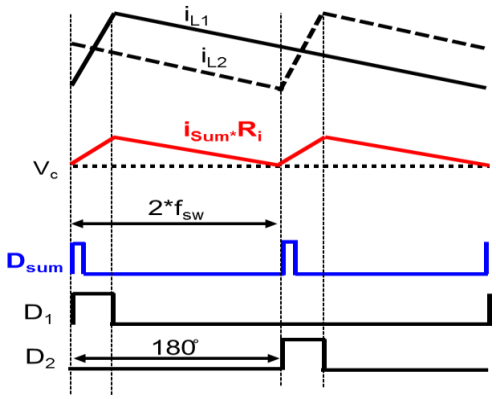

(a) **(b)**

Figure 1.24 Multiphase COT control with pulse-distribution method: (a) Structure, and (b) waveform.

One major issue of this pulse distribution method is noise sensitivity under the ripple-cancellation effect [A.38][A.40] of i_{Sum}. The magnitude ratio of i_{Sum} to i_{L1} in Figure. 1.26 indicates that there is one ripple-cancellation point at D=0.5 for two-phase and multiple points at D<0.4 for higher phase numbers. For four phases and D≈0.25, as an example, the current ripple of i_{Sum} around the cancellation point is too small, so any small noise can change the intersection point widely and cause duty-cycle jittering.

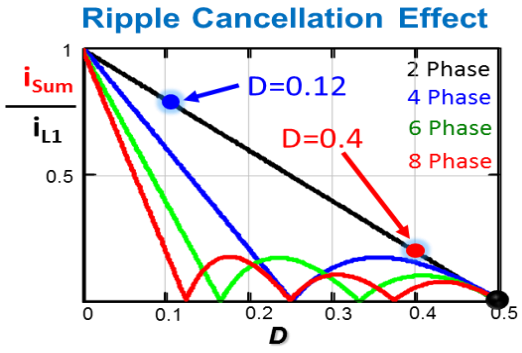

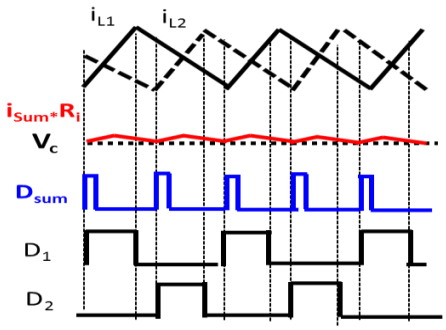

(a) (b)

Figure 1.25 (a) Ripple cancellation effect and (b) waveforms at ripple-cancellation point (at D=0.4 for two-phase operation).

C. Transient-Response Issue for Phase-Overlapping Limitation

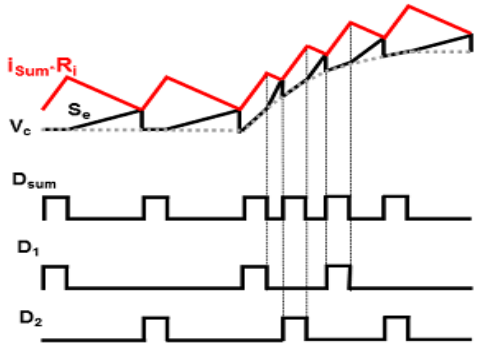

Figure 1.26 Phase-overlapping issue at load step-up transient.

Although the pulse-distribution structure is widely used for its many advantages, it suffers from slower transient response at load step-up because of its phase-overlapping limitation. In Figure. 1.27, the transient-response waveforms of COTCM with external ramp are presented for the load step-up transient. With the use of a large external ramp for better jittering performance, pulses will not be able to overlap, because the pulse-distribution method will hinder the total inductor increment at the transient and might create a large undershoot at the load step-up. If there is no external ramp or small external ramp, then Vc goes above the $I_{SUM}R_i$ in transient and makes the control loop to fail to operate. In that case, conventional COTCM controllers use different types of nonlinear controls to continue proper operation in transient instances. These nonlinear controls are very difficult to optimize for different transient conditions in VR applications.

1.3 Dissertation Outline

Today's high-performance multi-core microprocessors require their VRs to have large load currents with very fast dynamic steps. These VRs also need to support high-BW design to reduce output capacitance and to provide high efficiency at light loads, as microprocessors remain idle

most of the time. To support all these requirements, the COT control scheme with variable-frequency operation is very popularly used in recent VRs. In this variable-frequency configuration, a combined inductor-current ripple is used to achieve interleaving for multiphase operation. One issue with this configuration is that when the inductor-current ripple becomes zero to allow for the ripple-cancellation effect, the control becomes unable to work. State-of-the-art solutions add an external ramp to the system to solve this problem, but this solution degrades the small-signal property of the control. From the standpoint of the transient, one limitation of this COTCM control is its transient-response limitation in heavy load step-up and load step-down cases. In multiphase operation, limited pulse-overlapping capability at heavy load step-up transient might create a large undershoot at the output. State-of-the-art solutions add different nonlinear control methods in the transient to speed up the transient response; this solution is complex and difficult to optimize in different transient conditions triggered by microprocessors. Therefore, the research goal herein is to discover a new adaptive current-mode control scheme equipped with the following features: (1) utilizing COT control for its inherent benefits for VR application; (2) ability to work at the ripple-cancellation point without adding any external ramp; and (3) providing fast and optimized transient response without adding any nonlinear control to support the load-demand challenges of today's high-performance microprocessors.

This dissertation is organized into six chapters.

Chapter 1 provides an introduction to the background of the research in this dissertation. Today's high-performance multi-core CPUs demand high loads with very high slew rates from their VRs in order to support turbo-boost mode. These require the VRs to be able to support very high loads with very good transient responses while keeping the light-load efficiency very high,

since the average power levels in the CPUs are very low. The other key challenges in the VR design are the requirement for high BW to reduce passive components and to offer smooth operation capability with higher duty-cycle ranges. Current-mode control has been widely used to achieve AVP for powering microprocessors. For the VR applications, variable-frequency COT control is preferred over constant-frequency control, for their higher light-load efficiency, smaller switching delay, and higher-BW design capability.

Chapter 2 presents an overview of state-of-the-art COTCM control. Analysis shows that one issue plaguing this control method is its slow transient response, which is caused by its fixed T_{ON} operation. A method called 'FastAOT' control attempts to quickly increase the T_{ON} at load step-up and to also quickly decrease it at load step-down, to reduce the undershoot and overshoot at output or otherwise save the output capacitor. In multiphase, when the inductor-current ripple becomes very small because of the ripple-cancellation effect, control becomes very noise sensitive and creates jittering at the output. An external ramp is used to improve noise sensitivity, but at the expense of also slowing down the transient response. An adaptive external ramp method with variable slope is also proposed to improve the transient. These two methods can significantly improve the transient in conventional COTCM, but the fundamental ripple-cancellation and phase-overlapping issues in multiphase operation remain unresolved. Furthermore, the transient response in multiphase operation is also bottlenecked by the phase-overlapping limitation in CMCOT at the heavy-load step-up transient. State-of-the-art control methods solve this problem by adding various nonlinear control methods, which are difficult to optimize for widely variable transient conditions experienced in microprocessors. Thus, there is strong motivation to search for a new control technique that can resolve all these problems.

Chapter 3 proposes a new concept of charge-based control, called 'Inverse Charge Constant On-Time (IQCOT)' control, to replace the conventional ripple-based COTCM, with the goals of improving noise immunity at the ripple-cancellation point without adding any external ramp into the system, and to improve the load step-up transient performance in multiphase operation by achieving natural and linear pulse overlapping without adding any nonlinear control. Simulation and hardware test results in a standard VR platform are presented to verify the proposed concept. It is demonstrated that the ripple-cancellation issue of other ripple-based controls can also be eliminated by using proposed charge-based control in multiphase operation.

Chapter 4 discusses how the transient performance of the proposed IQCOT has been improved by naturally increasing or decreasing the on-time in the load step-up or step-down transient, and by naturally overlapping these extended pulses in multiphase operation without adding any nonlinear control. In today's VRs, high load current with very high slew rate is a very common requirement in microprocessor or memory applications. One issue of this ripple-based CMCOT control is that, in the heavy -load step-up transient, the increment of inductor current becomes limited by the on-time (T_{ON}) and minimum off-time (T_{OFF_MIN}) ratio in each cycle, which can create a large undershoot at the output. On the other hand, in the case of load step-down, if the load change occurs at the beginning of the fixed T_{ON}, a large overshoot can occur as well. For the multiphase-operation case, its limited pulse-overlapping capability is an issue at heavy-load step-up transient. State-of-the-art controllers add various nonlinear controls to the system to solve these issues. Test results for the proposed control with COTCM in a standard VR platform are also presented in this chapter.

In Chapter 5, a high-frequency model for the proposed IQCOT control is derived using the describing function. In order to design the proposed control with high-BW to support fast transient response, an accurate high-frequency small-signal model needed to be derived. The model is also verified by simulation and hardware results in different operating conditions. The derived model illustrates that the quality factor (Q) of one double pole set varies with changes in duty cycle, which complicates high-BW design for a wide duty-cycle range. To overcome this challenge, an auto-tuning method for Q-value control is also proposed in this chapter.

Chapter 6 provides conclusions of this research, with a summary of actions taken and directions for future work.

Chapter 2. Overview of State-of-the-Art Constant On-Time Control

The literature reviews in chapter 1 indicates that constant on-time control is a good candidate to meet today's VR challenges. In this chapter, state-of-the-art constant on-time current mode control is reviewed and some techniques are proposed to improve its limitations in single and multi-phase operation.

2.1 Review of Constant On-Time Current Mode (COTCM) Control

2.1.1 Review of Ripple based COTCM Control

A typical constant on-time (COT) control architecture with T_{ON} generating block (T_{ON} Gen) is shown in Figure 2.1 (a) while the operational waveforms are displayed in Figure 2.1 (b). When the inductor current sense voltage ($V_{IL}=i_LR_i$) touches the compensator output voltage (V_C), a new T_{ON} pulse is triggered by the duty cycle generating a flip-flop and the duty cycle (D), shown in Figure 2.1 (b), becomes high. At the same time, 'T_{ON} Gen' starts a V_{CAP} ramp to generate a fixed T_{ON} time

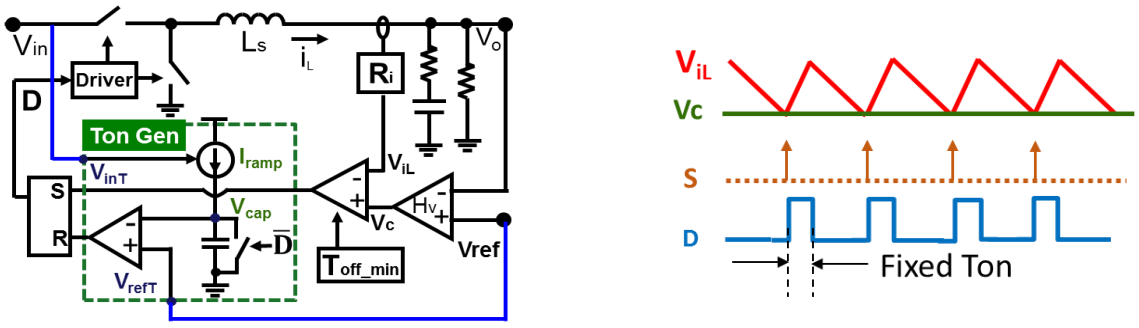

(a) (b)

Figure 2.1 Constant on-time control (a) control structure, and (b) Operation principle

and reset the flip-flip when V_{CAP} touches V_{refT} to end the T_{ON} pulse at D. At T_{ON} time, as high side gate is turned on and low side gate is turned off, inductor current I_L increases. After this fixed T_{ON}, the high side gate is turned off and again, I_L starts decreasing and sense voltage V_{IL} touches V_C again to start another new pulse.

$$f_{SW} = \frac{D}{T_{on}} \tag{2.1}$$

Furthermore, constant on time control has one significant drawback which is the variation of the switching frequency (f_{sw}) over the duty cycle range. The relationship between f_{sw} with duty cycle (D) and T_{ON} is shown in (2.1). It is clearly understood from (2.1) that if V_{in} or V_{out} changes, duty cycle (D) will be changed and as T_{ON} is constant in COT control, eventually converter switching frequency (f_{sw}) will be changed. One impact of this frequency variation with duty cycle is the efficiency drop when f_{sw} shifts higher. The second issue is that the beat-frequency ripples are introduced on both V_O and input current, when two DC-DC converters with slight frequency difference are connected.

$$T_{on} = k.D \tag{2.2}$$

$$f_{SW} = \frac{D}{T_{on}} = \frac{D}{k.D} = \frac{1}{k} \tag{2.3}$$

To solve this problem of variable switching frequency, nowadays, constant on time with adaptive on time (AOT) control is widely used in the VR industry. Basically, the AOT control structure is same as COT structure except T_{ON} is not constant at steady state over the duty cycle range anymore. In adaptive on time control, ideally, if T_{ON} is changed with duty cycle D (i.e. V_{in}

and V_{ref}) at steady state condition, as shown in (2.2), the operating frequency will be constant over the whole duty cycle range, shown in (2.3). Two implementation methods for AOT control are presently existed in the industry: one is using feed-forward control [B.1][B.2][B.3][B.4][B.5], and another is using Phase Lock Loop (PLL) [B.6][B.7][B.8].

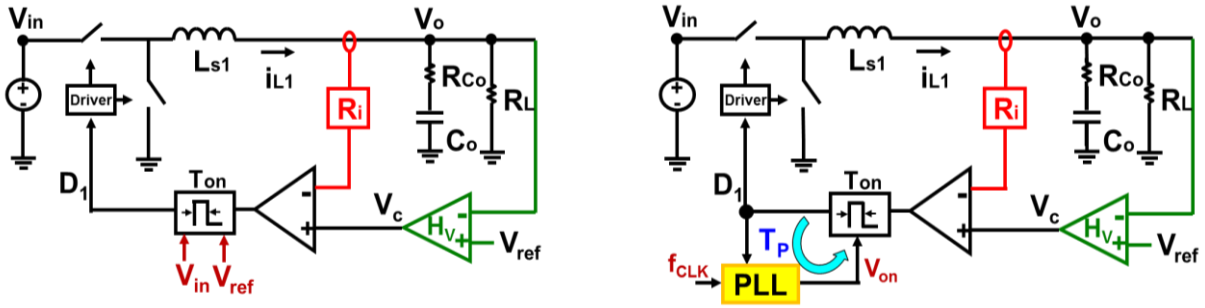

Figure 2.2 Adaptive on-time control with constant switching frequency operation: (a) using feed-forward control, and (b) using PLL loop

Figure 2.2 (a) shows the block diagram of the first method. T_{ON} is adjusted slowly by sensing V_{IN} and output voltage reference (V_{REF}) to the on-time generator, so f_{sw} variation becomes narrower. Figure 2.2 (b) shows the block diagram of the second method. The f_{sw} is slowly regulated by adjusting T_{ON} with the on-time control signal (V_{ON}) from a PLL loop, which locks the PWM signal with a fixed-frequency reference clock (f_{CLK}) in phase. Normally, PLL method is very accurate but suffers from additional PLL loop adjustment complexity for optimized operation. Therefore, V_{IN}/V_{REF} feed-forward method is widely used in the industry for its very simple and fast operation; though it may suffer from little inaccuracy issue for its feed-forward approach, which can be ignored for most of the applications.

2.1.2 Load Transient Response Limitations in COTCM Conrol

However, COT control still has some limitations in load step-up and load step-down transient responses. While a fast and large load step-up is applied, shown in Figure 2.3 (a), inductor current cannot immediately increase. Therefore, duty cycle becomes saturated and energy is supplied form output capacitor which creates an undershoot at the output. It is clearly seen that longer the inductor current I_L will take to catch the stepped up load, larger will be the undershoot. When the duty cycle is saturated, shown in box area in Figure 2.3 (a), V_C is higher than V_{IL} and beginning of T_{ON} cannot start with V_C and V_{IL} intersection like steady state operation any more. Instead a new T_{ON} is generated after the minimum off time (T_{OFF_MIN}) which is required to charge the bootstrap capacitor of the high side gate driver and fixed by the system power stage and load. From Figure 2.3 (a), it can be seen that, inductor current increment is limited by the length of T_{ON} and T_{OFF_MIN}. If T_{ON} is small and T_{OFF_MIN} is large, a large undershoot can occur at the output.

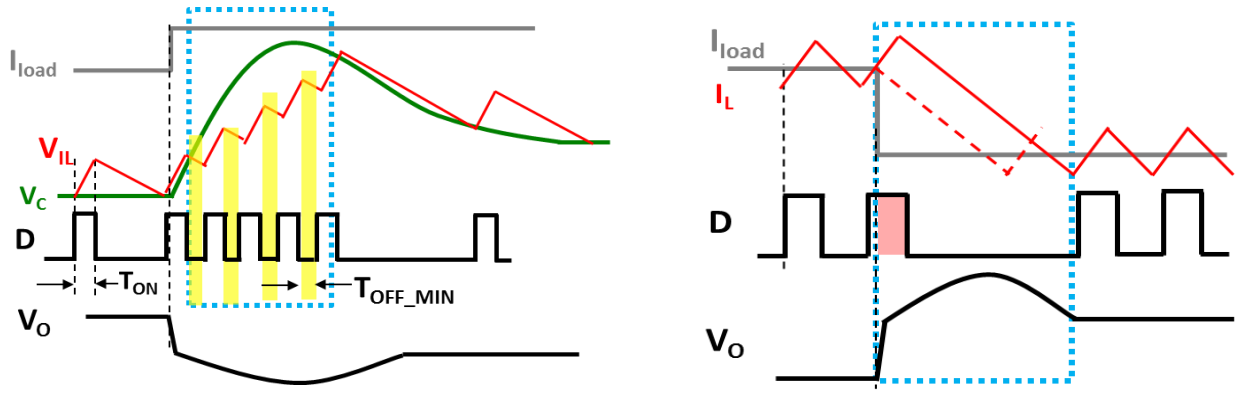

(a) (b)

Figure 2.3 Transient response limitation (a) load step-up, and (b) load step-down

On the other hand, in the load step-down case, for a given power stage, overshoot can be very large if load release is occurred at the beginning of the T_{ON} which is shown in Figure 2.3 (b). In

this Figure 2.3 (b) a load step-down is occurred at the beginning of the second pulse and inductor current is expected to start decreasing right at that point. But because of fixed T_{ON} time, I_L keeps increasing till T_{ON} expires and this extra inductor energy will be dumped in output capacitor and hence, create an overshoot at the output. It is easily understood that, value of overshoot will be higher for larger T_{ON}, provided that load step-down happens at the beginning of the T_{ON}

2.1.3 Prior Arts to Solve the Load Transient Issue in COT Control

Few attempts have been made to solve this issue before. A patent US20040257056 [B.9], published in 2004, proposed a method to replace the regular T_{ON} pulses by a longer pulse when output goes below the regulation point and the length of the longer pulse is equal to the amount of time the output stays out of regulation. A similar concept is proposed in a paper by J. Quintero, et al [B.10] for multiphase operation. The main problem of this method is that the over correction of V_O might be caused by a too long pulse and create a ring back at the output voltage shown in Figure 2.4. Another method is presented in patent US20130314060 [B.11], published in 2013. In this method when output of the compensator (which compares output voltage with reference voltage) goes above the regulation point, regular T_{ON} pulse is replaced by a predefined larger T_{ON}.

Maxim proposed 'Extended T_{ON}' feature which is demonstrated in their controller IC MAX17085B [B.12] where T_{ON} becomes twice when heavy undershoot occurs. Richtek also demonstrated similar kind of idea in their multiphase VR controller RT8888C [B.13]. In their control, when output goes below a certain predefined threshold voltage, then all the phases turned on together and T_{ON} also becomes extended to a predefined value fixed by the user. In the VR applications load step and load slew rate can vary a wide range. The disadvantage of this type of

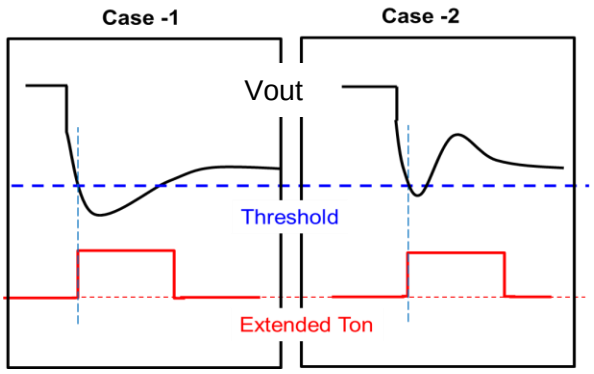

Figure 2.4 Ring back problem can be created by predefined threshold and predefined T_{ON} extension

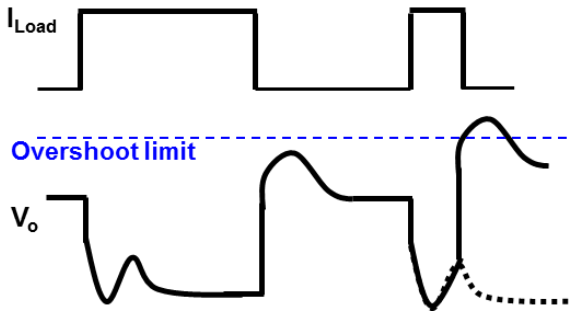

Figure 2.5 Load transient overshoot problem for V_O overcorrection at load repetitive case

predefined threshold and predefined T_{ON} extension is that if undershoot is not very large and just turned on the T_{ON} extension marginally, there is a chance of ring back in output voltage as shown in Figure 2.4. It is also very difficult to determine the proper value of the threshold which will be appropriate for all value of load amplitude and slew rate. If threshold is too close to regulation point to achieve very good transient performance, then larger T_{ON} might occur by a small undershoot or even by large noise at V_O which is shown in Figure 2.4 (case 2). If threshold is too far from regulation point to avoid this issue, then transient response might not be that good. Setting the length of predefined extended T_{ON} is also not very easy and suffer from similar kind of dilemma presented in case of threshold selection. It is also very difficult to determine the proper value of the threshold which will be appropriate for all value load and slew rate. For the high frequency

load repetitive case, load step-down can occur very quickly after load step up. In that case, as shown in Figure 2.5, V_O overshoot will be larger and it might cross the overshoot limit. That is why the 'ring-back' in V_O is dangerous for these VR applications.

2.2 Review of Constant On-Time Control for Multiphase Operation

The major issue of constant on-time (COT) control for multiphase operation is its complex interleaving. It can be understood easily that interleaving becomes challenging without any clock signal in variable frequency COT control.

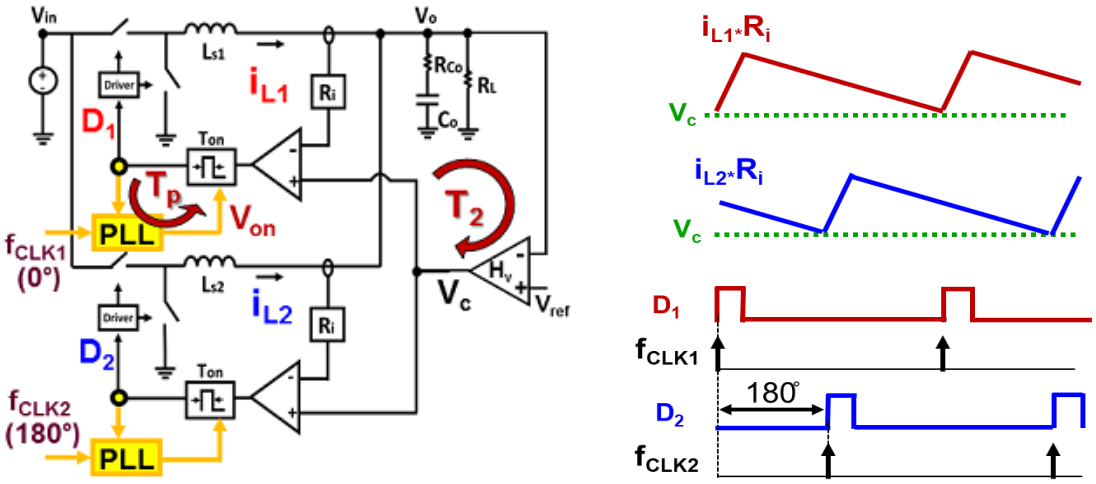

(a) (b)

Figure 2.6 Multiphase operation with PLL (a) structure, and (b) operating principle

Some commercial adaptive on-time controllers use PLL (phase locked loop) structure. Figure 2.6 (a) shows the two-phase configuration where pseudo constant frequency operation is achieved by adjusting T_{ON} of each on-time generator slowly with the on time control signal (Von) from the PLL loop in each phase. PLL forces each PWM signal to follow a fixed- frequency reference clock (f_{CLK}) in the same frequency and phase angle. It can be seen from the waveforms in Figure 2.6 (a)

that interleaving is achieved by phase-shifting the two clock signals in 180, Since the modulation of D1 and D2 is determined by the intersection between individual inductor current and V_C, the first benefit is less noise sensitive. Moreover, D1 and D2 can overlap naturally at step-up load transient. However, the first drawback is the circuit complexity in higher phase number, because each phase needs a PLL loop and a high-speed current-loop comparator. The second drawback is the complexity of PLL loop compensation, because Tp BW can affect its loop stability and system performance.

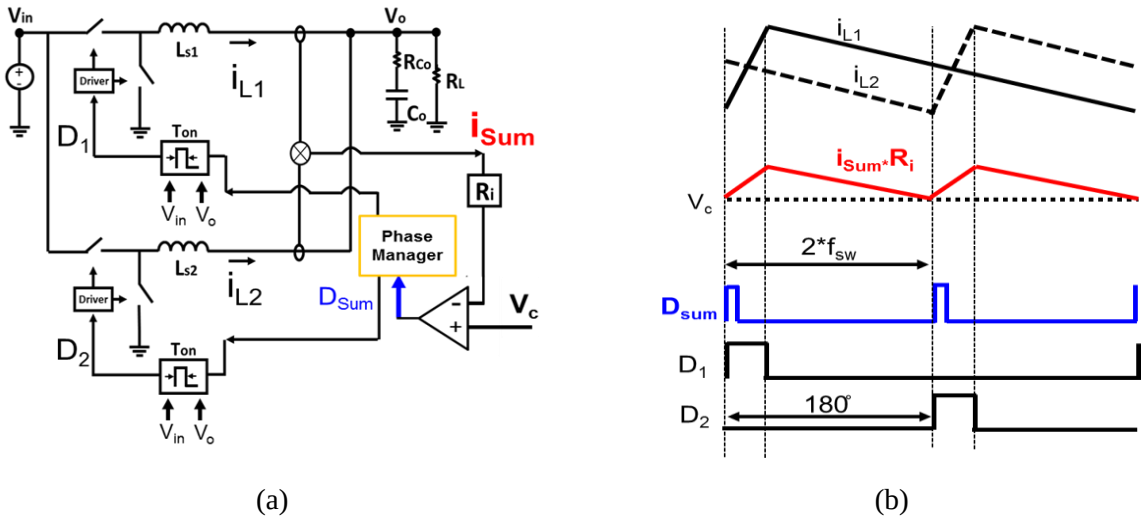

(a) (b)

Figure 2.7 Multiphase COT control with pulse distribution method: (a) structure, and (b) waveform

In constant on time control, for multiphase operation, pulse distribution method is very popular because of its design simplicity. In Figure 2.7, pulse distribution structure for 2-phase operation is shown where the basic control method is – when the summation of phase inductor currents (i_{SUM}) is equal to the compensator output V_C, a T_{ON} pulse is initiated which is mentioned as D_{SUM} and then the phase manager block distribute this D_{SUM} in phases. Though this structure is widely used for its many advantages, it suffers from slower transient response because of its aforementioned interleaving method.

2.2.1 Ripple Cancellation Issue in Pulse Distribution Method

One major issue is noise sensitivity under ripple cancellation effect [A.38][A.39][A.40] of i_{Sum}. The magnitude ratio of i_{Sum} to i_{L1} in Figure 2.8 (a) indicates that there is one ripple cancellation point at D=0.5 for two-phase and multiple points at D<0.4 for higher phase number. For two phases and D≈0.4 as example, the current ripple of i_{Sum} around the cancellation point is too small, shown in Figure 2.8(b), so any small noise can change the intersection point widely and cause duty cycle jittering. Obviously, when operating at D=0.5, control will not have any i_{Sum} ripple and will fail to operate. Furthermore, these ripple cancellation point count will increase with number of phase and will make the design more challenging, i.e., for 8-phase, ripple cancellation point is in D=0.12.

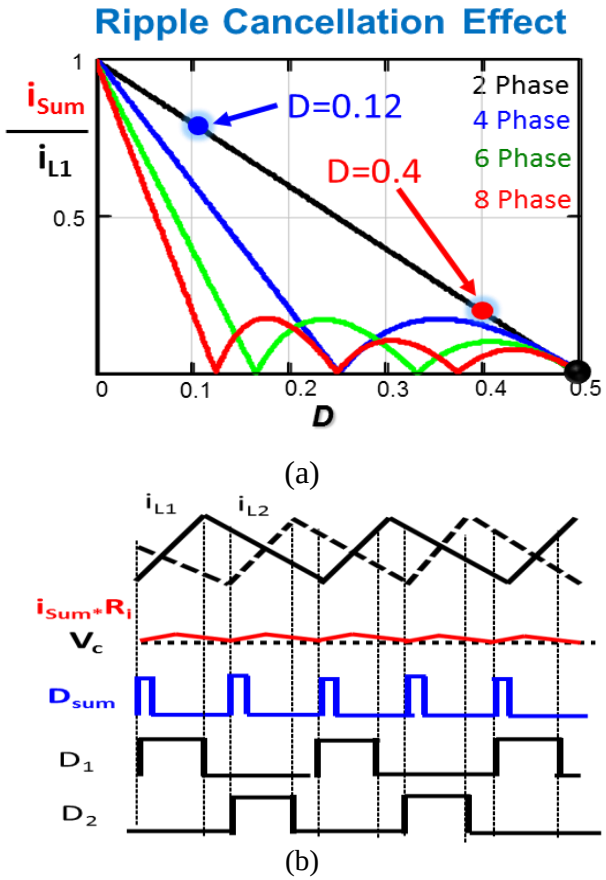

Figure 2.8 (a) ripple cancellation effect and (b) waveforms at D=0.4 for 2-ph

In this situation, adding external ramp [A.38][A.39] is the most common solution in industry which can easily be implemented by adding ramp signal to the system which is shown in Figure 2.9 (a). The waveforms of a 2-phase COTCM with external ramp at D=0.4 is shown in Figure 2.9 (b).

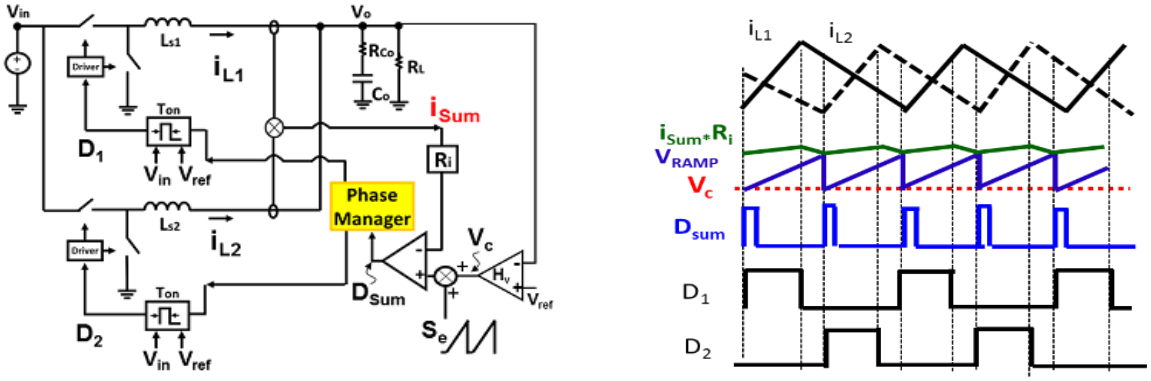

(a) (b)

Figure 2.9 Pulse distribution method with external ramp: a) Structure and (b) waveform

Figure 2.9(b), where it can clearly be seen that even if the I_{SUM} ripple is very small at D=0.4 for 2phase, when it interact with (V_C+V_{RAMP}) instead of V_C only, noise sensitivity or jittering can be much improved. TPS53625 [B.14], a 2 phase COTCM controller is tested with different amplitude of external ramps in same steady state condition (Vin=12V, Vo= 1V, I_{LAOD}= 14A) and results are presented in Figure 2.10(a) and Figure 2.10(b) where we can clearly see that jittering is smaller in Figure 2.10 (b) with larger value of ramp.

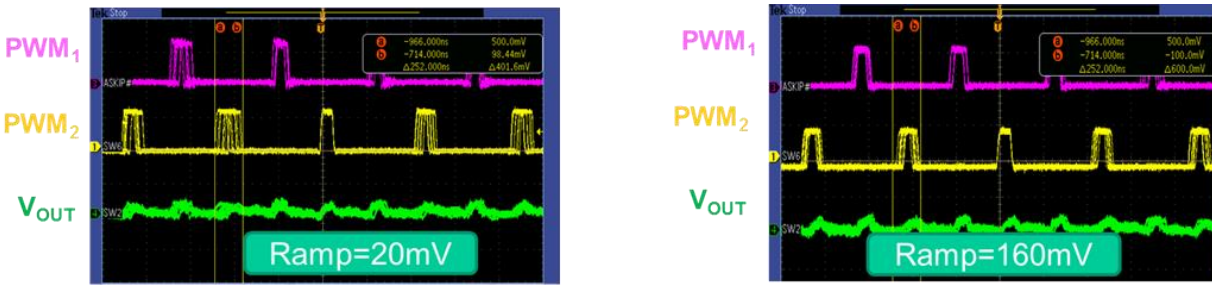

(a) (b)

Figure 2.10 Jittering Performance in TPS53625 with (a) 20mV ramp (b) 160mV ramp

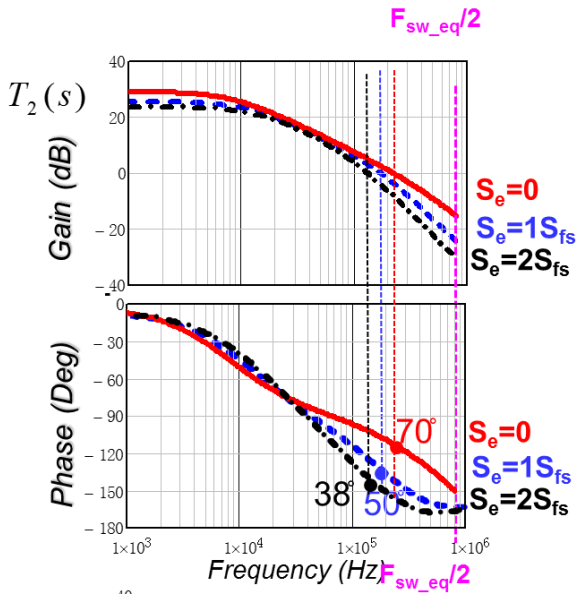

Figure 2.11 Loop gain of COTCM with additional external ramp

The small signal characteristic with external ramp is presented in [B.15]. The upper two pictures in Figure 2.11 show the gain and phase characteristics of constant on time control with external ramp compensation. We can see that with increment of the Se value, the high frequency pole is coming towards the low frequency pole and worsen the phase of the loop gain. In the same time the output impedance of the converter also starts becoming worse with the increment in the peaking. This peaking will make the transient response worse by creating undershoot or overshoot at the output.

2.2.2 Transient Response Issue in Multiphase Operation

Though pulse distribution structure is widely used for its many advantages, it suffers from slower transient response because of the interleaving method. In Figure 1.26, the transient response waveforms of COTCM with external ramp is presented in load step-up transient. If external ramp is large i.e. 100mV – 200mV for better jittering performance, it is difficult for the T_{ON} pulses overlap

because of pulse distribution method which will hinder the total inductor increment at transient and might create a large undershoot at load step-up.

In these cases, conventional state-of-the-art ripple based controllers add different types of nonlinear control to make each phase duty cycle overlap with other phases at transient. For instance, Richtek uses a threshold based nonlinear control called 'Quick Response (QR)' feature, shown in Figure 2.12, in their ripple based current mode COT controllers [B.13] to overlap the phases. In this method, when undershoot occurs at output, it is detected by a high-pass filter and when filter output crosses a user defined threshold voltage, a QR pulse is triggered. The width of this QR pulse is also defined by user. At transient, regular duty cycle pulses of all phases are overwritten by this QR pulse, as shown in Figure 2.13(a). In this context, similar type of nonlinear control called 'undershoot reduction (USR)' [B.16] is used by Texas Instruments. The circuit diagram of COTCM with USR feature is given in Figure 2.14. This USR feature is triggered when Vo goes below a certain threshold voltage and basically tries to force the duty cycle of all phases with some delay in

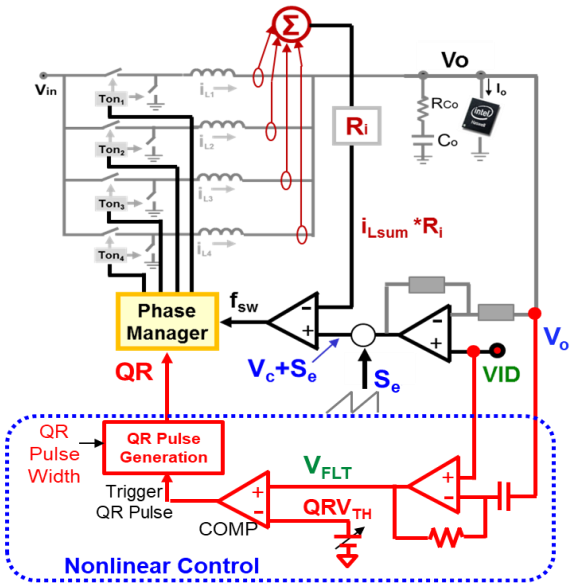

Figure 2.12 COTCM Control with 'QR' method by Richtek [B.13]

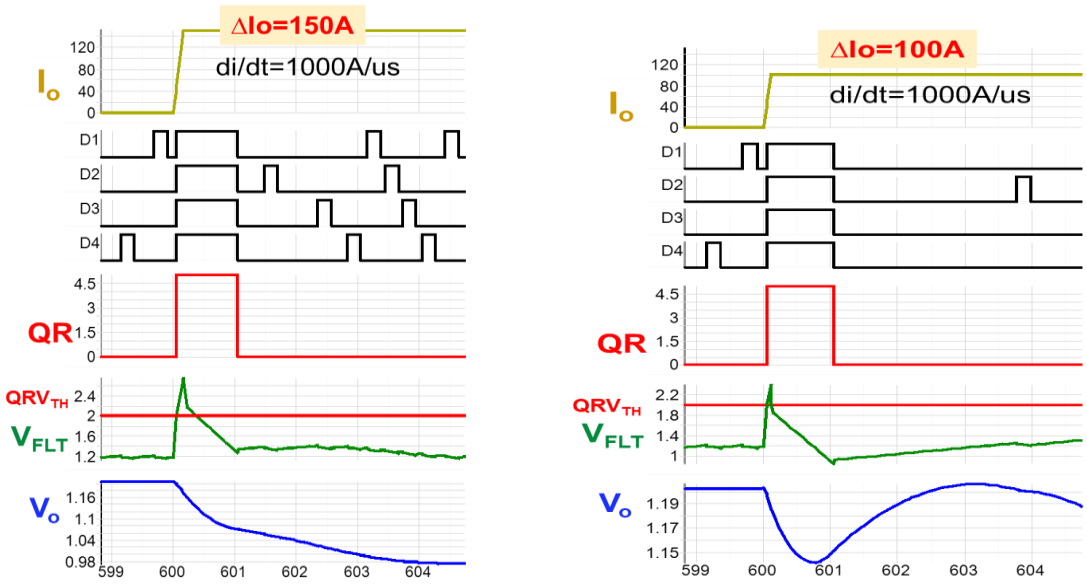

Figure 2.13 Transient response with ’QR’ method at load step of (a) 150A (b) 100A

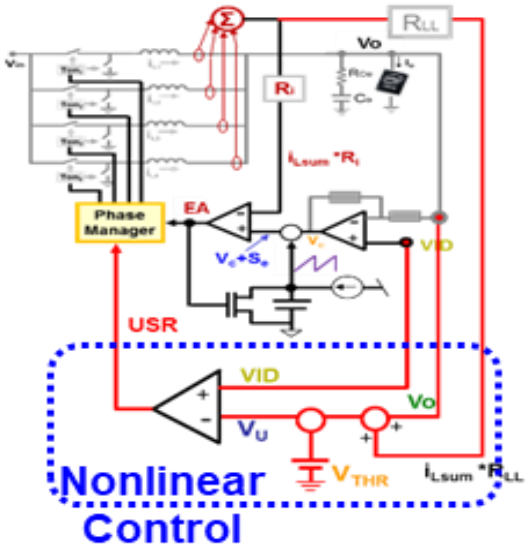

Figure 2.14 COTCM Control with ‘USR’ method by Texas Instruments [B.16].

load step-up transient. Maxim uses ‘Quick-PWM’ nonlinear control to overlap T_{ON} pulses at transient [B.17] .

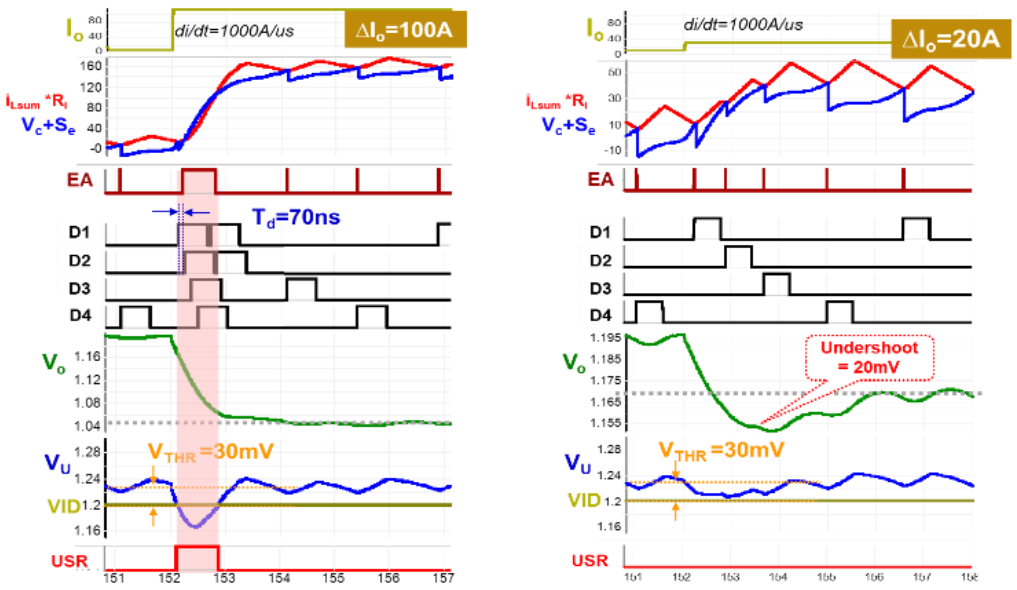

(a) (b)

Figure 2.15 Transient response with 'USR' method at load step of (a) 100A (b) 20A

The major issue of these nonlinear control is – they are not very easy to optimize for different transient setup. In different setup with different inductor or capacitor or different slew rate requirement, these nonlinear controls need to be revised to achieve an optimized transient performance, or there will be undershoot or overcorrection at the output. For example, when the 'Quick Response' method in Figure 2.13 (b) is applied to a 4phase VR with 150A load step, an optimized response is achieved, shown in Figure 2.13 (a). For the same setup when load step is reduced to 100A, shown in Figure 2.13 (b), output becomes over-corrected. Similarly, for USR method by Texas Instruments, when nonlinear control setup is make with V_{THR}=30mV and T_d=70ns, for 100A load step with di/dt=1000A/us Vo is perfect. But for the same setup when load step is lower down with same di/dt, Vo shows a 20mV undershoot as USR pulse did not trigger. Therefore, it can be said that although these nonlinear control improve the transient performance in

multiphase COTCM operation, they are not very easy to optimize for different transient condition in VR applications.

2.3 'Fast Adaptive On-Time (FastAOT)' Control for Transient Improvement

2.3.1 Proposed 'Fast Adaptive On-Time (FastAOT)' Control Concpet

The concept of achieving the best optimized transient performance is to initiate the T_{ON} increase/decrease as quickly as possible after the load transient to reduce the undershoot/overshoot and also to release the T_{ON} extension at the right time to avoid any overcorrection. A method has been proposed in this section, called 'Fast Adaptive On-Time (FastAOT)' control [B.18] which basically uses the derivative (dV/dt) of the V_O to increase or decrease the on time (T_{ON}) immediately after load step-up or load step-down to reduce the undershoot or overshoot. Since dV_O/dt produces a very fast detection the V_O undershoot or overshoot at transient, as proposed in the 'FastAOT' method, can initiate increase or decrease T_{ON} very quickly thus reducing significant undershoot or overshoot at the output.

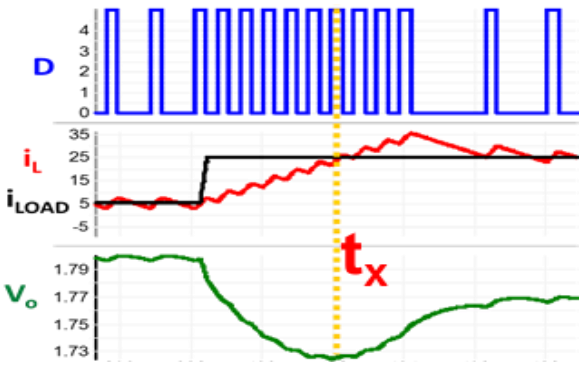

Figure 2.16 Review the cause of V_O undershoot at load step up

To achieve the proper T_{ON} extension in load step-up transient without any overcorrection problem, it is imperative to release the T_{ON} extension at the right time. For a better understanding of this transient response phenomenon at load step up, a typical undershoot case is shown in Figure 2.16. Since inductor current (I_L) is smaller than load current (I_{LOAD}) before the time instant tx the energy required by I_{LOAD} is taken from output capacitor thus causing the output voltage (V_O) to drop. When I_L becomes equal to I_{LOAD}, V_O becomes flat (where dVo/dt=0). When I_L becomes higher than I_{LOAD}, then V_O starts increasing as (I_L-I_{LOAD}) the current is charging the output capacitor. Therefore, in order to achieve the objective of having the best optimized transient performance without any overcorrection, T_{ON} should be extended up to tx point (where I_L<I_{LOAD}) so as to reduce undershoot and stop the T_{ON} extension at t_x to avoid any overcorrection; as I_L will be higher than I_{LOAD} after t_x, As proposed, the 'FastAOT' method uses dVo/dt to terminate the T_{ON} extension, which detects the valley of V_O (where dVo/dt=0) and eliminates any chance of overcorrection at the V_O thus producing a very fast and optimized transient response for COT control.

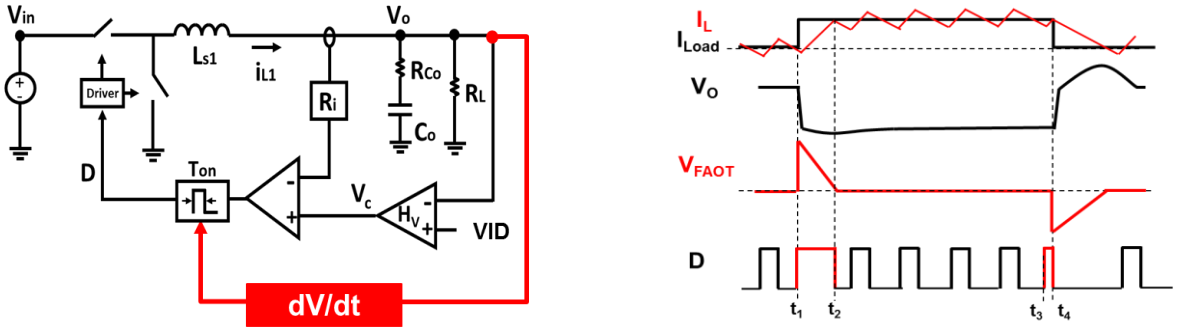

(a) (b)

Figure 2.17 Concept of proposed 'FastAOT' control (a) structure, and (b) operating principle

The Figure 2.17(a) shows the basic concept of the proposed method where the dV/dt block is used to create the derivative of the output voltage, called V_{FAOT}. The FAOT signal is inserted into

the T_{ON} generator block to increase or decrease the T_{ON} to reduce undershoot or overshoot. From Figure 2.17(b), it is obvious that V_O starts decreasing right after load step-up at t_1, and continues to decrease until the t_2 point, where I_L becomes equal to I_{Load} and starts increasing after t_2. Since dVo/dt is equal to zero at t_2, T_{ON} extension by using dVo/dt information will produce the maximum T_{ON} extension without encountering any ring-back issues. On the other hand, at the load step-down case, dVo/dt can detect the V_O change very quickly to truncate T_{ON} and thus can produce a significant V_O overshoot reduction. Hence, it can be stated that the proposed 'FastAOT' control can produce fast and optimized transient response for constant on time control.

2.3.2 Implementations of proposed 'FastAOT' Control

Implementation of the proposed 'FastAOT' method can be divided into two major steps. The first step is to create the FAOT signal by using a 'Transient Detector' block while the second step is to use the FAOT signal to modify T_{ON} in T_{ON} generator block. When V_O is passed through the 'Transient Detector' block, the dV/dt switching ripple also created at the output will create a jittering at the duty cycle and V_O if not eliminated. Hence, after the 'Transient Detector' block, a 'Ripple Eliminator' block is also added, as shown in Figure 2.18. In the case of the 'Transient Detector' block, a design of a conventional differentiator is used, however the dV/dt of the switching ripple will still be very high to eliminate. Therefore, 'FastAOT' control has proposed to use a band pass filter instead of a high pass filter or differentiator to fully or partially filter out the dV/dt of switching ripple noise. Then it becomes easier for the 'Ripple Eliminator' block to eliminate this noise completely. Detailed design guidelines for the band pass filter and ripple eliminator are given in the appendix A.

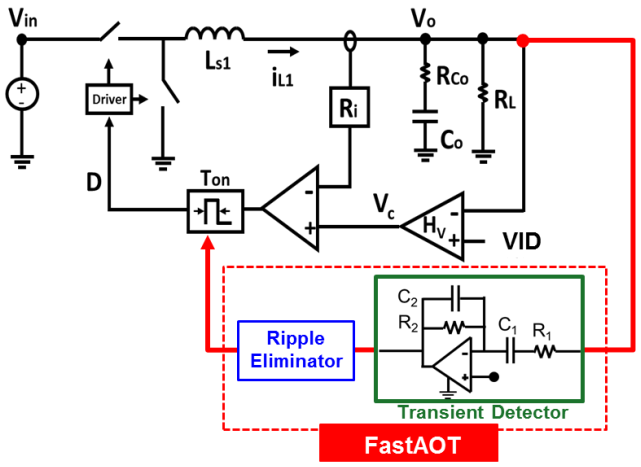

Figure 2.18 Implementation basic of proposed 'FastAOT' control

The FAOT signal can be created by using a dv/dt of both converter output (Vo) or compensator output (Vc). In comparison with Vo, V_C has less switching ripple noise than Vo, which is easier when using dV/dt but at the same time it might be slower than V_O (depending on the compensator design) which delays the response. Since V_C is the opposite polarity of Vo, if the dVc/dt is used, then it needs to be inverted before inserting it into the T_{ON} generator block.

In this dissertation, 3 basic implementation methods are shown. Implementation method 1 and 2 basically use the same 'Transient Detector' block but the 'Ripple Eliminator' and the T_{ON} pulse modification in the T_{ON} generator block are different. Method 3 shows how to use V_C instead of V_O to detect the transient and the modifications that need to be done in the 'Transient Detector block' to work with V_C. Implementation method 1 is presented here and two other methods are given in appendix A. The implementation of the proposed 'Fast Adaptive On Time (FastAOT)' is presented in this section, shown in Figure 2.19.

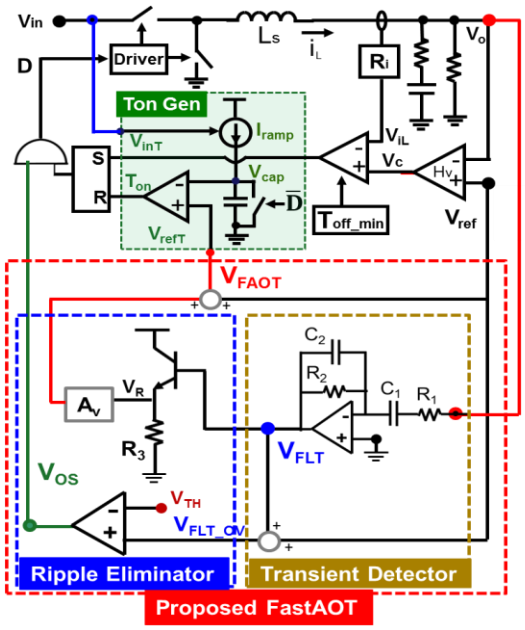

Figure 2.19 Implementation for proposed 'FastAOT' control

The load step-up response waveforms of COTCM control with proposed circuit are shown in Figure 2.20(a). When load step-up occurs, V_O drop because of AVP design, as seen in curve (a) in Figure 2.20(a). Then the bandpass filter passes only the high frequency part of the V_O undershoot and increases its output V_{FLT} as shown in curve (b) in Figure 2.20(a). Then in the next stage, an emitter follower is used to block the high frequency switching ripple at V_{FLT}, shown in curve (c) in Figure 2.20(a), where it is seen that the red band of V_{FLT} around zero in curve (b) does not exist in V_{FAOT} in curve (c). In this way, only the peak that is created in V_{FLT} by the V_{out} undershoot will pass through this stage and will be seen at the emitter follower output V_{FAOT} node. Then V_{FAOT} is used as the reference for the 'T_{ON} Gen' block (adaptive on time generator) and thus peak at the V_{FAOT} node will increase T_{ON} according to the undershoot magnitude shown in curve (c) and (d) in Figure 2.20(a).

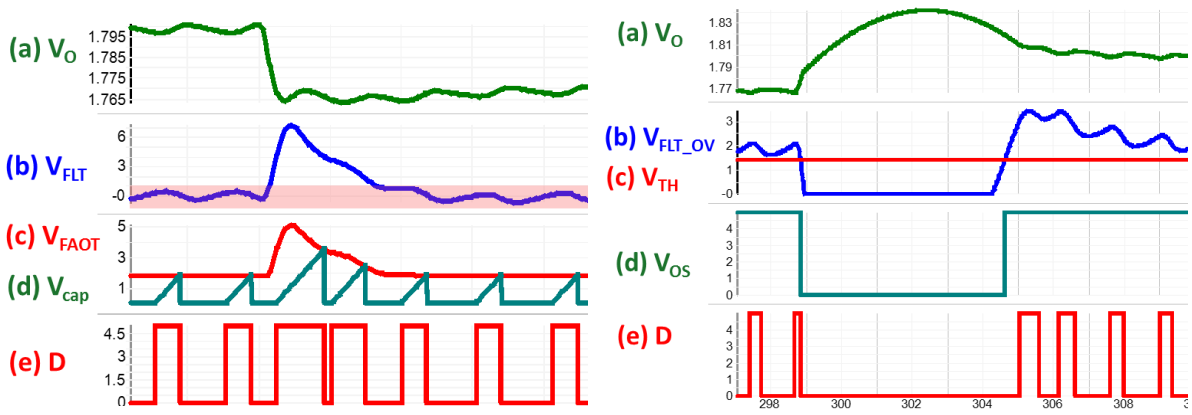

(a) (b)

Figure 2.20 Transient response of 'FastAOT' control: (a) load step-up, and (b) load step-down

In the load step-down case, when the band pass filter in proposed 'FastAOT' circuit detects any overshoot from the output of the converter, filters output, and V_{FLT} goes down very quickly. Then this signal is compared with predetermined threshold, like 80% of V_{REF} is set for example, to generate logic V_{OS} which eventually combined with T_{ON} using AND logic to expire T_{ON} immediately and reduce overshoot at output. In Figure 2.20(b), the waveforms at the load step-down condition are shown. It can also be observed that at the end of overshoot when V_O comes close to the regulation point, the on time extension occurs as well. This T_{ON} extension helps to eliminate the chance of any undershoot after the overshoot.

2.3.3 Optimization for Single Step Response at Load step-up Transient

The proposed method can achieve the fastest response from light load to high load in one step as shown in Figure 2.21(a) and Figure 2.21(b), where the indictor current can reach from initial value to final value in one step. We can also see that there is no overcorrection as T_{ON} extension ends up with dVo/dt. To achieve this single step response, voltage gain (Av) between V_{FLT} and V_R

signal needs to be very high. This will make the V_{FAOT} signal very high at transient and T_{ON} will be able to extend till the transient ends, as shown in Figure 2.21(a) and Figure 2.21(b) shows that single step response can be achieved smoothly in different load steps.

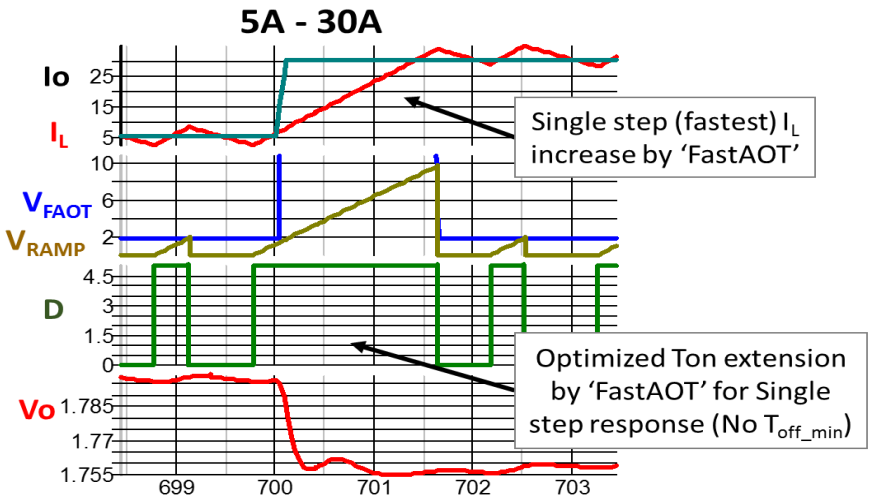

(a)

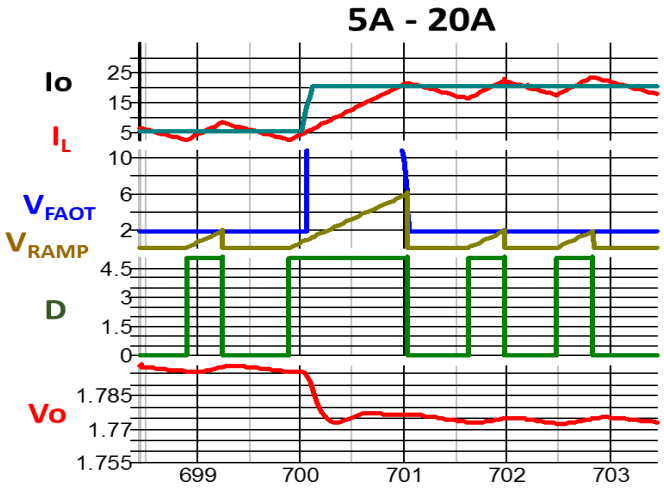

(b)

Figure 2.21 Single step response at Load step-up in proposed 'FastAOT' control (a)5-30A, and (b) 5-20A

2.3.4 Experimental Verification

In this section, concept of 'Fast Adaptive On-time (FastAOT)' has been verified with experimental test results. As parasitic model for CPU socket is a significant part in load transient aspect in VR applications [B.19], proposed method needed to be tested in a commercial VR platform. Therefore, to demonstrate the effectiveness of the T_{ON} modification by the proposed 'FastAOT' concept, an experiment has been done by adding a 'FastAOT' implementation method-1 circuit into a commercial VR evaluation board TPS59650 [19] through its VBAT pin. The test results for single phase operation are shown in Figure 2.22(a) and Figure 2.22(b) where test condition is V_{IN} =12V, V_{out}= 1.05V, switching frequency =600kHz, L=360nH, Co_bulk=470uF and Co_cer=12x22uF with load step ΔI_{LOAD} =17A. It is clearly evident that in Figure 2.22(a) where constant on time is used without 'FastAOT' method has a voltage undershoot which is eliminated in Figure 2.22(b) where T_{ON} is extended by using proposed 'FastAOT' method.

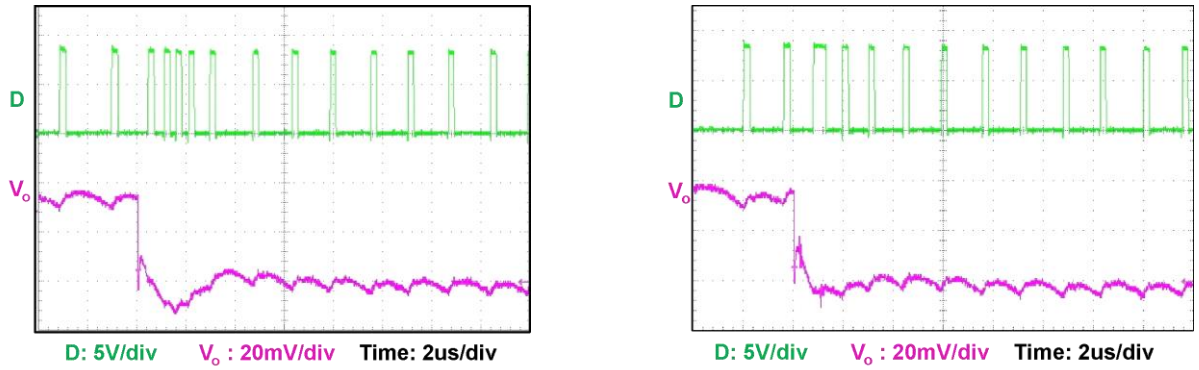

(a) (b)

Figure 2.22 Undershoot at load step-up: (a) without 'FastAOT', and (b) with 'FastAOT'

To demonstrate the transient response improvement in the multiphase operation by the proposed 'FastAOT' method, the same evaluation board TPS59650 is used. In the evaluation board, a 2-phase

operation is selected with the same test conditions as the single phase operation except that the load step is ΔI_{LOAD} =35A in this case. A load step-up response without a proposed method is given in Figure 2.23(a) where a 105mV output voltage droop is seen while the steady state output voltage is different because of finite output impedance of VR application, ΔV_{out} =70mV. Therefore, the transient undershoot is 35mV. In Figure 2.23(b) the same output voltage is seen with the proposed 'FastAOT' method where V_O droop is 90mV which means that the undershoot is reduced to 20mV from 35mV in the previous case.

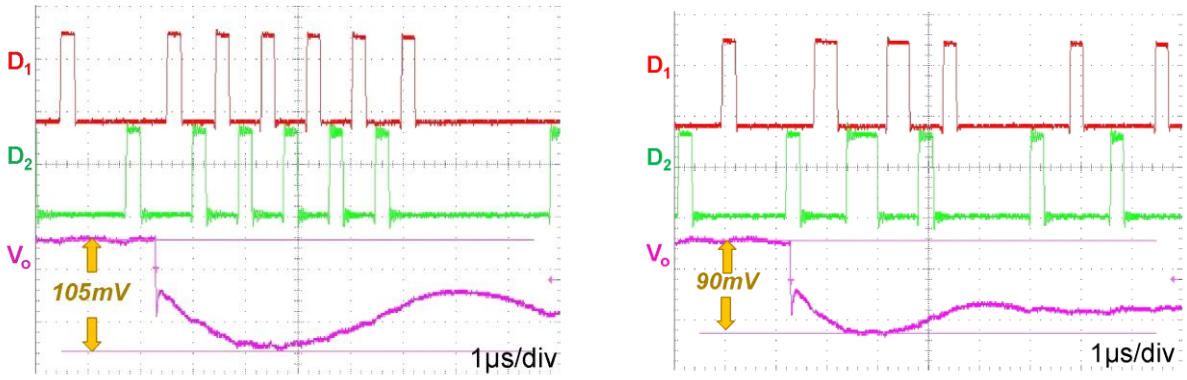

(a) (b)

Figure 2.23 Undershoot at load step-up in 2-phase: (a) without 'FastAOT', and (b) with 'FastAOT'

One limitation of using the controller in TPS59650EVM [B.4] is- in these two experiments as the VBAT pin of the controller is used to increase T_{ON}, instead of modifying the T_{ON} generator block in the controller. The T_{ON} extension is somewhat limited by a slow response in the VBAT pin in that case. But when this concept will be implemented in the IC level design of T_{ON} generator, maximum benefit of 'FastAOT' will be achieved.

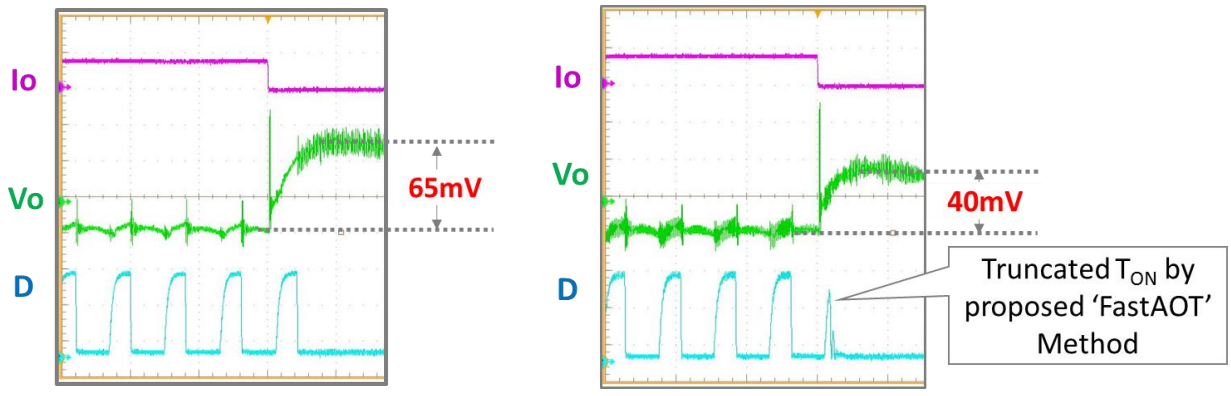

(a) (b)

Figure 2.24 Overshoot at load step-up: (a) without 'FastAOT', and (b) with 'FastAOT'

For load step-down case, a ΔI_{LOAD} =25A is given with same setup in EVM59650_GPU power stage where duty cycle is modified by proposed 'FastAOT' control circuit, shown in Figure 2.24(a) and Figure 2.24(b). In both cases, load step instances are tried to be kept as similar as possible to compare the effect of proposed control. Figure 2.24(b) shows a 25mV (65mV-40mV) overshoot reduction by T_{ON} truncation using 'FastAOT' control at load step down.

2.4 Adaptive External Ramp to Improve Transient Response

It has been found that, from transient point of view larger external ramp creates larger undershoot at load step-up transient. Figure 2.25(a) shows that, although V_C+V_{RAMP} interact with I_{SUM} to generate D_{SUM} signal, but if V_{RAMP} is shown separately in a separate axis, then it can be more visible and easy to investigate, especially at transient. Hence, the V_{RMAMP} is plotted in separate axis in all the simulation in this paper. Simulation results of TPS53625 [B.14] shows that in same load transient condition, COTCM control with larger external ramp produces larger undershoot at the

output, as shown in Figure 2.25(a) and Figure 2.25(b). The basic reason of this larger undershoot is that- the large ramp in system increases the steady state distance between I_{SUM} and V_C signal which makes it difficult for them to saturate the duty cycle very quickly at load

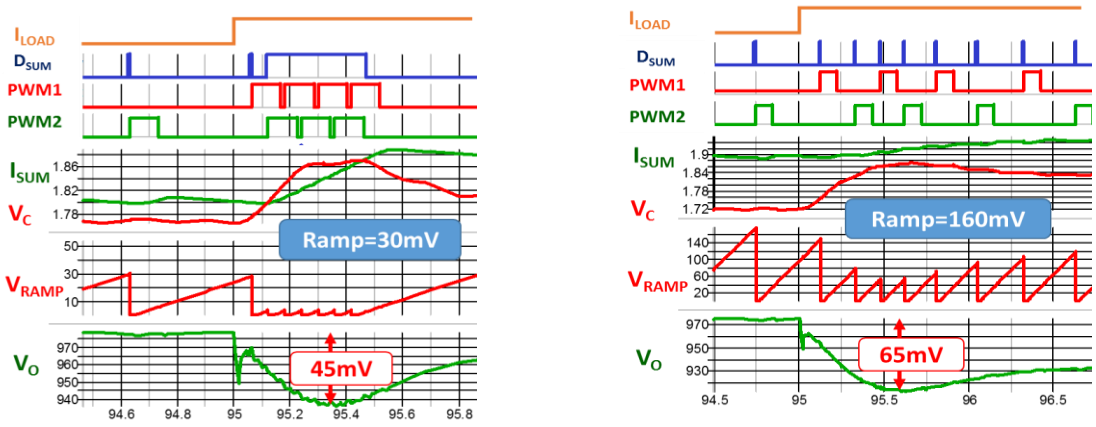

(a) (b)

Figure 2.25 Load step-up transient response with external ramp of (a) 30mV, and (b) 160mV

step-up transient. In Figure 2.25(a), the waveforms at load step-up transient with smaller ramp is shown. Again, the external ramp signal V_{RAMP} is plotted in different axis instead of its original position between V_C and I_{SUM}. In Figure 2.25(a), we can see that with smaller ramp, I_{SUM} and V_C signals are very close at steady state and very quickly can cross each other to saturate the duty cycle to increase the inductor current. In case of duty cycle saturation, COTCM control keeps producing each phase T_{ON} pulses continuously with a minimum off time between them which helps to increase the inductor current very quickly. But with the large ramp, as shown in Figure 2.25(b), I_{SUM} and V_C are comparatively far away from each other in steady state condition which makes them difficult to increase the duty cycle very quickly at transient. We can clearly see that PWM1 and PWM2 pulses are much further in Figure 2.25(b) (compared to Figure 2.25(a)) which produce larger undershoot at the output. Adding external ramp also impact the small signal

property of the system. With the increment of the external ramp value, loop bandwidth actually reduces [11] which eventually slows down the V_C to make transient response even worse.

2.4.1 Proposed Adaptive External Ramp Concept

The basic concept of the proposed method is to increase the ramp slope momentarily at the transient time by using the derivative of the compensator output (V_C) signal to improve transient performance [B.20]. As the duty cycle or the pulse frequency (D_{SUM}) increase is dependent on V_C and I_{SUM} difference, for large external ramp, they cannot come close very quickly and hence D_{sum} pulses cannot be increased very quickly, like shown in Figure 2.25(b). In the propose control, presented in Figure 2.26, the slope of the ramp can be increased very quickly at the beginning of transient. As a result, the pulses will be able to come close very quickly to increase the duty cycle immediately and thus improve the transient response. In that way, controllers will be able to use the large ramp to reduce the jittering the steady state and also same time get good transient performance like small external ramp.

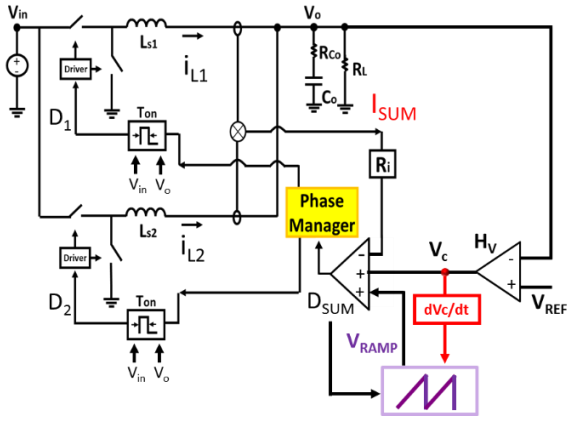

Figure 2.26 Block diagram of proposed adaptive external ramp with COTCM control

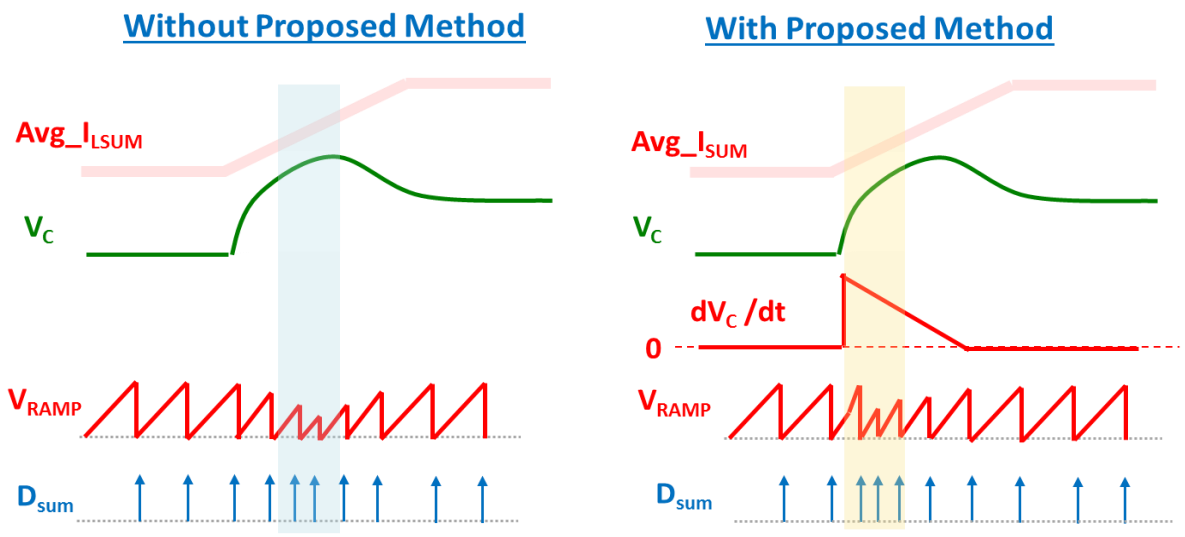

(a) (b)

Figure 2.27 Conceptual COTCM waveforms with (a) fixed external ramp, and (b) proposed adaptive external ramp method

The ramp slope difference can be easily seen in the shaded area of Figure 2.27(a) and Figure 2.27(b). A very important thing is noteworthy here; in Figure 2.27(a), without the proposed method, output of the modulator (D_{SUM}) frequency is maximum when V_C and I_{SUM} signal difference is minimum which occurs sometime after the load transient happens, which delays the response to create larger undershoot at output. But in proposed method, shown in Figure 2.27(b), as dV_C/dt is immediate, the slope of the ramp increases very quickly and maximum D_{SUM} frequency occurs at the beginning of transient which reduce significant amount of undershoot. Another important advantage of this method is- the proposed control allows controller to use large filter at the compensator to block the V_O noise from going into the IC. This large filter makes the V_C slower, but the proposed control can still produce fast transient by using dVc/dt to increase ramp slope. In that way also, the proposed control can reduce the noise sensitivity in the COTCM control.

2.4.2 Implementation of proposed Adaptive Ramp Method

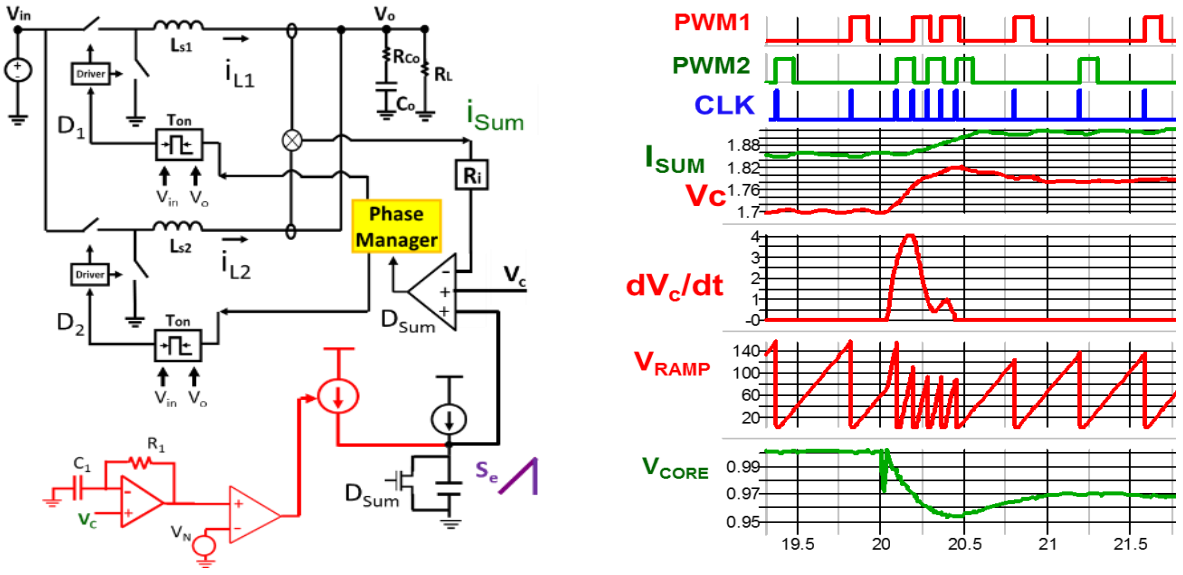

(a) (b)

Figure 2.28 Implementation of proposed adaptive external ramp: (a) structure, and (b) waveforms

Figure 2.28(a) shows the basic structure of COTCM control with proposed method which makes the derivative of V_C signal and add that with ramp block. In Figure 2.28(a), the implementation of proposed method is given where an Op-AMP based differentiator is used to differentiate V_C signal. Then, using a voltage source V_N, the dv/dt of steady state ripple is blocked. Therefore, the dv/dt signal does not impact the steady state control loop which helps to keep the small signal property of COTCM control intact. Only in transient it appears to change the slope to improve the undershoot. In the waveforms with proposed control method, shown in Figure 2.28(b), we can see that, dv/dt of V_C signal becomes high very quickly at the transient and increase the slope of the ramp very quickly at the load step-up transient.

2.4.3 Control Verification Results

The load step-up transient results of TPS53625 system model (correlated with hardware) in the standard VR platform with VR12 filter model [12] are compared in Figure 2.29(a) and Figure 2.29(b) in same scale when we can see that how quickly the ramp slope is increased in Figure 2.29(b) (shown by green circle) and also the PWM1 and PWM2 pulses are much closer in Figure 2.29(b) than Figure 2.29(a) which eventually reduce the undershoot 15mV in this particular case. Therefore, it is expected that use of proposed method will be able to reduce significant amount of output capacitors in the system. Authors have presented a paper about on-time extension using

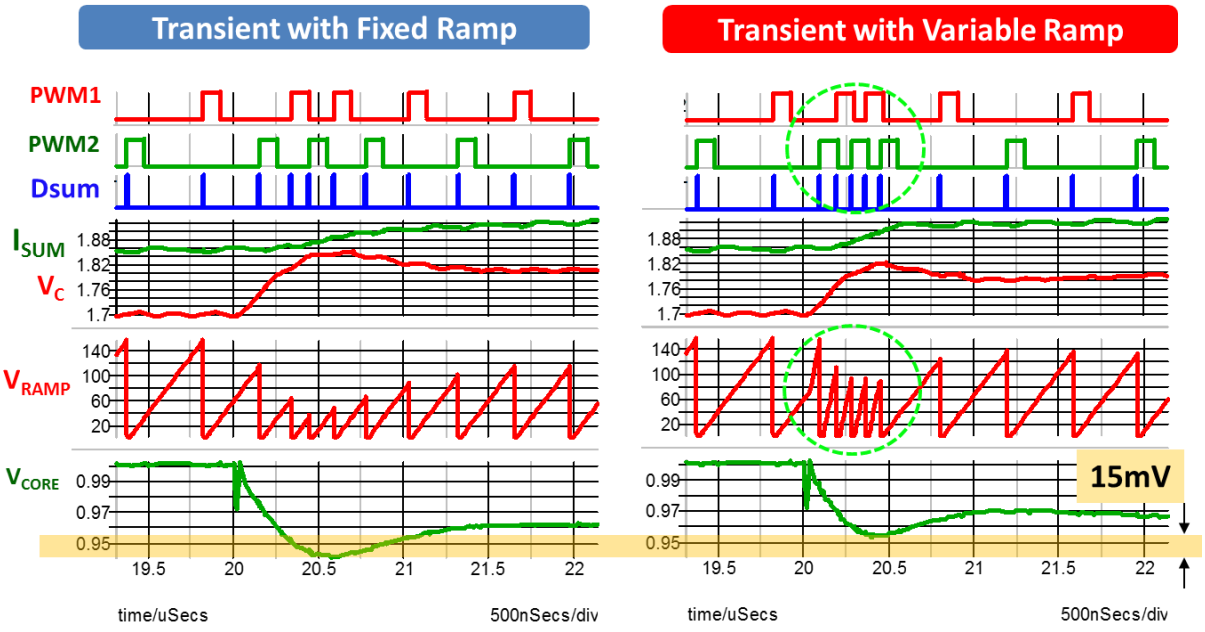

(a) (b)

Figure 2.29 Transient response of TPS53625 with (a) fixed external ramp, (b) proposed adaptive external ramp

dV_o/dt earlier [13]. As the concept proposed in this paper will give a very quick beginning of T_{ON} pulse and then extending the T_{ON} pulse by using the concept in [13] will make an overall ultrafast transient response at load step up.

2.5 Summary

The state-of-the-art constant on-time control has been discussed in details in this chapter. Its transient performance limitations in load step-up and load step-down are identified. Then, the state-of-the-art solutions and their limitations for VR applications are also discussed. Issues of COTCM in multiphase operation are also described along with their solution and limitations. Therefore, two different methods are proposed in this chapter to improve the transient performance of conventional COTCM control in both single and multiphase operation. Simulation and hardware results are also presented to verify the proposed methods.

Chapter 3. Proposed Inverse Charge Constant On-Time (IQCOT) Control

In previous sections, two different methods have been presented to improve the transient response; however, the dependence on an external ramp continues to exist. Thus, the COT control suffers from limitations in working at the ripple-cancellation point. In this chapter, a novel COT control, which is based on the inverse-charge control concept, is introduced; this version can work at the ripple-cancellation point in multiphase operation, without adding the external ramp. The simulation and experimental results are shown at the end of this chapter to verify the claim.

3.1 Review of State-of-the-Art Charge Control

The idea of controlling the output charge of a converter can be found as early as 1979 [C.1]. A complicated control circuit was employed in other work [C.1] for the purpose of controlling the output charge of a boost converter. A control scheme that uses the charge of the switch current as part of its control reference is proposed in previous work [C.2][C.3]. The attempts at controlling the input charge of a flyback converter for the purpose of power-factor correction (PFC) can also be found in other work [C.4][C.5].

3.1.1 Constant Frequency Charge Control with T_{ON} Integration

In [C.6], a current-mode charge control is described for PFC and battery-charger applications in which average input current is controlled. The basic structure of the control is presented in Figure 3.1(a), while Figure 3.1(b) shows the operational waveform of the control. Figure 3.1(a)

shows that the input current is first integrated by charging a capacitor, and then it is compared with V_C (compensated output of the V_{REF} –Vo). In this way the charge coming from the input is controlled in each cycle. The advantage of the charge-control method is that the control is less sensitive to noise as inductor current noise is filtered out by the charge-control capacitor.

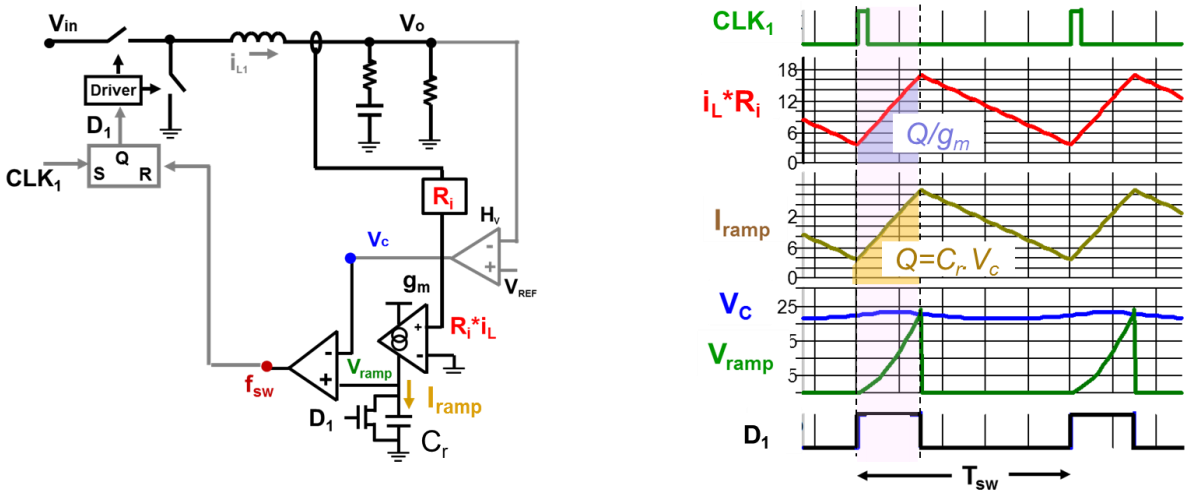

(a) (b)

Figure 3.1 Charge control with fixed-frequency operation: (a) structure, and (b) waveforms.

Another advantage of utilizing the charge-control method is that since the inductor-current ripple does not directly take part in modulation in charge control, conceptually there will be no ripple-cancellation effect in multiphase operation, as compared with ripple-based control. Figure 3.2(a) shows the charge-control operation in D=0.5 for two-phase operation while Figure 3.2(b) shows the waveforms indicating the inductor-current summation ($I_{SUM}R_i$) ripple is zero at D=0.5. But the V_{RAMP} created by the inductor current summation can be compared with V_C to create the duty cycle to achieve seamless operation at the ripple cancellation point for multiphase operation, as shown in Figure 3.2(b).

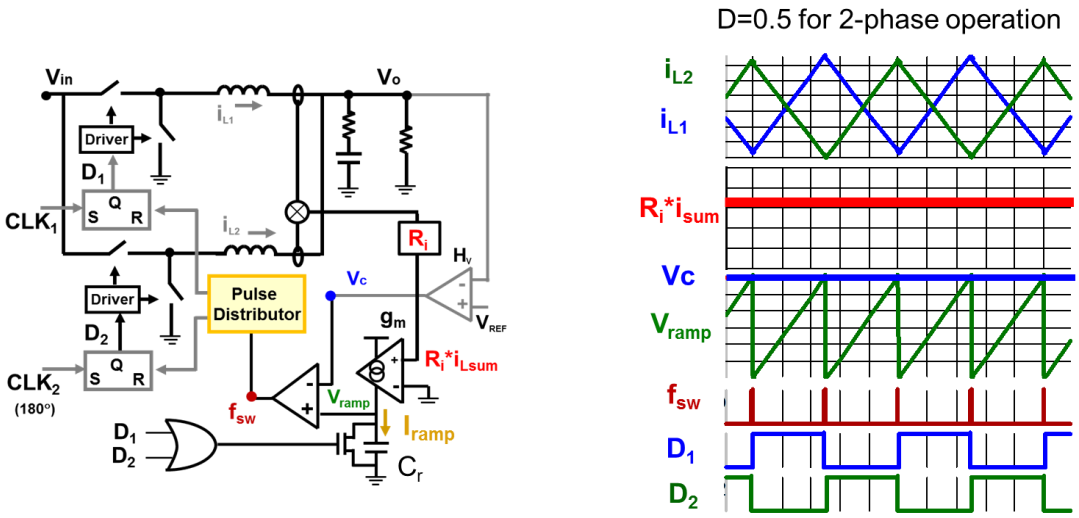

(a) (b)

Figure 3.2 Charge-control method in multiphase: (a) structure, and (b) waveforms.

However, the charge-control method mentioned previously [C.6] uses fixed-frequency operation and suffers from poor light-load efficiency and worse transient-response performance than variable-frequency (i.e., COT) control. Therefore, in the next section, an attempt is made to implement charge control with COT control to achieve these benefits.

3.1.2 Constant On-Time Charge Control with T_{OFF} Integration

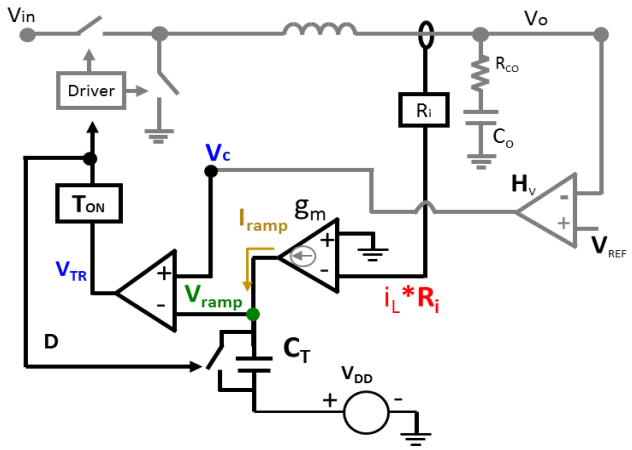

Figure 3.3 Possible control structure for COT charge control.

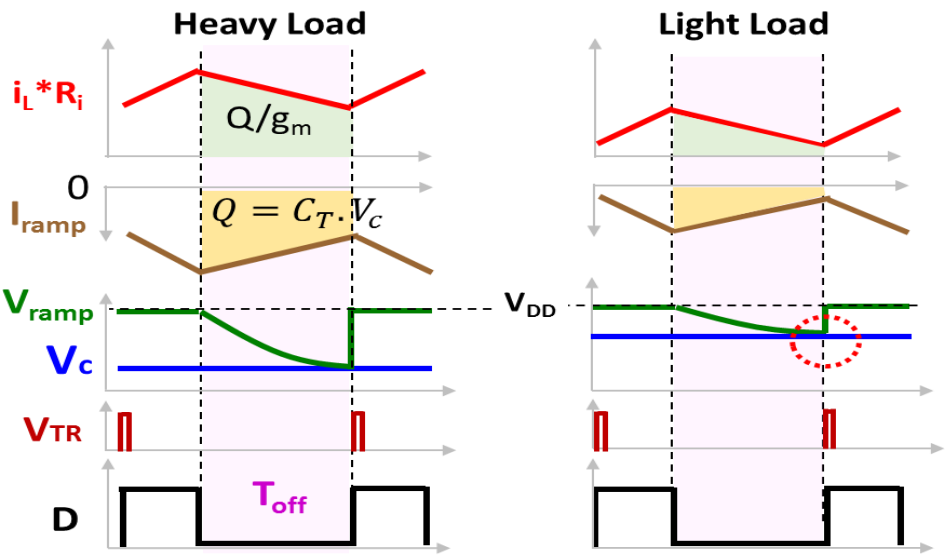

Figure 3.4 Basic waveforms of COT charge control at different loads.

When the charge-control concept is applied with COT control, then the control structure will look like that shown in Figure 3.3. In COT control, T_{OFF} time is modulated such that the falling edge of the inductor current is compared with V_C to control the duty cycle, instead of T_{ON} time modulation in fixed-frequency PCM control where the rising edge of inductor current makes that decision. Therefore, instead of T_{ON} time integration fixed-frequency control, integration of the inductor current is done in T_{OFF} time for COT charge control, as shown in Figure 3.4. One characteristics of this COT charge-control scheme is that when the inductor current becomes small at light-load operation, the V_{RAMP} slope becomes very small, as seen in Figure 3.4. This creates two major issues in control design. First, with smaller V_{RAMP} slope, control becomes more noise sensitive at light loads. Second, the loop gain also varies with load change. As the PWM modulator gain depends on V_{RAMP} slope, the total loop gain will be a function of the slope. As a result, at light loads, when the slope becomes very small, the gain will be very large, which may create instability in the system.

3.2 Concept of Proposed Inverse Charge Constant On-Time Control

3.2.1 Concept of IQCOT Control with T_{OFF} Time Integration

To solve the problems mentioned in the previous section, a new concept of improved COT charge control, as shown in Figure 3.5, is proposed [C.7][C.8][C.9]. This proposed structure is named 'Inverse Charge Constant On-Time (IQCOT)' control. Instead of comparing the integration of the inductor current (V_{RAMP}) with the compensator output (V_C) in the COT charge control, shown in Figure 3.3, or comparing the inductor current ripple (i_LR_i) directly with V_C as with ripple-based COTCM control, shown in Figure 1.3, in this proposed IQCOT control, in essence, the difference between V_C and i_LR_i is integrated. Implementation of this proposed IQCOT control is presented in Figure 3.5, which shows that the initial difference between V_C and i_LR_i is converted into current by using a transconductance (g_m) amplifier, and then this current is used to charge a capacitor, C_T in Figure 3.5. Next, this capacitor voltage (V_{RAMP}) is compared with a fixed threshold voltage (V_{TH}) in every cycle to create the V_{TR} pulse, which triggers the T_{ON} pulse through the T_{ON} generator block, as presented in the waveforms in Figure 3.6.

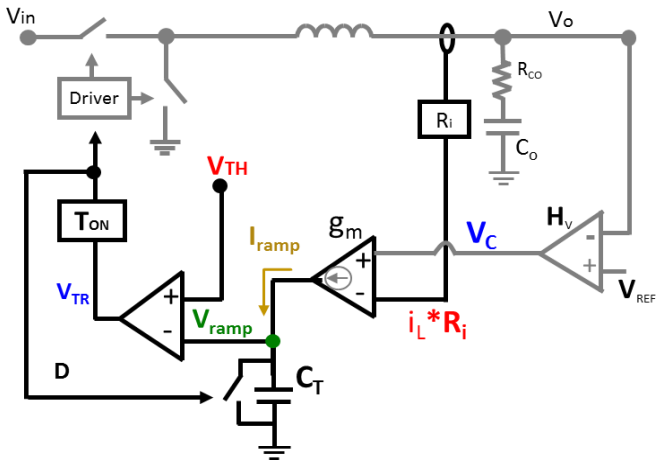

Figure 3.5 Basic control structure of proposed IQCOT control.

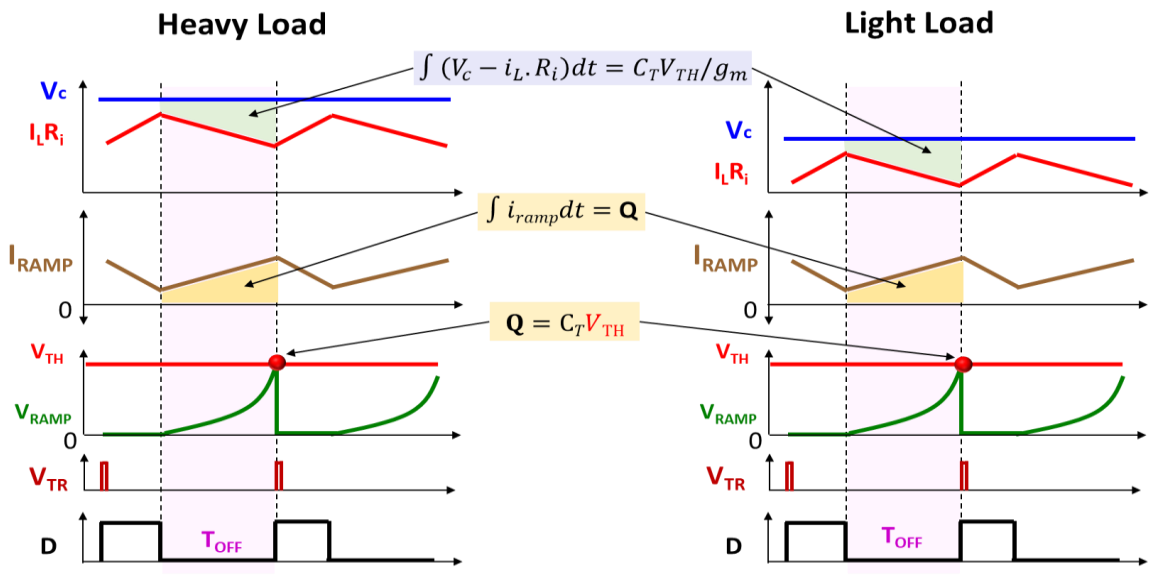

Figure 3.6 Waveforms of proposed IQCOT control at different loads.

As V_{RAMP} begins being charged from zero in every cycle, and the charging ends when V_{RMAP} reaches the V_{TH} value, the charge stored in the capacitor in every cycle can be expressed as:

$$Q = C_T V_{TH} \tag{3.1}$$

As V_{TH} is a constant value, charge (Q) in capacitor C_T in every cycle is constant, as expressed in Eq. (3.1). The proposed control structure in Figure 3.6 shows that Q is basically the integration of capacitor-charging current (I_{RAMP}) over T_{OFF} time, which is equal to g_m times transconductance amplifier input (V_C - $i_L R_i$) as expressed in Eq. (3.2) and (3.3).

$$\int_0^{T_{off}} i_{ramp} dt = C_T V_{TH} \tag{3.2}$$

$$\int_0^{T_{off}} g_m [v_c(t)dt - i_L(t)R_i]dt = C_T V_{TH} \tag{3.3}$$

$$\int_0^{T_{off}} [v_c(t)dt - i_L(t)R_i]dt = \frac{C_T V_{TH}}{g_m} = \text{Constant} \quad (3.4)$$

Therefore, the integral of (V_C - $i_L R_i$), which is the green area ($C_T V_{TH}/g_m$) in Figure 3.6, is also constant in every switching cycle, and C_T, V_{TH} and g_m values are constant in Eq. (3.4). In fact, Eq. (3.4) describes the basic control law of this proposed IQCOT control. This control law actually makes the inductor current follow V_C cycle by cycle, which is the basic property of any current-mode control. There are several benefits of this proposed IQCOT structure. The operational waveforms of the proposed IQCOT control structure at both heavy and light loads are presented in Figure 3.6. As the charge Q in the capacitor is fixed ($Q=C_T V_{TH}$) in every cycle regardless of the load condition, the V_{RAMP} waveform is also the same at different loads, which allows the control to be independent of the load in the system, as shown in Figure 3.6. Furthermore, as the slope of V_{RAMP} is always rising and constant, regardless of load condition, it improves the noise sensitivity of the control.

3.2.2 Limitation of T_{OFF} time Integration in Multiphase Operation

The proposed IQCOT control with T_{OFF} time integration can easily be extended to multiphase operation by using a simple pulse-distribution method. Figure 3.7 shows a two-phase IQCOT control with pulse-distribution method. The basic operation can be explained from Figure 3.8 with duty cycle D= 25%. First, all phase inductor current ripples are summed to create the $I_{SUM}R_i$ signal, which is subtracted from V_C to create capacitor-charging current I_{RAMP} through the transconductance amplifier. Since the capacitor is charged at T_{OFF} time only, for example, the capacitor is charged between t_1 and t_2 time periods in Figure 3.8; t_1 and t_2 is the time period between

two phase duty cycles when both high-side switches are off. When this capacitor voltage V_{RMAP} is compared with V_{TH}, it creates the combined T_{ON} triggering pulse V_{TR_SUM}. Then this V_{TR_SUM} is

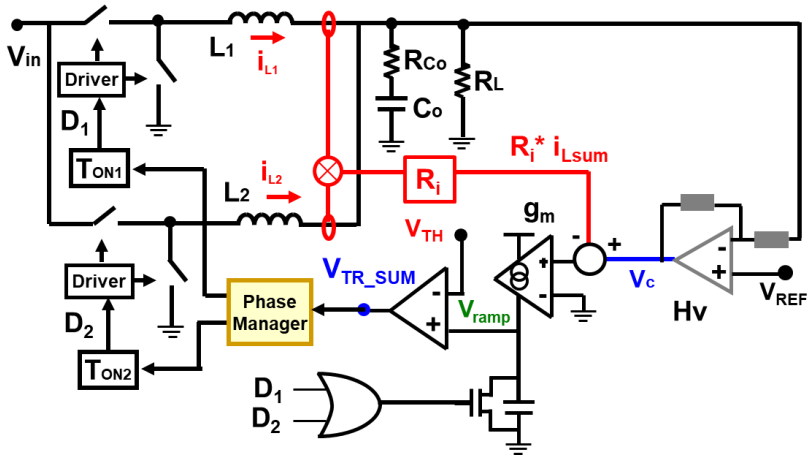

Figure 3.7 Two-phase structure of proposed IQCOT control with T_{OFF} integration

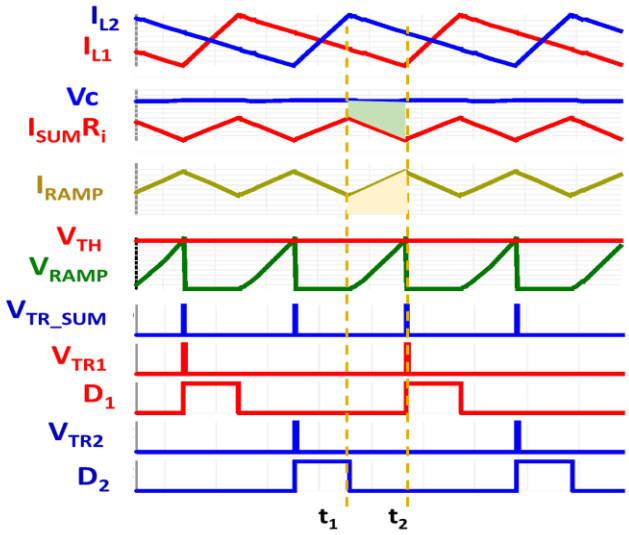

Figure 3.8 Two-phase operational waveforms of proposed IQCOT control with D=25%.

distributed alternatively between both phases by the phase-manager block in the pulse-distribution method, as V_{TR_SUM} is distributed in V_{TR1} and V_{TR2} alternatively in Figure 3.8. These V_{TR1} and V_{TR2} signals trigger T_{ON} pulses to create duty cycles D_1 and D_2 in corresponding phases to the

drive power stage. It is very obvious that when the duty cycle is approaching the ripple-cancellation point, (t_2-t_1) time period will become smaller and smaller. Right at the ripple-cancellation point for two-phase operation, where D=50%, the time period between t_1 to t_2 is zero. Therefore, the capacitor will not have a chance to be charged, and there will not be any V_{RAMP} to generate duty cycle. As a result, although IQCOT control with T_{OFF} time integration can work in multiphase operation, it will not be able to operate properly at the ripple-cancellation point. In the next section, a different charging period is applied to investigate whether or not there is another way in which IQCOT can operate at the ripple-cancellation point in multiphase operation.

3.2.3 Concept of IQCOT Control with (T_{ON} +T_{OFF}) Time Integration

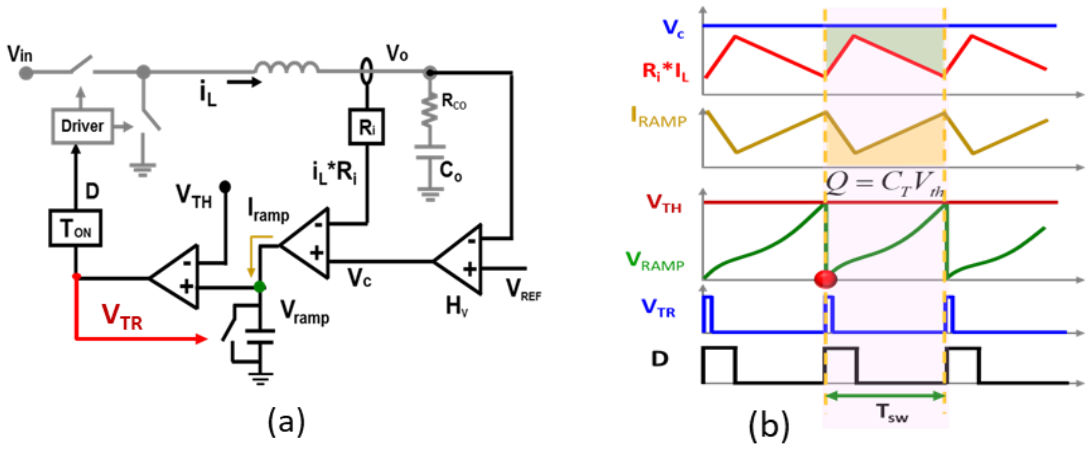

Figure 3.9 IQCOT control with full switching cycle (T_{ON}+T_{OFF}) integration: (a) control structure, and (b) key waveforms.

This section explores another concept for achieving the proposed IQCOT control, in which the capacitor charge (Q) generated by integrating (V_C - i_LR_i) for a full switching cycle (T_{ON}+T_{OFF}), as shown in Figure 3.9, is utilized instead of integrating only the T_{OFF} time, as shown in Figure 3.6.

$$\int_0^{T_{on}+T_{off}} [v_c(t)dt - i_L(t)R_i]dt = \frac{C_T V_{TH}}{g_m} = \text{Constant} \quad (3.5)$$

To implement this concept, charge-control capacitor C_T is reset by the V_{TR} signal, as shown in Figure 3.9 (a), in comparison to the case shown in Figure 3.5, where C_T is reset by duty cycle (D) signal. As a result, the V_{RAMP} signal charging starts immediately after it is reset to zero by the V_{TR} signal. The advantages of this full-cycle integration concept are manifold. First of all, for the same value of Q, full-cycle integration has higher control gain than T_{OFF} integration. In the load step-up transient, the duty-cycle increment is higher than in the T_{OFF} integration case, which helps to produce a faster transient response in the control; this concept will be presented in detail in Chapter 4. In multiphase operation, this implementation helps to achieve the capability of working at the ripple-cancellation point without requiring any external ramp being added to the system, as will be discussed in Section 3.4.

This proposed IQCOT with (T_{ON}+T_{OFF}) time integration can seamlessly work at the ripple cancellation point in multiphase operation. Details will be presented in Section 3.4 in this chapter.

3.3 Properties of Proposed IQCOT Control with (T_{ON}+T_{OFF}) Integration

3.3.1 Current-Mode Property of IQCOT Control

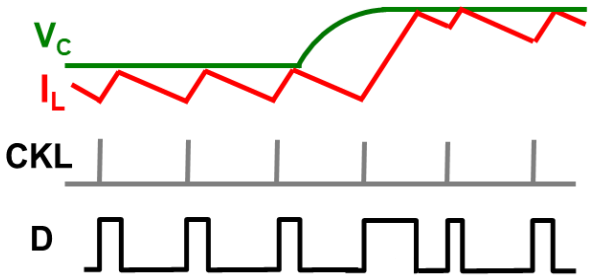

(a)

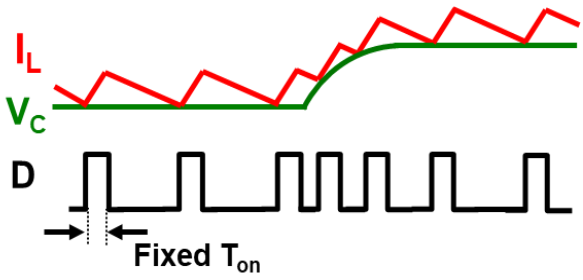

(b)

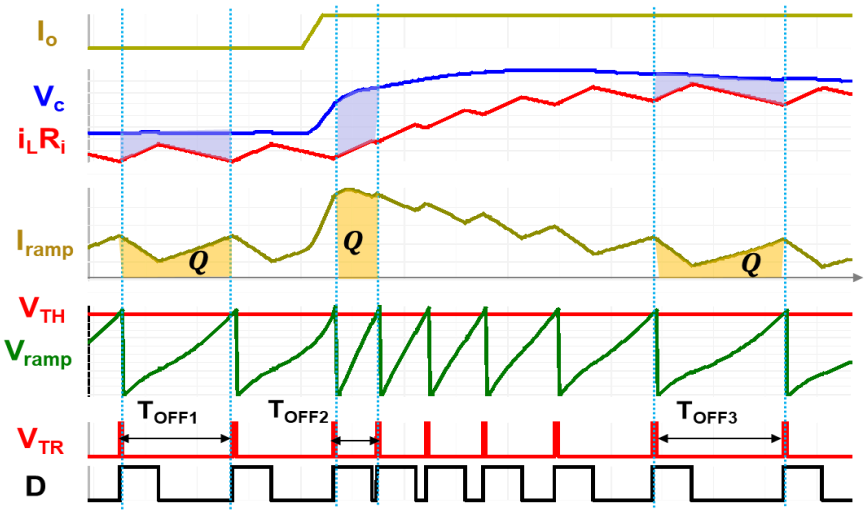

(c)

Figure 3.10 Various current-mode control structures: (a) PCM, (b) COT, and (c) IQCOT control.

According to the fundamental condition of current-mode control, the inductor current needs to follow compensator output V_C. Figure 3.10(a) shows that the peak of the inductor current is controlled by V_C, and at the transient when V_C increases, the inductor current also increases with that by increasing the duty cycle. In the same way, in the COT control shown in Figure 3.10(b), the valley of the inductor current is controlled by V_C, and when V_C moves, the valley of the inductor current moves with V_C. When V_C increases in IQCOT control, the inductor current also increases to keep the charge constant in every cycle.

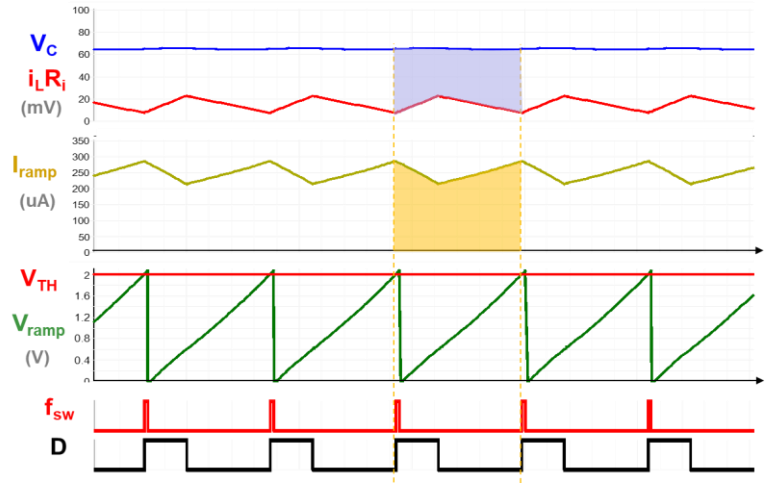

(a)

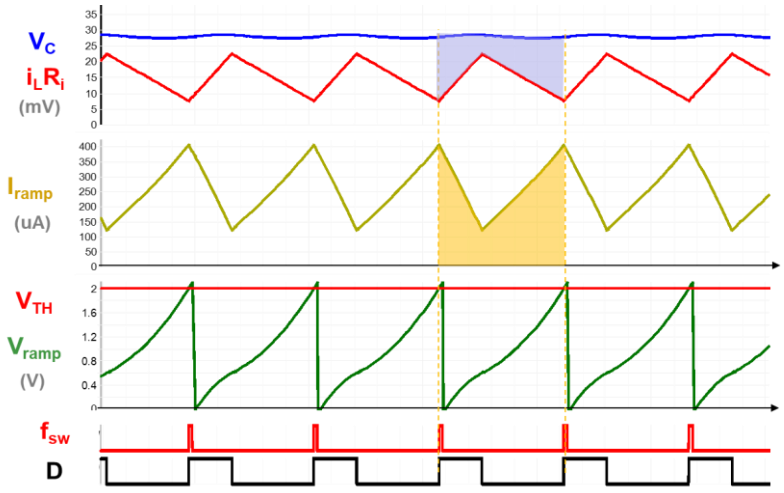

(b)

Figure 3.11 Effect of g_m in IQCOT control operation with (a) low g_m, and (b) high g_m

The effect of different levels of g_m in IQCOT control is simulated and shown in Figure 3.11. The average distance between Vc and i_LR_i depends on the g_m value, as shown in Figure 3.11. When g_m is low, as shown in Figure 3.11(a), Iramp has less AC ripple (100uA, peak to peak) and the DC is around 250uA. Since the g_m is small, to create this I_{ramp}, the average (Vc- i_LR_i) is almost 50mV. The simulation is also done in the same condition with higher g_m. In that case, the AC ripple in I_{ramp}

becomes larger (300uA, peak to peak), and the DC remains the same. This large AC ripple also causes the V_{RAMP} shape to be more curved, instead of a straight line. Since, g_m is larger, the (V_c- $i_L R_i$) is also smaller, and is almost 15mV in this case. Basically, a higher g_m reflects higher gain in the feedback loop. The smaller (V_c- $i_L R_i$) means, $i_L R_i$ follows V_c more closely. This phenomenon helps to achieve faster transient response. Hence, higher g_m is important for achieving fast transient response.

3.3.2 Transient Response of IQCOT Control

The previous section demonstrated how the inductor current in IQCOT control can follow the compensator output V_C while it changes with the load. This feature demonstrates the current mode property of proposed IQCOT control. In this section, the response of the control is presented at heavy-load step transient, and its unique features, like its controllability during transient instance and natural T_{ON} extension at load step-up transient, are compared with the conventional COTCM control as well.

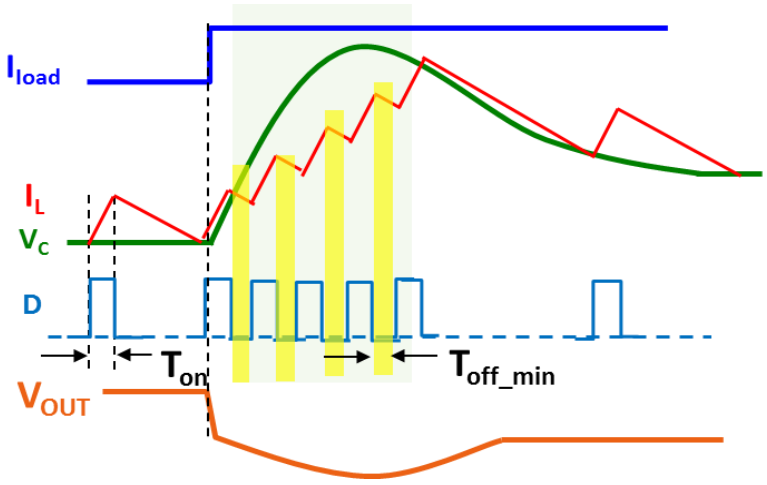

(a)

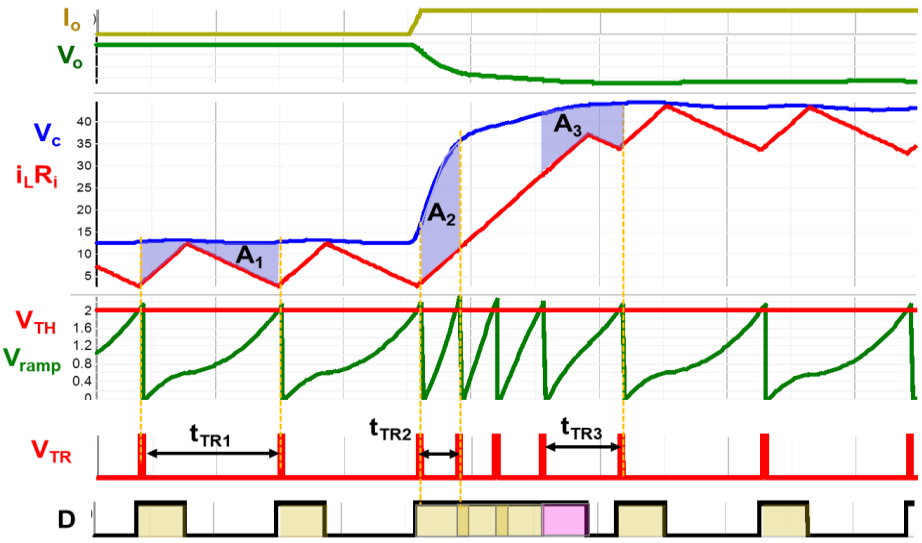

(b)

Figure 3.12 Heavy-load transient response: (a) COTCM control, and (b) IQCOT control.

In the case of COTCM control, shown in Figure 3.12(a), in a heavy load step, when V_O decreases and V_C increases very quickly after the load step-up, inductor current I_L cannot follow V_C; as a result the COTCM loses control. When the duty cycle is saturated, V_C becomes higher than V_{iL} (i_LR_i) and T_{ON} pulse cannot be triggered by V_C and V_{iL} intersection as happens in steady-state operation. Instead, a new T_{ON} is generated after the minimum off-time (T_{OFF_MIN}), which is required for charging the bootstrap capacitor of the high-side gate driver and which is fixed by the system's power stage and load. Figure 3.12 (a) shows that the inductor-current increment is limited by the length of T_{ON} and T_{OFF_MIN}. If T_{ON} is small and T_{OFF_MIN} is large, a large undershoot can occur at the output.

A. Natural T_{ON} Extension for IQCOT Control

At the transient response in the proposed IQCOT control, increases in the distance between V_C and I_L causes the frequency of V_{TR} pulse to increase naturally. Then, the T_{ON} pulses can merge

together to create a longer T_{ON} time. Along with steady-state operation, the transient response of the proposed IQCOT control in load step-up is also shown in Figure 3.12. In a load step-up transient period, the compensator output V_C very quickly becomes high by following the fall of the output voltage Vo. If inductor current I_L cannot follow the V_C, then the difference (V_c- i_LR_i) becomes larger, as shown in Figure 3.12. As the capacitor charging current is proportional to (V_c- i_LR_i), charging current also becomes high, and therefore the slope of capacitor voltage, V_{RAMP}, becomes high. In that way, the frequency of output pulse V_{TR} increases very quickly after the load transient step-up. This frequency increment is subject to the control law expressed in (3.5). Areas A_{SS} and A_1, enclosed by V_C and i_LR_i in Figure 3.12, are equal to C_TV_{TH}/g_m. When the height of A_1 increases, the width of area A_1 decreases proportionally. If this V_{TR} increment is very high and t_{TR1}, shown in Figure 3.12, becomes smaller than the T_{ON} time period, then consecutive T_{ON} pulses will merge together to create an extended T_{ON}. This extended T_{ON} helps to increase the inductor current close to its final value in one step. When i_LR_i becomes close to V_C, then the height of A_2 becomes smaller and t_{TR2} becomes larger, and if it is larger than the length of T_{ON}, T_{ON} extension will end and eventually the duty cycle will revert to its original state.

B. IQCOT Never Loses Cotnrol

Now, one very important aspect of the proposed IQCOT control is that, in comparison to the load transient response in ripple-based current-mode control, shown in Figure 3.12(a), in which V_C goes above I_L R_i during the heavy load step-up and loses control of the duty cycle, the proposed approach never loses control. Pulse frequency V_{TR} is always proportional to (V_c - i_LR_i) in all the conditions. This property enables IQCOT control to adjust its duty cycle according to load-step characteristics. This benefit of IQCOT control is discussed in detail in the next section.

3.3.3 Optimized Response at Different Transient Conditions

This T_{ON} extension is under loop control and always produces optimized T_{ON} extension, which eliminates the chance of any overcorrection. In Figure 3.12(b), when $i_L R_i$ becomes closer to the V_C signal, the slope of V_{RAMP} becomes lower, which decreases the V_{TR} pulse frequency. When height A_3 becomes smaller than A_2, the width of A_3 becomes larger, and t_{TR3} becomes larger than T_{ON}, which causes the T_{ON} extension to stop at that cycle.

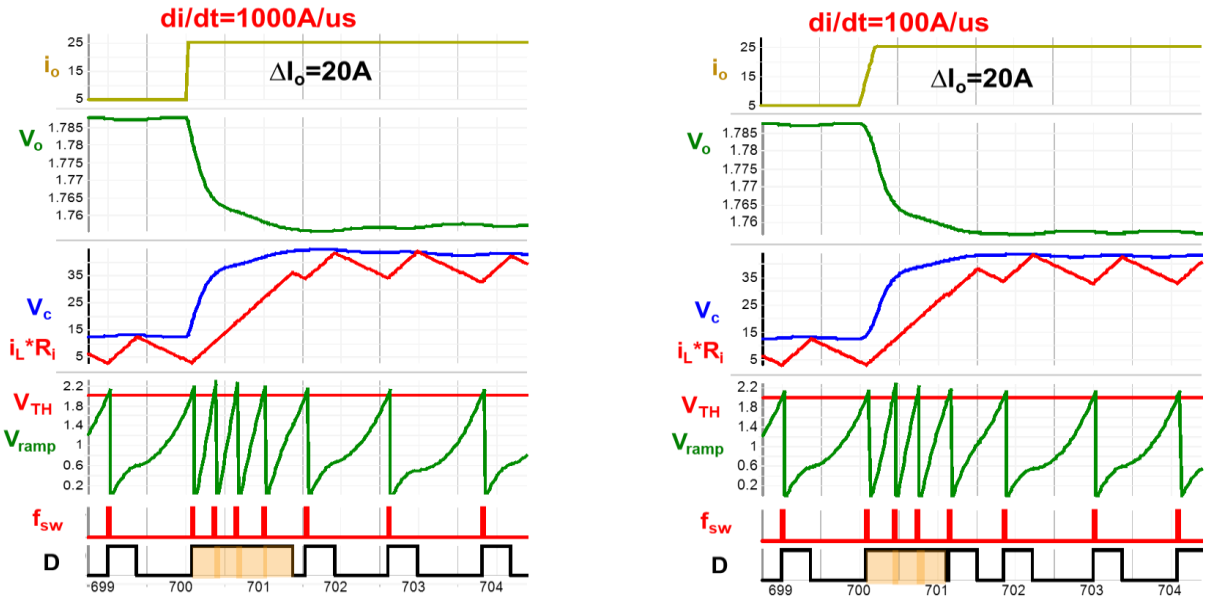

(a) (b)

Figure 3.13 Load step-up waveforms at slew rate: (a) di/dt=1000A/us, and (b) di/dt=100A/us.

Figure 3.13 shows the T_{ON} extension in different load transient conditions; four V_{TR} pulses create a longer T_{ON} extension when a 20A load step is given with 1000 A/us. But when the slew rate is reduced to 100 A/us, only three V_{TR} pulses merge together to create a smaller T_{ON} extension. In both cases, the inductor current reaches its higher steady-state value in a single cycle via one larger T_{ON} pulse. As the width of the extended T_{ON} pulse is adaptive to the applied transient step (i.e., a smaller T_{ON} extension for smaller slew rate), as shown in Figure 3.13, there is no overcorrection at

the output voltage Vo. Moreover, if somehow the T_{ON} extension becomes excessive, $i_L R_i$ goes above V_C, which will make V_C- $i_L R_i$ negative. In that case, capacitor C_T will no longer be charged and no new V_{TR} pulse will be created. In this case, the inductor current will immediately be back to its steady state.

3.3.4 Self Current Limiting During Over Load Condition

As mentioned earlier, inductor current is controlled by V_C in IQCOT control, just as with other current-mode controls. This means that the inductor current cannot go over V_C in the transient instance. It has been seen clearly in previous sections that in IQCOT control, the charge is constant in every cycle. Therefore, in every cycle inductor current is controlled by V_C. In the T_{ON} extension time at transient, one fear is that the inductor current may become so high that it may saturate the inductor. To resolve this issue, if the V_C voltage is clamped to a certain voltage, then the inductor current will also be clamped by V_C. Therefore, the current will not cross V_C and will not saturate

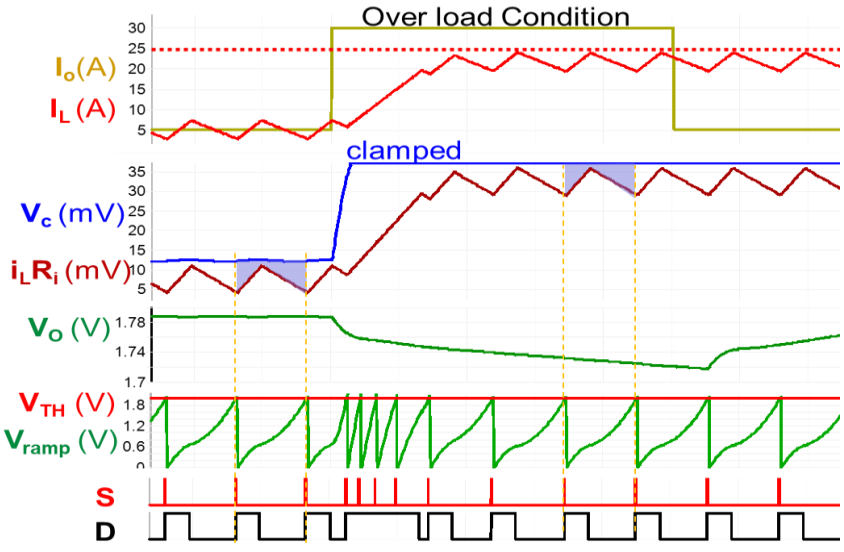

Figure 3.14 Self-current limiting property of IQCOT control at over load condition

the inductor, which mitigates a significant industry concern for the case of T_{ON} extension. IQCOT offers a very good benefit in that it can extend the T_{ON} but also will not saturate the inductor at the transient.

In Figure 3.14, an overload condition in IQCOT control has been shown. In the overload condition, when the load increases, the Vo voltage reduces and then Vc increases. Because of the overload condition, Vo will quickly become very low and Vc also becomes very high. In that case, Vc can be clamped in a predefined voltage (38mV in this example). Then $i_L R_i$ is also clamped by V_C at 38 mV. As R_i =1.5mΩ, the inductor current is also clamped at 25 A, as shown in Figure 3.14. So therefore the current limit is 25 A.

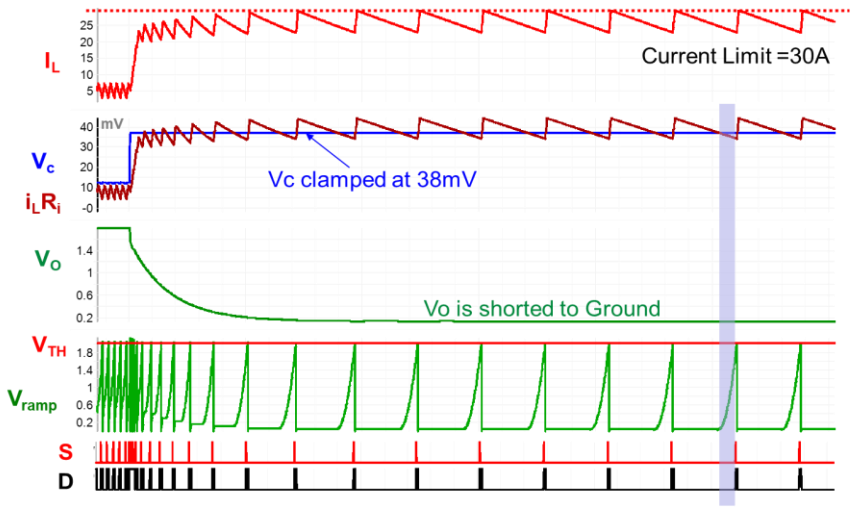

Figure 3.15 Self-current limiting property of IQCOT control at short-circuit condition

Figure 3.15 presnets, the waveforms of IQCOT control in short circuit condition is presented. When Vo is almost zero, the falling slope of inductor current also becomes very low. As a result, the effective operating switching frequency also becomes very low as seen in Figure 3.15. In this case, $i_L R_i$ is below Vc only part of the T_{OFF} time and that (Vc- $i_L R_i$), as shown under the blue area

in Figure 3.15, charges the capacitor to create V_{RAMP}. In this case, as some part of the $i_L R_i$ is above the Vc, the inductor current limit is a little bit higher than the overloading current limit.

3.4 Multiphase Operation of Proposed IQCOT Control

The proposed IQCOT control can easily be extended to multiphase operation by using the simple pulse-distribution method without being affected by the ripple-cancellation effect. Figure 3.16 shows a two-phase IQCOT control with pulse-distribution method. The basic operation can be explained from Figure 3.17 with duty cycle D= 25%. First, the inductor current ripples of each phase are summed to create the $I_{SUM}R_i$ signal, which is subtracted from V_C to create capacitor charging current I_{RAMP} through the transconductance amplifier. When this capacitor voltage V_{RMAP} is compared with V_{TH}, it creates combined T_{ON}, triggering pulse V_{TR_SUM}. Then this V_{TR_SUM} is distributed alternatively between both phases by the phase-manager block in the pulse-distribution method, as V_{TR_SUM} is distributed alternatively between V_{TR1} and V_{TR2}, as shown in Figure. 10(a). These V_{TR1} and V_{TR2} signals trigger T_{ON} pulses to create duty cycles D_1 and D_2 in corresponding phases to the drive power stage.

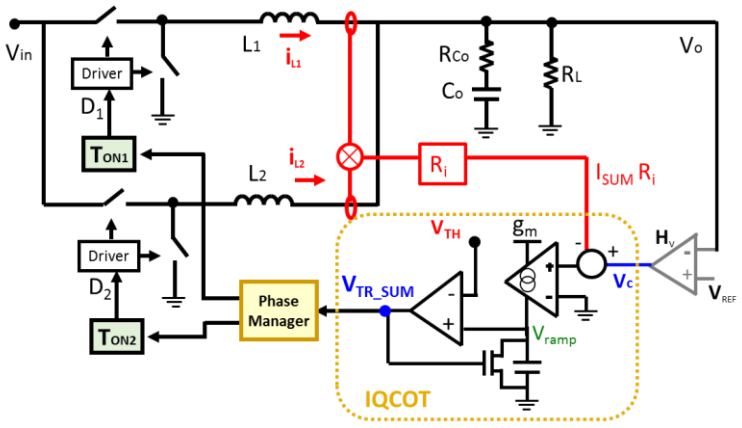

Figure 3.16 Two-phase operation of the proposed IQCOT control.

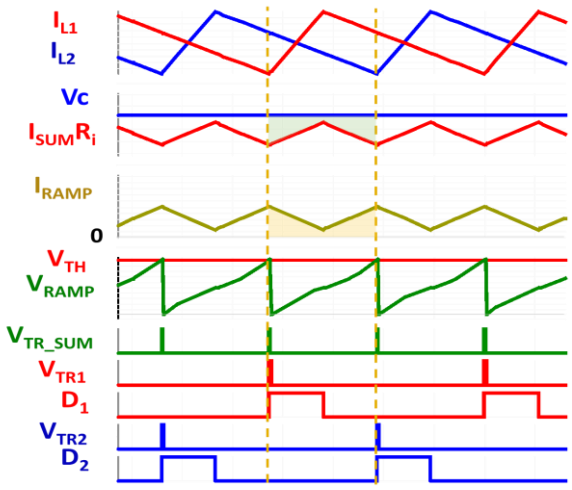

Figure 3.17 Two-phase operational waveforms of proposed IQCOT control with D=25%.

3.4.1 IQCOT Resolves Ripple-Cancellation Effect in Multiphase Operation

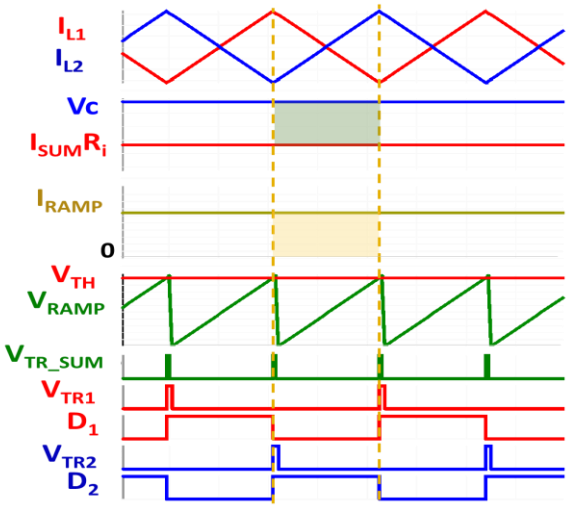

Figure 3.18 Two-phase operational waveforms of proposed IQCOT control with D=50%.

Figure 3.18 shows the proposed IQCOT control operation at the ripple-cancellation point, which is D=50% for two-phase operation. As the phase current ripples are equal and opposite in the D=50% case, they cancel each other, and the I_{SUM} ripple becomes zero, as shown in Figure

3.18. In conventional control, $I_{SUM}R_i$ is compared with V_C, as shown in Figure 2.7(b), to generate the combined control signal V_{TR_SUM}. When $I_{SUM}R_i$ becomes zero at D=50% for two-phase operation, there is no $I_{SUM}R_i$ ripple to create control signal V_{TR_SUM} and thus the control fails to work. But Figure 3.18 shows that the proposed IQCOT control can work seamlessly at this condition, as control is not dependent on the I_{SUM} R_i ripple. In Figure 3.18, although $I_{SUM}R_i$ does not have any ripple, but (V_C - $I_{SUM}R_i$) voltage still creates V_{RAMP} to easily generate duty cycle. This feature helps the proposed IQCOT to work at the ripple-cancellation point in multiphase operation without requiring any external ramp in the system, which contrasts conventional control methods.

It is important to mention that, in these situations in which the ripple is very small or zero, state-of-the-art ripple-based controls add external ramps to the system to improve the noise performances or to reduce jittering. From the standpoint of system design, it is always challenging to optimize the external ramp value with a good tradeoff between noise performance and system stability. Furthermore, the value of the ramp also needs to be dynamically updated with changes in duty cycle and phase number to ensure proper stability and transient performance of the system.

3.4.2 Extension of Proposed Inverse-Charge Control Concept for Variable On-Time Variable Off-Time Control

In the variable-on variable-off time control, both on-time and off-time vary with changes in duty cycle. Among this type of control, ramp pulse modulation (RPM) [C.10][C.11][C.12][C.13] is one popular control method, and therefore RPM control, shown in Figure 3.19, is taken as an example of variable on-time variable off-time control. Then proposed inverse charge control concept is

applied with RPM to demonstrate the ability of inverse charge variable on-time variable off-time control to work at the ripple cancellation point.

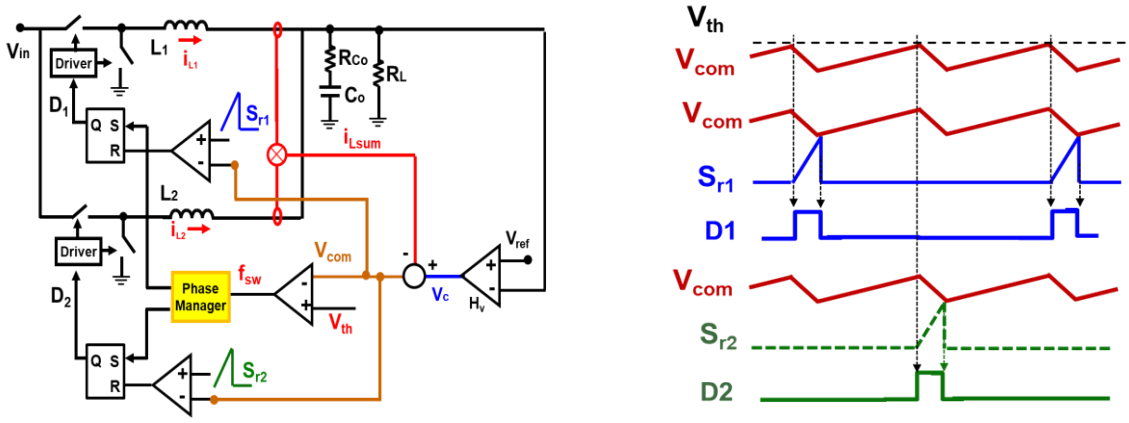

(a) (b)

Figure 3.19 Conventional variable-on variable-off time control for multiphase operation: (a) control structure, and (b) operational waveforms.

In Figure 3.19, multiphase operation of conventional RPM control is presented; all phase currents are summed as I_{LSUM} and are then subtracted from V_C to generate V_{COM} for multiphase operation. In can be seen that when the V_{COM} ripple touches the V_{TH} voltage, f_{sw} pulses are generated to initiate the on-time and are then distributed in the phases by the phase-manager block. Similar to COT control, RPM control is also dependent on the I_{LSUM} signal for modulation, and hence, at multiphase operation when I_{LSUM} becomes zero at the ripple-cancellation point, Vcom ripple also becomes zero and this control scheme does not work.

In this case, inverse-charge control can be utilized with RPM control to resolve this issue. Figure 3.20 shows the structure and basic waveforms of inverse-charge variable-on and variable-off time control with multiphase operation, in which instead of the V_{COM} signal, the V_{RAMP} signal and V_{TH}

voltage create the f_{sw} signal to trigger the T_{ON} pulses. Therefore, when the V_{COM} signal is zero at the ripple-cancellation point, V_{RAMP} continues to generate the f_{sw} pulses to keep the modulation running.

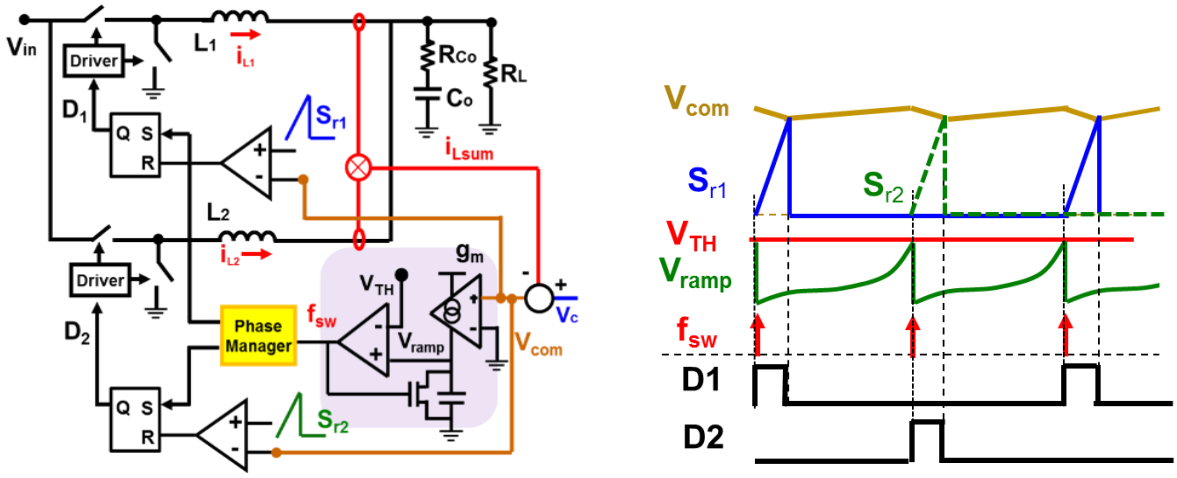

(a) (b)

Figure 3.20 Proposed inverse-charge variable-on variable-off time control for multiphase operation: (a) control structure, and (b) operational waveforms.

The operation of the inverse charge control method with variable on-time variable off-time control is verified with simulation results. Figure 3.21(a) shows the steady state operation with following test conditions: V_{IN} = 8.4V, V_O = 1.8V, equivalent f_{sw} (per phase) = 2MHz, L=120nH, Co_cer = 36x22uF, V_{TH}=2V. In Figure 3.21(a), Vcom signal is creating the V_{RAMP} signal and when the V_{RAMP} signal is compared with V_{TH}, then the f_{sw} pulse is generated. This f_{sw} pulse is distributed between two phases to trigger individual T_{ON} pulses. Two individual ramps S_{r1} and S_{r2} are compared with the Vcom signal to generate individual T_{ON} pulses, as shown in Figure 3.21(a). The operation at the ripple cancellation point is presented in Figure 3.21(b), in which the inverse charge variable on-time and variable off-time is working at D=0.5 (Vin =3.6V, Vo=1.8V) for two phase operation.

In can be clearly seen that although there is no ripple at Vcom signal, the control can still generate the duty cycle via f_{sw} and the V_{RAMP} signal which is created by Vcom.

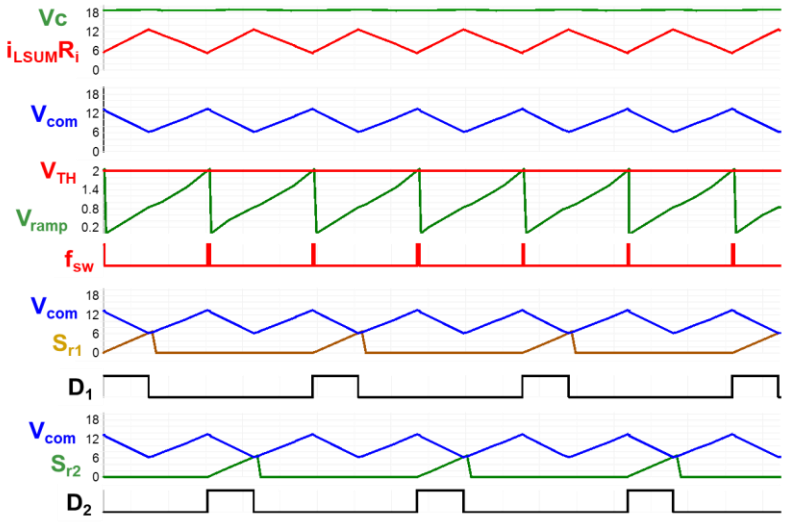

(a)

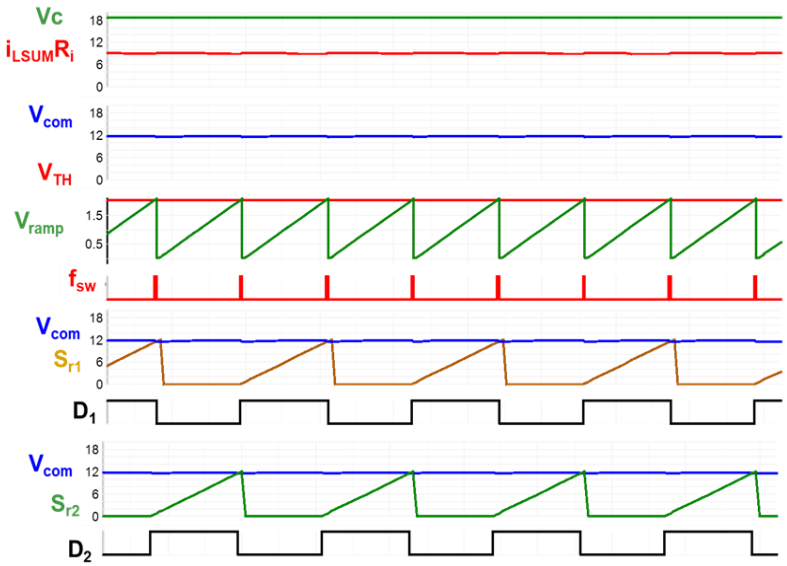

(b)

Figure 3.21 Simulation waveforms of inverse charge variable on-time variable off-time at (a) D=0.25, and (b) D=0.5

3.5 Experimental Verification for IQCOT Control

3.5.1 Experimental Setup Design

In this section, details of the IQCOT control experimental setup design are presented and the concept of this proposed control is verified with some experimental test results. As the parasitic model for CPU socket plays a significant role in the load-transient response in VR applications, the proposed IQCOT control board is tested in a commercial VR platform. In this regard, the control board is designed and implemented in a separate board and is then connected with TPS53625 - a commercial two-phase VR power-stage board with CPU/GPU socket and standard output filter components. The block diagram of this design is shown in Figure 3.22 and pictures of the implementation boards are presented in Figure 3.23.

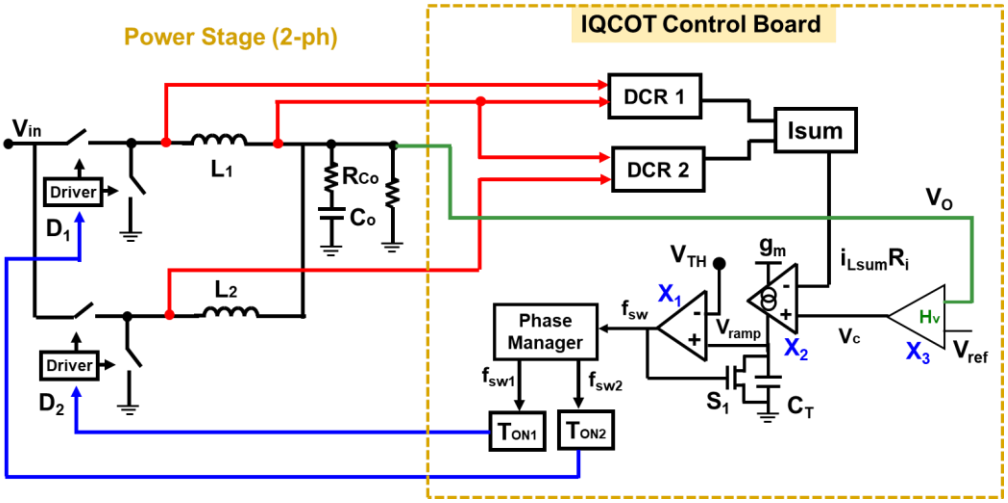

Figure 3.22 Block diagram of IQCOT 2- phase test board design

The inductor current is sensed through the DCR current sensing. Then the individual sensed voltages are summed by an adder circuit to generate $I_{LSUM}R_i$. In this case the Op-Amp THS4222 has been used for its high bandwidth design capability. Vc is generated from a proportional gain

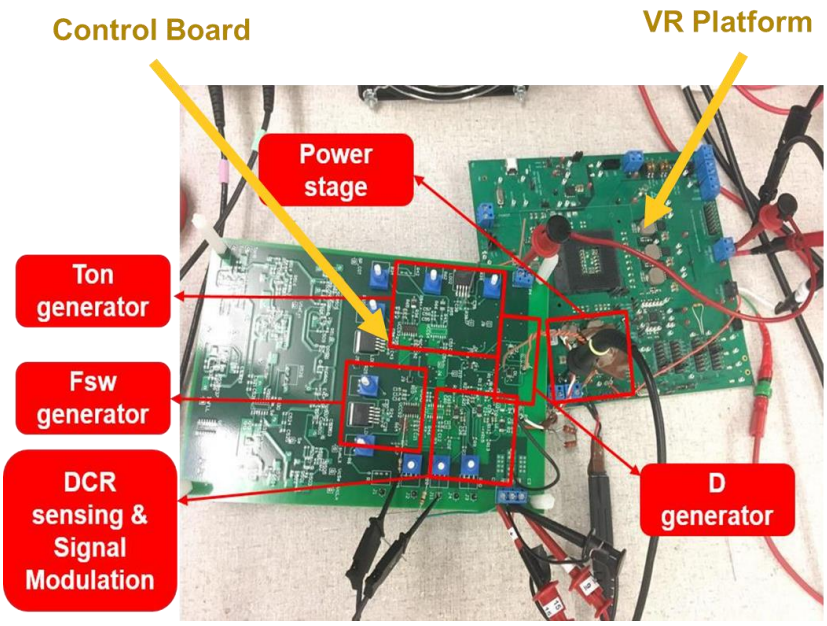

Figure 3.23 Proposed IQCOT control structure implemented in 2-phase operation

compensator, X_3 in Figure 3.22, using THS4222 Op-Amp. Then (V_c-$I_{LSUM}R_i$) is given as an input to a transconductance (g_m) amplifier (X_2). This transconductance amplifier design is important and hence, some details will be presented in this section. The capacitor-charging current I_{RAMP} charges the capacitor C_T and when V_{RAMP} touches V_{TH}, the comparator (X_1) creates f_{sw} pulses. In this case, delay in the comparator is a very important issue. If the delay is large, then that might limit the maximum f_{sw} frequency at the load step-up transient. Therefore, it is imperative to select a fast comparator and also to reduce the delay from the comparator to the path of discharging switch S_1 in the board layout. In this case single supply LT1712 is chosen as comparator for its low (4.5ns) delay. Then the f_{sw} pulses are sent to phase manager for pulse distribution in two phases. To design the phase manager, basically a frequency divider circuit is created by using several D- flip flops. The SN74LVC2G74 is used in this case. The distributed f_{sw} pulses – f_{sw1} and f_{sw2} triggers the T_{ON} in each T_{ON} generator block (T_{ON1} & T_{ON2}). These T_{ON} generator blocks are adaptive T_{ON} generator

where T_{ON} is adaptive to V_{IN} and V_{REF} (V_O). Also, the design has the ability to merge the T_{ON} pulses in load step-up transient. The details of T_{ON} generator design are given in Chapter 4. The same Op-Amp OPA615 is used in the T_{ON} generator block.

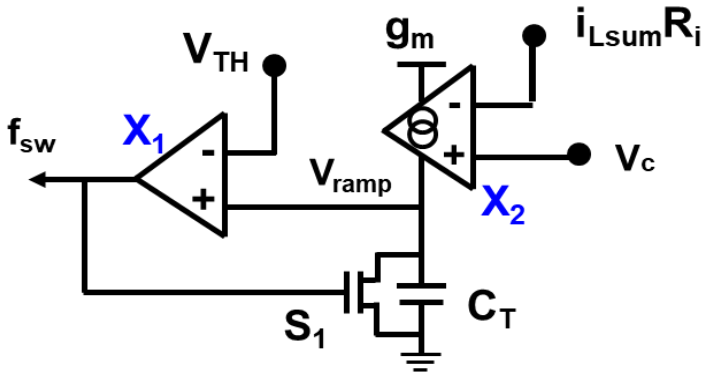

Figure 3.24 f_{sw} generator design in IQCOT control

The T_{ON} pulse triggering signal f_{sw} is generated from Vc and I_L information in f_{sw} generator block, shown in Figure 3.24, so this block is the core of the IQCOT control scheme and therefore, the design of this block needs to be done very carefully. The comparator X_1 is a very important component in this block design as the delay of the comparator plays a significant role in the transient response in IQCOT control. In Figure 3.25, a transient simulation result is shown with a particular setup where Vin=8V, Vo=1.2V, L=300nH, Co=36 x 22uF, f_{sw}=666KHz, ΔIo=25A, di/dt=500A/us. In f_{sw} generator block, g_m=10mS, V_{TH}=2V, and comparator delay =100ns. It can be seen that during transient the f_{sw} frequency increment becomes limited by the delay t_{d1} and t_{d2}. When V_{RAMP} is discharging and crosses V_{TH}, the f_{sw} pulse becomes low after the comparator's high-to-low delay, t_{d1}=100ns. After that, V_{RAMP} starts increasing and takes t_{RAMP} time to reach V_{TH}. When V_{RAMP} crosses V_{TH}, the f_{sw} pulse becomes high to discharge C_T after comparator low to high delay t_{d2}=100ns. In Figure 3.25, the distance between two f_{sw} pulses, t_{sw}=360ns at the transient, where the

total comparator delay $t_{d1}+t_{d2}$=200ns. Therefore, the pulse frequency increment in transient can be limited by X_1 delay if it is too large. In this case, T_{ON} is smaller than 360ns, which results in no T_{ON} extension in the transient.

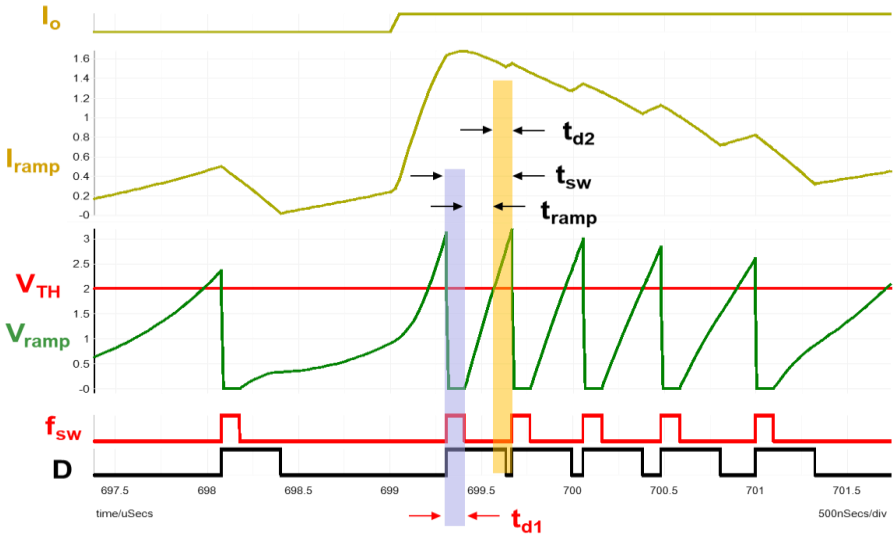

Figure 3.25 Transient response with comparator delay t_d=100ns

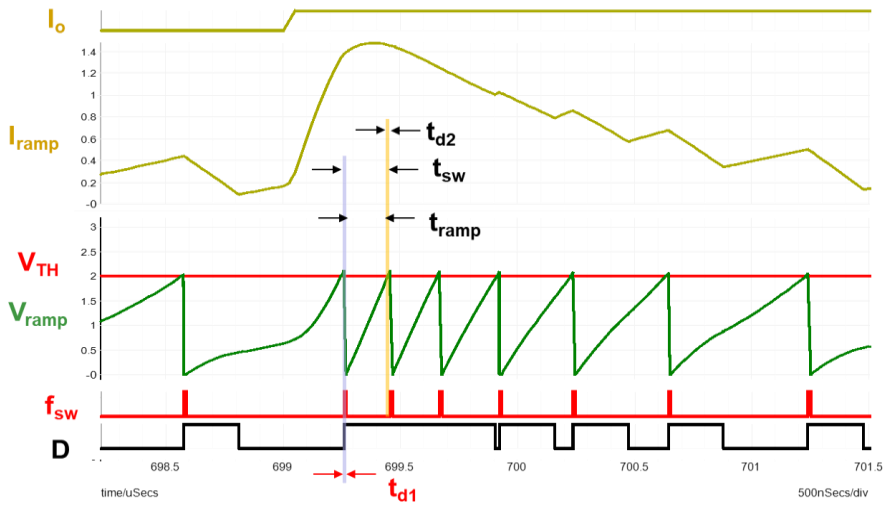

Figure 3.26 Transient response with comparator delay t_d=10ns

In Figure 3.26, when the same transient simulation is done with exactly the same setup except with comparator delay t_d=10ns, the pulse frequency increment becomes much higher and T_{ON}

extension also occurrs. In Figure 3.26, while t_{d1} and t_{d2} are 10ns, which is almost negligible, the distance between two f_{sw} pulse t_{sw} becomes 195ns, compared to 360ns in Figure 3.25. Therefore, the selection of a comparator with very low propagation delay is very important for fast transient response; especially for very high frequency applications. In fact, the delay td1 can be reduced by making the f_{sw} pulse shorter using additional circuitry. But delay td2 will always exist and the only way to reduce it is to use a faster comparator. The signal path from output of the comparator to the gate of the MOSFET in board layout also need to be done very carefully to reduce the parasitic components on that path.

A. Comparator Selection

Besides looking for smaller propagation, it is also vital to make sure that its drive ability is enough for the driving function, since the output of the comparator is used to drive the MOSFET. Table 1 shows a comparison of some high performance comparator ICs.

Table 1 Comparator selection for f_{sw} generator block

Part Number	Vcc-Vee	Vs	Ib/Ios (uA)	Tr/tf (ns)	Td (ns)	Bandwidth, Power Supply	Io
LT1715C/I	2.7-12	2.7-6	-2.5/0.2	2/2	6	150MHz, independent in & out supply	-+20mA
LT1720/1	2.7-6		-6 /0.6	2.5/2.2	4.5	Single supply, 62.5MHz	-+20mA
LT1711/2	2.4-7	2.7-6	-5/0.2	2/2	4.5	Single supply, 100MHz	-+20mA
LTV3501	5.5		2p/10p			80M	

Table 1 shows that all of these ICs have small a propagation delay. Finally, the LT1712 is chosen, as it also has very high bandwidth. Based on the datasheet, if V- =0, V+ =5V is used to supply this comparator, it can be easily figured out that its output pulse of 11ns width is enough to drive the MOSFET with low input-capacitor value.

B. Transconductance (g_m) Amplifier IC Selection

This IC is critical for the control board, since the performances of the f_{sw} generator rely on it. The selected transconductance amplifier IC should meet the following requirements: high trans-conductance, high bandwidth, high input and output impedance, and large linear range of input voltage. In addition, it should also have gain adjustability so that it can be adjusted based on the different operating conditions. Based on these principles, several transconductance amplifiers are compared in Table 2.

Table 2 Transconductance (g_m) amplifier selection

Type	bandwidth	Input impedance	Output impedance	Output current	trans conductance
OPA860	80MHz	455k||2.1pF	54k||2pF	15mA	95mA/V
OPA615	710MHz	7M||1.5pF	1.2M||2pF	20mA	72mA/V
LT1228	75MHz	1000M||3pF	8M||6pF	100uA	1mA/V
LM13700	2MHz				9.6mA/V
NE5517	2MHz				9.6mA/V
NJM13600	2MHz				9.6mA/V

Through this comparison of those that meet the requirements, the OPA615 is selected. Although it has a smaller g_m as compared to OPA860, it has much higher bandwidth (720MHz) than OPA860. It also has the largest output-current capability.

C. Charge Capacitor C_T Calculation

The V_{RAMP} equation can be written as:

$$V_{ramp} = \frac{1}{C_T}\int_0^{T_{on}+T_{off}} i_{ramp}(t)dt \tag{3.5}$$

Assuming, the capacitor charging current $i_{ramp}(t)$ has an average value I_{ramp}, Eq. (3.5) can be re-written as:

$$V_{ramp} = \frac{1}{C_T} I_{ramp}(T_{on} + T_{off}) = \frac{I_{ramp}}{C_T f_{sw}} \tag{3.6}$$

The maximum output current of the transconductance amplifier IC, OPA615 is 20mA. Under the transient condition, the switching pulse must be 10 times higher than that in the steady state, in order to implement the T_{ON} extension. Therefore, the maximum current in the steady state should be 2mA.

Assuming, V_{TH} =1V, C_T=1nF, the maximum switching frequency can be 2MHz. For OPA615, the maximum linear input voltage is related to the output current. In the linear range, it has: I_{ramp} =g_m x V_{input} ($I_{ramp} \leq$20mA). In the steady state condition, if set g_m =8mA/V, the input voltage should be 250mV.

Although commercial ICs have been used to implement the proposed IQCOT control board design, the experimental result has not reached up to the quality of the commercial controllers. The main reason is that those ICs used in this control method are not specifically designed for the proposed application. In addition, many parameters of those ICs cannot be modified. Therefore, it is difficult to compare the test results with the ideal SIMPLIS simulation results. It is also not fair to compare these performance results with commercial state-of-the-art COTCM controllers as the

delays and other design parameters are optimized for the operation inside the ICs. However, special attention has been paid in hardware design to minimize the delays in the board and to make the performance of the control board as close as possible to the ideal simulation

3.5.2 Experimental Verification Result for Single Phase Operation

The steady-state waveforms for single-phase IQCOT control are shown in Figure 3.27, in which the test conditions are: V_{IN} = 7V, V_O = 1.8V, switching frequency = 500kHz, L=360nH, Co_bulk = 2x470uF, and Co_cer = 12x22uF. The (V_C-$i_L R_i$) signal charges the capacitor in every cycle and generates the ramp signal, V_{RAMP}. As shown, the slope of the V_{RAMP} changes in different instances; this is basically caused by variations in i_L.

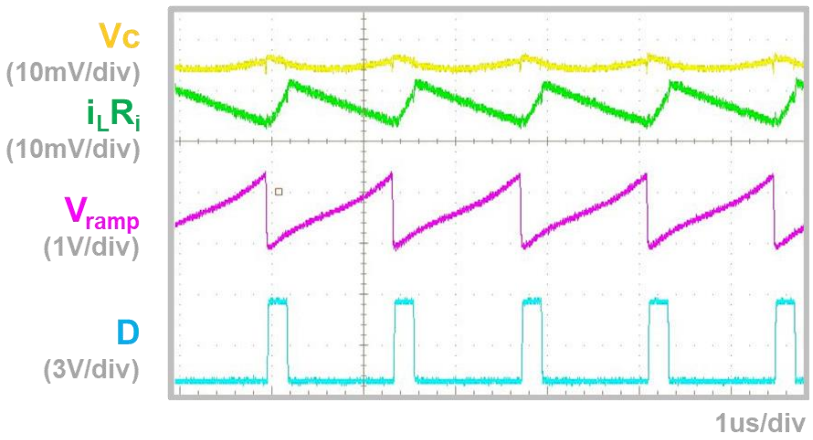

Figure 3.27 Key waveforms of proposed IQCOT control.

As it has been seen previously that the V_{RAMP} shape is different for different transconductance gains g_m. Figure 3.28 shows the V_{RAMP} in IQCOT control for different level of g_m.

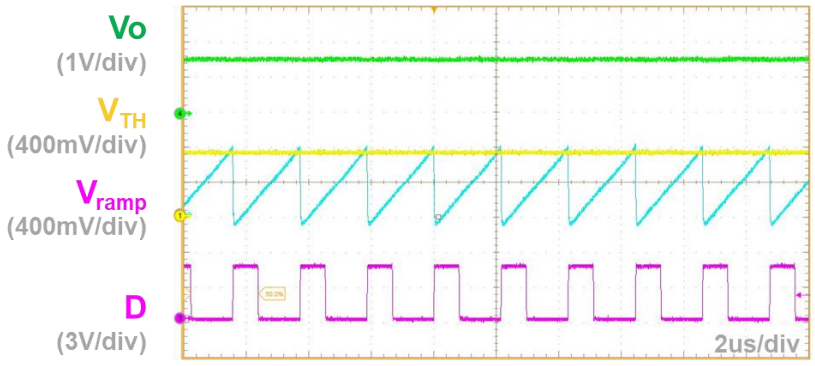

(a)

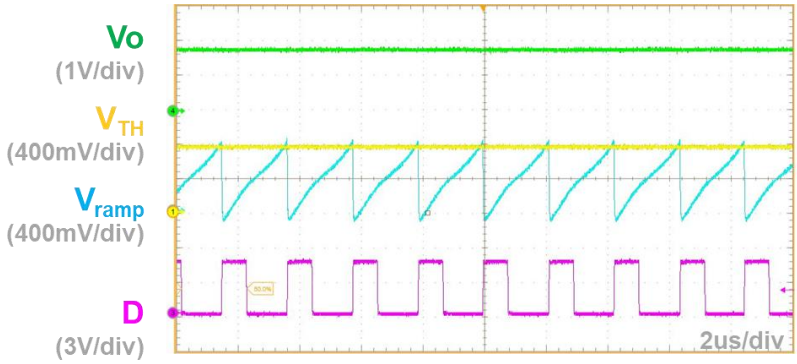

(b)

Figure 3.28 Key waveforms of IQCOT control with (a) low g_m, and (b) high g_m.

Figure 3.28 (a) shows the V_{RAMP} waveforms with low g_m where V_{RAMP} is more like a straight line. This is because the I_{RAMP} has more DC and AC ripple which means the distance between Vc and $i_L R_i$ is very large. On the contrary, Figure 3.28 (b) shows the V_{RAMP} waveform with high g_m where V_{RAMP} is more like a curved line. This is because the I_{RAMP} has some AC ripple along with DC which means the distance between Vc and $i_L R_i$ is small. This test result verifies the simulation results shown in Figure 3.11.

3.5.3 Experimental Verification Result for Multiphase Operation

The simulation results of the proposed IQCOT control method for multiphase operation are presented and explained in the previous sections. In this section, some hardware verifications are presented to support the proposed concept. The proposed approach is first implemented in a control board, and is then connected with a commercial two-phase VR power-stage board with CPU/GPU socket and output filter model. The test conditions are: V_{IN} = 10V, V_O = 1.2V, equivalent f_{sw} (per phase) = 500kHz, L=360nH, Co_bulk = 330uF, Co_cer = 12x22uF, V_{TH}=600mV, and the given load step is ΔI_{LOAD}=20A. In this operation, the output impedance is set to zero (no AVP case). In the design procedure, some component selection is very sensitive. One example is the transconductance (g_m) amplifier. In the design used in this research, the OPA615 is selected, as it has high g_m value along with high bandwidth.

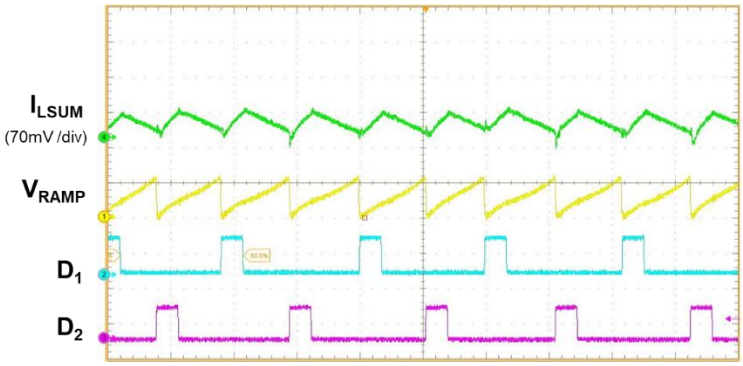

Figure 3.29 Steady-state IQCOT waveforms in multiphase operation.

In Figure 3.29, some key waveforms of steady-state operation of the proposed IQCOT control are presented. The I_{SUM} waveform is the summation of the two-phase inductor current times the sense gain of the current loop. I_{SUM} contributes to V_{RAMP} generation, which interacts with V_{TH} voltage (600mV) to create the duty-cycle signal, which is then distributed in both phases.

To demonstrate the ability of the proposed IQCOT control to operate at the ripple-cancellation point, the converter is set up at very close to 50% duty cycle for two phases where V_{IN} = 2.5V. In Figure 3.30, it can be seen that the I_{SUM} ripple is very small (i.e., only 7mV).

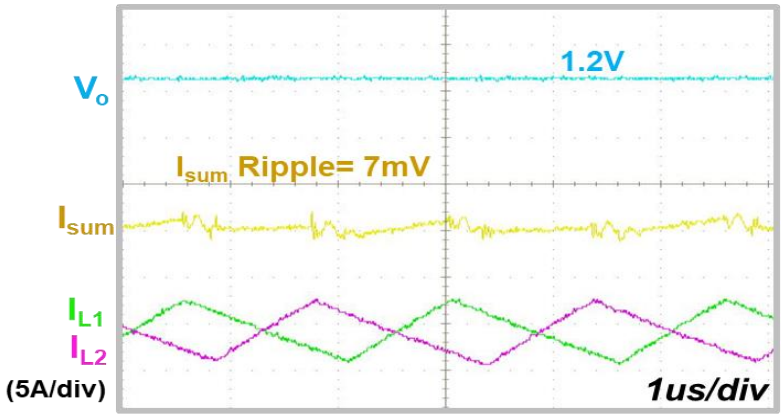

Figure 3.30 Waveform at close to ripple-cancellation point (D ≈50% for two-phase operation).

3.6 Summary

In ripple-based variable-frequency COT control for multiphase operation, when the ripple becomes zero because of the ripple-cancellation effect, the control becomes unable to work. Charge-based control schemes have been investigated to solve this ripple-cancellation issue. In this chapter, a novel inverse-charge constant on-time (IQCOT) control has been proposed; as presented, it can seamlessly operate at the ripple-cancellation point. The current-mode property and other features of the proposed IQCOT control have also been discussed. Extension of this inverse-charge concept to the variable-on and variable-off time control scheme is also mentioned. Finally, the concept of IQCOT control and its ability to work at the ripple-cancellation point are verified in hardware, both in single and multiphase operations.

Chapter 4. Transient Performance of IQCOT Control

One issue of the conventional ripple based CMCOT control is that, in the heavy load step-up transient, inductor current increment or decrement becomes limited by its fixed on time (T_{ON}) operation. For the multiphase operation case, its phase overlapping limitation hinders the inductor current increment at load step-up transient. State-of-the-art controllers use different nonlinear controls in the system to solve these issues which are not easy to optimize at different transient condition. In previous section a novel concept of IQCOT control is proposed which solves the ripple cancellation issue in multiphase operation. In this section, transient performance improvements by proposes IQCOT control in both single and multiphase are discussed.

4.1 Load Step-Up Transient Response in IQCOT Control

4.1.1 Transient Response of IQCOT with T_{OFF} Integration

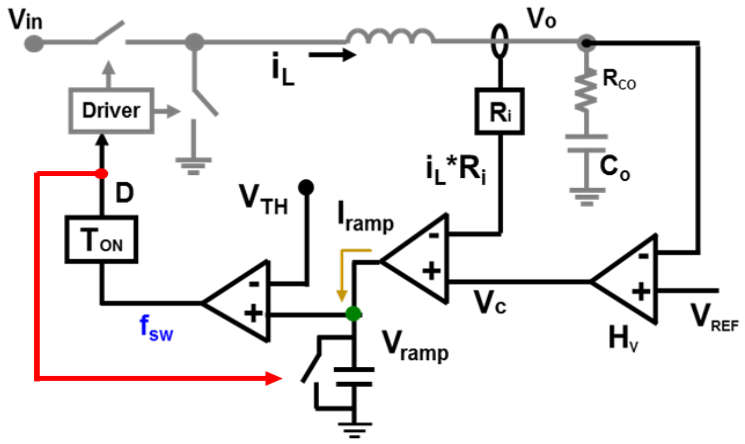

Figure 4.1 Control structure of proposed IQCOT control with T_{OFF} integration

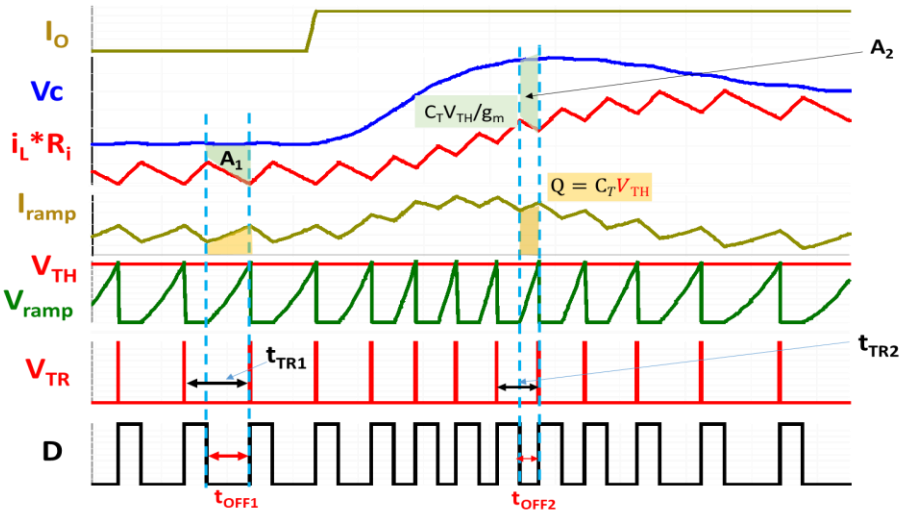

Figure 4.2 Load step-up waveforms of proposed IQCOT control with T_{OFF} integration

To implement the T_{OFF} period integration in proposed IQCOT control, the charge control capacitor C_T is reset by duty cycle signal D. In the Figure. 4.1, it can also be seen that, at load step-up transient, if I_L cannot follow V_C properly, t_{OFF2} becomes smaller to keep charge in the capacitor constant in each cycle. According to the control law in (3.4), area of ($Vc-i_LR_i$) is constant every cycle; which means A1 and A2 are equal in every cycle. In transient when distance between Vc between i_LR_i has increased, the height of area A2 is increased and as a result the width of A2,

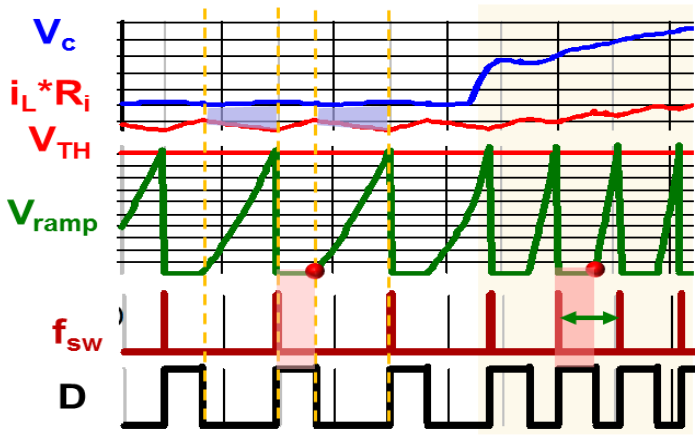

Figure 4.3 Transient response of IQCOT control with T_{OFF} integration

which is t_{OFF2}, needs to decrease to keep the area constant. Hence, the distance between each f_{sw} pulse becomes closer at transient and duty cycle increase automatically to increase i_L to supply more current to the output. One limitation this T_{OFF} period integration in IQCOT control by resetting the capacitor is the limitation of f_{sw} increment in transient as shown in Figure. 4.2. It can be seen in Figure. 4.3 that the pulse frequency (f_{sw}) increment at transient response in limited by the T_{ON} pulse width which eventually limits the transient response.

4.1.2 Transient Improvement with (T_{ON}+T_{OFF}) Time Integration

To improve this situation, the resetting of the capacitor has been changed. Pulse frequency (f_{sw}) signal has been used to reset the capacitor. The advantage of this modification is that the increment of the f_{sw} is not limited by T_{ON} pulse width anymore. Therefore, distant between two pulses can become very small at transient. In that case, as pulse can repeat before end of a T_{ON} pulse, T_{ON} pulses can merge together to create a longer pulse at transient and can make the transient response faster. But unfortunately, the conventional T_{ON} generators cannot retrigger a T_{ON} pulse before one T_{ON} pulse ends. Hence, a modification in T_{ON} generator is also required.

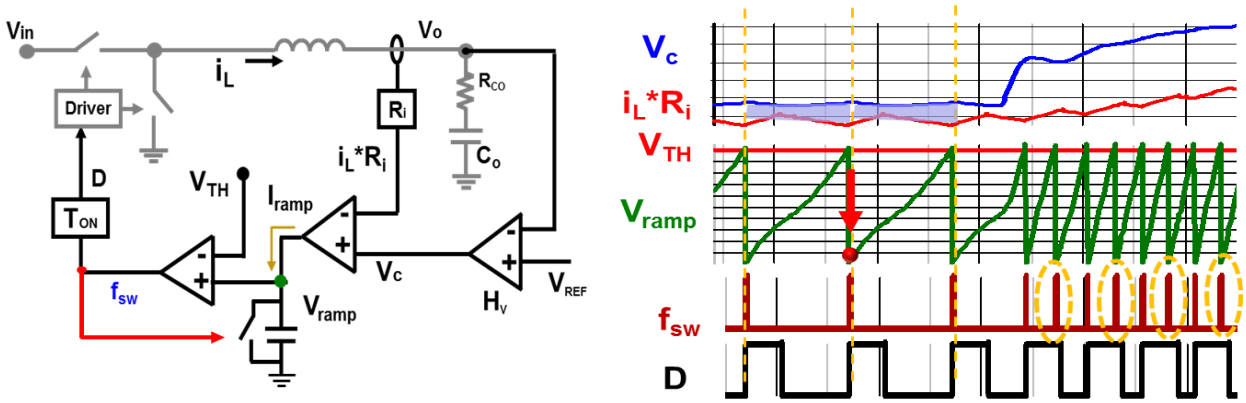

Figure 4.4 Transient response of IQCOT control with (T_{ON}+T_{OFF}) period integration

4.1.3 T_{ON} Generator Block Improvement for Adaptive T_{ON} Extension

In this section proposed IQCOT control is presented with a modified on time generator to improve the load step-up transient response. In Figure 4.5 (a) the 'T_{ON}' block is presented which contains the state-of-the-art T_{ON} generator circuit [D.1]. Unlike the conventional ripple based current mode COT control, in the proposed inverse charge control based structure, f_{sw} pulses can occur even before end of on time. With this state-of-the-art T_{ON} generator circuit shown in Figure 4.5 (a), when the f_{sw} pulses of proposed IQCOT control will come very close at load step-up transient, some pulses will not be able to generate on time because it is within the T_{ON} time or minimum off time shown in Figure 4.6 (a).

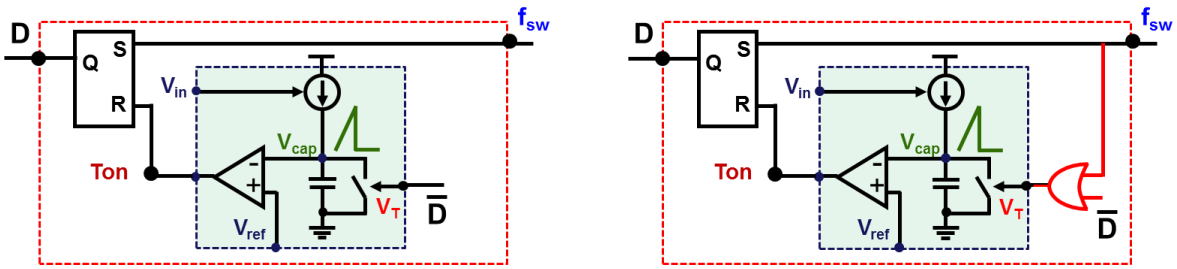

Figure 4.5 T_{ON} generator block: (a) conventional structure, and (b) structure with proposed modification for T_{ON} extension

As a result, inductor current increment will be slowed down by the presence of the off time periods between the T_{ON} periods. But if the on time (T_{ON}) periods triggered by the f_{sw} pulses can be merged together to create a longer on time at the load step-up case, then inductor current will be able to rise much faster and significant undershoot reduction can be done at the output. The proposed T_{ON} generator is presented in Figure 4.5 (b) where f_{sw} is ORed with $\overline{D}$ to add this feature and the waveforms are presented in Figure 4.6 (b).

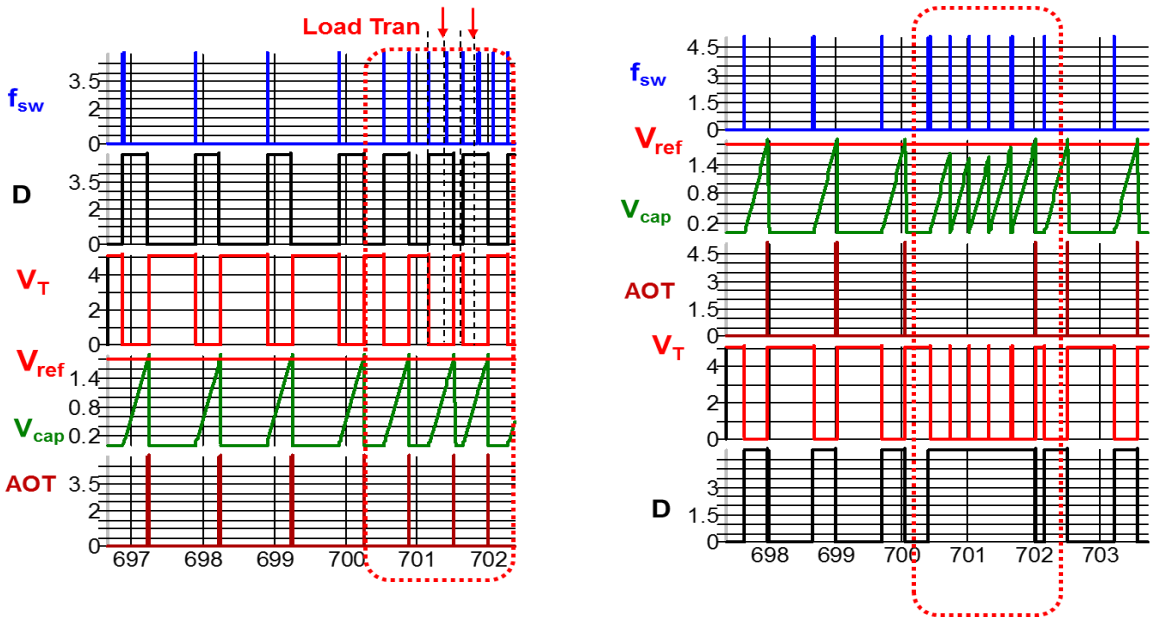

Figure 4.6 Key Waveforms of state of art T_{ON} generator (a) conventional structure, and (b) structure with proposed modification for T_{ON} extension

4.1.4 Single Step Response with Adaptive T_{ON} Extension in IQCOT Control

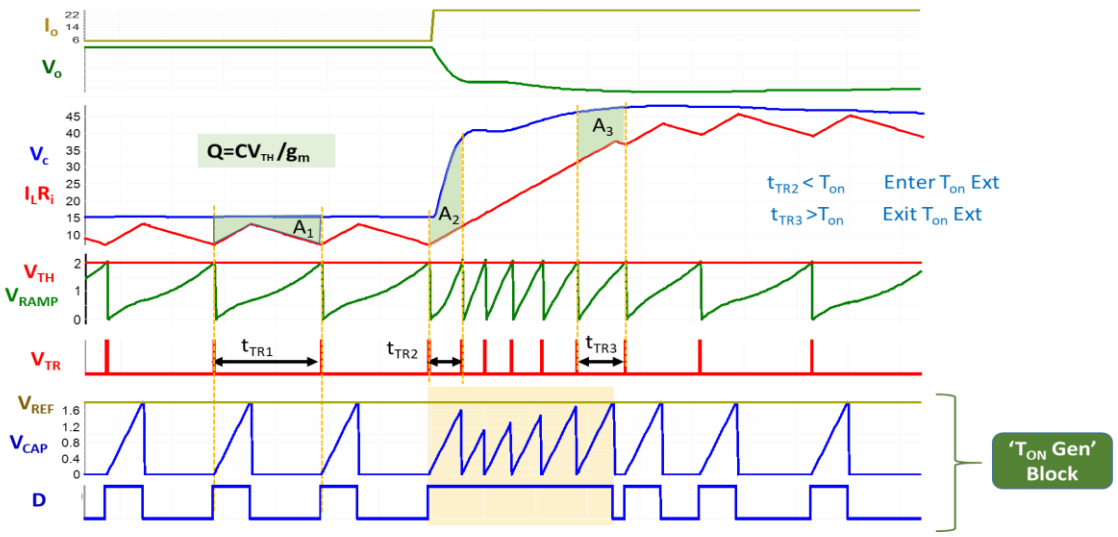

Figure 4.7 Load step-up waveforms with proposed control

The complete transient response in load step-up is given in Figure 4.7, where it can be seen that a larger T_{ON} can be generated at load step-up to maximize the inductor current slope at transient. Along with steady state operation, the transient response of proposed IQCOT control in load step-up is also shown in Figure 4.7. In a load step-up transient, the compensator output V_C goes high very quickly by following the fall down of the output voltage Vo. If inductor current I_L cannot follow the V_C then, difference (V_c- i_LR_i) becomes larger as shown in Figure 4.7. As the capacitor charging current is proportional to (V_c-i_LR_i); that current also becomes high and therefore the slope of capacitor voltage, V_{RAMP} becomes high. In that way, the frequency of output pulse V_{TR} increases very quickly after the load transient step up. This frequency increment is controlled by the control law expressed in (3.4). Area A_{SS} and A_1 enclosed by V_C and i_LR_i in Figure 4.7 are equal to C_TV_{TH}/g_m. When height of A_1 increases, the width of the area A_1 decreases proportionally. If this V_{TR} increment is very high and t_{TR1}, shown in Figure 4.7, becomes smaller than T_{ON} time period, then consecutive T_{ON} pulses will merge together to create an extended T_{ON}. This extended T_{ON} helps to increase the inductor current close to its final value in one step. When i_LR_i becomes close to V_C, then height of A_2 becomes smaller and t_{TR2} becomes larger and if it is larger than T_{ON} length, T_{ON} extension will be ended and eventually duty cycle will go back to original state again.

Now, one very important aspect of the proposed IQCOT control is that, in comparison to the load transient response in ripple based current mode control where V_C goes above I_L R_i in heavy load step-up and lost the control on duty cycle, the proposed control never lose control. Pulse frequency V_{TR} is always proportional to (V_c - i_LR_i) in all the conditions. This property enables IQCOT control adjust its duty cycle according to load step characteristics.

4.2 Load Step-Up Transient Response in Multiphase IQCOT Control

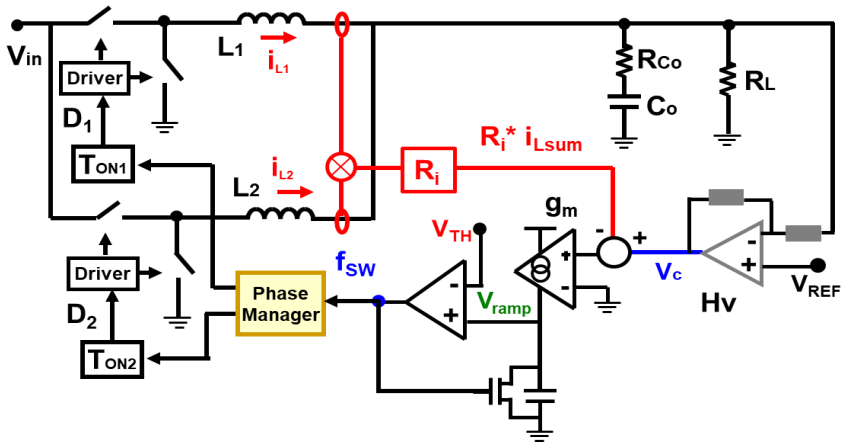

Figure 4.8 Proposed IQCOT control structure in multiphase operation

IQCOT control with pulse distribution structure for multiphase operation with 2 parallel phases is presented in Figure 4.8. In the control, all the phase currents are summed (called I_{SUM}), and then subtracted from compensator output V_C. The compensator is a proportional gain compensator for AVP implementation for VR applications as mentioned in Chapter 1. Then (V_C-I_{LSUM}Ri) is used to charge the capacitor to generate the frequency f_{sw}. As the V_{RAMP} starts from beginning of the T_{ON}, shown in Figure 4.9, the pulses can come very quickly after the previous pulse regardless of what is the T_{ON} time period. If a large load step-up transient is given and an undershoot is occurred at the output, then f_{sw} pulses will be very close as shown in Figure 4.9 and the frequency increment of f_{sw} pulses is proportional to the magnitude of the undershoot. In Figure 4.9, it can be seen very clearly that the pulses can overlap to improve the transient performance and the overlapping is proportional to the output undershoot.

4.2.1 Phase Overlapping property for Transient Improvement in Multiphase

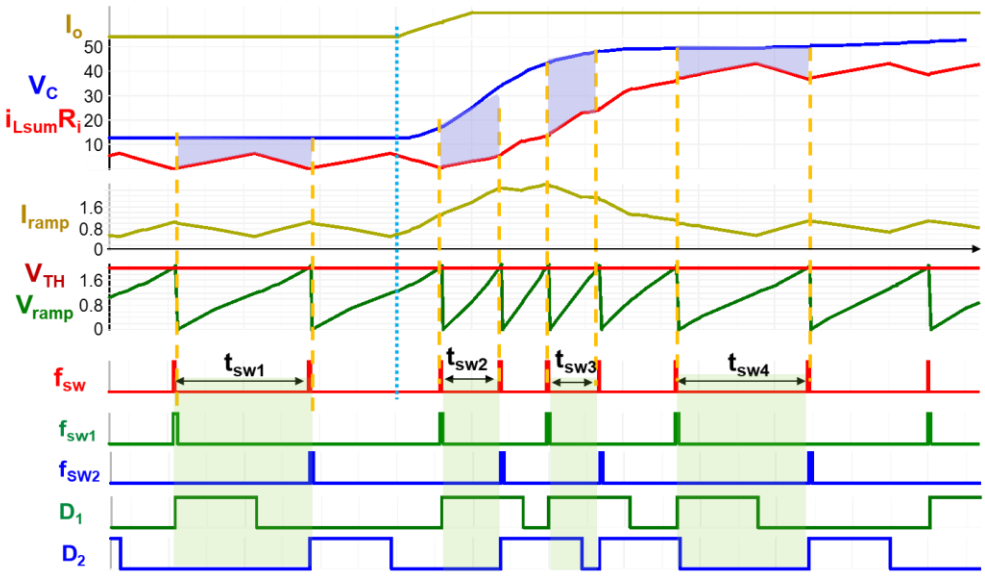

Figure 4.9 Natural phase overlapping feature in multiphase IQCOT control

In the multiphase operation, the proposed IQCOT control can improve the load step-up transient performance by achieving natural pulse overlapping feature. When a large load step-up transient is given, the response waveforms of different signals are given in in Figure 4.9. At the response of load step up, first the output will start to fall. Then the V_C will immediately go high. If the inductor current increment is not fast enough and cannot cope up with V_C change, then difference between these two signals (V_c - $I_{LSUM}Ri$) will immediately become very large, and as a result V_{TR_SUM} pulse frequency will be very high. As, there is no limit of the V_{TR} frequency like ripple based control, V_{TR_SUM} frequency can be very high and distance of two consecutive pulses can be easily smaller than on time of the system. In that case when these pulses will be distributed, T_{ON} pulses of each phase will be overlapped with each other. Furthermore, if the load transient is very severe, then V_{TR_SUM} pulse frequency can be so high that after the V_{TR_SUM} pulses are distributed in phases, each

phase V_{TR} pulse frequency can still be very high to merge together to create an extended T_{ON} pulse in each phase. This case has been shown in in Figure 4.9. In that way total inductor current increment will be faster and will be able to reduce the undershoot or the amount output capacitor significantly.

4.2.2 Auto Optimized Phase Overlapping to Avoid Overcorrection

One important aspect of proposed IQCOT control is – it not only creates the faster transient response but also produce the optimized response which helps to avoid any type of overcorrection in the system. As, it can clearly be seen form in Figure 4.9 that the frequency increment of V_{TR} pulses is linearly proportional to the magnitude of the undershoot, the phase overlapping is also linearly proportional to (V_C - $I_{SUM}R_i$) which is somehow proportional to the output undershoot. This phenomenon will eliminate the chance of any overcorrection or ring-back of output voltage.

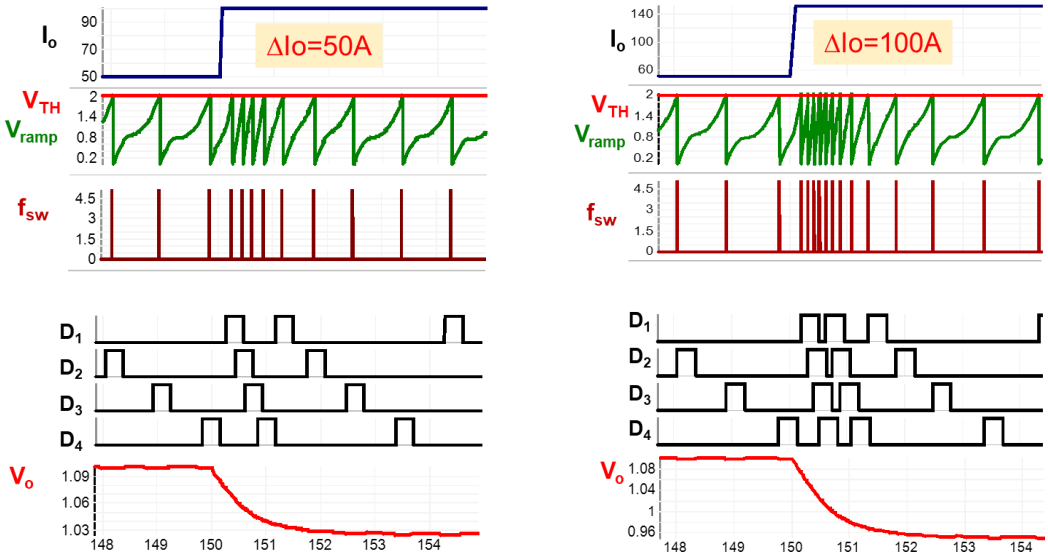

Figure 4.10 Optimized phase overlapping in different load step-up transient

In Figure 4.10(a), simulation results of 4 phase VR with IQCOT control is presented where a 50A load step-up with 1000A/us slew rate is applied with V_{IN}=12, Vo=1.2, combined eq. f_{sw}=1MHz, L=330nH, Co=36*22uF decoupling cap with standard socket filter model.

Here, it can be seen very clearly that when load step is increased from 50A to 100A in Figure 4.10(b), the V_{TR} pulse frequency has been increased proportionally and as a result, the delay between D1 and D2 is decrease which means that overlapping between then has been increased. In both cases, V_O settles very smoothly without any overcorrection.

4.2.3 Pulse Overlapping with T_{ON} Extension at Heavy Load Step-Up Transient

In multiphase operation, the proposed control can improve the performance by achieving natural and proportional pulse overlapping with naturally extended T_{ON} pulses mentioned earlier. Figure. 4.22 shows a 2-phase structure of buck converter with proposed control and Figure. 4.23 presents the transient performance simulation results at load step-up where (V_c - $I_{Lsum}R_i$) goes very

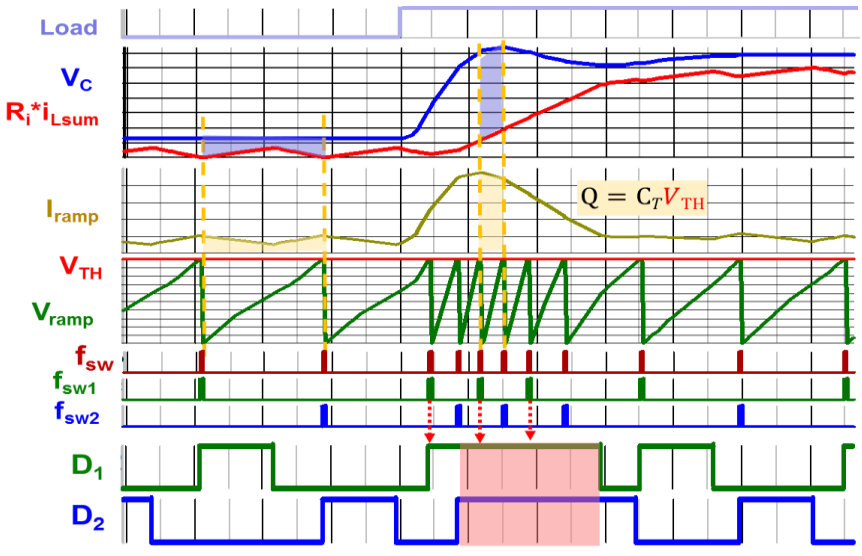

Figure 4.11 Transient response of proposed IQCOT in multiphase operation

high immediately after load step-up and makes the f_{sw} frequency very high. As there is no limitation in f_{sw} frequency increment, when they are distributed in 2 phases, they can easily overlap with each other and if the distributed pulses of each phase are close enough, they can merge to create a longer pulse as seen in Figure. 4.23.

In this way natural pulse overlapping with natural T_{ON} extension can reduce the undershoot or reduce the number of output capacitors in the board significantly and as both features are natural and linearly proportional to output undershoot, any chance of ring-back will also be eliminated.

4.2.4 Fast and Optimized Response at Heavy Load Step-Up Transient

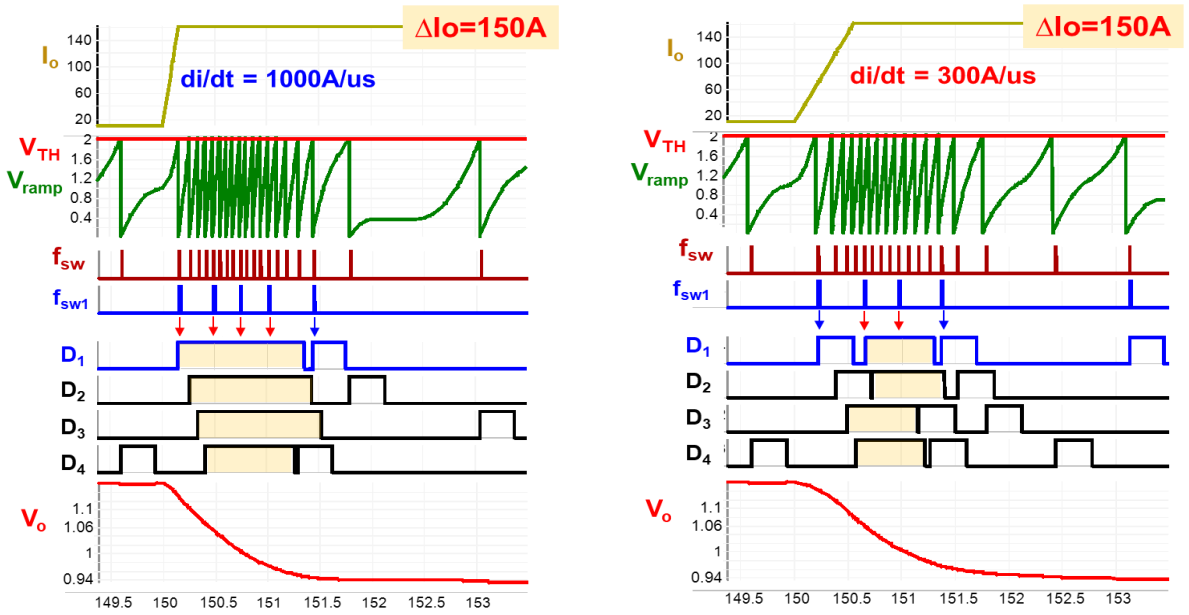

(a) (b)

Figure 4.12 Optimized phase overlapping with optimized T_{ON} extension in different load step-up (a) di/dt= 1000A/us, and (b) di/dt=300A/us

In Figure 4.12(a), a higher loads step of 150A is applied in similar condition where it can be seen that T_{ON} pulses in each phase has been merged to create an extended T_{ON} in each phase to support larger load step. Again, when the slew rate is reduced from 1000A/us to 300A/us for same 150A load step in Figure 4.12 (b), both T_{ON} extension and phase overlapping has been reduced to produce optimized output without any overcorrection. In VR application the load step and slew rate both changes very frequently. As this T_{ON} extension of each phase and their overlapping at transient is adaptive to transient requirement, it always produce optimized response which eliminates any chance of ring-back or overcorrection.

4.3 Overshoot Reduction at Load Step-Down Transient

In the case of the load step-down transient, when the load very quickly becomes lower than the inductor current, an overshoot is created in the output. Following the output overshoot, the compensator output V_C becomes low and V_C and $i_L R_i$ starts to become smaller and eventually V_C

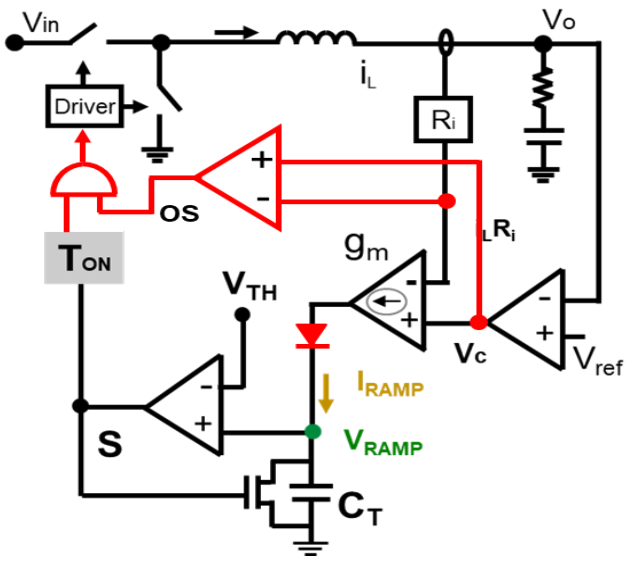

Figure 4.13 Modification in IQCOT control to improve load step-down transient

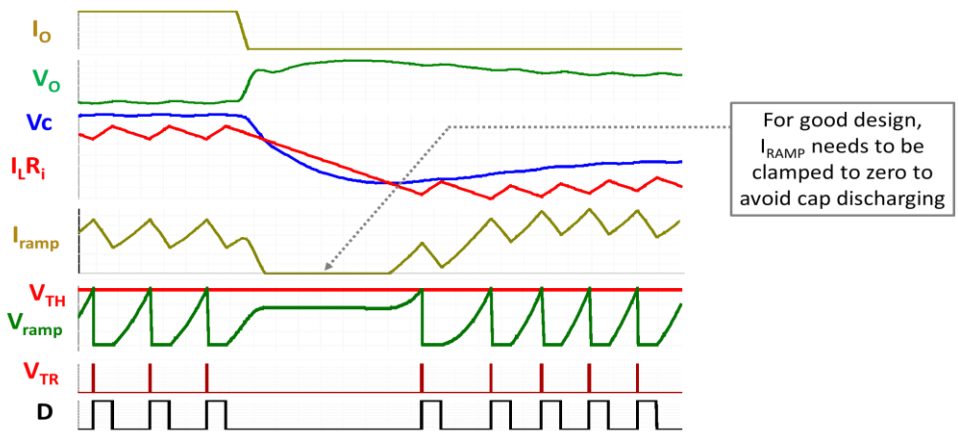

Figure 4.14 Load step-down waveforms with proposed IQCOT control

becomes smaller than $i_L R_i$ as shown in Figure 4.14. When (V_C - $i_L R_i$) becomes negative, then I_{RAMP} will also become negative if not clamped to zero. In this case, I_{RAMP} is clamped to zero as shown in Figure 4.14, which will essentially make the V_{RAMP} slope zero and no more duty cycle pulse is created. Hence, the inductor current will reduce to the lower settling value. However, if I_{RAMP} is allowed to become negative, then the capacitor C_T will be discharged at that instance which will create a delay to resume the duty cycle while returning from the load step-down.

As mentioned earlier, if the load step occurs at the beginning of fixed T_{ON}, there can be a large overshot at the output. This issue can be solved in the proposed IQCOT control by making a

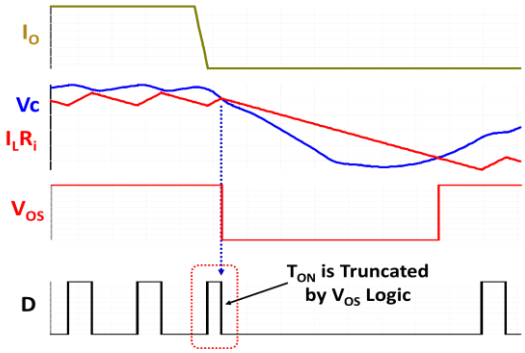

Figure 4.15 Waveforms of proposed modification for overshoot reduction feature in load step-down

small modification. When at the load step-down, V_C very quickly goes low, V_C will cross the i_LR_i immediately and make (V_C - i_LR_i) negative, as shown in Figure 4.15(b), which is always positive at steady state operation. Hence, a logic signal V_{OS} can be created by comparing V_C and i_LR_i which becomes low when the load step-down occurs. This way, the control will detect an overshoot at the load step-down without using any addition circuit. If this logic is ANDed with the duty cycle D, as shown in Figure 4.15(a), then the predefined fixed T_{ON} pulse can be truncated immediately and thereby will reduce the overshoot at the output.

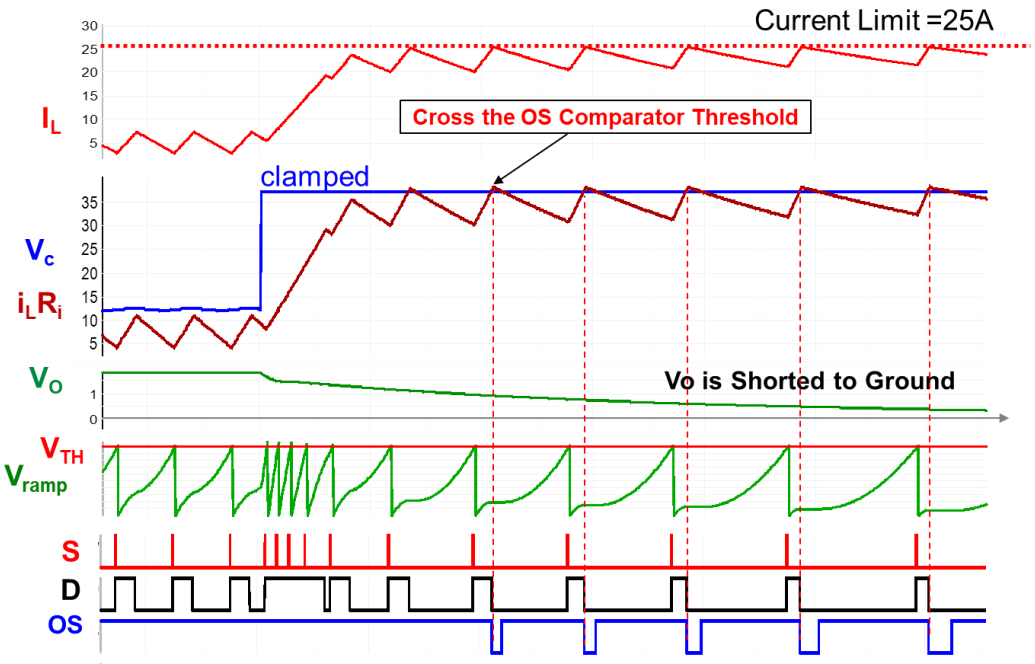

Figure 4.16 Short-circuit current limit feature improvement by using OS logic

Another benefit of this OS logic is that it can be used to improve the short circuit current limit in IQCOT control. In Figure 4.16, it can be seen that short circuit current limit is little higher than current limit in overload condition. This is because, in short circuit condition, some part of the i_LR_i waveforms is above Vc. In this case, T_{ON} can be truncated by using OS logic when i_LR_i tries to go

above Vc. In that way, peak of $i_L R_i$ will be clamped by Vc and inductor current will also be limited to a predefined value corresponding to predefined Vc clamping voltage, as shown in Figure 4.16.

4.4 Transient Comparison with state-of-the-art Constant On-time Controls

4.4.1 Comparison with Constant On-Time Current Mode (COTCM) Control

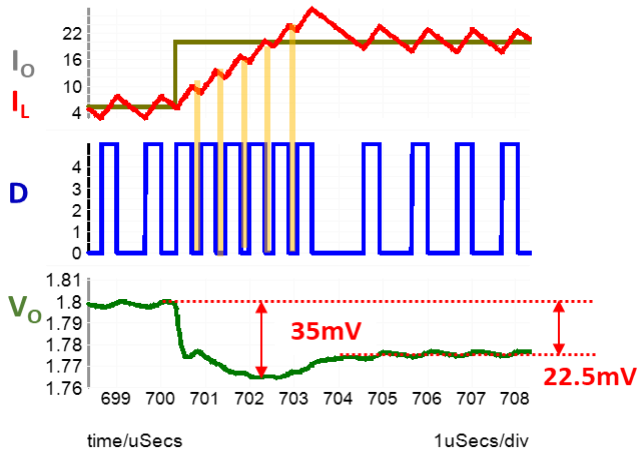

(a)

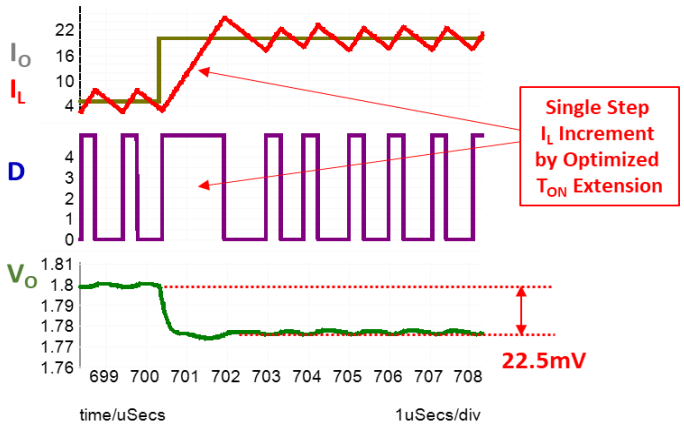

(b)

Figure 4.17 Load step-up waveforms: (a) ripple based CMCOT control, and (b) proposed IQCOT control

The proposed IQCOT control method is simulated in a single phase VR platform using SIMPLIS simulator. The simulation condition is V_{IN} =5.2V, V_O =1.8V, R_{LL}=1.5mΩ, C_O=23x22uF (Ceramic), ΔI_{LOAD}=15A, Slew rate =1000A/μs, T_{ON} =346ns, and equivalent switching frequency =1MHz. In Figure 4.17 (a) and Figure 4.17 (b), the comparison of V_O undershoot between COTCM and propose IQCOT control method is presented where it is clearly seen that in Figure 4.17 (b) gate signal D is immediately increased by IQCOT control right after the undershoot occurs and enables the inductor current I_L to catch I_{LOAD} very quickly in single step compared to Figure 4.17 (a). This action eventually causes a smaller undershoot in Figure 4.17 (b) than the undershoot in Figure 4.17 (a) where T_{ON} is constant at transient period. A transient response at load step-up comparison is shown in Figure 4.17 (a) and Figure 4.17 (b), it can be clearly seen that undershoot can be reduced at load transient by using IQCOT control.

4.4.2 Comparison with Constant On-Time V^2 Control

Constant on-time V^2 control [D.2][D.3] has been used in the industry for simple structure and fast transient response [D.4][D.5][D.6][D.7][D.8]. There are two voltage feedback loops for V^2 control. The inner loop is a direct voltage feedback loop: the output voltage signal is directly fed into the modulator. Usually the outer loop is slower than inner loop: the voltage feedback will go through a compensation network to generate the control signal. When the output voltage varies due to disturbances either from the input voltage or the load variations, the duty cycle will change immediately since the modulator will directly see the output voltage change through the inner feedback loop. Therefore, one advantage for V^2 control is that it can provide faster transient response [D.9][D.10][D.11][D.12][D.13]. Especially, it can provide faster load transient response compared with current mode. Since for current mode control, when load transient happens, the duty

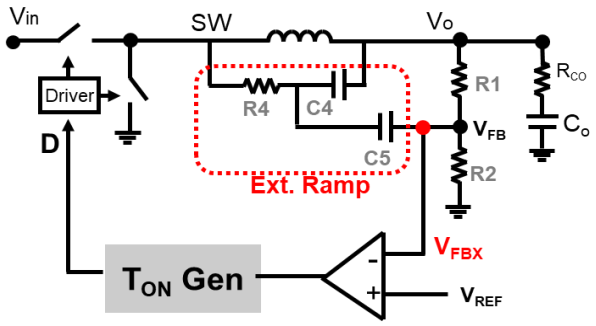

Figure 4.18 structure of constant on-time V^2 control with external ramp

cycle response through the outer loop compensation which is intuitively slower compared with the direct feedback inner loop in V^2 control. Sub-harmonic problem occurs for constant-on-time V^2 control using ceramic caps because of its smaller ESR value [D.14][D.15]. To solve the instability problem, external ramp is added to the system. Another reason to add external ramp is to improve the noise immunity as V_O ripple may become may small in V_2 control with ceramic cap. In that case larger the external ramp will produce better noise immunity. Here a transient simulation is presented in Figure 4.19 for COT V^2 control with 10mV external ramp. Following the guideline given in [D.16][D.17], the simulation setup is - f_{sw}=1MHz, V_{IN}=5.2, Vo=1, Co=5*47uF, L=750nH, ESR=0.8m, i_o=0-15A, di_o/dt=40A/us, and T_{OFF_MIN}=100ns.

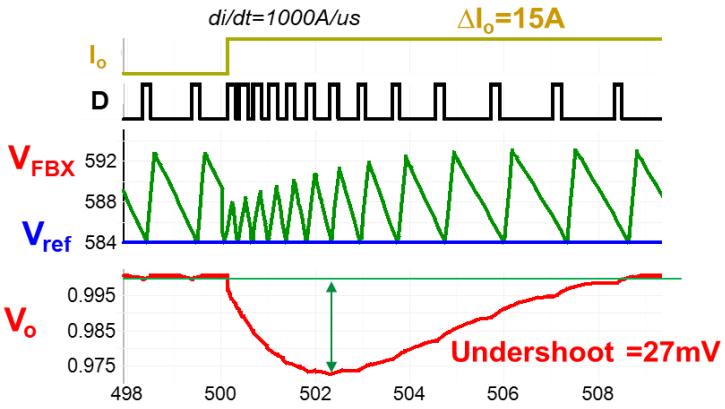

Figure 4.19 Transient response of constant on-time V^2 control with external ramp

To compare the transient performance IQCOT has been simulate din the same condition. In this case a type II compensator is used with IQCOT control, as shown in Figure 4.20, to achieve transient response without AVP. The transient simulation waveform is shown in Figure 4.21 where an extended T_{ON} pulse is generated ay transient by merging the T_{ON} pulses which helps to reduce the undershoot. Comparing transient response in Figure 4.19 and Figure 4.21, it can easily be seen that undershoot has been reduced from 29mV to 19mV in case of IQCOT control for its T_{ON} extension. It can also be seen that there is no ring-back in IQCOT while COT V2 control shows significant ring-back in Figure 4.19.

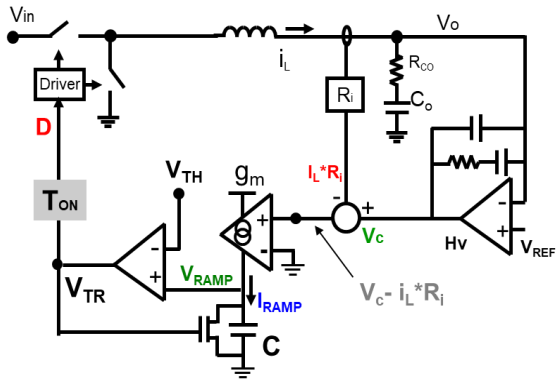

Figure 4.20 IQCOT control structure without AVP

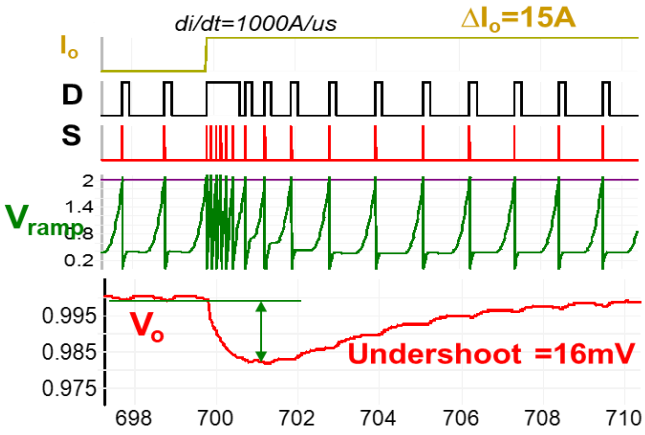

Figure 4.21 Transient response of IQCOT control without AVP

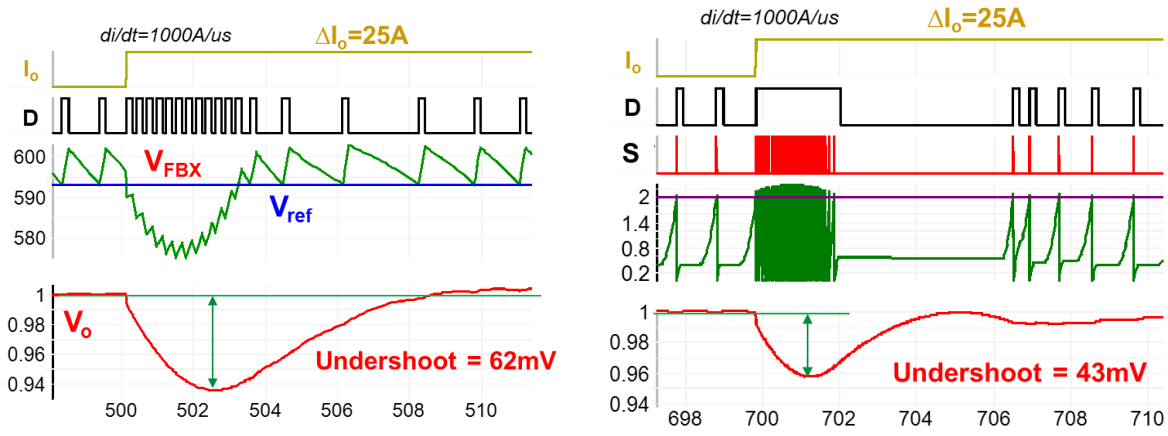

(a) (b)

Figure 4.22. Load step-up comparison (a) V2 COT control, and (b) IQCOT control

In Figure 4.22, the V^2 COT control and IQCOT control has been compared side by side for 25A load step in same test setup. When 25A load step with 1000A/us slew rate is applied to V^2 control, V_{FBX} immediately goes below the V_{REF} and saturate the duty cycle. In this situation, each T_{ON} pulse occurs after a minimum off time and a 62mV undershoot will occur at output. On the contrary, in IQCOT control, a large extended T_{ON} will be generated which will reduce the undershoot to 43mV, in same test condition.

4.4.3 Analytical Calculation for Transient Performance Improvement

In this section, the analytical expression for output voltage droop for the converter is derived and by using that equation, it is also determined how much the capacitor can be saved by using the proposed method. Then these calculations are also verified by simulation results.

A. Load step-up Case

The equation for output voltage droop for a given load step-up case and output capacitor is given below:

$$\Delta V_o = \frac{\Delta I_o^2 \times (T_{on} + T_{off\_min}) \times L}{2C_o \times [V_{in}T_{on} - V_o(T_{on} + T_{off\_min})]} \quad (4.1)$$

Here, ΔI_o = load step, T_{OFF_MIN} = minimum off time required, C_o= output capacitor. Now, the proposed IQCOT control can improve the transient by a single step response where a large T_{ON} can make the inductor current reach from initial load to final load level in a single step, in which case T_{OFF_MIN} will be zero. In that case, equation for V_O droop will be -

$$\Delta V_{o\_IQCOT} = \frac{\Delta I_o^2 \times L}{2C_o \times (V_{in} - V_o)} \quad (4.2)$$

The V_O droop in Fig. 16(a) can be calculated from equation (4.1), where it can be seen that at transient V_O droop is approximately 35mV while the steady state error is 22.5mV because of AVP. The V_O droop is calculated by using the equation (4.1) which also is almost 38mV. By using the equation (4.2) we can also found the droop for a single step response which is 22.5mV.

To calculate the capacitor saving by IQCOT control, we need to calculate how much cap will be needed in CMCOT to achieve a similar performance of IQCOT i.e. 22.5mV. To calculate that following equation can be used.

$$C_o = \frac{\Delta I_o^2 \times (T_{on} + T_{off\_min}) \times L}{2\Delta V_o \times [V_{in}T_{on} - V_o(T_{on} + T_{off\_min})]} \quad (4.3)$$

While proposed IQCOT control can achieve 22.5mV droop with around 506uF, by using equation (4.3) it is found that conventional CMCOT will require approximately 870uF to achieve the same droop. Therefore, it can be said that capacitor savings by proposed IQCOT control is-

$$\frac{870uF - 506uF}{870uF} \times 100 = 41.8\%$$

B. Load step-down Case

In Figure 4.23(a), load is released at the beginning of a T_{ON} in the gate signal D and inductor current I_L keeps increasing because of fixed T_{ON}. This creates additional charge Q1 in output capacitor which increase the overshot at the output. Figure 4.23(b) shows that if the control can immediately truncate the T_{ON} right after load step down, only Q2 charge will create overshoot as Q1 is negligible compared to Q2, which eventually will reduce overshoot. Eq. (4.4) gives the expression for overshoot voltage at output for conventional constant on-time control while Eq. (4.5) shows the case for proposed IQCOT control. Clearly, overshoot in Eq. (4.5) is smaller as Q2 needs to be discharged instead of (Q1+Q2).

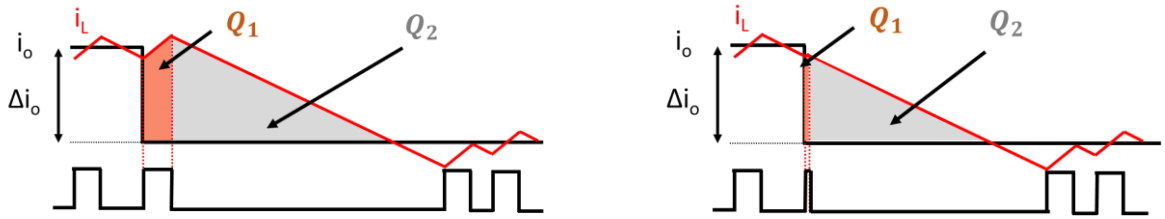

(a) (b)

Figure 4.23 Load step down transient performance (a) without T_{ON} Truncation (b) with T_{ON} Truncation

$$\Delta V_o = \frac{1}{C_o}(Q_1 + Q_2) \approx \frac{1}{C_o}(\Delta I_o . T_{on} + \frac{\Delta I_o^2 . L}{2V_o}) \quad (4.4)$$

$$\Delta V_{o\_IQCOT} \approx \frac{Q_2}{C_o} \approx \frac{1}{C_o}(\frac{\Delta I_o^2 . L}{2V_o}) \quad (4.5)$$

Simulation comparison of Conventional COTCM and proposed IQCOT control at the load step-down case is presented in Figure 4.24 (a) and Figure 4.24 (b). The simulation condition is V_{IN}

=5.2V, V_O =1.8V, R_{LL}=1.5mΩ, C_O=23x22uF (Ceramic), ΔI_{LOAD}=15A, Slew rate =1000A/µs, T_{ON} =346ns, and equivalent switching frequency =1MHz. It can be clearly seen that around 20mV the overshoot can be reduced by using the proposed IQCOT control.

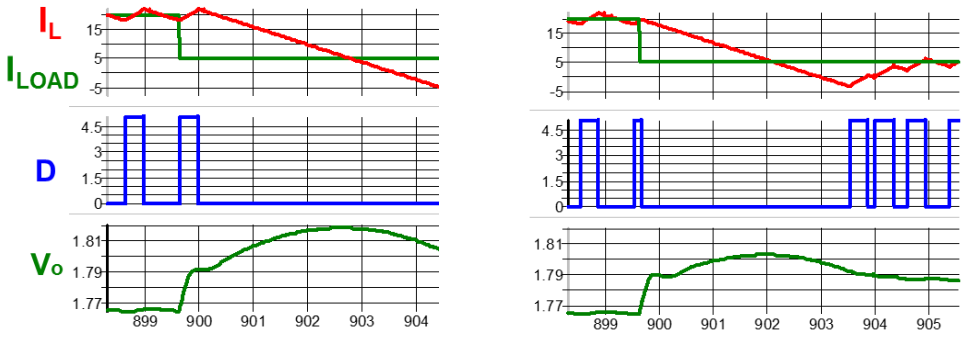

(a) (b)

Figure 4.24 Load step-down waveforms in

(a) Ripple based COTCM control (b) proposed charge based control

It has been discussed earlier that overshot in constant on-time control can be reduced, if T_{ON} can be expired right at the time of load release. This is done at Figure 4.24 using the proposed IQCOT control circuit. Comparing Figure 4.24 (a) and Figure 4.24 (b), it can be clearly seen that in Figure 4.24 (b) the gate signal D expires right after load step-down and hence produce a smaller overshoot. Putting the experimental setup values in Eq. (4.5), overshoot is found 55mV which is same as simulation results in Figure 4.24. In the simulation result with IQCOT method, in Figure 4.24(b), overshoot reduction is around 20mV. However, for higher duty cycle operation, Q1/Q2 ration will higher and will produce larger overshoot reduction in the system.

4.4.4 Comparison of IQCOT with Nonlinear Controls in Multiphase Operation

In the conventional multiphase constant on-time controls, various nonlinear controls are applied to make the phases to overlap with each other at load step-up transient. In some cases, these nonlinear controls are also used to extend the T_{ON} to increase the inductor current very quickly. In Figure 4.25, the nonlinear control 'Quick Response' by Richtek is shown. Figure 4.26 (a) shows that if the parameters are optimized for a particular load transient setup, ΔIo= 150A, di/dt=1000A/us. For this example, V_O looks good with no undershoot or overcorrection. But when the load step condition is changed by reducing ΔIo= 100A with same di/dt, shown in Figure 4.26 (b), then it can be seen that V_O has significant ring-back.

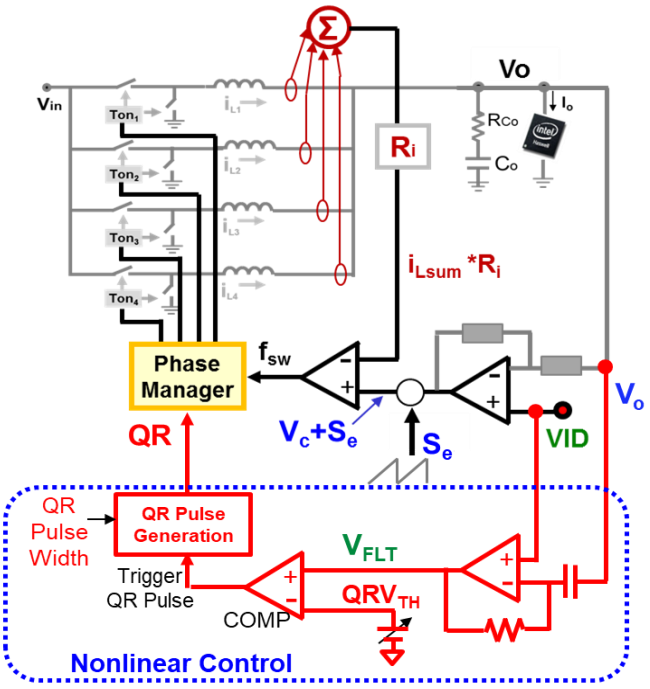

Figure 4.25 COTCM Control with pulse merging by proposed charge based control method

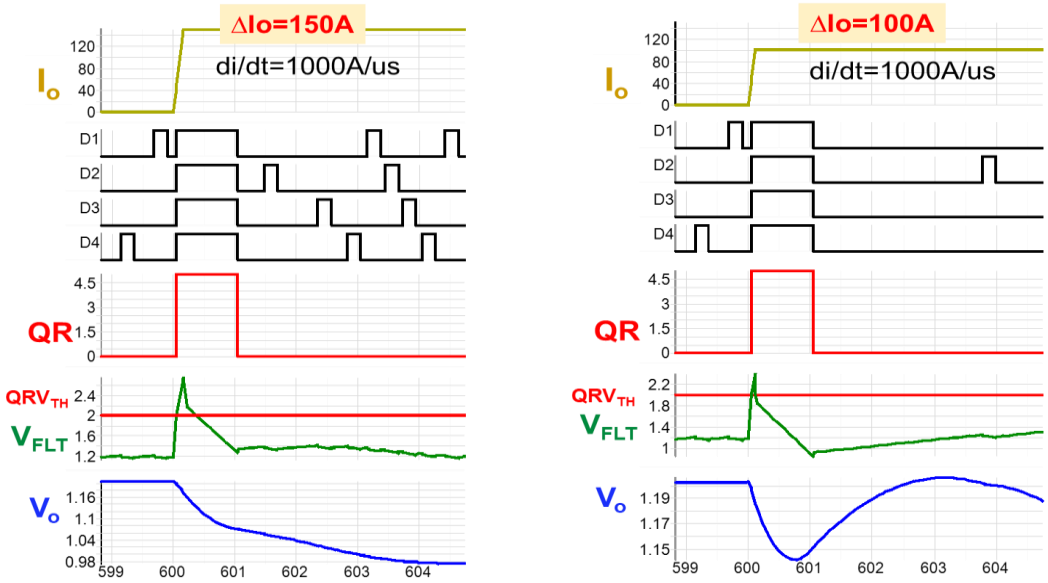

(a) (b)

Figure 4.26 Nonlinear control response at load step (a) 150A (b) 100A

In proposed IQCOT control, when the load step is large, i.e. ΔIo= 150A, delay between each phase T_{ON} pulses and T_{ON} extension are adjusted to provide the optimized V_O response. When this

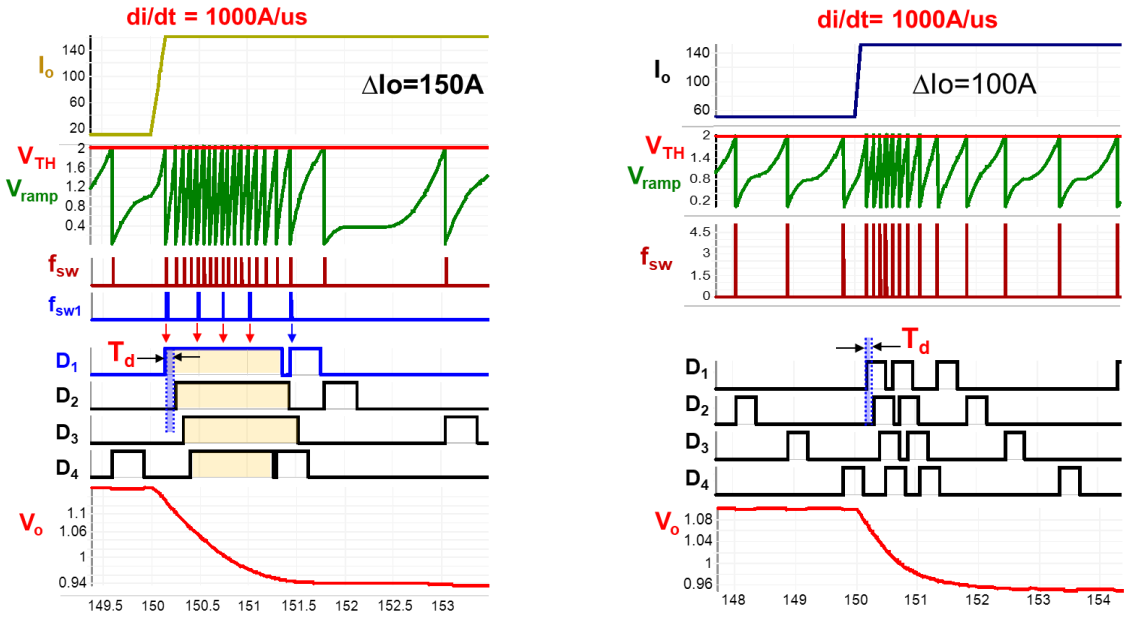

(a) (b)

Figure 4.27 IQCOT load step-up transient at load step (a) 150A, and (b) 100A

load-step is change to ΔIo= 100A, in the same way, the duty cycle and delay Td is adjusted to give optimized V_O response. In this case it can be seen in Figure 4.27 (b) that when load step is reduced, T_{ON} triggering pulse (f_{sw}) frequency is reduced proportionally and eventually T_{ON} pulses in each phases are not extended. When load step is even reduced to ΔIo= 50A, T_{ON} pulse overlapping got reduced more, compared to Figure 4.27 (b), to keep an optimized V_O response.

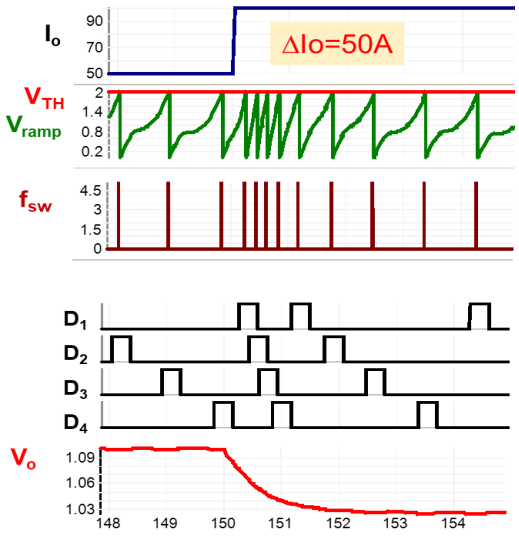

Figure 4.28 IQCOT load step-up transient at load step 50A

4.5 Experimental Verifications of IQCOT Transient Response

4.5.1 Experimental Verification of Single Phase Operation

In this section, concept of 'Inverse Charge Constant On-time (IQCOT)' control has been verified with experimental test results. As, the parasitic model for CPU socket plays a significant role in load transient response in VR applications, proposed IQCOT control method is tested in a commercial VR platform. The steady state waveforms for single phase IQCOT control are shown in Figure 4.29 where test condition is: V_{IN} = 7V, V_O = 1.8V, equivalent switching frequency =

800kHz, L=360nH, Co_bulk = 2x470uF, and Co_cer = 12x22uF. (V_C-i_LR_i) signal charges the capacitor in every cycle and generates the ramp signal, V_{RAMP}. It can be seen that slope of the V_{RAMP} is different in different instance in one switching cycle. As, (V_C-i_LR_i) becomes smallest at the end of T_{ON}, V_{RAMP} slope is also minimum as that point.

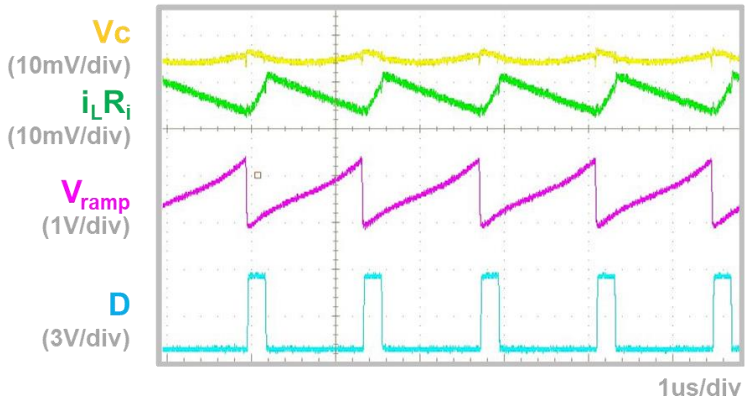

Figure 4.29 Key waveforms of proposed IQCOT control

In Figure 4.30, control waveforms are presented at the load step-up transient instance with load step ΔI_{LOAD}=20A, where the slope of V_{RAMP} has been increased immediately after load transient occurs. As a result, the increased pulse frequency merged together to crease large T_{ON}

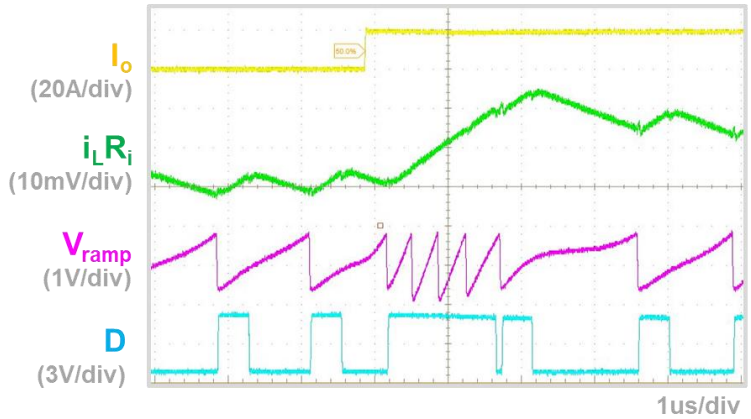

Figure 4.30 Key waveforms of IQCOT control at load step-up transient

which helps to increase inductor current at maximum possible speed, as shown in Figure 4.30. It can also be seen that when $i_L R_i$ reached close to its final value, inductor current slope decreases again to exit from T_{ON} extension and go back to original duty cycle.

In Figure 4.31, the waveforms are presented at load step-down case where V_{RAMP} becomes flat which in return does not create any duty cycle and helps to reduce the inductor current. Figure 4.32 shows that if load step-down occurs at beginning of T_{ON} then using V_C and $i_L R_i$ crossover point T_{ON} can be truncated which helps to reduce inductor current immediately.

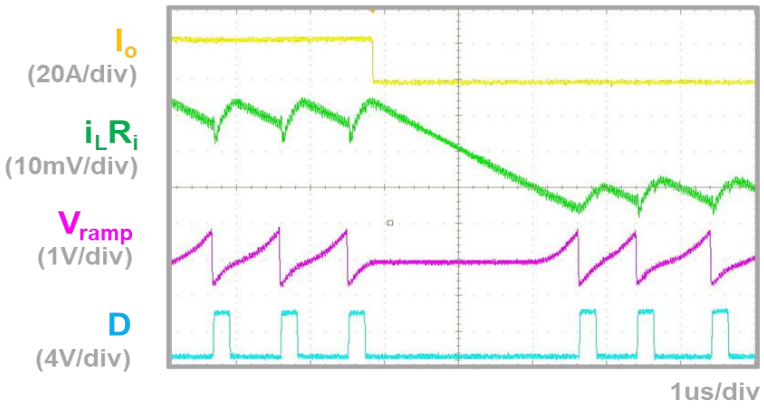

Figure 4.31 Key waveforms at load step-down transient

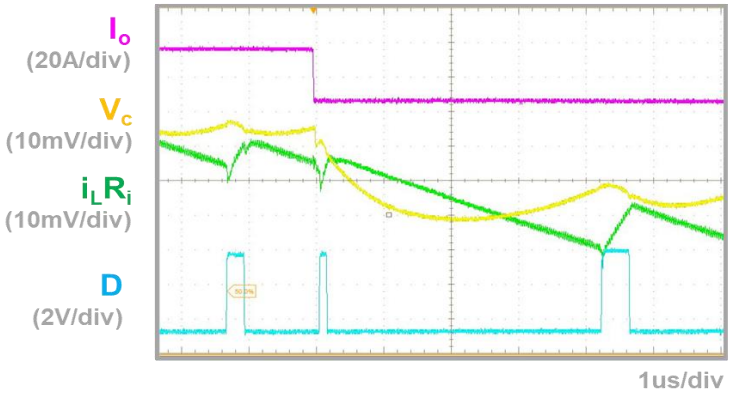

Figure 4.32 T_{ON} pulse truncation at load step-down transient

In Figure 4.33, the waveforms are presented at ΔI_{LOAD}=10A without pulse merging to create an optimized Vo. But in the load step-up response with ΔI_{LOAD}=30A, in Figure 4.33(b), shows the pulse merging has occurred to create optimized Vo. Hence, it can also be said, for different transient requirement i.e. different load step, the proposed IQCOT control adjust the duty cycle to always create the optimized output.

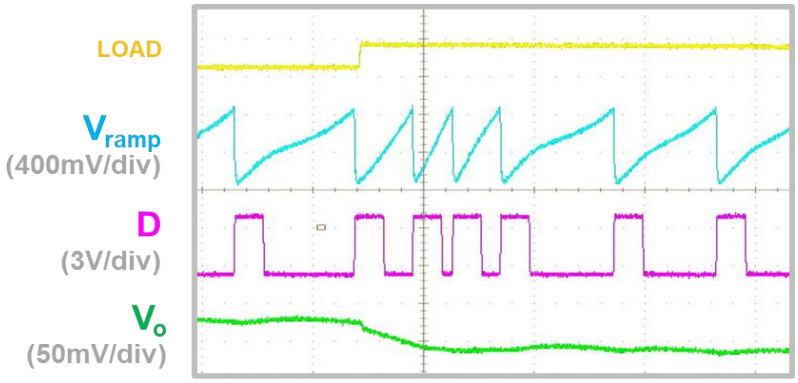

Figure 4.33 IQCOT control without pulse merging at ΔI_{LOAD}=10A

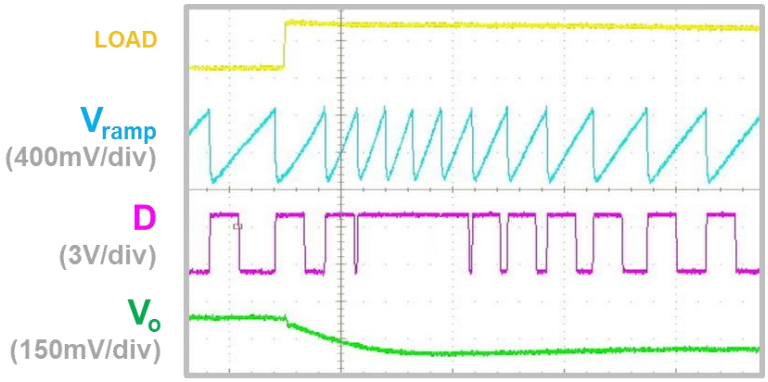

Figure 4.34 IQCOT control without pulse merging at ΔI_{LOAD}=30A

4.5.2 Experimental Verification of Multiphase Operation

The simulation results of the proposed IQCOT control method for multiphase operation are presented and explained in the previous sections. In this section some hardware verifications are presented to verify the proposed concept. The proposed control is implemented in a control board first and then connected with a commercial 2-phase VR power stage board with CPU/GPU socket and output filter model. The test condition is: V_{IN} = 10V, V_O = 1.2V, Equivalent f_{sw} (per phase) = 500kHz, L=360nH, Co_bulk = 330uF, Co_cer = 12x22uF, V_{TH}=600mV and the load step given ΔI_{LOAD}=20A.

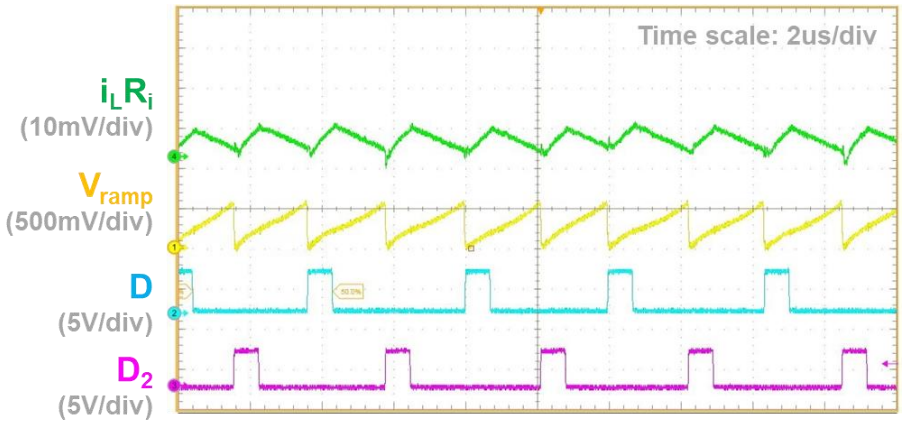

Figure 4.35 Steady state IQCOT waveforms in multiphase operation

In Figure 4.35, some key waveforms of the steady state operation of proposed IQCOT control has been presented. The I_{SUM} waveform is the summation of 2 phase inductor current times the sense-gain of the current loop. I_{SUM} contributes in V_{RAMP} generation which interact with V_{TH} voltage (600mV) to duty cycle signal which is districted in both phases.

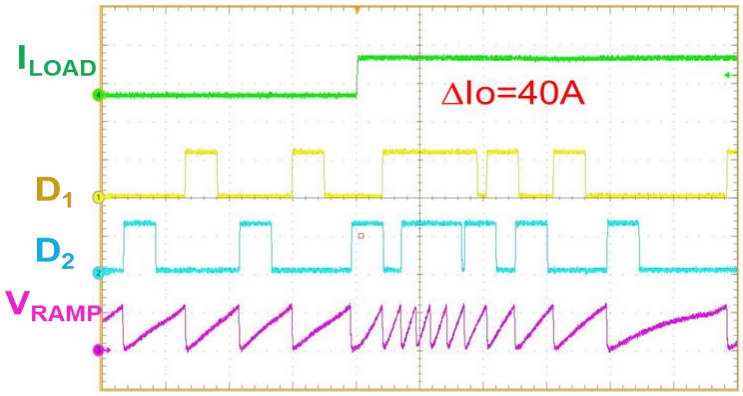

Figure 4.36 Load step-up response waveforms in multiphase operation

A 2-phase operation in implemented in hardware to demonstrate natural and linear pulse overlapping with naturally merged T_{ON}. Figure 4.36 shows that at load step-up transient slope of V_{RAMP} increases to create T_{ON} extension in each phase and also overlapping between them. Details of this phenomenon is explained in simulation in previous sections.

4.6 Summary

Firstly, the transient performance of proposed IQCOT control has been discussed in details. Then various improvements in IQCOT control method are proposed to improve the transient response both in load step-up and step-down case. Phase overlapping property of IQCOT control to improve transient in multiphase operation along with its adaptive response at different transient to eliminate any chance of overcorrection are also discussed. Simulations with the proposed control are done in the standard VR platform with the standard output filter model and results are compared with state of art solutions. Hardware verifications in single and multi-phase operation are also presented in this section.

Chapter 5. High Frequency Model of IQCOT Control

The concept of a new control scheme called ‘inverse charge constant on-time (IQCOT)’ control along with its advantages in single and multiphase operations is presented in the previous sections. In order to design the proposed IQCOT control with high bandwidth to support fast transient response, an accurate high-frequency small-signal model needs be derived for it. In this chapter, a high frequency model for proposed IQCOT control is derived using describing function.

5.1 Review of Constant On-Time Control Modeling using Describing Function

The power converter is a nonlinear dynamic system. Under a perturbation frequency excitation, the state variables, such as inductor current, contain a perturbation frequency component and its sideband components. Since the current feedback loops do not have any low-pass filters to attenuate the sideband frequencies in current-mode controls, the sideband components have an important impact in their the small-signal properties. Average models [E.1][E.2] only consider the perturbation frequency component in the current feedback loop. Consequently, they cannot predict subharmonic oscillation in constant frequency modulation current mode controls. All the previous high-frequency models for constant-frequency current-mode controls consider sideband components by modeling the sample-and-hold effect of the current feedback loop. These successful models for constant frequency control include the discrete time model [E.3], the sample-data model [E.4], and modified average models based on the sample-and-hold concept However, due to the failure of the sample-and-hold concept [E.5]-[E.15] in variable-frequency controls, these models are not applicable to variable frequency current-mode controls like constant on-time (COT) control. To model variable frequency controls, the describing

function method based on continuous time-domain analysis was introduced by [E.15]-[E.18]. As this modeling method is also applicable to constant frequency modulations, [E.19] provided accurate small signal models for both constant frequency and variable frequency current mode controls in a uniform way and demonstrated their fundamental differences.

According to the modeling approach presented in [E.19] the current loop in current-mode control is considered a single entity, and a perturbation at frequency f_m is injected into the control signal V_C. Then, based on the perturbed inductor current waveform, the describing function from the control signal V_C to the inductor current I_L can be found by mathematical derivation. Using the V_C to I_L relationship, a V_C to V_O transfer function also can be derived by adding output capacitor network into the derivation.

5.2 Modeling of Proposed IQCOT Control

In this section, an accurate high-frequency small-signal model is derived for the proposed IQCOT current-mode control. Similar to the method presented in [E.19], the current feedback loop in IQCOT control is considered as a single entity, as shown in Figure 5.1, and the describing function modeling approach is used to derive the high-frequency small-signal model of this IQCOT control.

However, the modulation scheme of the proposed IQCOT control is more complex than the conventional ripple-based COTCM control. In ripple-based COTCM control, when the falling edge of R_iI_L is equal to V_C, a new T_{ON} starts; while in the proposed IQCOT control, the (Vc- R_iI_L) signal will generate an I_{RAMP} current to charge a capacitor; and when the capacitor voltage V_{RAMP} is equal to a fixed threshold voltage V_{TH}, a new T_{ON} starts. Therefore, the model derivation procedure will

essentially be very different and more complex than conventional ripple-based COT control. In Figure 5.1, it can clearly be seen that the current feedback is considered as a single entity to model the proposed non-ripple-based IQCOT Control with V_C perturbation.

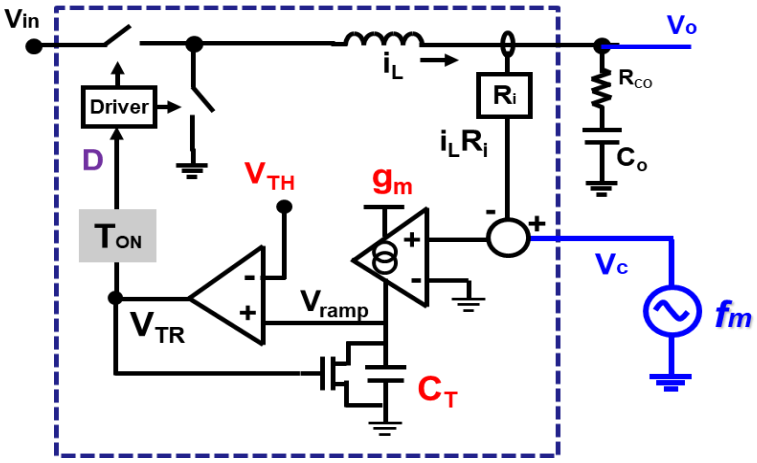

Figure 5.1 Modeling methodology for proposed IQCOT control

For the IQCOT implementation the small-signal model is derived as follows. As shown in Figure. 5.2, a sinusoidal perturbation with a small magnitude at the frequency f_m is injected through the control signal v_c. Then, based on the perturbed i_L waveform, the DF from v_c to i_L can be obtained. Three assumptions are made before applying the DF method: (i) the magnitude of the inductor current slopes during the on-period and the off-period remains constant; (ii) the magnitude of the perturbation signal is very small; and (iii) the perturbation frequency (f_m) and the switching frequency (f_{sw}) are commensurable, which means that $N \times f_{CLK} = M \times f_m$, where N and M are positive integers. The T_{OFF} is modulated by the perturbation signal: $v_c(t)=V_C+\hat{r}\sin(2\pi f_m \cdot t+\theta)$, where v_c is the steady state value, $\hat{r}$ is the perturbation magnitude, and θ is the initial angle.

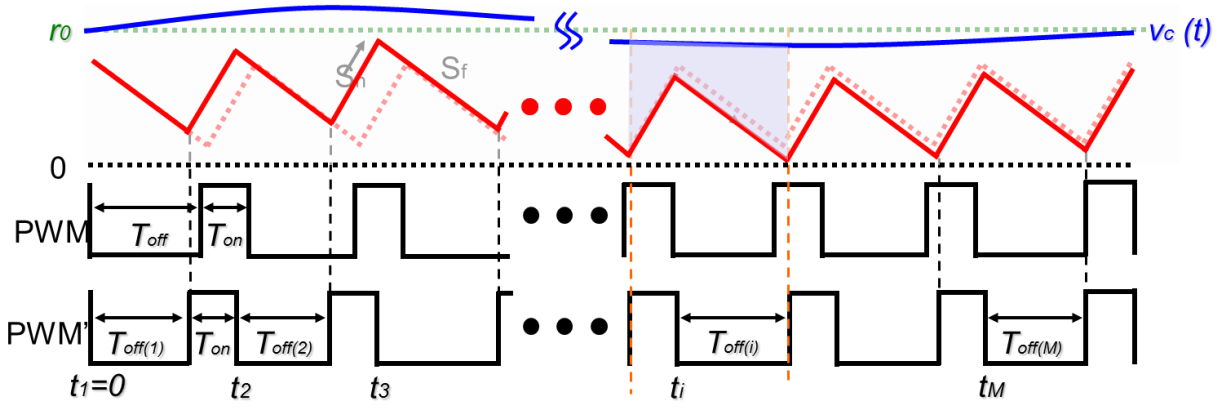

Figure 5.2 Key perturbed waveforms of IQCOT control with v_c perturbation

The modulated duty cycle and the perturbed $i_L(t)$ waveform are shown in Figure 5.2. Based on the modulation law, shown in Eq. (3.4) in chapter 3, it is found that:

$$\int_{t_{i-1}+T_{off(i-1)}}^{t_i+T_{off(i)}} [v_c(t)dt - i_L(t)R_i]dt = \frac{C_T V_{th}}{g_m} \tag{5.1}$$

The integration of $v_C(t)$ and $i_L(t)$ can be done separately and the expressions are

$$\int_{t_{i-1}+T_{off(i-1)}}^{t_i+T_{off(i)}} v_c(t)dt = r_0(T_{on}+T_{off(i)}) - \frac{\hat{r}}{\pi f_m}\sin(\pi f_m T_{sw})\cdot\sin\{2\pi f_m[(i-1)T_{sw} - \frac{T_{on}-T_{off}}{2}] - \theta\} \tag{5.2}$$

$$\int_{t_{i-1}+T_{off(i-1)}}^{t_i+T_{off(i)}} i_L(t)dt = [T_{sw}I_L R_i + T_{sw}s_f\sum_{i=1}^{i-1}\Delta T_{off(k)} - (I_L R_i - \frac{1}{2}s_f T_{off})\Delta T_{off(i)}] \tag{5.3}$$

Where, $\Delta T_{off(i)}$ is the i^{th} cycle off-time, $s_n=R_i(V_{in}-V_o)/L$, $s_f=R_iV_o/L$, R_i is the current feedback gain, and t_{sw} is the equivalent switching frequency for a specific T_{ON} and duty cycle. Details of these integration process are given in Appendix B.

Next, by substituting (5.3) and (5.2) into (5.1), and after some calculation which is given in Appendix B, it is found that

$$[\frac{C_T V_{th}}{g_m}+\frac{1}{2}s_f T_{off}]\Delta T_{off(i)}+[s_f T_{sw}-(\frac{C_T V_{th}}{g_m}+\frac{1}{2}s_f T_{off})]\Delta T_{off(i-1)}$$
$$=\frac{\hat{r}}{\pi f_m}\sin(\pi f_m\cdot T_{sw})\cdot[\sin\{2\pi f_m[(i-2)\cdot T_{sw}-\frac{T_{on}-T_{off}}{2}]-\theta\}-\sin\{2\pi f_m[(i-1)\cdot T_{sw}-\frac{T_{on}-T_{off}}{2}]-\theta\}] \quad (5.4)$$

Then, the perturbed duty cycle d(t) and inductor current $i_L(t)$ can be expressed by

$$d(t)\Big|_{0\le t\le t_M+T_{off(M)}+T_{on}}=\sum_{i=1}^{M}[u(t-t_i-T_{off(i)})-u(t-t_i-T_{off(i)}-T_{on})] \quad (5.5)$$

$$i_L(t)\Big|_{0\le t\le t_M+T_{off(M)}+T_{on}}=\int_0^t[\frac{V_{in}}{L_s}d(t)-\frac{V_o}{L_s}]dt+i_{L0} \quad (5.6)$$

After that, Fourier analysis can be performed on the $i_L(t)$ as

$$c_m=j\frac{2f_m}{N}\int_0^{t_M+T_{off(M)}+T_{on}}i_L(t)\cdot e^{-j2\pi f_m t}dt$$

$$c_m(i_L)=-\frac{V_{in}}{N\pi L}e^{-j2\pi f_m T_{off}}(1-e^{-j2\pi f_m T_{on}})\sum_{i=1}^{M}[e^{-j2\pi f_m[(i-1)T_{sw}]}\cdot\sum_{k=1}^{i}\Delta T_{off(k)})] \quad (5.7)$$

Where, c_m is the Fourier coefficient of $i_L(t)$ at the perturbation frequency f_m.

By substituting (5.4) into (5.7), the coefficient can be calculated as:

$$c_m = \frac{V_o}{j2\pi f_m L}\frac{1}{j2\pi f_m T_{on}}\cdot[\frac{(1-e^{-j2\pi f_m T_{on}}).(1-e^{-j2\pi f_m T_{sw}})}{(\frac{C_T V_{th}}{g_m}+s_f T_{off})+[s_f\frac{V_{in}T_{on}}{V_o}-(\frac{C_T V_{th}}{g_m}+s_f T_{off})]e^{-j2\pi f_m T_{sw}}}](\hat{r}e^{-j\theta}) \tag{5.8}$$

Since the Fourier coefficient at perturbation frequency f_m for the control signal $v_c(t)$ is $\hat{r}e^{j\theta}$, the describing function of v_c-to-i_L transfer function in the s-domain can be calculated as:

$$\frac{i_L(s)}{v_c(s)} = \frac{V_o}{sL}\frac{1}{sT_{on}}\cdot[\frac{(1-e^{-sT_{on}}).(1-e^{-sT_{sw}})}{(\frac{C_T V_{th}}{g_m}+s_f T_{off})+[s_f\frac{V_{in}T_{on}}{V_o}-(\frac{C_T V_{th}}{g_m}+s_f T_{off})]e^{-sT_{sw}}}] \tag{5.9}$$

For the detail derivation, refer to Appendix B.

In order to consider the variation of the inductor-current slopes, similar methodology is used to derive additional terms that represent the influence from the output voltage v_o, as shown in Figure 5.3.

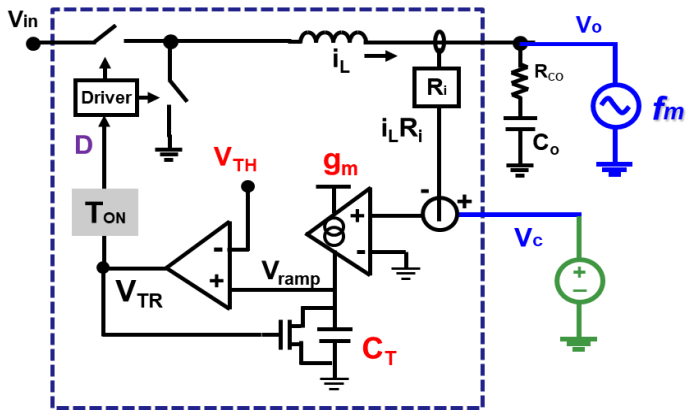

Figure 5.3 Modeling for the influence of the output voltage v_o in IQCOT control

The transfer functions from the output voltage to the inductor current are calculated as:

$$\frac{i_L(s)}{v_o(s)} = \frac{1}{L_s s} \cdot [\frac{f_s(1-e^{-sT_{on}})(1-e^{-sT_{sw}})}{(\frac{C_T V_{th}}{g_m} + s_f T_{off}) + [s_f T_{sw} - (\frac{C_T V_{th}}{g_m} + s_f T_{off})]e^{-sT_{sw}}} \frac{1}{s \cdot L_s / R_i} \cdot V_{in} - 1] \quad (5.10)$$

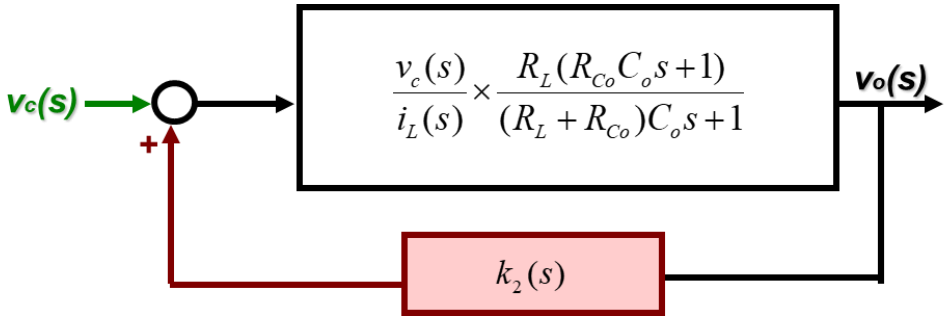

Figure 5.4 Complete block diagram to calculate v_c to v_o transfer function

The feedback factor k_2 can be calculated using the structure shown in Figure 5.4.

$$\text{Where, } k_2 = \frac{i_L(s)/v_o(s)}{i_L(s)/v_c(s)} \quad (5.11)$$

The exponential term e^{-sTon} and e^{-sTsw} in (5.9) and (5.10) can be simplified by using the Pade' approximation:

$$1-e^{-sT_{on}} = \frac{sT_{on}}{1+\frac{s}{Q_1\omega_1}+\frac{s^2}{\omega_1^2}} \quad (5.12)$$

Where, $\omega_1=\pi/T_{ON}$ and $Q_1=2/\pi$. This approximation is valid up to the frequency of $1/(2T_{ON})$.

$$1-e^{-sT_{sw}} = \frac{sT_{sw}}{1+\frac{s}{Q_2\omega_2}+\frac{s^2}{\omega_2^2}} \quad (5.13)$$

Where, $\omega_2=\pi/T_{sw}$ and $Q_2=2/\pi$. This approximation is valid up to the frequency of $1/(2T_{sw})$.

Therefore, using the expression in (5.12) and (5.13) in k_2 expression in (5.11) can be simplified as:

$$k_2 = \frac{1}{L_s s}\{R_i - R_i(1+\frac{s}{Q_2\omega_2}+\frac{s^2}{\omega_2{}^2}).(1+\frac{s}{Q_2"\omega_1}+\frac{s^2}{\omega^2})\} \tag{5.14}$$

Therefore, after some calculation and some approximation finally the control-to-output transfer function can be calculated as:

$$\frac{v_o(s)}{v_c(s)} \approx K_c \frac{R_{Co}C_o s+1}{s/\omega_a+1}\frac{1}{1+\frac{s}{Q_1\omega_1}+\frac{s^2}{\omega_1^2}}\frac{1}{1+\frac{s}{Q_2''\omega_2}+\frac{s^2}{\omega_2^2}} \tag{5.15}$$

Where, $K_c = \frac{R_L}{R_i(1-k_2/R_i \cdot R_L)}$, $\omega_a = \frac{1-R_L k_2/R_i}{(R_L+R_{Co})C_o - R_L R_{Co} C_o k_2/R_i}$

$$\omega_1 = \frac{\pi}{T_{on}},\ Q_1 = \frac{2}{\pi},\ \omega_2 = \frac{\pi}{T_{sw}}, \text{ and } \quad Q_2" = \frac{2s_f T_{sw}}{\pi(\frac{2CV_{TH}}{g_m T_{sw}} - s_f T_{on})}$$

5.3 Model Verification

5.3.1 Model Verification with Simulation Results

The model has been verified with SIMPLIS simulation results at different duty cycle and transconductance gain g_m, shown in Figure 5.5 and Figure 5.6.

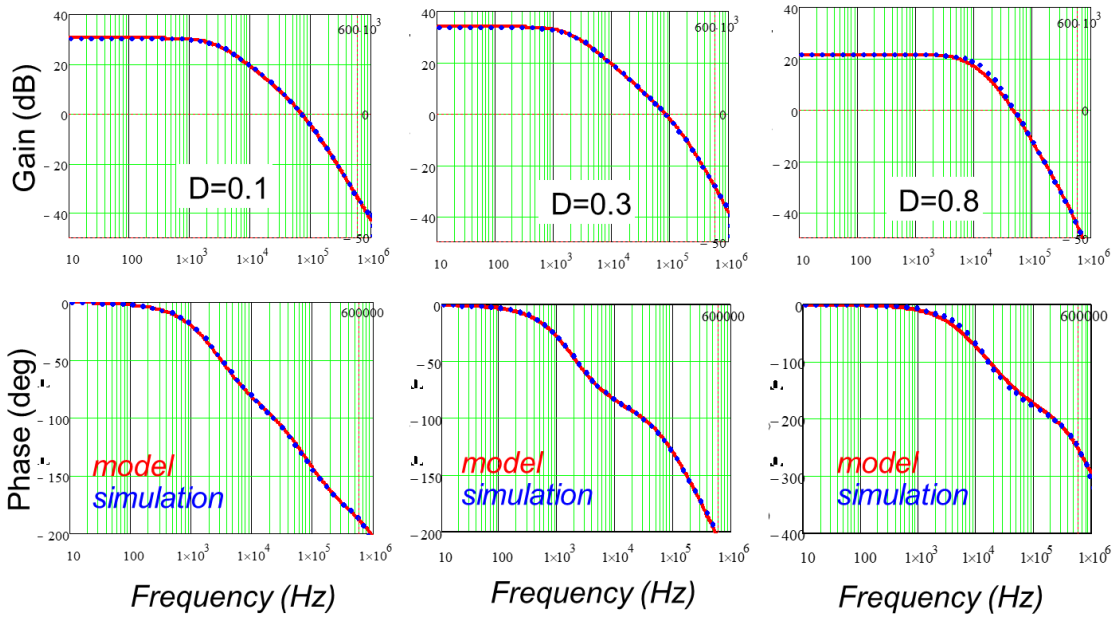

Figure 5.5 v_c to v_o transfer function verification at different duty cycle (D).

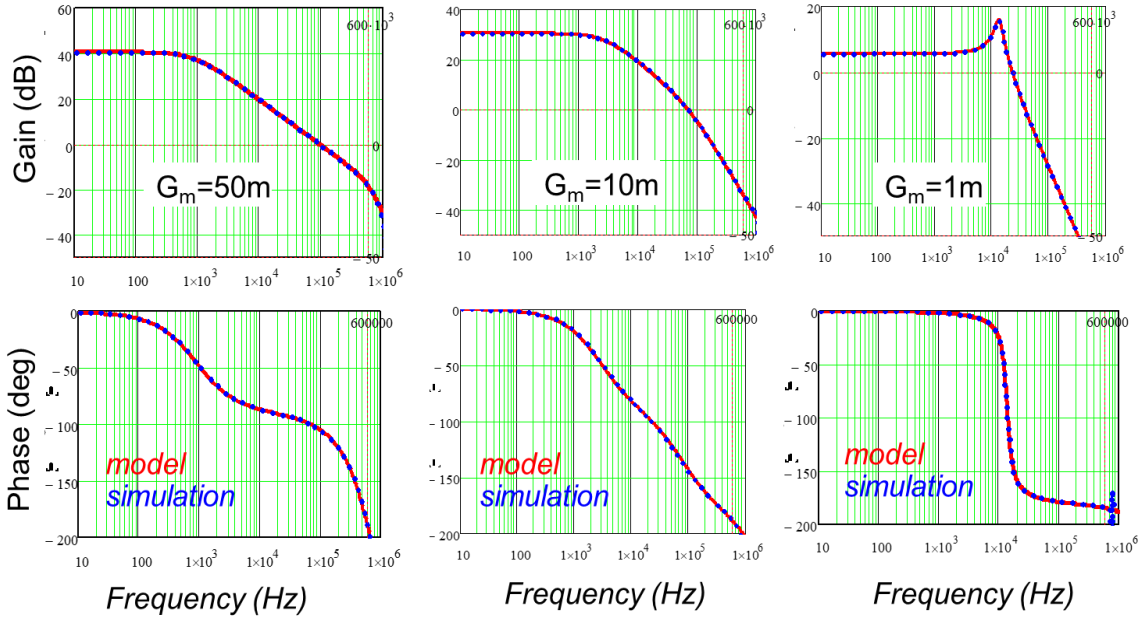

Figure 5.6 v_c to v_o transfer function verification at different g_m

In the derivation and simulation, the model parameters are: equivalent operating frequency f_{sw}=1.2MHz, L=120nH, Co=1.12mF, g_m=10mS, C_T=120pF, V_{TH}=2V. It can be seen that the derived model for v_c to v_o transfer function in Figure 5.5 matches very well with simulation results. The model has also been verified with different g_m as shown in Figure 5.6. In SIMPLIS simulation the simulation setup is: D=0.1, V_{IN}=12V, V_o=1.2V, T_{ON}=83.33ns, equivalent operating frequency f_{sw}=1.2MHz, L=120nH, Co=1.12mF, C_T=120pF, and V_{TH}=2V. It can be seen that the derived model for v_c to v_o transfer function in Figure 5.6 matches very well with simulation results. It can also be seen that, at very low g_m the v_c to v_o shows the double pole in the low frequency which is similar to voltage mode control. This phenomenon is discussed in later sections with pole-zero mapping.

5.3.2 Model Verification with Hardware Testing Results

In this section model verification with hardware testing result is presented. In Figure 5.7, the bode plot of vc to vo is shown. The test setup is: D=0.1, V_{IN}=12V, V_o=1.2V, T_{ON}=83.33ns, equivalent operating frequency f_{sw} =800 kHz, L=120nH, Co=1.12mF, C_T=120pF, and V_{TH}=2V.

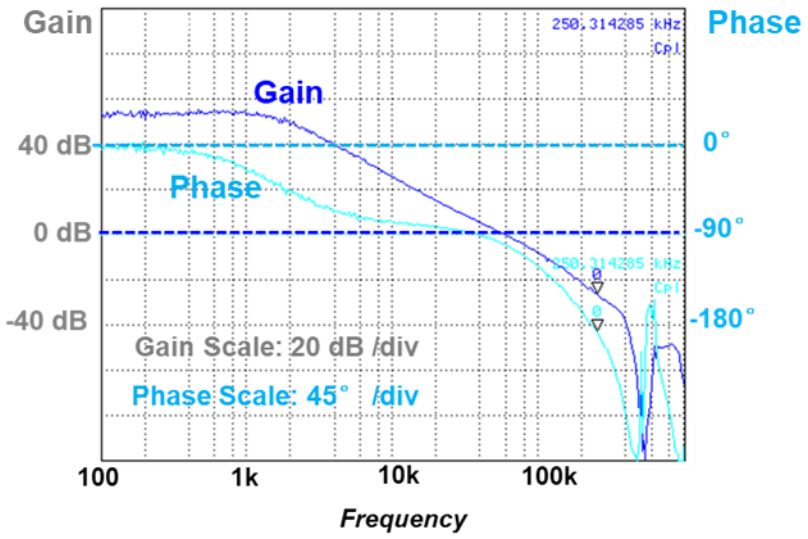

Figure 5.7 v_c to v_o transfer function measured from IQCOT test board

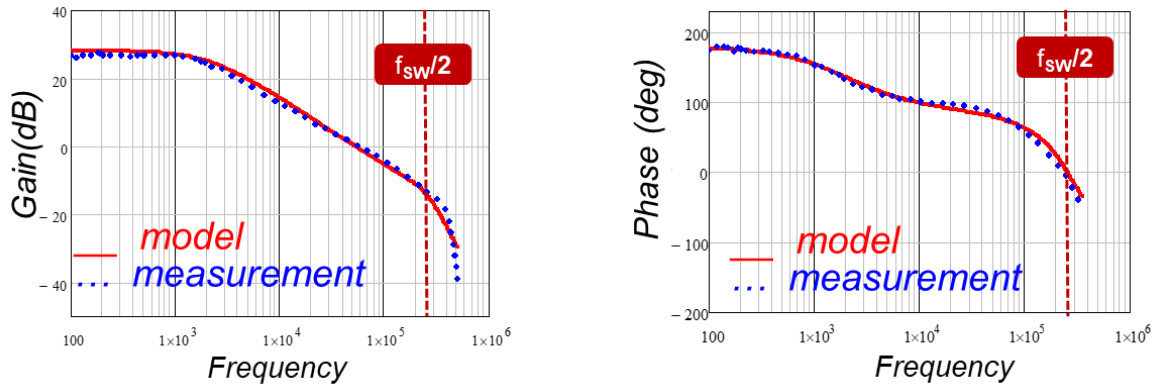

Figure 5.8 Correlation of IQCOT v_c to v_o measurement results with derived model

The correlation of measured v_c to v_o bode plot with derived model is shown in Figure 5.8. The Figure 5.8 shows that model matches well with measured bode plot gain and phase curves.

5.4 Q-Value Design Guideline for IQCOT Control

Q-value in the (5.15) can be re-written as-

$$Q_2" = \frac{2 s_f T_{sw}}{\pi\left(\frac{1}{G}\frac{2}{T_{sw}} - s_f T_{on}\right)} \tag{5.16}$$

Where, $G = \frac{g_m}{C_T V_{TH}}$ and G can be called as 'system gain factor'.

From Q-value expression in (5.16), it is obvious that, for a given inductor falling slope (s_f), on-time period (T_{ON}), and equivalent operating frequency (f_{sw}) for specific duty cycle, the Q-value can be tuned by changing this gain factor G. Obviously G can be tuned by changing g_m, V_{TH} or C_T. If C_T is kept constant, G can be tuned by changing two other parameters- g_m and V_{TH} which can easily be done from circuit point of view. For convenience, among g_m and V_{TH}, V_{TH} is kept constant in this example and g_m is varied to check the pole-zero movement and Q-value change.

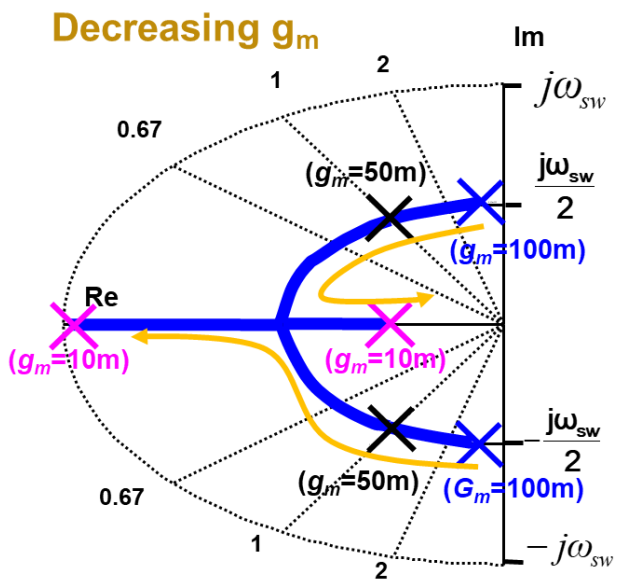

Figure 5.9 System pole zero mapping as a function of g_m

The pole zero mapping is shown in Figure 5.9, and Q-value change as a function of g_m is given in Figure 5.10. Simulation parameters are - D=0.1; f_{sw}=1MHz, L=120nH, Co=1.12mF, and V_{TH}=1V.

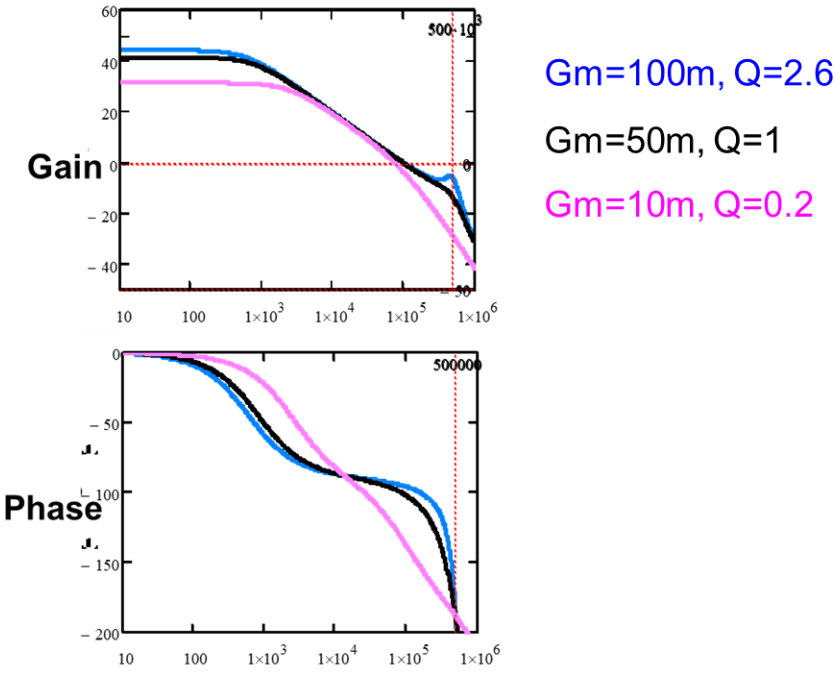

Figure 5.10 Gain and phase of v_c to v_o as a function of g_m

It can be seen from Figure 5.10 that, reducing the gain factor G, or to be more specific, reducing the g_m in this example, reduces the DC loop gain of the control loop. Then Q-value also decreases with the decrement of g_m. When g_m is very low, then eventually the double pole becomes separated as shown in case of g_m=10m in Figure 5.10. This case is not very desirable as phase drops very quickly and reduces the phase margin. This criterion set the minimum value for g_m in loop gain design. On the other hand, it can be understood that if g_m is too large, Q-value will become very high and eventually will become negative to make the system unstable. This sets the maximum value for g_m which also determine the stability criterion for IQCOT control.

The stability criterion for IQCOT:

$$g_m < \frac{2Lf_{sw}^2 CV_{TH}}{R_i} \frac{1}{DV_o} \tag{5.17}$$

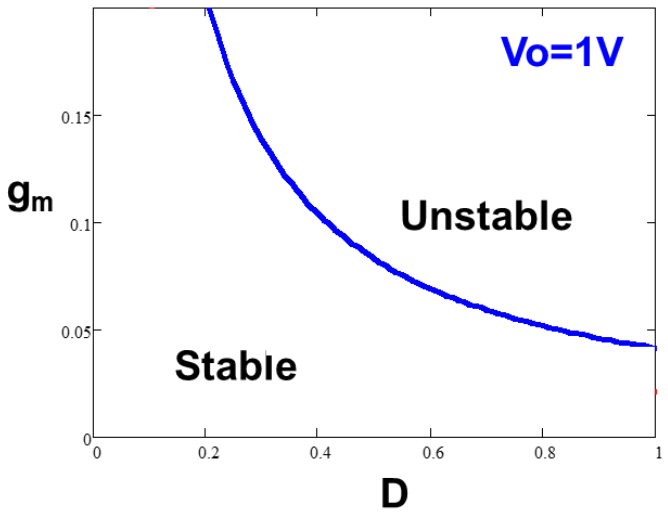

Figure 5.11 Stability criterion for IQCOT control design

Figure 5.11 shows the stability criterion for g_m design for determining the loop gain. In fact, this kind stability criterion can be set for V_{TH} also in the similar way, by considering g_m constant. In Figure 5.11, the top-right side is the unstable region which should be avoided. Figure 5.11 shows that for a particular V_O voltage, maximum g_m limit decreases with duty cycle. For a given duty cycle, higher V_O will reduce the g_m limit.

5.5 Proposed Constant Q Auto-Tuning Method for IQCOT Control

The expression of quality factor of the double pole Q_2" in (5.16) can be re-written as

$$Q_2" = \frac{2s_f \frac{T_{on}}{D}}{\pi\left(\frac{C_T V_{TH}}{g_m}\frac{2D}{T_{on}} - s_f T_{on}\right)} \tag{5.18}$$

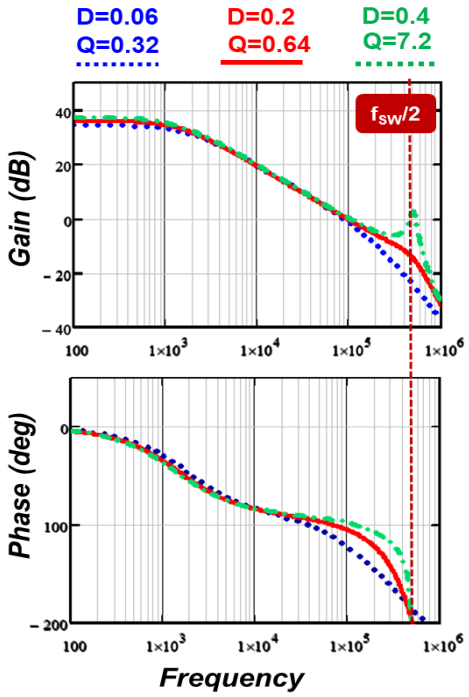

Figure 5.12 Q-value variation in v_c to v_o as a function of D

From (5.18), it is found that the expression of quality factor of the double pole Q_2" is a function of duty cycle D. Therefore, the Q-value will change with duty cycle change. It has been found that duty cycle variation can be large at laptop VR applications like D=0.06 to D=0.4, as discussed in section 1.1.2.D This type of Q-value variation with duty cycle may make the control loop design more challenging from small signal stability point of view. The Q-value variation with duty cycle in IQCOT control is presented in Figure 5.12. To make this comparison, first the Q-value is set at $\pi/2$ =0.64 for D=0.2. The other model parameters are L=250nH, C_T=0.2nF, Ri=1mΩ, R_{TH}=1.2V and g_m=100mS. When duty cycle is varied from D=0.25 to D=0.06, Q-values becomes 0.32 and when duty cycle is increased to D=0.4, then Q-value becomes 7.2. It is obvious that for larger duty cycle, Q-value will be even larger and peaking will be higher at half switching frequency.

5.5.1 Concept of Constant Q Auto-Tuning Method

A. For adaptive on-time control

These days adaptive on-time (AOT) control is more commonly used in the industry to minimize the operation frequency variation in constant on-time (COT) control. AOT control has been discussed in details in section 2.1. In adaptive on-time (AOT) control T_{ON} is adjusted at steady state with V_{IN} and V_O to keep the steady state operation frequency constant. Therefore, using (5.20), it can be found that

$$\left(\frac{V_{TH}}{V_o}\right)\left(\frac{1}{g_m}\right)=\frac{T_{sw}^2 R_i}{2LC} \tag{5.19}$$

$$\frac{V_{TH}}{V_o}=\frac{T_{sw}^2 R_i g_m}{2LC}=K' \tag{5.20}$$

$$V_{TH} = K'V_o \tag{5.21}$$

In this case, if V_{TH} is kept such as $V_{TH}=KV_{o.}$ For example, T_{sw}=1us, L=250nH, C=0.2nF, R_i=1m, and g_m=100m makes K'=1. If Vo=V_{TH} then Q-value will be auto tuned to 2/π value.

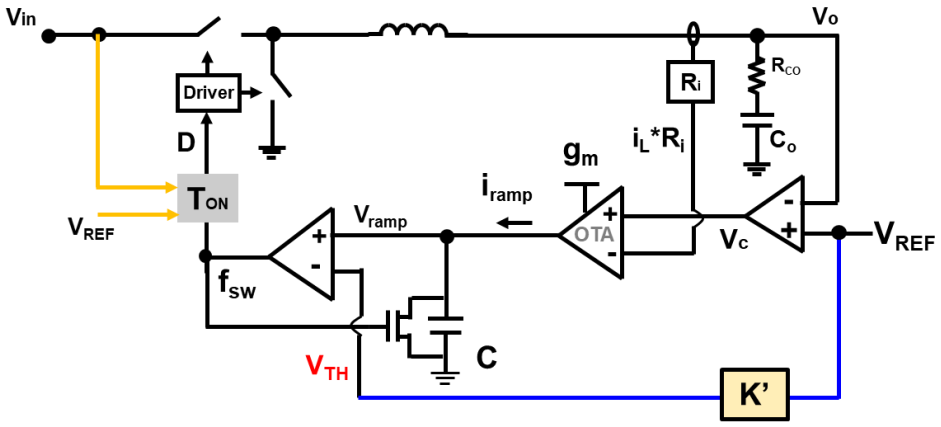

Figure 5.13 Block diagram of proposed Q auto-tuning method for AOT control

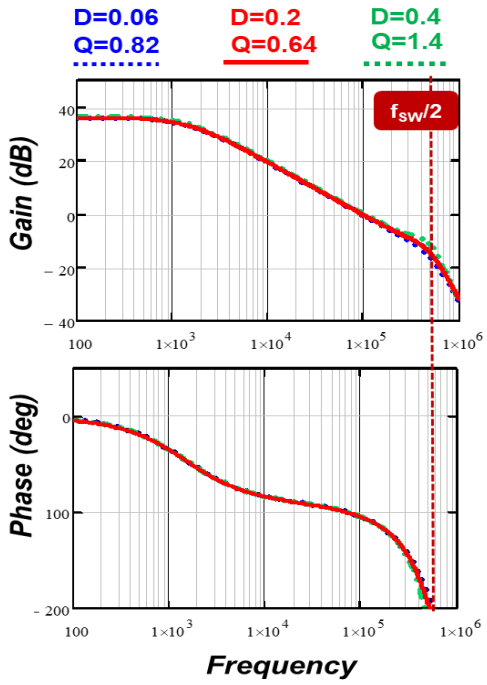

Figure 5.14 v_o/v_c at different D with proposed auto-tuning method

The effect of the proposed Q-value auto-tuning method is presented in Figure 5.14 for AOT control. In Figure 5.14, v_c to v_o transfer function of proposed model is plotted as different duty cycle. The model parameters are kept same as Figure 5.12. It can be seen that when duty cycle vary from D=0.06 to D=0.4, Q-value varies from Q=0.82 to Q=1.4 which was Q=0.32 to Q=7.2 in without auto-tuning case presented in Figure 5.12. Hence, the Q-value variation is significantly minimized by applying simple Q-value auto-tuning method.

B. For constant on-time control

To resolve that issue, an auto-tuning method has been proposed in this section to control Q-value variation with duty cycle change. For tuning the Q-value at 2/π, set $Q_2" = \frac{2}{\pi}$. Then putting $T_{on} = DT_{sw}$ and $s_f = \frac{V_o R_i}{L}$ the quality factor (Q) expression can be rewritten for as

$$\frac{2C_T V_{TH}}{g_m T_{sw}} = \frac{V_o R_i}{L} T_{sw}(1+D) \tag{5.22}$$

For low duty cycle the expression can be approximated as

$$\frac{2C_T V_{TH}}{g_m T_{sw}} = \frac{V_o R_i}{L} T_{sw} \tag{5.23}$$

For constant on-time (COT) control, T_{ON} is fixed and $T_{sw} = \frac{T_{on}}{D}$.Then the equation can be re-written as:

$$\left(\frac{V_{TH}}{V_{in}^2}\right)\left(\frac{V_o}{g_m}\right) = \frac{T_{on}^2 R_i}{2LC_T} = K \tag{5.24}$$

Where $\frac{T_{on}^2 R_i}{2LC_T} = K$ and K is a constant for fixed T_{ON}, R_i, L and charge-control capacitor C_T.

Constant K can be separated as K=k1.k2. Therefore, the equation will be-

$$\left(\frac{V_{TH}}{k_1 V_{in}^2}\right)\left(\frac{V_o}{k_2 g_m}\right) = 1 \tag{5.25}$$

Therefore, it can be clearly understood that to keep $Q_2" = \frac{2}{\pi}$ control needs to maintain,

$$V_{TH} = k_1 V_{in}^2$$

and, $V_o = k_2 g_m$

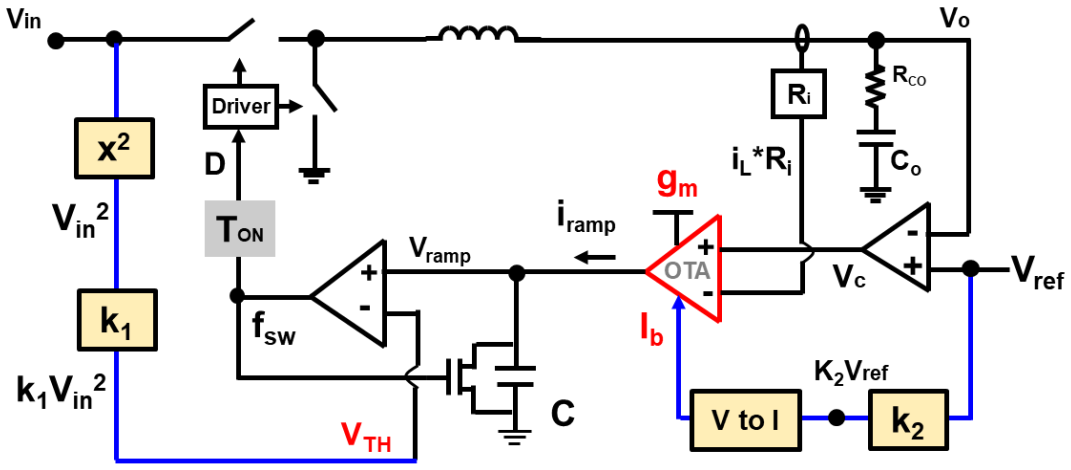

Figure 5.15 Block diagram of proposed Q auto-tuning method for COT control

For example, if T_{ON}=100ns, L=250nH, C=0.2nF, Ri=1mΩ, then K=1/10. Setting k_1=1/100 and k_2=10. Then for V_{IN}=12V, V_{TH} will be1.44V and for Vo=1.2V, g_m will be 120mS.

5.5.2 Implementation of Constant Q Auto-Tuning Method

As, adaptive on-time (AOT) control is mostly used is the industry these days to minimize the operating frequency variation, the implementation of proposed Q-value auto-tuning method is presented with AOT control in this dissertation.

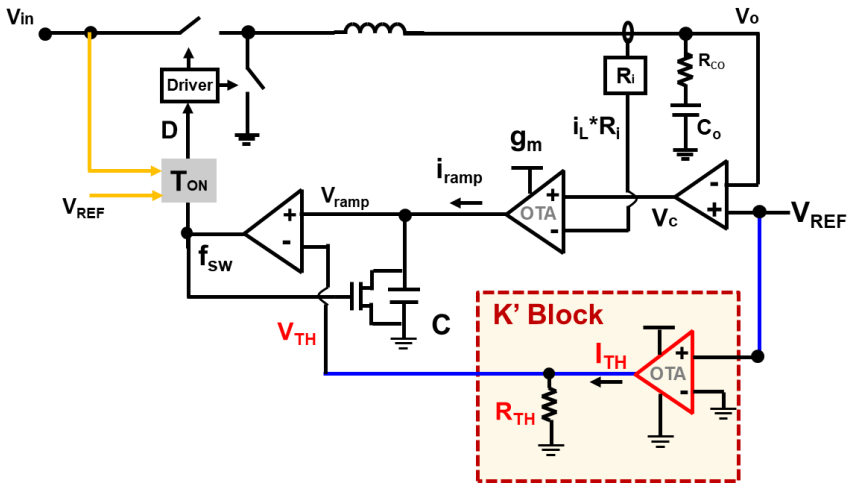

Figure 5.16 Implementation of Q-value auto-tuning for AOT control

According to Eq. (5.25), $V_{TH} = K'V_o$ while $K' = \frac{T_{sw}^2 R_i g_m}{2LC}$. In the earlier example K'=1. Obviously, K' can be a different value, depending on the value of circuit parameters. For instance, K' will be different for different operating frequency in AOT control. For this, in the auto-tuning implantation circuit for AOT control, shown in Figure 5.16, option to change K' value is kept. In K' block, if R_{TH} is changed the K' value will be different as $K' = I_{TH}R_{TH}$.

5.5.3 Simulation and Experimental Verification

A simulation has been done in SIMPLIS to verify the Q-value auto-tuning for AOT control. In the simulation steady state frequency has been set as 1MHz while adaptive T_{ON} generator in

Figure 5.16 change the T_{ON} to keep the operating frequency constant. The other parameters are - L=250nH, C=0.2nF, Ri=1mΩ, and g_m=100mS which makes the K'=1.

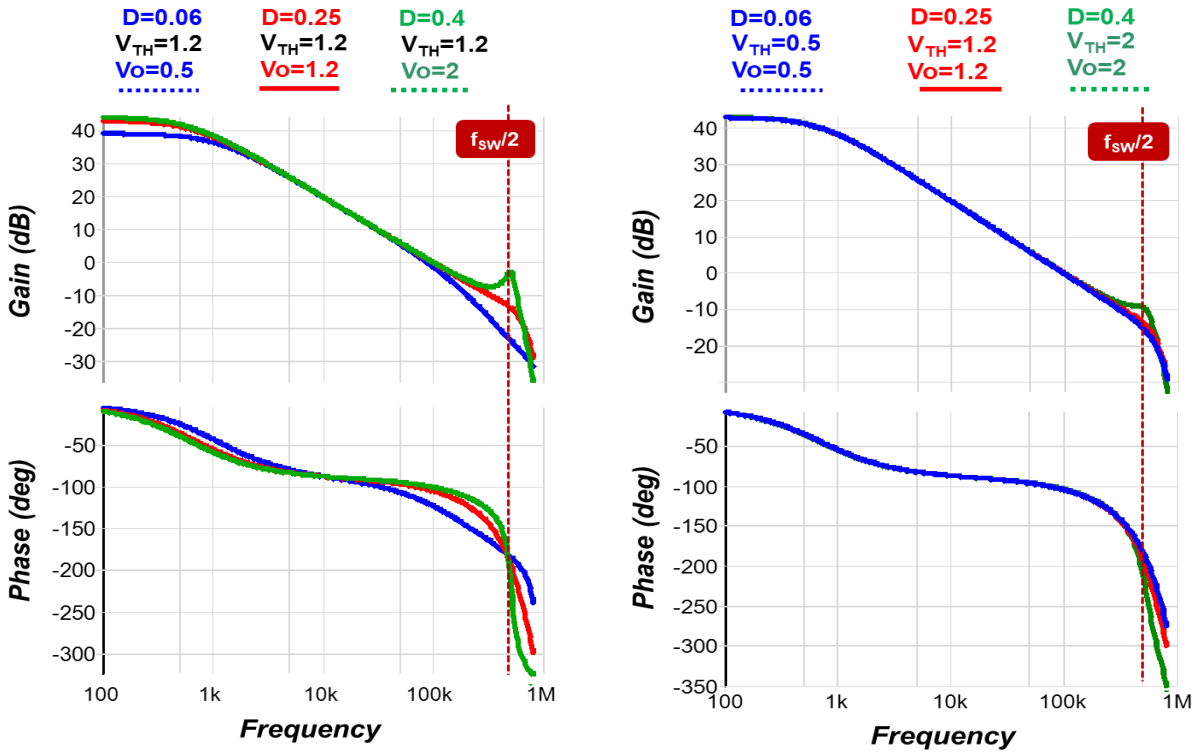

(a) (b)

Figure 5.17 v_o/v_c simulation results at different D with (a) no auto-tuning, and (b) with auto-tuning

In Figure 5.17 (a), first the Q-value variation is determined without any auto-tuning. It has been mentioned in chapter 1 that D variation is more dominant in laptop applications where D can vary form D=0.6 (V_{in}=8.4, Vo=0.5) to D=0.4 (V_{in}=5.2, Vo=2). This D variation is used to verify the proposed auto-tuning method. At the beginning, V_{TH} is set to 1.2V for D=0.2 (V_{in}=6, Vo=1.2) to achieve Q=2/π. When D is varied from 0.06 to 0.4, the bode plot shows the Q-value variation very clearly. But using the auto-tuning method when V_{TH} is also varied with V_O, then it can be seen from Figure 5.17 (b) that Q-variation becomes much smaller.

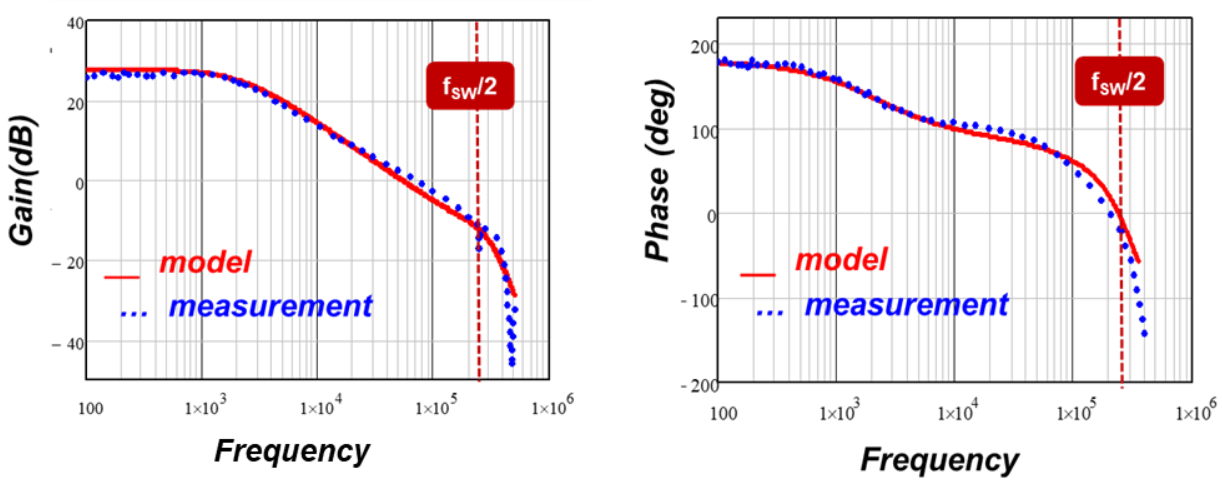

Figure 5.18. Bode plot of IQCOT loop gain with Q=1 with Vo=1.8V and V_{TH}=0.9V

In Figure 5.18, the experimental result and derived model of loop gain of IQCOT control is shown with D=0.3 where V_{IN}=6V and V_O=1.8V. The other parameters are- f_{sw}=500KHz, Co=1mF, L=330nH, Ri=3m, g_m=10mS, C_T=220pF. These parameters make the K' value equals to 0.5 according to (5.24) and hence, the V_{TH} is set as 0.9V to make the Q=1. Now, when the duty cycle is made D=0.1 where V_{IN}=8V and V_O=0.8V, if the V_{TH} value is kept 0.9, the Q-value will be 0.4 as shown in Figure 5.19.

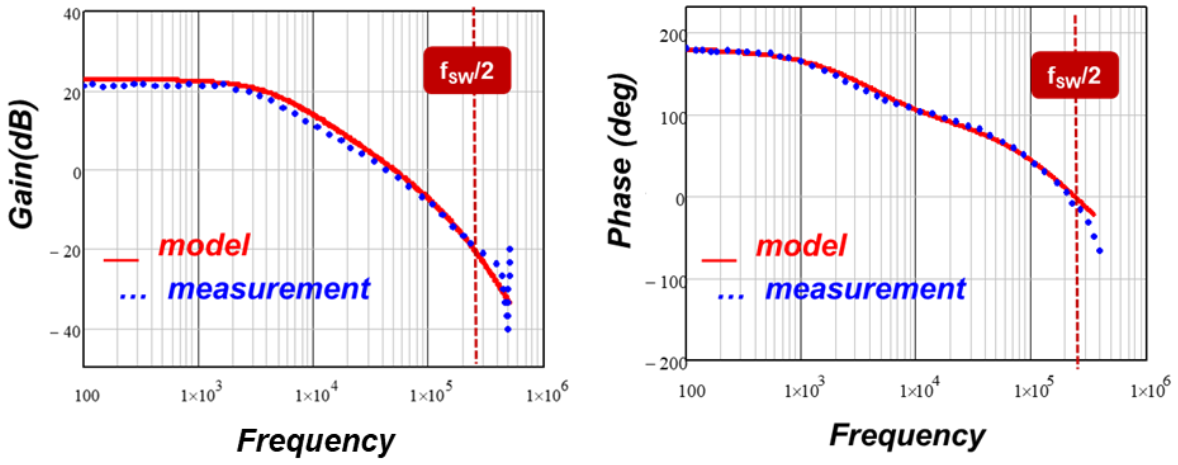

Figure 5.19. Bode plot of IQCOT loop gain with Q=0.4 with Vo=0.8V and V_{TH}=0.9V

For V_O=0.8V, when the V_{TH} is made V_O x K'=0.8V x 0.5=0.4V, the Q-value becomes Q=0.95, almost equal to 1. This case is shown in Figure 5.20.

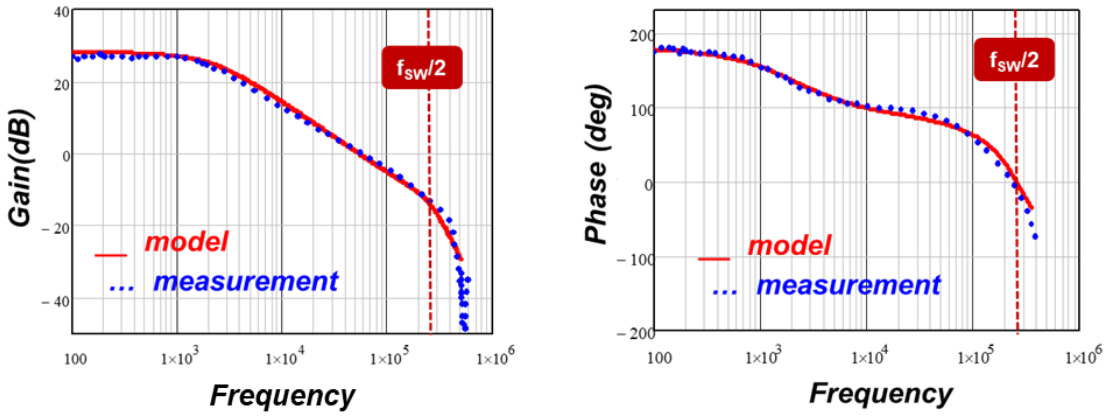

Figure 5.20. Bode plot of IQCOT loop gain with Q=0.95 with Vo=0.8V and V_{TH}=0.4V.

5.6 Comparison of IQCOT Small Signal with Other COT Control

Small signal property of COTCM is given below according to [E.19].

$$\frac{v_o(s)}{v_c(s)} \approx Kc \frac{R_{Co}C_o s+1}{s/\omega_a+1} \frac{1}{(1+\frac{s}{Q_1\omega_1}+\frac{s^2}{\omega_1^2})} \tag{5.26}$$

Where. K_c is DC gain, (s/ω_a+1) is the load pole, $1/(1+\frac{s}{Q_1\omega_1}+\frac{s^2}{\omega_1^2})$ is the high frequency double pole with $\omega_1=\pi/T_{ON}$ and $Q_1=2/\pi$, and $(R_{Co}C_o s+1)$ is the ESR zero.

Apart from COTCM control there are some other controls that use COT controls, for example- COT V^2 control, COTCM with external ramp, COT V^2 control with external ramp etc. Although the small signal property of COTCM is very simple, but these modified COT controls demonstrate

more complex small signal property. It has been found that the modified COT controls has additional double pole which is located at half of the switching frequency ($f_{sw}/2$). The general transfer function for modified COT structures can be written as-

$$\frac{v_o(s)}{v_c(s)} \approx K_C \frac{R_{Co}C_o s+1}{s/\omega_a+1} \frac{1}{(1+\frac{s}{Q_1\omega_1}+\frac{s^2}{\omega_1^2})} \frac{K_Z}{(1+\frac{s}{Q_2\omega_2}+\frac{s^2}{\omega_2^2})} \tag{5.27}$$

$K_C(R_{Co}C_o s+1)/(s/\omega_a+1)$ part in (5.27) is the low frequency part in the transfer function where value of K_c and location of (s/ω_a+1) can be different for different control. For COT V^2 control this low frequency part is equal to 1. As, only the high frequency characteristics are compared in this section, this low frequency part differences are not discussed. The high frequents part of (5.27) is compared in Table 3. Q factor of the additional double pole is different for different modified

Table 3 High frequency component comparison of COT controls

Modified COT Controls	Q2 for double pole	K_z Expression
COT with External Ramp	$Q_2=\frac{2}{\pi(1+2s_e/s_f)}$	$1+\frac{s}{Q_z\omega_2}+\frac{s^2}{\omega_2^2}$ *Where,* $\omega_2=\frac{\pi}{T_{sw}}, Q_z=\frac{2}{\pi}$
COT V^2 Control	$Q_2=\frac{T_{sw}}{(R_{Co}C_o-\frac{T_{on}}{2})\pi}$	1
COT V^2 Control with External Ramp	$Q_2=\frac{T_{sw}}{[(1+\frac{2S_e}{S_f})R_{Co}C_o-\frac{T_{on}}{2}]\pi}$	1
IQCOT	$Q_2=\frac{2s_fT_{sw}}{\pi(\frac{2CV_{TH}}{g_mT_{sw}}-s_fT_{on})}$	1

COT structure. The following table shows the different Q value for different control. In case of COT with Se, in the $S_e = S_f$ which is a very common industry practice, which makes Q-value very low, i.e. Q=0.2. If the S_e is larger to improve the noise immunity, the Q-value will be even smaller.

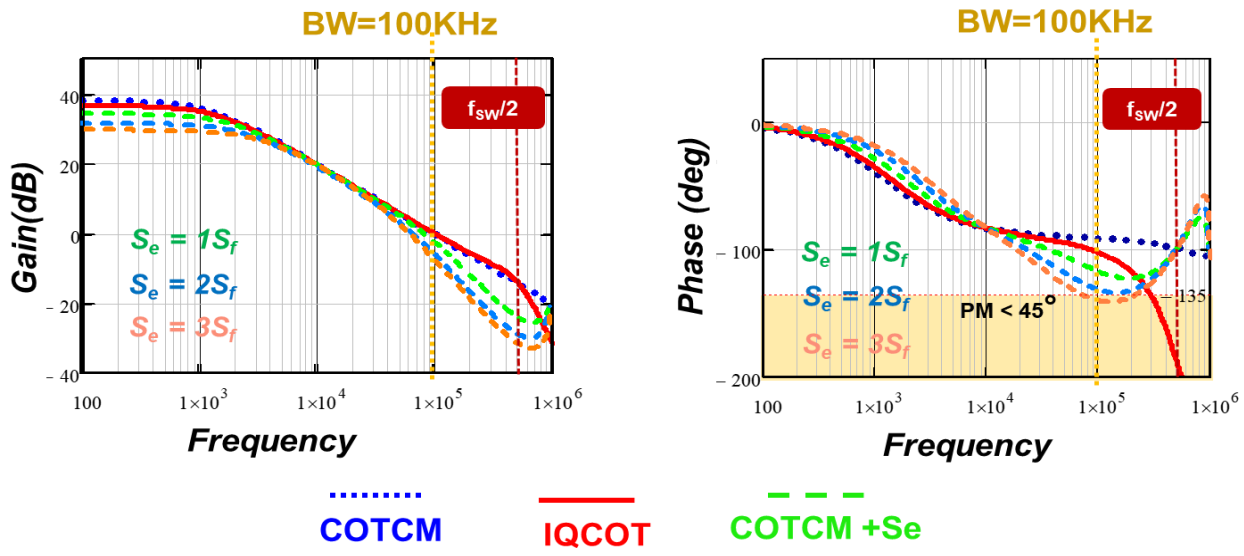

Figure 5.21 Loop gain comparison of IQCOT with COT and COT+Se control at different Se.

With the increment of Se, double pole basically split and one pole move toward the lower frequency, as described in [B.15]. In Figure 5.21, loop gain (with proportional gain compensator) comparison of proposed IQCOT control with conventional constant on-time (COT) control and COT control with external ramp (COT+Se) are given. The circuit parameters are - V_{IN}=12, V_o=1.2, f_{sw}= 1MHz, L=220nH, C_o=1.12mF, Ri=1.5m, g_m=50mS, V_{TH}=2, C_T=220pF, Q=1.

It can be seen in the Figure 5.21 that, increasing the Se will reduce the bandwidth. From the phase margin point of view, in case of COT with external ramp, first phase drops for split low frequency pole and then goes up for zero in the half of the switching frequency. Hence, in Figure

5.21, up to 200KHz phase of IQCOT control is better than COT with Se. If bandwidth is set below 200KHz, the phase margin for IQCOT will be better.

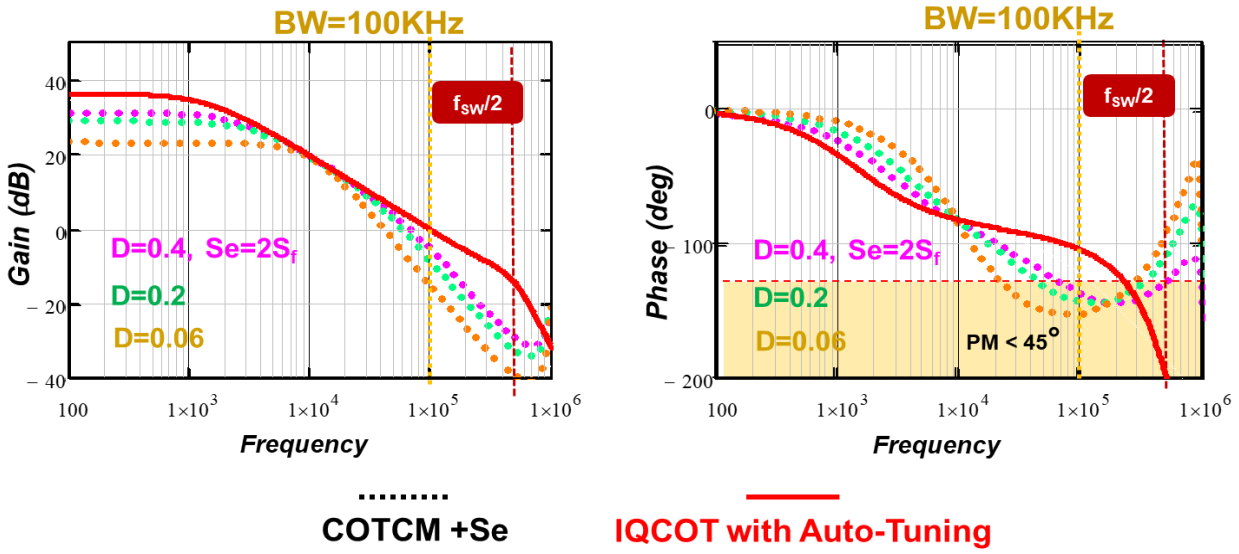

Figure 5.22. Loop gain comparison of IQCOT with COT and COT+Se control at different D.

In Figure 5.22, the phase margin variation with different duty cycle for COTCM+Se and IQCOT control are shown. In case of COTCM+Se, the bode plot curves are presented in dotted lines. First, the external ramp (Se) is fixed as $Se=2S_f$ for D=0.4, where the circuit parameters are: V_{IN}=5.2V, Vo=2V, f_{sw}= 1MHz, L=220nH, C_o=1.12mF, Ri=1.5m, g_m=50mS, V_{TH}=2, C_T=220pF, Q=1. Then the Se value is kept fixed and duty cycle is changed to different value like D=0.2 (V_{IN}=6V, Vo=1.2V) and D=0.06 (V_{IN}=8.4V, Vo=0.5V). The Figure 5.22 shows that for a fixed external ramp value, the phase margin is dropping with the decrement of duty cycle and make the loop more unstable for COTCM+Se control. But for the case of IQCOT, as the Q-value is almost constant with duty cycle variation, one red curve can represent the IQCOT loop gain in Figure 5.22. As, loop gain is almost unchanged in IQCOT control with proposed auto-tuning method, once the Q-value is set for one duty cycle, then no need to worry about the duty cycle variation for IQCOT control.

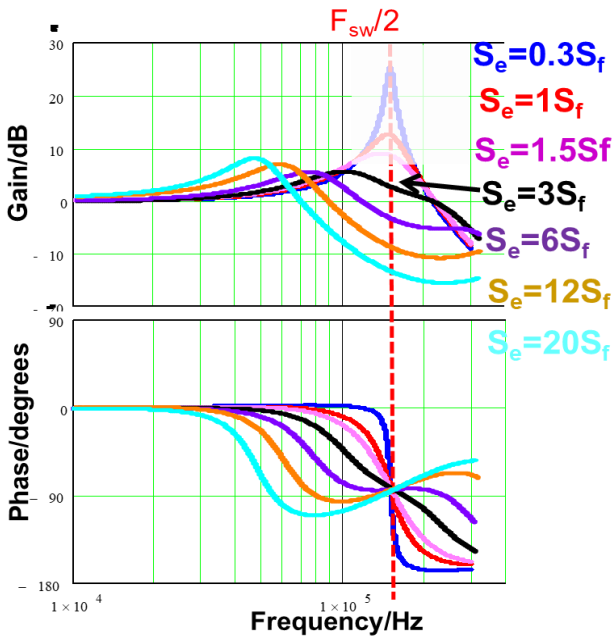

Figure 5.23 Vo/Vc small signal property of V2 COT control with external ramp [E.20]

In case of V^2 control with external ramp [E.20][E.21] shows that with increment of Se, one set of double pole moves towards the origin which makes the phase margin lower, as presented in Figure 5.23. Therefore, V^2 with Se also suffers from the same issues like COTCM with Se, in comparison to IQCOT control.

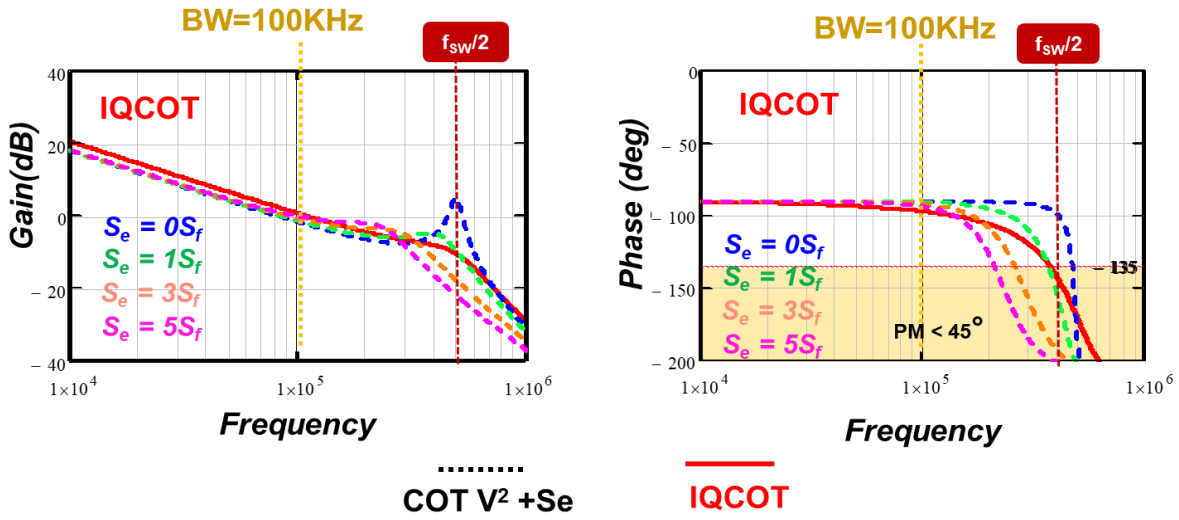

Figure 5.24 Loop gain comparison of IQCOT with COT and V^2+Se control at different Se.

In Figure 5.24, the loop gain comparison between V^2 COT control with external ramp and IQCOT control has been presented. IQCOT control is modelled with type II compensator for non AVP case. It can be seen that the phase margin is similar for both the controls at BW=100KHz. Another thing is, the phase margin in V^2 COT control with external ramp is dropping with the increment of external ramp which makes the control design more challenging with larger external ramp.

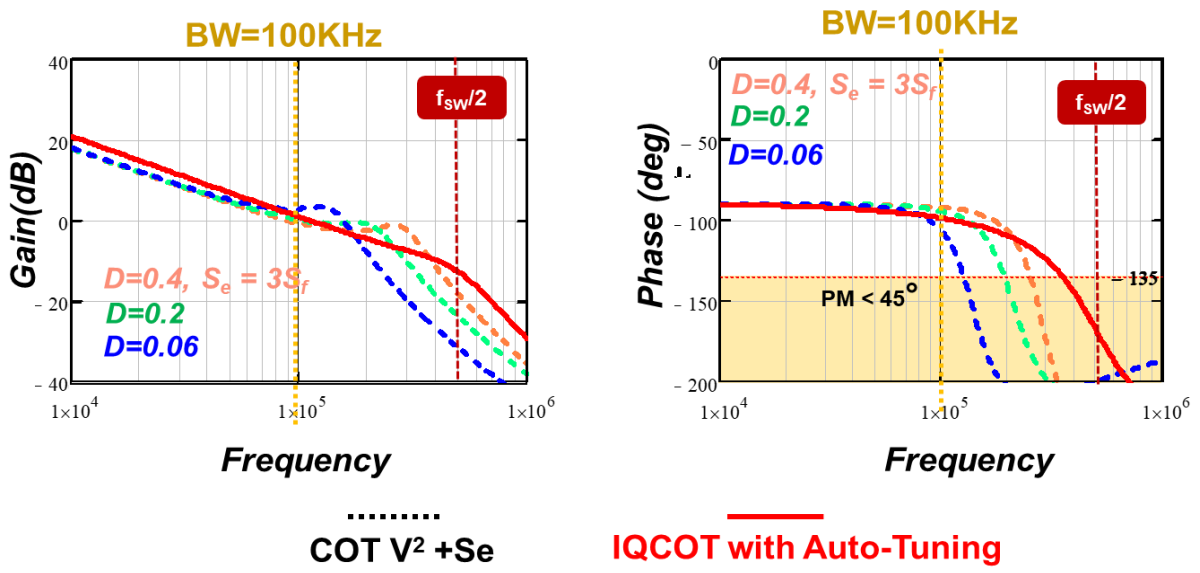

Figure 5.25 Loop gain comparison of IQCOT with COT and V^2+Se control at different D.

In Figure 5.25, the phase margin variation with different duty cycle for both V^2 COT and IQCOT control are shown. In case of V^2 COT control, the bode plot curves are presented in dotted lines. First the external ramp (Se) is fixed as $Se=3S_f$, for D=0.4 where the circuit parameters are: V_{IN}=5.2V, Vo=2V, f_{sw}= 1MHz, L=220nH, C_o=1.12mF, Ri=1.5m, g_m=50mS, V_{TH}=2, C_T=220pF, Q=1. Then the Se value is kept fixed and duty cycle is changed to different value like D=0.2 (V_{IN}=6V, Vo=1.2V) and D=0.06 (V_{IN}=8.4V, Vo=0.5V). The Figure 5.25 shows that for a fixed

external ramp value, the phase margin is dropping with the decrement of duty cycle and make the loop more unstable for V^2 COT control. But for the case of IQCOT, as the Q-value is almost constant with duty cycle variation for Q-value auto-tuning, one red curve can represent the IQCOT loop gain in Figure 5.25. One the Q-value is set for one duty cycle, there are not much variation in loop gain with duty cycle variation for IQCOT control.

5.7 Summary

A high frequency model for proposed IQCOT control has been derived using describing function in this section which matched with simulation and hardware test results very well. Q-value variation with D and its safe operating range with control design guideline has been discussed. Then an auto-tuning method by changing g_m and V_{TH} for Q-value control is also proposed. The high frequency characteristics of proposed IQCOT control is compared with COT control along with other modified COT controls.

Chapter 6. Conclusion

6.1 Summary of the Dissertation

The current-mode control architecture has been a very good candidate to fulfill the AVP requirement in multiphase voltage regulators (VRs) for the microprocessor applications. In the future, more critical transient requirements of multi-core microprocessors and higher power-density demands of VRs will impose a new challenge on the multiphase VRs to perform good transient response with minimum number of output capacitors. Although idle most of the time, it wakes up in nanoseconds to support sudden workload demands, which are becoming increasingly severe in today's multi-core processors with large core count. From the standpoint of its voltage regulator (VR) design, it must have very good efficiency at light loads, while also supporting a very fast transient response. Thus, the variable-frequency constant on-time current-mode (COTCM) control scheme is widely used in the VRs, as it can automatically reduce its switching frequency during light-load conditions. From the transient point of view, it has some limitations in response to heavy-load demands by microprocessors; this is resolved by adding different nonlinear controls in state-of-the-art control schemes. These nonlinear controls are difficult to optimize for the widely variable transient conditions in processors. Another major issue for this ripple-based COTCM control is that when the combined inductor-current ripple in multiphase operation becomes zero because of the ripple-cancellation effect, COTCM loses its controllability. Therefore, the goal of this research is to discover a new adaptive COT control scheme that is concurrently very efficient at light-load conditions and also provides a fast and optimized transient

response without adding any nonlinear control; hence providing a complete solution for today's high-performance microprocessors.

Firstly, the overview of state-of-the-art COTCM control is discussed in detail, and its limitations are analyzed. Analysis shows that one issue plaguing the COTCM control is its slow transient response in both single and multiphase operation. Chapter 1 presents two methods that have been proposed to improve the transient performance of conventional COTCM control in single and multiphase operation. These two methods can effectively reduce the output capacitor count in system, but the ripple-cancellation issues in multiphase operation remain unresolved. This provides motivation to search for a new COT control technique that can solve all these problems.

Therefore, a new concept of inverse charge constant on-time (IQCOT) control is proposed to replace the conventional ripple-based COTCM; the goals are to improve noise immunity at the ripple-cancellation point without adding any external ramp into the system, and to improve the load step-up transient performance in multiphase operation by achieving natural and linear pulse overlapping without adding any nonlinear control. Additionally, the transient performance of the proposed IQCOT has been further improved by naturally increasing or decreasing the T_{ON} time during the load step-up or step-down transient period without adding any nonlinear control. As this transient property is inherent in proposed IQCOT control, it is adaptive to the widely variable transient requirements of processors, and always produces an optimized transient response.

In order to design the proposed control with high bandwidth for supporting fast transient response, an accurate high-frequency small-signal model needs to be derived. Therefore, a high-frequency model for the proposed IQCOT control is derived using the describing function method. The model is also verified by simulation and hardware results in different operating conditions.

From the derived model it is found that the quality factor (Q) of one double-pole set varies with changes in duty cycle. To overcome this challenge, an auto-tuning method for Q-value control is also proposed in this dissertation.

6.2 Future Work

The proposed IQCOT control has been implemented with constant on-time control and variable on-time variable off-time control to demonstrate different benefits. Proposed concept can also be implemented with other control schemes for different types of application. In the implementation proposed Q-value auto-tuning concept, auto-tuning is shown by changing one parameter only. Conceptually, auto-tuning can be done by changing few other circuit parameters as well. In future, different implementation by changing different parameters can be done along with their optimization for different applications.

Appendix A. 'FastAOT' Control Design Details

Motivation and concept of proposed 'Fast Adaptive On-time (FastAOT) control has been discussed in chapter 2 section 2.3. Implementation method -1 for proposed concept has also been presented in the same section. In this appendix the other implementation methods and design guidelines of FastAOT control is discussed.

A1. Details of FastAOT Implementation Method - 2

Another implementation of the proposed 'Fast Adaptive On Time (FastAOT)' is presented in Figure A.1, where the ramp generating current in the T_{ON} generator (I_{RAMP}) is controlled to increase or decrease the on time, T_{ON}. In Figure A.1, the proposed circuit is shown inside the red box while the circuit implementation of T_{ON} generator is shown inside the box.

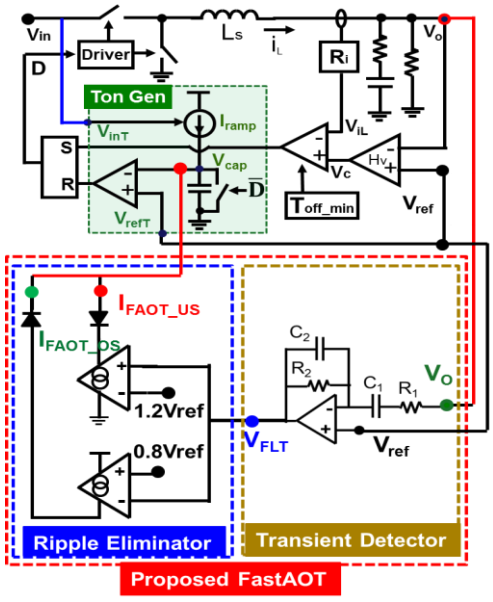

Figure A.1 Implementation for proposed 'FastAOT' control method-2

In this method, after detecting the undershoot or overshoot at the output voltage, the band pass filter produces signal V_{FLT} in the same way implementation -1 (same 'Transient Detector' block). Then this V_{FLT} voltage signal is converted into a current by using the transconductance (g_m) amplifiers. The waveforms for the undershoot and overshoot case are shown in Figure A.2 (a). In the load step up case in Figure A.2 (a), when V_{FLT} crosses a predefined threshold voltage (i.e. 1.2 V_{REF}), transconductance amplifier g_{m1} generates a pulling down current (I_{FAOT_US}) which is subtracted from the ramp generating current (I_{RAMP}) in the T_{ON} generator circuit. This will reduce the cap charging current I_{CAP} which will reduce the slope of the V_{CAP}. Hence, it will increase the on time (T_{ON}) in the T_{ON} generator circuit.

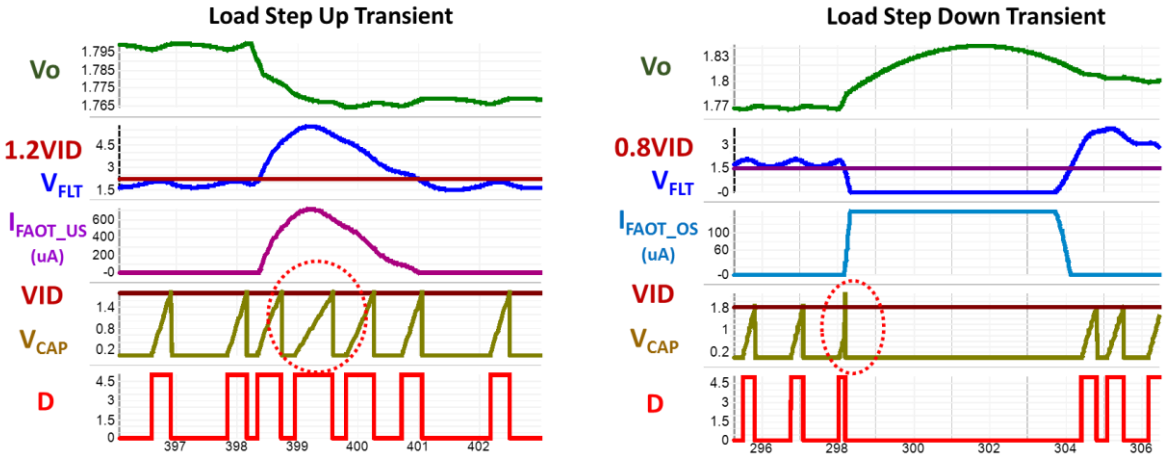

(a) (b)

Figure A.2 Transient response of implementation method #2; (a) load step-up, (b) load step-down

A load step down case is shown in Figure A.2(b), where we can see that when the band pass filter detects an overshoot in the output, the filter output V_{FLT} falls immediately and a push up current is generated in g_{m2} when V_{FLT} cross $0.8V_{ref}$ (predefined threshold in this example). This current will be added with the original ramp generating current (I_{RAMP}) in the T_{ON} generator block and increase the ramp in the V_{CAP} (shown by the red circle in Figure A.2) immediately to end the

on time without any delay. In this way T_{ON} is truncated right after an overshoot has occurred at the output to reduce the overshoot amplitude.

A2. Optimization of Method -2 for Single Step Response at Load Step Up Transient

In the proposed 'FastAOT' method the T_{ON} extension can be controlled by modifying the transonductance gain (g_m) of the two operational tranconductance amplifiers (OTAs). In Figure A.3, the key waveforms of the load step up transient are shown with a higher g_m1 value where it can be clearly seen that after transient occurs, I_{CAP} starts decreasing and becomes zero. Then the V_{CAP} also stops increasing and becomes flat. When V_{FLT} starts decreasing, I_{CAP} and V_{CAP} also start

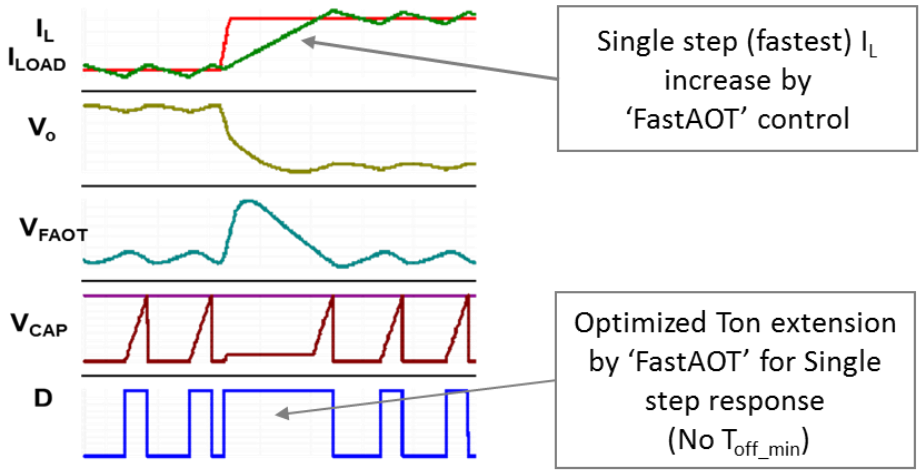

Figure A.3 Single step response at Load step-up in proposed FastAOT implementation method -2

increasing and at some point touch VID to end T_{ON}. In the implementation of method -2, if a very high g_{m1} is used, then I_{FAOT_US} will be very large immediately after transient occurs and the cap charging current (I_{CAP}) will be zero or negative. For proper operation, I_{CAP} needs to be clamp to zero to avoid the cap discharging as I_{FAOT_US} is very large. When I_{CAP} will be zero, it will stop charging the cap and V_{CAP} will also be flat at that time and hence, will increase the T_{ON} in the T_{ON}

generator circuit to achieve single step response. Figure A.3 shows the example of increasing the I_L in one step in method -2 at load step up transient using optimized T_{ON} extension without any overcorrection.

A3. Design Guideline for 'Transient Detector' and 'Ripple Eliminator' Blocks

The 'Transient Detector' block in the proposed 'FastAOT' method is a band pass filter which allows the undershoot or overshoot part of the output signal to pass to the next stage. From the band pass design point of view, the objective is to maximize the pass band for the band pass filter. But there are some limitations in maximizing this pass band. The structure of the band pass filter and lower and higher frequency cutoff points in a band pass filter gain curve are shown in Figure A.4.

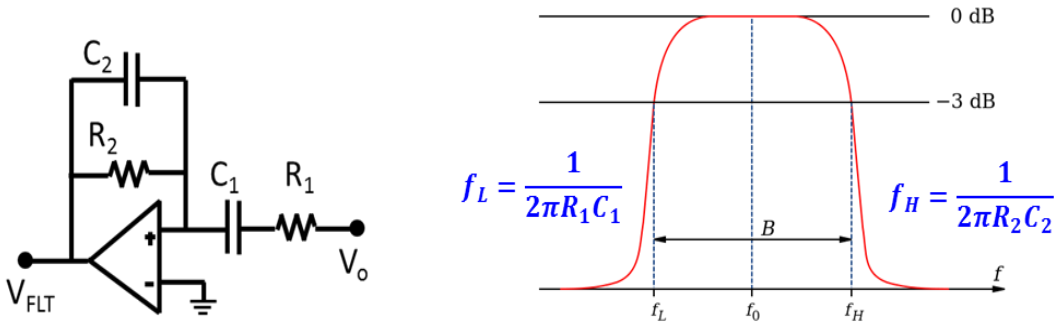

(a) (b)

Figure A.4 Band Pass Filter and its gain curve with high and low cut off frequencies

i) Design Guideline for Setting the Higher Cutoff frequency, f_H

According to expression of higher cutoff frequency (f_H), it can be set by selecting R_2 and C_2 values. There is a tradeoff in setting f_H. From a design point of view f_H is desired to be set at as high a frequency as possible in order to maximize the bandwidth of the filter. However, the problem is that the output ripple at the switching frequency will also be amplified to a very large

value and will be very difficult to eliminate. Therefore, f_H cannot be set very high. On the other hand, if f_H is set at very low frequency, gain for the required frequency to increase the undershoot or overshoot part of the output signal will not be high enough to increase T_{ON} significantly.

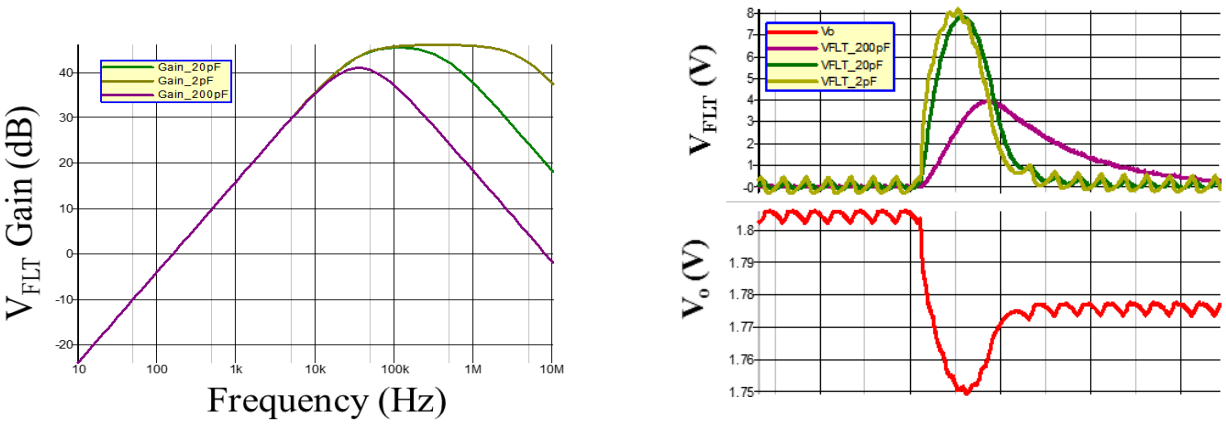

(a) (b)

Figure A.5 Effect of different C2 in band pass filter (a) Gain curve, (b)Vo undershoot

In the Figure A.5 (a) using the SIMPLIS simulator, simulation of gain curve for filter output V_{FLT} is given for different values of C_2 like 2pF, 20pF and 200pF with R_2=20kΩ, R_1=100Ω and C_1=50nF while corresponding transient simulation results of filter output V_{FLT} for certain Vo undershoot are shown in Figure A.5 (b). It can clearly be observed that the green curve with C_2= 20pF is preferable than the other two choices as it has a high enough bandwidth to capture the undershoot properly with a reasonably lower ripple value shown in Figure A.5 (b).

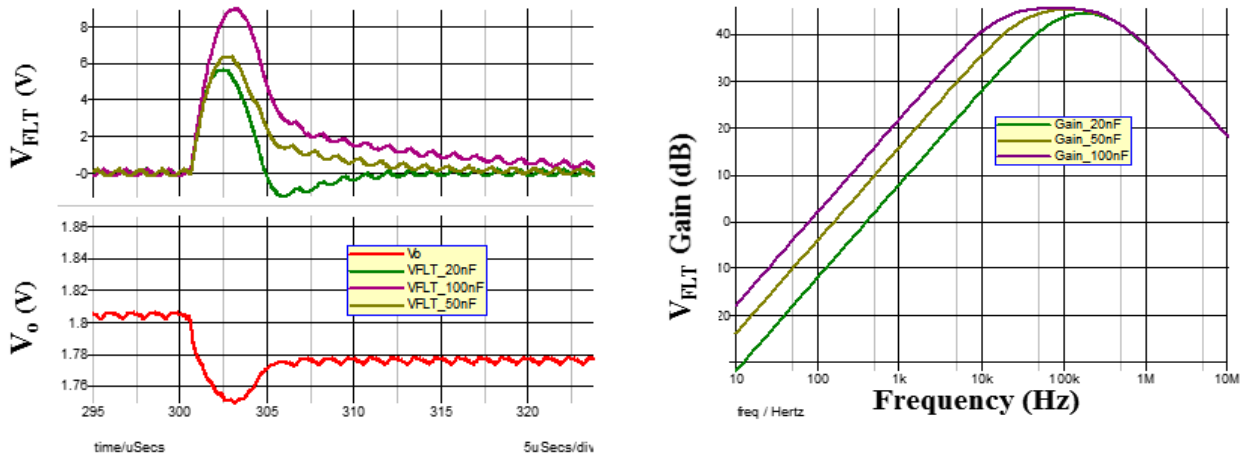

(a) (b)

Figure A.6 Effect of different C1 in band pass filter (a) Gain curve, (b) Vo undershoot

ii) Design Guideline for Setting the Lower Cutoff frequency f_L:

The lower cutoff frequency, f_L can be set by selecting the capacitor C_1 and resistance R_1 in the band pass filter. Increasing the value for the C_1, the f_L will move left toward the lower frequency and will increase the bandwidth of the band pass filter. Hence, it is definitely desirable to set the value of C_1 as high as possible. But increasing the C_1 value has some boundaries. In the Figure A.6 (a) the output of the filter V_{FLT} has been plotted for the C_1 value = 20nF, 50nF and 100nF while R_1=100Ω with R_2=20kΩ and C_2=20pF. It can be seen in Figure A.6 (a) that amplitude of the filter output is increasing with a higher value of C_1, but at the same time because of the higher gain at the lower frequency, the settling time for the peak of V_{FLT} has been increased. This may keep the T_{ON} extension even after the undershoot is over which is not desirable. The second problem with increasing C_1 too much is that it will take more space in the board or IC. Therefore, from Figure A.6 (b) it is clearly evident that the proper choice to set the value for C_1 will be some value between 20nF to 50nF considering other elements' value constant.

iii) Design Guideline for Ripple Eliminator Block:

After designing the band pass filter properly, there should be a small enough ripple which can be easily eliminated in the ripple eliminator stage. In method -1, if the ripple amplitude is less than V_{BE}, then they can be easily eliminated. If this ripple amplitude is more than V_{BE} but less than $2V_{BE}$, then two cascaded transistors can be used to eliminate the ripple. For method -2 it is even easier. The threshold voltages in Op-Amp g_{m1} and g_{m2} need to be adjusted to eliminate the ripple, depending on the ripple amplitude at filter output V_{FLT}. For example, if g_m1/g_m2 gain is set high for single step response, then ripple will also be high unless higher order band pass filter is used. In that case, threshold voltages in 'Ripple Eliminator' block also need to be set higher.

A.4 Proposed 'FastAOT' Implementation Method -3:

As, we mentioned before, Vc can also be used instead of Vo in the FastAOT method. As shown in Figure A.7, the polarity of the band pass filter output has to be inverted as the polarity of the Vc is opposite to Vo. The example shown in Figure A.7 uses the 'Ripple Eliminator' block and T_{ON}

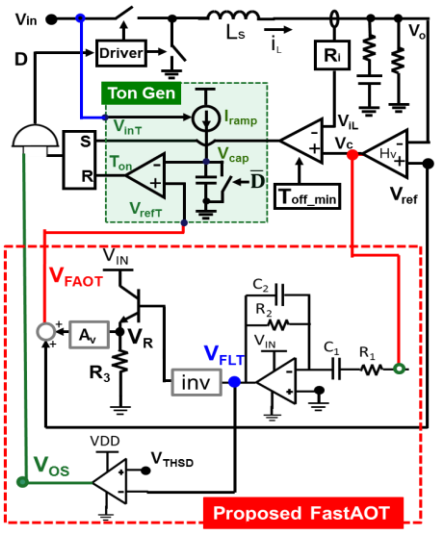

Figure A.7 Proposed Implementation -3 for 'Fast Adaptive On-Time (FastAOT)' control

modification are same as method-1. But, obviously the 'Ripple Eliminator' block and T_{ON} modification can be the same as method -2 without any change in the 'Transient Detector' block. In comparison between method-1 and method-2, method-1 uses the reference voltage in T_{ON} generator circuit to change the T_{ON} while method-2 modifies the capacitor charging current to do so. In board level design where voltage manipulation is easier than current, method-1 will be certainly more applicable. At the same time, method-2 can be more appropriate in IC level design where current manipulation is more common design tactics. Furthermore, if the compensator is fast enough, the transient detection technique in method-3 can be used with better noise performance.

Appendix B. Describing Function Derivation for IQCOT Control

The appendix provides the detail derivations for the describing functions used in the modeling of proposed inverse charge constant on-time control.

B1. Details of $v_c(t)$ and $i_L(t)$ integration

The integration of $v_c(t)$ and $i_L(t)$ can be done separately. The integration of $v_c(t)$ is given below:

$$
\begin{aligned}
&\int_{t_{i-1}+T_{off(i-1)}}^{t_i+T_{off(i)}} v_c(t)dt \\
&= \int_{t_{i-1}+T_{off(i-1)}}^{t_i+T_{off(i)}} r_0 + \hat{r}\sin(2\pi f_m t - \theta)dt \\
&= r_0(T_{on}+T_{off(i)}) - \frac{\hat{r}}{2\pi f_m}[\cos\{2\pi f_m(t_i+T_{off(i)}) - \theta\} - \cos\{2\pi f_m(t_{i-1}+T_{off(i-1)}) - \theta\}] \\
&= r_0(T_{on}+T_{off(i)}) - \frac{\hat{r}}{\pi f_m}\sin\{\pi f_m(t_i+T_{off(i)}+t_{i-1}+T_{off(i-1)}) - \theta\}.\sin\{\pi f_m(t_i+T_{off(i)}-t_{i-1}-T_{off(i-1)})\} \\
&= r_0(T_{on}+T_{off(i)}) - \frac{\hat{r}}{\pi f_m}\sin\{\pi f_m(T_{on}+T_{off(i)})\}.\sin\{\pi f_m(t_i+T_{off(i)}+t_{i-1}+T_{off(i-1)}) - \theta\} \\
&\approx r_0(T_{on}+T_{off(i)}) - \frac{\hat{r}}{\pi f_m}\sin(\pi f_m \cdot T_{sw})\cdot\sin\{2\pi f_m \cdot [(i-1)T_{sw} - \frac{T_{on}-T_{off}}{2}] - \theta\}
\end{aligned}
\tag{B1}
$$

The integration of iL(t) is given below:

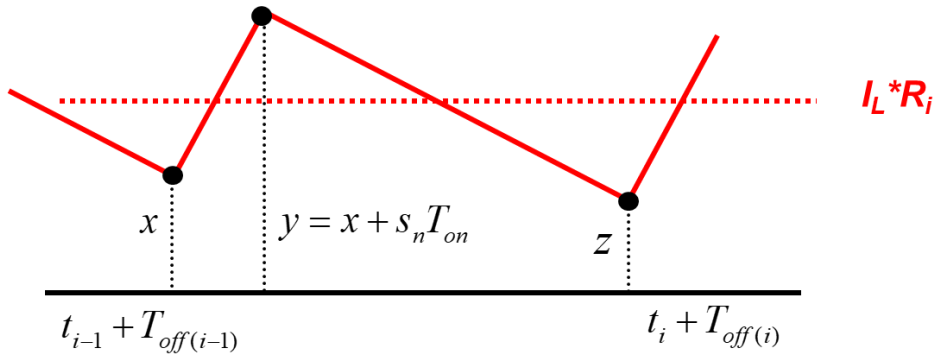

$$x = I_L R_i - \frac{1}{2} s_f T_{off} - s_f \sum_{k=1}^{i-1} \Delta T_{off(k)}$$
$$z = I_L R_i - \frac{1}{2} s_f T_{off} - s_f \sum_{k=1}^{i} \Delta T_{off(k)} \quad \text{(B2)}$$

$$\int_{t_{i-1}+T_{off(i-1)}}^{t_i+T_{off(i)}} i_L(t).R_i dt = \frac{1}{2} T_{on}(x+y) + \frac{1}{2}(T_{off} + \Delta T_{off(i)})(y+z)$$
$$= \frac{1}{2} T_{on}[2I_L R_i - s_f T_{off} - 2s_f \sum_{k=1}^{i-1} \Delta T_{off(k)} + s_n T_{on}] + \frac{1}{2}(T_{off} + \Delta T_{off(i)})[2I_L R_i - s_f T_{off} - s_f \sum_{k=1}^{i-1} \Delta T_{off(k)} - s_f \sum_{k=1}^{i} \Delta T_{off(k)} + s_n T_{on}]$$
$$= \frac{1}{2} T_{on}[2I_L R_i - 2s_f \sum_{k=1}^{i-1} \Delta T_{off(k)}] + \frac{1}{2}(T_{off} + \Delta T_{off(i)})[2I_L R_i - s_f \sum_{k=1}^{i-1} \Delta T_{off(k)} - s_f \sum_{k=1}^{i} \Delta T_{off(k)}]$$
$$= [T_{on} I_L R_i - T_{on} s_f \sum_{k=1}^{i-1} \Delta T_{off(k)}] + (T_{off} + \Delta T_{off(i)}) I_L R_i - \frac{1}{2}(T_{off} + \Delta T_{off(i)})[2s_f \sum_{k=1}^{i-1} \Delta T_{off(k)} + s_f \Delta T_{off(i)}]$$
$$= (T_{on} + T_{off} + \Delta T_{off(i)}) I_L R_i - T_{on} s_f \sum_{k=1}^{i-1} \Delta T_{off(k)} - \frac{1}{2}(T_{off} + \Delta T_{off(i)})[2s_f \sum_{k=1}^{i-1} \Delta T_{off(k)} + s_f \Delta T_{off(i)}]$$
$$= (T_{sw} + \Delta T_{off(i)}) I_L R_i - (T_{sw} + \Delta T_{off(i)}) s_f \sum_{k=1}^{i-1} \Delta T_{off(k)} - \frac{1}{2}(T_{off} + \Delta T_{off(i)})[s_f \Delta T_{off(i)}]$$
$$= T_{sw} I_L R_i + \Delta T_{off(i)} I_L R_i - T_{sw} s_f \sum_{k=1}^{i-1} \Delta T_{off(k)} - \Delta T_{off(i)} s_f \sum_{k=1}^{i-1} \Delta T_{off(k)} - \frac{1}{2} T_{off} s_f \Delta T_{off(i)}$$
$$= T_{sw} I_L R_i - T_{sw} s_f \sum_{k=1}^{i-1} \Delta T_{off(k)} + [I_L R_i - s_f \sum_{k=1}^{i-1} \Delta T_{off(k)} - \frac{1}{2} T_{off} s_f] \Delta T_{off(i)} \quad \text{(B3)}$$

B2. Calculation details of T_{off} derivation and C_m Calculation

As in the steady state operation, each cycle charge is equal, it can be written that-

$$\int_{t_{i-1}+T_{off(i-2)}}^{t_i+T_{off(i-1)}} v_c(t)dt - \int_{t_{i-1}+T_{off(i-2)}}^{t_i+T_{off(i-1)}} i_L(t) R_i dt = \int_{t_{i-1}+T_{off(i-1)}}^{t_i+T_{off(i)}} v_c(t)dt - \int_{t_{i-1}+T_{off(i-1)}}^{t_i+T_{off(i)}} i_L(t) R_i dt = \frac{C_T V_{th}}{g_m}$$

This equation can be rewritten as-

$$\int_{t_{i-1}+T_{off(i-2)}}^{t_i+T_{off(i-1)}} v_c(t)dt - \int_{t_{i-1}+T_{off(i-1)}}^{t_i+T_{off(i)}} v_c(t)dt = \int_{t_{i-1}+T_{off(i-2)}}^{t_i+T_{off(i-1)}} i_L(t) R_i dt - \int_{t_{i-1}+T_{off(i-1)}}^{t_i+T_{off(i)}} i_L(t) R_i dt \quad \text{(B4)}$$

Calculating the left hand side of (A4):

$$\int_{t_{i-1}+T_{off(i-2)}}^{t_i+T_{off(i-1)}} v_c(t)dt - \int_{t_{i-1}+T_{off(i-1)}}^{t_i+T_{off(i)}} v_c(t)dt$$
$$= r_0(T_{off(i-1)} - T_{off(i)}) - \frac{\hat{r}}{\pi f_m}\sin(\pi f_m \cdot T_{sw}) \cdot [\sin\{2\pi f_m \cdot [(i-2)T_{sw} - \frac{T_{on}-T_{off}}{2}] - \theta\} - \sin\{2\pi f_m \cdot [(i-1)T_{sw} - \frac{T_{on}-T_{off}}{2}] - \theta\}]$$

Calculating the right hand side of (A4):

$$\int_{t_{i-1}+T_{off(i-2)}}^{t_i+T_{off(i-1)}} i_L(t)R_i dt - \int_{t_{i-1}+T_{off(i-1)}}^{t_i+T_{off(i)}} i_L(t)R_i dt$$
$$= T_{sw}s_f \Delta T_{off(i-1)} + [I_L R_i - \frac{1}{2}T_{off}s_f]\Delta T_{off(i-1)} - [I_L R_i - \frac{1}{2}T_{off}s_f]\Delta T_{off(i)} + s_f \sum_{k=1}^{i-1} \Delta T_{off(k)}\Delta T_{off(i)} - s_f \sum_{k=1}^{i-2} \Delta T_{off(k)}\Delta T_{off(i-1)}$$
$$= [I_L R_i - \frac{1}{2}T_{off}s_f + T_{sw}s_f]\Delta T_{off(i-1)} - [I_L R_i - \frac{1}{2}T_{off}s_f]\Delta T_{off(i)}$$

Therefore, using equation (A.4)

$$[\frac{C_T V_{th}}{g_m} + \frac{1}{2}s_f T_{off}]\Delta T_{off(i)} + [s_f T_{sw} - (\frac{C_T V_{th}}{g_m} + \frac{1}{2}s_f T_{off})]\Delta T_{off(i-1)}$$
$$= \frac{\hat{r}}{\pi f_m}\sin(\pi f_m \cdot T_{sw}) \cdot [\sin\{2\pi f_m[(i-2)\cdot T_{sw} - \frac{T_{on}-T_{off}}{2}] - \theta\} - \sin\{2\pi f_m[(i-1)\cdot T_{sw} - \frac{T_{on}-T_{off}}{2}] - \theta\}] \quad \text{(B5)}$$

Then, the perturbed duty cycle d(t) and inductor current $i_L(t)$ can be expressed by:

$$d(t)\Big|_{0\le t\le t_M+T_{off(M)}+T_{on}} = \sum_{i=1}^{M}[u(t-t_i-T_{off(i)}) - u(t-t_i-T_{off(i)}-T_{on})] \quad \text{(B6)}$$

$$i_L(t)\Big|_{0\le t\le t_M+T_{off(M)}+T_{on}} = \int_0^t [\frac{V_{in}}{L_s}d(t) - \frac{V_o}{L_s}]dt + i_{L0} \quad \text{(B7)}$$

After that, Fourier analysis can be performed on the $i_L(t)$ as:

$$c_m = j\frac{2f_m}{N}\int_0^{t_M+T_{off(M)}+T_{on}} i_L(t)\cdot e^{-j2\pi f_m t}dt$$

$$c_{m(i_L)} = \frac{1}{N\pi}\frac{V_{in}}{L_s} e^{-j2\pi f_m T_{off}} (e^{-j2\pi f_m T_{on}} - 1)\sum_{i=1}^{M}[e^{-j2\pi f_m [(i-1)T_{sw}]} \cdot \sum_{k=1}^{i} \Delta T_{off(k)})] \quad \text{(B8)}$$

where c_m is the Fourier coefficient of $i_L(t)$ at the perturbation frequency f_m.

Therefore, it can be written that-

$$Ac_{m(i_L)} + Bc_{m(i_L)} e^{-j2\pi f_m T_{sw}} = \frac{1}{N\pi}\frac{V_{in}}{L_s} e^{-j2\pi f_m T_{off}} (e^{-j2\pi f_m T_{on}} - 1)\sum_{i=1}^{M}[e^{-j2\pi f_m [(i-1)T_{sw}]} \cdot \sum_{k=1}^{i} (A\Delta T_{off(k)} + B\Delta T_{off(k-1)})] \quad \text{(B9)}$$

Where, $A = (\frac{C_T V_{th}}{g_m} + \frac{1}{2} s_f T_{off}), \quad B = s_f T_{sw} - (\frac{C_T V_{th}}{g_m} + \frac{1}{2} s_f T_{off})$

Hence, $C_m(i_L)$ can be derived from (B9) as:

$$c_{m(i_L)} = \frac{1}{N\pi}\frac{V_{in}}{L_s} e^{-j2\pi f_m T_{off}} (e^{-j2\pi f_m T_{on}} - 1)\sum_{i=1}^{M}[e^{-j2\pi f_m [(i-1)T_{sw}]} \cdot \sum_{k=1}^{i} [\frac{A\Delta T_{off(k)} + B\Delta T_{off(k-1)}}{A + Be^{-j2\pi f_m T_{sw}}}] \quad \text{(B10)}$$

By substituting value of A and B in (B10), the coefficient can be calculated as:

$$c_m = \frac{V_o}{sL}\frac{1}{sT_{on}} \cdot [\frac{(1 - e^{-sT_{on}}).(1 - e^{-s\frac{V_{in}T_{on}}{V_o}})}{(\frac{C_T V_{th}}{g_m} + s_f T_{off}) + [s_f \frac{V_{in}T_{on}}{V_o} - (\frac{C_T V_{th}}{g_m} + s_f T_{off})]e^{-s\frac{V_{in}T_{on}}{V_o}}}](\hat{r}e^{-j\theta}) \quad \text{(B11)}$$

References

A. Introduction

[A.1] Intel document, "Moore's law timeline," available at http://download.intel.com/pressroom/kits/events/moores_law_40th/MLTimeline.pdf.

[A.2] Intel document, "Multicore: the software view," available at http://download.intel.com/corporate/education/emea/event/af12/files/cownie.pdf.

[A.3] S. Rusu, "High-performance digital – 2013 Trends," *IEEE International Solid-State Circuits Conf. (ISSCC)'13*, pp. 9-11, Nov. 2012, available at http://isscc.org/doc/2013/2013_Trends.pdf.

[A.4] Intel document, "Enhanced Intel SpeedStep technology for the Intel Pentium M processor," in *Intel White Paper*, Mar. 2004, available at http://download.intel.com/design/network/paper/30117401.pdf.

[A.5] Intel document, "Intel Centrino Duo mobile technology," in *Intel Technology Journal*, Volume 10, Issue 02, May. 2006, available at http://www.intel.com/technology/itj/2006/volume10issue02/.

[A.6] R. Basmadjian, S. Rainer, and H. deMeer, "A generic methodology to derive empirical power consumption prediction models for multi-core processors," in *IEEE Cloud and Green Computing (CGC)'13*, pp. 167-174, Sept. 2013.

[A.7] H. Esmaeilzadeh, E. Blem, R. S. Amant, K. Sankaralingam, and D. Burger, "Power challenges may end the multicore era," in *Communications of the ACM*, vol. 56, no. 2, Feb. 2013.

[A.8] Intel document, "First the tick, now the tock: Intel microarchitecture (Nehalem)," Feb. 2009, available at http://www.intel.com/content/dam/doc/white-paper/intel-microarchitecture-white-paper.pdf.

[A.9] Glenn HinTon, "Key Nehalem choices," Feb. 2010, available at http://web.standford.edu/class/ee380/Abstracts/100217.html.

[A.10] S. Chennupaty, H. Jiang, and A. Sreenivas, "Technology insight: Intel's next generation 14nm microarchitecture for client and server," in Intel Developer Forum (IDF) 2014.

[A.11] Intel document, "Voltage regulator module (VRM) and enterprise voltage regulator-down (EVRD) 12.5 design guidelines," Dec. 2013, available at http://www.intel.com.

[A.12] Intel document, "Voltage regulator module (VRM) and Enterprise voltage regulator-down (EVRD) 11.1Design Guidelines," Sept. 2009, available at http://www.intel.com.

[A.13] ASUS document, "MAXIMULS III FORMULA user's manual," Sept. 2009, available at http://www.asus.com.

[A.14] Pei-Hsin Liu, "Advanced Control Schemes for High-Bandwidth Multiphase Voltage Regulators" *Ph. D Dissertation,* Virginia Tech, 2015.

[A.15] K. Yao, Y. Meng P. Xu and F.C. Lee, "Design considerations for VRM transient response based on the output impedance," in *Proc. IEEE APEC,* 2002, pp. 14-20.

[A.16] K.Yao, Y. Ren, J. Sun, K. Lee, M. Xu, J. Zhou, and F. C. Lee, "Adaptive voltage position design for voltage regulators," in *Proc. IEEE APEC,* 2004, pp. 272–278.

[A.17] Intel document, "Shark Bay desktop and Denlow-WS platform," Sept. 2012, available at http://www.intel.com.

[A.18] Jia Wei and Fred C. Lee, "Two-stage voltage regulator for laptop computer CPUs and corresponding advanced control schemes to improve light-load performance," in *Proc. IEEE Appl. Power Electron. Conf. (APEC'04),* 2004, pp. 1294-1300.

[A.19] Yuancheng Ren, Ming Xu, Kaiwei Yao, Yu Meng, Fred C.Lee and Jinghong Guo, "Two-stage approach for 12V VR," in *Proc. IEEE Appl. Power Electron. Conf. (APEC'04)*, 2004, pp. 1306-1312.

[A.20] Jia Wei, "High frequency high-efficiency voltage regulators for future microprocessors," *Ph. D Dissertation,* Virginia Tech, 2004.

[A.21] Yuancheng Ren, "High frequency, high efficiency two-stage approach for future microprocessors," *Ph. D Dissertation,* Virginia Tech, 2005.

[A.22] Intel document, "Narrow VDC Extended Battery Life (EBL) technique," Sept, 2003, available at http://www.intel.com.

[A.23] X. Li, P. Li, and G. Jayakanthan, "Evaluation of narrow Vdc-based power delivery architecture in mobile computing system," *IEEE Trans. Industry Applications.*, vol. 47, no. 6, Nov. 2011.

[A.24] X. Liang, G. Jayakanthan, and M. Wang, "Design consideration for narrow Vdc based

power delivery architecture in mobile computing system," in *IEEE APEC'10 Conf.*, pp. 794-800

[A.25] A. Uan-Zo-li, and A. keates, "Power delivery architecture and design," in *Intel Ultrabook for Shark Bay Platform Enabling Training,* Jun. 2012.

[A.26] C. Chen, D. Chen, M. Lee, and E. K. Tseng, "Design and modeling of a novel high-gain peak current control scheme to achieve adaptive voltage positioning for DC power converters," in *Proc. IEEE PESC'08 Conf.,* Jun. 2008.

[A.27] RT8856 datasheet, "Multi-phase PWM controller for CPU core power supply," available on http://www.richtek.com.

[A.28] R2J20751NP datasheet, "Peak current mode synchronous buck controller, with Power MOSFETs," available on http://am.renesas.com.

[A.29] Y. Qiu, J. Sun, M. Xu, K. Lee, and F. C. Lee, "Bandwidth improvements peak-current controlled voltage regulators," *IEEE Trans. Power Electron.*, vol. 22, no. 4, pp. 1253-1260, Jul. 2007.

[A.30] X. Duan and A. Q. Huang, "Current-mode variable-frequency control architecture for high-current low-voltage DC-DC converters," *IEEE Trans. Power Electron.*, vol. 21, no. 4, pp. 1133-1137, Jul. 2006.

[A.31] Y. Chen, D. Chen, Y. Lin, and C. Chen, "A novel constant on-time current mode control Scheme to achieve adaptive voltage positioning for DC power converters," in *Proc. IEEE IECON,* pp. 104-109, Oct. 2012.

[A.32] Texas Instruments document, "Single-phase, D-CAP and D-CAP2 controller with 2-bit flexible VID control," available at http://www.ti.com.

[A.33] Pit-Leong Wong and Fred C. Lee, "Switching Action Delays in Voltage Regulator Modules," APEC 2002.

[A.34] Texas Instruments document, "Application Report- Multiphase Buck Design" available on http://www.ti.com.

[A.35] Y. Yan, F. C. Lee, and P. Mattavelli, "Comparison of small signal characteristics in current mode control schemes for point-of-load buck converter applications," *IEEE Trans., Power Electron.*, vol. 28, no. 7, pp. 3405−3414, Jul. 2013.

[A.36] Y. Yan, F. C. Lee, and P. Mattavelli, "Unified three-terminal switch model for current

mode controls," *IEEE Trans. Power Electron.*, vol. 27, no. 9, pp. 4060-4070, Sept. 2012.

[A.37] Y. Yan, "Unified three-terminal switch model for current mode controls," in *Master Thesis*, Virginia Tech, Nov. 2010.

[A.38] K. Cheng, F. Yu, Y. Yan, and F. C. Lee, "Analysis of Multi-phase Hybrid Ripple-Based Adaptive On-time Control for Voltage Regulator Modules," in Proc. IEEE APEC'12, pp.1088−1095.

[A.39] Texas Instruments, "TPS51650A Datasheet: Dual-Channel (3-Phase CPU/1-Phase GPU) SVID, D-CAP+TM Step-Down Controllers for IMVP-7 VCORE with Two Integrated Drivers," www.ti.com

[A.40] J. Sun, "Characterization and performance comparison of ripple based control for voltage regulator modules," IEEE Trans. Power Electron.,vol. 21, no. 2, pp. 347-353, Mar. 2006.

B. Overview of state-of-the-art constant on-time current mode control

[B.1] Hung-Chih Lin, Bou-Ching Fung, and Tsin-Yuan Chang "A Current Mode Adaptive On-Time Control Scheme for Fast Transient DC-DC Converters" in Proc. IEEE ISCAS'08, pp. 2602-2605.

[B.2] B. Sahu, "Analysis and design of a fully-integrated current sharing scheme for multi-phase adaptive on-time modulated switching regulators," in *Proc. IEEE PESC'08 Conf.*, pp. 3829-3835.

[B.3] C. Cheng, J. Huang, and C. Li, "Circuit and methods for constant on-time control for an interleaved multiphase voltage regulator," U.S. Patent, no. US 8159197 B2, Apr. 2012.

[B.4] Texas Instruments, TPS59650 datasheet, available at http://www.ti.com.

[B.5] Richtek, RT8859 datasheet, available at http://www.richtek.com.

[B.6] ST electronics, "Clocked Asynchronous DC/DC Controllers", http://sites.amd.com/, 2011

[B.7] C. B. Umminger, R. G. Flatness, "Circuit and Methods for Synchronizing Non-constant Frequency Switching regulators with a Phase Locked Loop," U.S. Patent US 2002/0180413, issued Dec., 2002.

[B.8] Linear Technology, LTC3709 datasheet, available at http://www.linear.com.

[B.9] US 20040257056 A1: "Switching regulator with improved load transient efficiency and method thereof" by Jian-Rong Huang (Hsinchu City, Taiwan) Dec 23, 2004

[B.10] J. Quintero, M. Sanz, A. Lázaro, C. Fernández, A. Barrado, "Reduction of the Switching Frequency and the Number of Phases in multiphase VRM by applying Linear – Non – Linear Control," PESC06.

[B.11] US 20130314060 A1 : "Load Transient of a Cot Mode Power Supply" by Richtek Corp. Pub: Nov 2013

[B.12] Maxim Integrated Products, MAX17085B datasheet, 'Integrated Charger, Dual Main Step-Down Controllers, and Dual LDO regulators', http://www.maxim-ic.com

[B.13] Richtek Technology Corporation, RT8888C datasheet, '3-Phase Controller with Triple Integrated Driver for VR12.5 Mobile CPU Core Power Supply', http://www.richtek.com

[B.14] Texas Instruments, TPS53525 datasheet, available at http://www.ti.com.

[B.15] S. Tian, F. C. Lee, Q. Li, J. Li, and P. Liu, "Equivalent circuit model of constant on-time current mode control with external ramp compensation," in Proc. IEEE ECCE'14, pp. 3747-3754.

[B.16] "3-Phase+1-Phase, D-CAP+ step down controller for IMVP7 CPU/GPU Vcore, TPS51640 datasheet," Texas Instruments document.

[B.17] "3-Phase+1-Phase, Quick-PWM Controller for VR12/IMVP7, MAX17039 datasheet," Maxim document.

[B.18] http://www.ti.com/http://www.ti.com/S. Bari, Q. Li, and F. C. Lee, "Fast adaptive on time control for transient performance improvement," in Proc. IEEE APEC 2015, pp. 397-403.

[B.19] Y. Ren, K.Yao, M. Xu, and F. C. Lee, "The analysis of the power delivery path from 12 V VR to the microprocessor," in Proc. IEEE Applied Power Electronics Conf. Expo, 2004, pp. 285–291.

[B.20] S. Bari, B. Cheng, Q. Li, and F. C. Lee, "Variable Slope External Ramp to Improve the Transient Performance in Constant On-Time Current Mode Control" in Proc. IEEE ECCE 2016.

C. Concept of inverse charge constant on time (IQCOT) control

[C.1] A. Capel, “Charge controlled conversion principle in dc/dc regulators combines dynamic performance and high output power,” in P roc. IEEE Power Electron. Specialists’ Conf.’, 1979, pp. 264-276.

[C.2] A. S. Kislovski, “A new control principle for switching regulators,” in Proc. PCIlMotorcon, 1983, pp. 175-186.

[C.3] A. S. Kislovski, R. Redl, and N. 0. Sokal, Dynamic Analysis of Swifching-mode DCiDC Converters. New York: Van Nostrand Rein- hold, 1991.

[C.4] D. W. Edwards, “A new offline converter topology draws sinusoidal input current,” in Proc. of POWERCON 11, 1984.

[C.5] A. R. Prasad, P. 0. Ziogas, and S. Manias, “A new active power factor correction method for single-phase buck-boost ac-dc converter,” in Proc. IEEE Applied Power Electron. Conf.. 1992, pp. 814820.

[C.6] W. Tang, F. C. Lee, R. B. Ridley, and I. Cohen, “Charge control: modeling, analysis, and design,” IEEE Trans. Power Electron., vol. 8, pp. 396-403, Oct. 1993.

[C.7] S. Bari, Q. Li, and F. C. Lee, “A new current mode control for higher noise immunity and faster transient response in multi-phase operation” in Proc. IEEE ECCE 2015, pp. 2078-2083.

[C.8] S. Bari, Q. Li, and F. C. Lee, “A New Current Mode Constant On Time Control with Ultrafast Load Transient Response” in Proc. IEEE APEC’16, pp. 3259-3265.

[C.9] Patent App US20150280556A1: S. Bari, et al, “Inverse Charge Current Mode (IQCM) Control for Power Converter”

[C.10] T. F. Schiff, “Switching power supply control,” *U.S. Patent,* no. US7595617, Sept. 2009

[C.11] G. Chen, and T. F. Schiff, “Power supply control circuits including enhanced ramp pulse modulation,” *U.S Patent,* no. US8148966, Apr. 2012.

[C.12] K. Lee, and H. Zou, “Comparison between ramp pulse modulation (RPM) and constant frequency modulation for the beat frequency oscillation in voltage regulators,” in *Proc. IEEE ECCE’10,* pp. 3101-3106, Sept. 2010.

[C.13] Monolithic Power Systems document, “4-phase PWM controller for VR12.5 Applications,” available at http://www.MonolithicPower.com.

D. Transient Response of IQCOT Control

[D.1] Hung-Chih Lin, Bou-Ching Fung, and Tsin-Yuan Chang “A Current Mode Adaptive On-Time Control Scheme for Fast Transient DC-DC Converters” in Proc. IEEE ISCAS’08, pp. 2602-2605.

[D.2] C. B D. Goder and W. R. Pelletier, “V2 architecture provides ultra-fast transient response in switch mode power supplies," in proc. HFPC’96, pp. 19-23.

[D.3] D. Goder, “Switching regulators,” U.S. Patent, 5,770,940, 1998.

[D.4] (2009,Jul.)Texas Instruments, TPS51116 datasheet, http://focus.ti.com/lit/ds/symlink/ tps51116.pdf.

[D.5] (2012,Jun.)Monolithic power systems, MP38900 datasheet, http://www.monolithicpower.com/.

[D.6] (2009, Sep.)Maxim, MAX1545 datasheet, http://datasheets.maxim-ic.com/en/ds/MAX1519MAX1545.pdf.

[D.7] (2013, Feb.)National Semiconductor, LM34919 datasheet, http://www.national.com/ds/LM/ LM34919.pdf.

[D.8] (2008, Mar.)Intersil, ISL6237 data sheet, www.intersil.com/data/fn/fn6418.pdf.

[D.9] J. Cortes, V. Svikovic, P. Alou, J. Oliver and J. Cobos, “Comparison of the behavior of Voltage Mode, V2 and V2Ic control of a buck converter for a very fast and robust dynamic response,” in Proc. IEEE APEC, 2014, pp.2888-2894.

[D.10] G. Zhou, J. Xu, J. Sha, and Y. Jin,” Valley V2 Control Technique for Switching Converters with Fast Transient Response,” in Proc. IEEE ECCE Asia, 2011, pp. 2788-2791.

[D.11] Y. Lin, C. Chen, D. Chen, B. Wang , “A Ripple-Based Constant On-Time Control With Virtual Inductor Current and Offset Cancellation for DC Power Converters,” IEEE Trans. Power Electron., vol. 27, no. 10, pp.4301-4310, Oct. 2012.

[D.12] C. Tsai, S. Lin, and C. Huang, "A Fast-Transient Quasi-V2 Switching Buck Regulator Using AOT Control With a Load Current Correction (LCC) Technique," IEEE Trans. Power Electron., vol. 28, no. 8, pp. 3949-3957,Aug, 2013.

[D.13] W. Chen, J. Chen, T. Liang, L. Wei, J. Huang, and W. Ting, "A Novel Quick Response of RBCOT With VIC Ripple for Buck Converter," IEEE Trans. Power Electron., vol. 28, no. 9,pp. Sep, 2013.

[D.14] W. Huang and J. Clarkin, "Analysis and design of multiphase synchronous buck converter with enhanced V2 control," in Proc. HFPC,2000, pp. 74–81.

[D.15] S. Tian, F. C. Lee, P. Mattavelli, K. Cheng and Y. Yan, "Small-signal Analysis and Optimal Design of External Ramp for Constant On-Time V2 Control with Multilayer Ceramic Caps," IEEE Trans. Power Electron., vol.29, no.8, pp.4450-4460, Aug. 2014.

[D.16] (2017, Jun) Monolithic power systems, MPQ8636 datasheet: High Efficiency, 4/10/20A, 18V Synchronous, Step-Down Converter, http://www.monolithicpower.com/.

[D.17] (2017, Mar) Monolithic power systems, MPM3840 datasheet: 2.8V-5.5V, 4A, Power Module, Synchronous Step-Down Converter with Integrated Inductor, http://www.monolithicpower.com/.

E. High Frequency Model for IQCOT Control

[E.1] R. D. Middlebrook, "Topics in multiple-loop regulators and current mode programming," in Proc. IEEE Power Electron. Spec. Conf., 1985, pp. 716– 732.

[E.2] S. P. Hsu, A. Brown, L. Rensink, and R. D. Middlebrook, "Modeling and analysis of switching dc-to-dc converters in constant-frequency current programmed mode," in Proc. IEEE Power Electron. Spec. Conf., 1979, pp. 284–301.

[E.3] D. J. Packard, "Discrete modeling and analysis of switching regulators," Ph.D. dissertation, Dept. Electr. Eng., Cal. Tech., CA, May 1976.

[E.4] A. R. Brown and R. D. Middlebrook, "Sample-data modeling of switched regulators," in Proc. IEEE Power Electron. Spec. Conf., 1981, pp. 349–369.

[E.5] F. D. Tan and R. D. Middlebrook, "A unified model for current programmed converters,"

IEEE Trans. Power Electron., vol. 10, no. 4, pp. 397–408, Jul. 1995.

[E.6] R. B. Ridley, "A new, continuous-time model for current-mode control," IEEE Trans. Power Electron., vol. 6, no. 2, pp. 271–280, Apr. 1991.

[E.7] G. C. Verghese, C. A. Bruzos, and K. N. Mahabir, "Averaged and sample data models for current mode control: A reexamination," in Proc. IEEE Power Electron. Spec. Conf., 1989, pp. 484–491.

[E.8] R. Redl, "High-frequency extension of the small-signal model of the constant-frequency current-mode-controlled converter," in Proc. IEEE Appl. Power Electron. Conf., 1991, pp. 466–472.

[E.9] R. Tymerski and D. Li, "State-space models for current-programmed pulse width-modulated converters," IEEE Trans. Power Electron., vol. 8, no. 3, pp. 271–278, Jul. 1993.

[E.10] D. J. Perreault and G. C. Verghese, "Time-varying effects and averaging issues in models for current-mode control," IEEE Trans. Power Electron., vol. 12, no. 3, pp. 453–461, May 1997.

[E.11] E. A. Mayer and A. J. King, "An improved sampled-data current-mode control which explains the effects of the control delay," IEEE Trans. Power Electron., vol. 16, no. 3, pp. 369–374, May 2001.

[E.12] B. Bryant and M. K. Kazimierczuk, "Modeling the closed-current loop of PWM dc-dc converters operating in CCM with peak current-mode control," IEEE Trans. Circuits Syst., vol. 52, no. 11, pp. 2404–2412, Nov. 2005.

[E.13] N. Kondrath and M. K. Kazimierczuk, "Control current and relative stability of peak current-mode controlled pulse-width modulated dc-dc converters without slope compensation," IET Power Electron., vol. 3, no. 6, pp. 936–946, Nov. 2010.

[E.14] M. K. Kazimierczuk, Pulse-Width Modulated DC-DC Power Converters. Chichester, U.K: Wiley, 2008.

[E.15] N. Kondrath and M. K. Kazimierczuk, "Loop gain and margins of stability of inner-current loop of peak current-mode-controlled PWM dcdc converters in continuous conduction mode," IET Proc. Power Electron., vol. 4, no. 6, pp. 701–707, 2011.

[E.16] Y. Jang and R. W. Erickson, "Physical origins of input filter oscillations in current programmed converters," IEEE Trans. Power Electron., vol. 7, no. 4, pp. 725–733, Oct.

1992.

[E.17] S.-Y. Chen and J.-J. Chen, "Study of the effect and design criteria of the input filter for buck converters with peak current-mode control using a novel system block diagram," IEEE Trans. Ind. Electron., vol. 55, no.8,pp. 3159–3166, Aug. 2008.

[E.18] J. Sun, "Small-signal modeling of variable-frequency pulse width modulators," IEEE Trans. Aerosp. Electron. Syst., vol. 38, no. 3, pp. 1104–1108, Jul. 2002.

[E.19] J. Li and F. C. Lee, "New modeling approach and equivalent circuit representation for current-mode control," IEEE Trans. Power Electron., vol. 25, no. 5, pp. 1218–1230, May 2010.

[E.20] S. Tian, F. C. Lee, P. Mattavelli, K. Cheng and Y. Yan, "Small-signal Analysis and Optimal Design of External Ramp for Constant On-Time V2 Control with Multilayer Ceramic Caps," IEEE Trans. Power Electron., vol.29, no.8, pp.4450-4460, Aug. 2014.

[E.21] S. Tian, K.Y. Cheng, F. C. Lee and P. Mattavelli, "Small-signal model analysis and design of constant on-time V2 control for low-ESR caps with external ramp compensation," in Proc. IEEE ECCE, 2011, pp. 2944-2951.

---------- Thank You ----------